



HAL
open science

Shipborne Global Navigation Satellite Systems for Offshore Atmospheric Water Vapor Monitoring

Aurélie Panetier

► **To cite this version:**

Aurélie Panetier. Shipborne Global Navigation Satellite Systems for Offshore Atmospheric Water Vapor Monitoring. Electronics. ENSTA Bretagne - École nationale supérieure de techniques avancées Bretagne, 2023. English. NNT : 2023ENTA0011 . tel-04639124v2

HAL Id: tel-04639124

<https://hal.science/tel-04639124v2>

Submitted on 24 Sep 2024

HAL is a multi-disciplinary open access archive for the deposit and dissemination of scientific research documents, whether they are published or not. The documents may come from teaching and research institutions in France or abroad, or from public or private research centers.

L'archive ouverte pluridisciplinaire **HAL**, est destinée au dépôt et à la diffusion de documents scientifiques de niveau recherche, publiés ou non, émanant des établissements d'enseignement et de recherche français ou étrangers, des laboratoires publics ou privés.

THÈSE DE DOCTORAT DE

L' ENSTA BRETAGNE

ÉCOLE DOCTORALE N° 648
Sciences Pour l'Ingénieur et le Numérique
Spécialité : *Électronique*

Par

Aurélie PANETIER

Shipborne Global Navigation Satellite Systems for Offshore Atmospheric Water Vapor Monitoring

Système Mondial de Navigation par Satellite Embarqué sur Porteur Marin pour
l'Observation de la Vapeur d'Eau Atmosphérique en Mer

Thèse présentée et soutenue à Brest, le 21 Décembre 2023
Unité de recherche : Lab-STICC UMR 6285

Rapporteurs avant soutenance :

Olivier BOCK
Laurent MOREL

Directeur de Recherche, Ministère de l'Écologie, IGN/IPGP, Paris, FR
Professeur des Universités, Directeur ESGT, Le Mans, FR

Composition du Jury :

Présidente : Marie-Noëlle BOUIN
Examineur : Laurent DUSSEAU
Examineur : Jean-Marc LE CAILLEC
Dir. de thèse : Ali KHENCHAF
Encadrant : Pierre BOSSER

Chargée de Recherche, CNRM, Brest, FR
Professeur des Universités, CSUM, Montpellier, FR
Professeur, IMT Atlantique, Brest, FR
Professeur des Universités, ENSTA Bretagne, Brest, FR
Enseignant-Chercheur, ENSTA Bretagne, Brest, FR

SHIPBORNE GLOBAL NAVIGATION SATELLITE SYSTEMS FOR OFFSHORE
ATMOSPHERIC WATER VAPOR MONITORING

AURÉLIE PANETIER

Systeme Mondial de Positionnement par Satellite Embarqué sur Porteur Marin pour l'Observation de
la Vapeur d'Eau Atmosphérique en Mer

21 Décembre 2023 – ENSTA Bretagne, Brest, France

Aurélie PANETIER: *Shipborne Global Navigation Satellite Systems for Offshore Atmospheric Water Vapor Monitoring*, © December 21th, 2023

SUPERVISEURS:

Direction: Ali KHENCHAF

Encadrement: Pierre BOSSER

ÉTABLISSEMENT:

École Nationale Supérieure de Techniques Avancées Bretagne, Brest

À ma plus fidèle compagne.



Diskette
2008 – 2024

ABSTRACT

Vous trouverez le résumé en français ci-après.

The Global Navigation Satellite System (GNSS) is mostly known as a positioning tool. However, it has also established itself in the field of meteorology and climate studies. Indeed, in order to get more precise positioning, the delay caused by the passing of the signal through the troposphere between the satellites and the receiver has to be precisely determined. GNSS turns out to be an accurate tool for measuring atmospheric precipitable water vapor.

To compensate for the lack of offshore measurement for water vapor monitoring, several studies applied this process to shipborne GNSS antennas. Indeed, ships are constantly sailing the oceans from one part of the world to another, carrying GNSS antennas useful for navigation. The data measurement is then already set, waiting to be processed. Although more and more studies are showing the contribution of this measurement technique to offshore water vapor monitoring, the assessment of the shipborne GNSS data processing strategy is not set yet.

This thesis proposes an automation of shipborne GNSS data processing. The work is based on three main axes.

First, we study the water vapor retrieval from GNSS antennas. It relies on the general knowledge of GNSS data processing technique, and the highlight of the precipitable water vapor retrieval from the GNSS solution. Moreover, a state of the art analyzing the main studies that have been published about shipborne GNSS water vapor monitoring is set up. The implemented processing strategies and their statistical results of comparison to usual water vapor measuring techniques are carefully investigated. This permits us to underline the need to assess the impact of the GNSS processing strategy on the quality of the retrieved water vapor.

Second, we establish a processing strategy suitable for water vapor retrieval from shipborne GNSS antenna measurements. The aim is to release a better-performing processing strategy for water vapor retrieval specifically from shipborne GNSS antennas. A bunch of processing scenarii are applied to a real dataset in the first instance, and then to a home-made simulated dataset. The real dataset comes from the ENSTA Bretagne survey vessel used for teaching the hydrography and robotic fields students. The different processing strategies are assessed by comparing the GNSS solutions to external data and to the initial simulated signal for the survey vessel and the simulation respectively.

Third, we estimate and assess the troposphere water vapor from five research vessels of the French Oceanographic Fleet (FOF), operated by IFREMER (France). The optimum processing strategy highlighted before was applied to the GNSS acquired by the FOF during their research campaigns between 2015 and 2022, in an automated process suitable for the considered binary dataset.

This thesis brings novelty to the field of research through the recommendation of a GNSS processing strategy suitable for offshore water vapor retrieval; as well as the development of an algorithm for the automated water vapor retrieval from long-term binary GNSS datasets from several ships. The offshore water vapor retrieval all around the globe shows the suitability of the precipitable water vapor from shipborne

GNSS for the global climate study. This processing algorithm could be adapted to routine measurement of water vapor established on a ship, to use this data for weather forecasting.

RÉSUMÉ

Ce manuscrit de thèse est rédigé en anglais, cependant un résumé étendu en français est disponible en Annexe D.

Dans le but d'améliorer la précision du calcul de la position d'une antenne du Système Mondial de Navigation par Satellite GNSS - communément connu sous le nom de GPS, il est nécessaire de déterminer le retard dû à la propagation de l'onde dans l'atmosphère. Ce retard a lieu lorsque le signal GNSS traverse la troposphère, entre son émission par le satellite et sa réception par l'antenne. Ce retard, estimé en parallèle de la position dans l'analyse GNSS, est dû à la présence de vapeur d'eau dans l'atmosphère. Il est directement lié à la vapeur d'eau précipitable nécessaire à la prévision météorologique, et à l'étude climatique. En tant que technologie permettant une mesure précise de la vapeur d'eau précipitable contenue dans l'atmosphère, le GNSS s'est peu à peu imposé comme outil de mesure atmosphérique, au service de l'étude du climat et de la prévision météorologique à terre.

Afin de pallier le manque d'observation de la vapeur d'eau atmosphérique en mer, différentes études ont eu l'idée d'appliquer ce processus à des antennes GNSS embarquées sur porteur marin. En effet, les océans sont sans cesse sillonnés de bateaux équipés d'antennes GNSS de tout type utiles à la navigation. La donnée est donc déjà présente, et ne demande qu'à être valorisée. Cependant, si de plus en plus d'études sont publiées afin de montrer l'apport de cette technologie à l'étude de l'atmosphère hauturière, l'influence de la configuration de l'analyse de la donnée GNSS en positionnement ponctuel précis cinématique n'est pas abordée.

Les travaux de recherche menés durant cette thèse ont pour objectif de proposer une automatisation de l'analyse de données GNSS d'antennes embarquées sur porteur marin. Ils sont menés en trois étapes principales.

La première partie repose sur l'étude du processus d'extraction de la vapeur d'eau par analyse de données GNSS. Elle se compose, d'une part, de la compréhension du processus d'analyse de données GNSS, et de la mise en exergue de la possibilité d'extraire de la solution GNSS l'information de vapeur d'eau précipitable. D'autre part, l'élaboration d'un état de l'art complet des études publiées jusqu'à présent, portant sur l'extraction de vapeur d'eau précipitable à partir de données d'antennes GNSS embarquées sur bateau. Les stratégies d'analyse adoptées dans ces études, ainsi que les différences obtenues par comparaison avec des données provenant de techniques usuelles de mesure de vapeur d'eau atmosphérique, sont étudiées en détail. Cela permet de souligner la nécessité d'évaluer l'impact du choix de la stratégie d'analyse GNSS sur la qualité de la vapeur d'eau extraite.

La deuxième partie consiste en l'établissement d'une stratégie d'analyse, afin de révéler une configuration adaptée au positionnement ponctuel précis cinématique d'une antenne embarquée sur bateau. Ces travaux se basent sur une multitude d'analyses de données GNSS faisant intervenir différentes combinaisons de configuration d'analyse. Les données GNSS permettant d'effectuer ces tests proviennent de la vedette hydrographique de l'ENSTA Bretagne à Brest, ainsi que de signaux provenant d'une antenne GNSS embarquée en mer, simulés par un algorithme développé pour l'occasion. L'évaluation des différentes configurations d'analyse GNSS est effectuée en comparant

les estimations à partir des données réelles à des données de référence provenant de différents capteurs localisés dans le port de Brest. L'évaluation des estimations provenant des signaux simulés est effectuée, quant à elle, par comparaison aux séries temporelles issues des simulations initiales.

La troisième partie repose sur l'estimation et l'analyse de la troposphère au-dessus des routes de cinq navires de recherche de la Flotte Océanographique Française (FOF) opérée par l'IFREMER. La configuration optimale retenue en deuxième étape a ensuite servi à analyser les données de la FOF acquises lors des campagnes océanographiques effectuées entre 2015 et 2022, dans un processus d'analyse automatisée adaptée aux jeux de données binaires variés considérés. La vapeur d'eau précipitable ainsi extraite est évaluée par comparaison à d'autres sources de données.

La recommandation d'une modélisation de l'analyse GNSS adaptée à l'observation de la vapeur d'eau atmosphérique en mer ; ainsi que le développement d'un algorithme pour la récupération automatisée de la vapeur d'eau à partir d'un jeu de donnée GNSS binaire, sur le long terme et impliquant plusieurs navires, constituent l'originalité de cette thèse. La récupération de la vapeur d'eau lors d'une multitude de campagnes océanographiques autour du globe permet de montrer en conditions réelles la bonne adéquation de l'extraction de vapeur d'eau précipitable par GNSS embarqué sur bateau à l'étude climatique. Une adaptation de cet algorithme de calcul à des données provenant d'une routine de mesure mise en place sur un bateau pourrait permettre d'utiliser cette donnée à des fins de prévision météorologique.

PUBLICATIONS

▷ *Publication dans les actes d'une conférence :*

Aurélié Panetier, Pierre Bosser, and Ali Khenchaf. "Sensitivity of Shipborne GNSS Troposphere Retrieval to Processing Parameters." In: Springer, 2022. DOI: [10.1007/1345_2022_177](https://doi.org/10.1007/1345_2022_177)

▷ *Présentations orales dans des conférences :*

Aurélié Panetier, Pierre Bosser, and Ali Khenchaf. "Investigation of shipborne GNSS ZTD retrieval processing parameters by simulation." In: *EGU General Assembly Conference Abstracts*. Vol. 2022. 2022, EGU22-5237. DOI: [10.5194/egusphere-egu22-5237](https://doi.org/10.5194/egusphere-egu22-5237)

Aurélié Panetier et al. "Retrieval of Six Years of ZTD Over the Oceans from a French Oceanographic Fleet Vessel Shipborne GNSS Antenna." In: *AGU Fall Meeting Abstracts*. Vol. 2022. 2022, G33A-02

▷ *Publication dans une revue à comité de lecture :*

Aurélié Panetier, Pierre Bosser, and Ali Khenchaf. "Sensitivity of Shipborne GNSS Estimates to Processing Modeling Based on Simulated Dataset." In: *Sensors* 23.14 (2023), p. 6605. DOI: [10.3390/s23146605](https://doi.org/10.3390/s23146605)

▷ *Autres publications :*

Pierre Bosser et al. "A low-cost GNSS buoy for water vapour monitoring over the Oceans." In: *EGU General Assembly Conference Abstracts*. Vol. 2022. 2022, EGU22-1811. DOI: [10.5194/egusphere-egu22-1811](https://doi.org/10.5194/egusphere-egu22-1811)

REMERCIEMENTS

« Lorsque deux forces sont jointes, leur efficacité est double » - Isaac Newton

Ce manuscrit est l'aboutissement de trois ans de travaux de recherche intenses. Durant ma thèse de doctorat, j'ai dû apprendre à conjuguer lecture de la littérature, analyse de données, interprétation de résultats, communication scientifique et rédaction. Je tiens donc à adresser mes remerciements aux personnes qui m'ont accompagnée jusqu'à l'aboutissement de mes travaux.

En premier lieu, je tiens à remercier mon directeur de thèse, Ali Khenchaf. Il m'a fait bénéficier de son expérience du monde de la recherche, m'écartant ainsi de quelques écueils. Il m'a motivée et guidée pour atteindre dans les temps chaque étape qui jalonne le parcours du doctorant, me menant ainsi à une soutenance dès la fin de ma troisième année, tout en développant un parcours engagé dans les instances administratives.

De même, merci à mon encadrant Pierre Bosser, tout d'abord pour m'avoir donné l'opportunité de travailler sur un sujet aussi passionnant, alliant ingénierie et recherche académique. Il a accompagné mes premiers pas en géodésie, une discipline fondamentale et méconnue dans laquelle je m'épanouis professionnellement aujourd'hui. D'autre part, il m'a accompagnée tout au long de mes travaux de thèse, de l'analyse des données jusqu'aux deux relectures complètes de ce manuscrit, et m'a permis de présenter mes travaux lors de conférences internationales.

Les membres de mon CSI, Marie-Noëlle Bouin et Jean-Marc Le Caillec, ont soigneusement suivi mon parcours par le biais de nos points annuels qui donnaient lieu à des discussions intéressantes. Ils ont par ailleurs accepté de tenir le rôle d'examineurs de ma thèse - Marie-Noëlle ayant même performé dans le rôle de présidente de mon jury de soutenance - et je les en remercie. Je remercie également mes deux rapporteurs, Olivier Bock et Laurent Morel, pour leur relecture assidue et critique de mon manuscrit, ainsi que leurs questions pertinentes et les débats lors de ma soutenance.

Je remercie mes collègues du bâtiment M de l'ENSTA Bretagne, pour les innombrables activités, repas et pauses café, qui ont été l'occasion de discussions passionnantes en ZRS - "Zone de Réflexion Scientifique" ou ailleurs. Je remercie en particulier Rodéric pour les nombreux dépannages informatiques et l'introduction à Pandas, ainsi que Clémence qui a su porter un avis avisé et précieux sur ma présentation de soutenance, et évidemment les secrétaires du Lab-STICC pour leur travail indispensable.

Merci à tous mes amis d'avoir toujours été là, quelle que soit la distance qui nous sépare. Ils m'ont permis de maintenir un équilibre essentiel entre vie personnelle et professionnelle sur l'ensemble des trois années de mon doctorat.

Ma famille m'offre un soutien inconditionnel dans tous les moments de ma vie, merci beaucoup. Je remercie en particulier mes sœurs Eva et Vanessa, sans qui mon public de soutenance n'aurait pas été si bien accueilli, ainsi que ma mère Muriel, qui s'est déplacée jusqu'à Brest pour venir assister à ma soutenance malgré un calendrier défavorable.

Enfin, un grand merci à Auguste, pour tout.

CONTENTS

List of Figures	xv
List of Tables	xvii
List of Algorithms	xviii
List of Acronyms	xix
List of Notations and Symbols	xxv
1 General Introduction	1
1.1 Motivation	1
1.2 Objectives	6
1.3 Methodology	6
1.4 Structure of the Thesis	7
 GNSS Tools and their Application to Water Vapor Retrieval at Sea	
2 Principles of GNSS	11
2.1 GNSS Systems and Services	11
2.2 GNSS Positioning Principles	14
2.3 Sources of Errors and Delays in the GNSS Signal	16
2.4 Kalman Filtering for GNSS	28
2.5 GNSS Atmospheric Water Vapor Observation Principle	33
2.6 Conclusion on GNSS Principles	35
3 Shipborne GNSS for Precipitable Water Vapor Retrieval	37
3.1 Offshore Precise Point Positioning Issues	37
3.2 Litterature on Shipborne GNSS for Precipitable Water Vapor Retrieval	38
3.3 Studies Features	40
3.4 Assessment of Shipborne GNSS PWV Quality	43
3.5 Conclusion on the Shipborne GNSS Litterature	50
 Influence of the Processing Modeling on the Precise Point Positioning of Shipborne GNSS Antennas	
4 GNSS PPP Processing Modeling on Real Dataset	57
4.1 Data and Processing Method	57
4.2 Assessment of Survey Vessel Processing Models	67
4.3 Conclusion on the Real Dataset Processing Strategy Assessment . . .	73
5 Processing Modeling Assessment of Simulated Shipborne GNSS signal	75
5.1 Simulation of a GNSS Signal Acquisition	76
5.2 Processing Methods for the Estimation	80
5.3 Results and Comparison of the Processing Models	82
5.4 Discussion on a Suitable Processing Modeling	86
5.5 Impact of Simulation Features on Processing	91
5.6 Conclusion on the Simulated Shipborne GNSS Processing Modeling .	97
 Water Vapor Monitoring During the French Oceanographic Fleet Campaigns between 2015 and 2022	
6 Assessment of the French Oceanographic Fleet Dataset	101
6.1 Data and Methods	101

6.2	Evaluation of Shipborne GNSS PWV Results	112
6.3	Conclusion on the FOF Processing	119
7	FOF PWV Dataset for Atmospheric Water Vapor Monitoring	121
7.1	Impact of the Latitude on the PWV Comparisons	121
7.2	Impact of the Season on the PWV Comparisons	125
7.3	Contribution of the FOF Dataset to the Climate Study	128
7.4	Conclusion on the Contribution of Shipborne PWV to Atmosphere Water Vapor Monitoring	133
8	General Conclusion and Outlook	135
8.1	Context	135
8.2	Overview of the Undertaken Work and Achieved Outcomes	136
8.3	Future Prospects	137

Appendices

A	Statistical Results of the ENSTA Bretagne Hydrographic Vessel Comparison to the BRST Ground-Based GNSS Station	141
B	Statistical Results of the Estimation Errors from Simulated Dataset	145
C	Available FOF Dataset Campaigns Description	153
D	Résumé Étendu	161
D.1	Introduction	161
D.2	Principe du GNSS, Mesure de la Vapeur d'Eau Atmosphérique en Mer	165
D.3	Étude de la Stratégie de Traitement des Données GNSS	167
D.4	Observation de la Vapeur d'Eau Atmosphérique lors des Campagnes de Recherche de la Flotte Océanographique Française entre 2015 et 2022	168
D.5	Conclusion	169
	Bibliography	173

LIST OF FIGURES

Figure 1.1	Techniques of water vapor measurement	2
Figure 1.2	EUMETNET GPS Water Vapour Programme (E-GVAP) Network of Global Navigation Satellite System (GNSS) Stations over Europe	4
Figure 1.3	Delay in GNSS signal	5
Figure 2.1	Orbits of Global Navigation Satellite System (GNSS) satellites	13
Figure 2.2	Illustration of the Snell's law	20
Figure 2.3	Right-hand circularly polarized (RHCP) propagation of a Global Navigation Satellite System (GNSS) electromagnetic wave . .	24
Figure 2.4	Multipath error for a Global Navigation Satellite System (GNSS) antenna	27
Figure 2.5	Phase center variation (PCV) calibration maps	27
Figure 4.1	Schematic of Panopée survey vessel	58
Figure 4.2	Map of the Bay of Brest with the Panopée course and surrounding sensors location	59
Figure 4.3	Global Navigation Satellite System (GNSS) data quality indicators	60
Figure 4.4	Tested weighting function of the elevation of the satellites .	62
Figure 4.5	Random walk process noise (RWPN) effect on the zenithal wet delay (ZWD) time series	63
Figure 4.6	Photo of the Penfeld tide gauge	64
Figure 4.7	Photo of the BRST antenna	65
Figure 4.8	Global Navigation Satellite System (GNSS) processing ambiguity resolution	66
Figure 4.9	Statistical results of the height difference between the survey vessel and Brest tide gauge	68
Figure 4.10	Statistical results of the precipitable water vapor (PWV) difference between the survey vessel and BRST ground Global Navigation Satellite System (GNSS) station	70
Figure 4.11	Precipitable water vapor (PWV) time series from different measurement techniques	72
Figure 5.1	Simulated height and zenithal wet delay (ZWD) time series .	79
Figure 5.2	Weighting function of the elevation of the observed satellites tested on simulated dataset	81
Figure 5.3	Correlation coefficients for the different processing models tested on the simulated signal	83
Figure 5.4	Root mean squared error (RMSE) of the height bias	84
Figure 5.5	Root mean squared error (RMSE) of the height standard deviation	85
Figure 5.6	Root mean squared error (RMSE) of the zenithal wet delay (ZWD) bias	86
Figure 5.7	Root mean squared error (RMSE) of the zenithal wet delay (ZWD) standard deviation	87
Figure 6.1	Map of the French Oceanographic Fleet (FOF) research vessels (R/Vs) trajectories	102

Figure 6.2	Time series of the French Oceanographic Fleet (FOF) research vessels (R/Vs) Global Navigation Satellite System (GNSS) acquisition	103
Figure 6.3	Map of satellite-based microwave radiometer (SMWR) water vapor sensing	109
Figure 6.4	Map of the ground stations crossed by French Oceanographic Fleet (FOF) research vessels (R/Vs) from 2015 to 2022	110
Figure 6.5	Maps of the crossings of the French Oceanographic Fleet (FOF) research vessels (R/Vs)	112
Figure 6.6	Scatter plot of 5th ECMWF ReAnalysis (ERA5) total column water vapor (TCWV) product as of the shipborne retrieved precipitable water vapor (PWV)	113
Figure 6.7	Map of the shipborne precipitable water vapor (PWV) comparison to satellite-based microwave radiometer (SMWR)	115
Figure 6.8	Scatter plot of satellite-based microwave radiometer (SMWR) precipitable water vapor (PWV) product as of the shipborne retrieved precipitable water vapor (PWV)	116
Figure 6.9	precipitable water vapor (PWV) scatter plot between shipborne Global Navigation Satellite System (GNSS) antenna and nearby ground-based Global Navigation Satellite System (GNSS) stations	117
Figure 6.10	Histogram of the differences between the shipborne antennas and the crossed coastal ground-based Global Navigation Satellite System (GNSS) stations	117
Figure 6.11	Precipitable water vapor (PWV) time series of the research vessel (R/V) crossings	119
Figure 7.1	Precipitable water vapor (PWV) scatter plot between shipborne Global Navigation Satellite System (GNSS) antenna and 5th ECMWF ReAnalysis (ERA5) for different latitudes	122
Figure 7.2	Precipitable water vapor (PWV) scatter plot between shipborne Global Navigation Satellite System (GNSS) antenna and satellite-based microwave radiometer (SMWR) for different latitudes	123
Figure 7.3	Precipitable water vapor (PWV) scatter plot between shipborne Global Navigation Satellite System (GNSS) antenna and Nevada Geodetic Laboratory (NGL) ground stations for different latitudes	125
Figure 7.4	Precipitable water vapor (PWV) scatter plot between shipborne Global Navigation Satellite System (GNSS) antenna and 5th ECMWF ReAnalysis (ERA5) for different latitudes	126
Figure 7.5	Precipitable water vapor (PWV) scatter plot between shipborne Global Navigation Satellite System (GNSS) antenna and satellite-based microwave radiometer (SMWR) for different seasons	127
Figure 7.6	Precipitable water vapor (PWV) scatter plot between shipborne Global Navigation Satellite System (GNSS) antenna and Nevada Geodetic Laboratory (NGL) ground stations for different seasons	128

Figure 7.7	Shipborne Global Navigation Satellite System (GNSS) precipitable water vapor (PWV) as a function of the latitude	129
Figure 7.8	Statistics of the precipitable water vapor (PWV) distribution in each region	129
Figure 7.9	Statistics of the precipitable water vapor (PWV) distribution in each season	130
Figure 7.10	precipitable water vapor (PWV) and sea surface temperature (SST) time series from the French Oceanographic Fleet (FOF) .	131
Figure 7.11	French Oceanographic Fleet (FOF) precipitable water vapor (PWV) and sea surface temperature (SST) measurements . . .	133
Figure 8.1	Near real-time (NRT) and post-processed zenithal troposphere delay (ZTD) time series from a shipborne Global Navigation Satellite System (GNSS) antenna	138

LIST OF TABLES

Table 2.1	Main frequencies of Global Navigation Satellite System (GNSS) constellations	13
Table 2.2	Description and units of the terms of the observation Equations	15
Table 2.3	Types of ephemeris products from the International GNSS Service (IGS)	17
Table 3.1	Published studies on shipborne Global Navigation Satellite System (GNSS) precipitable water vapor (PWV) retrieval . . .	39
Table 3.2	Processing model of published studies on shipborne Global Navigation Satellite System (GNSS) precipitable water vapor (PWV) retrieval	40
Table 3.3	random walk process noise (RWPN) tests in Fan et al. (2016) [Fan 16] study	43
Table 3.4	Statistical results of published studies on shipborne Global Navigation Satellite System (GNSS) precipitable water vapor (PWV) retrieval	44
Table 4.1	Precise point positioning (PPP) processing modeling tested on the survey vessel dataset	61
Table 5.1	Description of the simulated carrier-phase signal	77
Table 5.2	Setup for the simulated measurement	78
Table 5.3	Precise point positioning (PPP) processing modeling tested on simulated dataset	82
Table 5.4	Minimum standard deviation for different processing models tested on the simulated signal	88
Table 5.5	Average standard deviations for different weighting models tested on the simulated signal	89
Table 5.6	Average standard deviations for the recommended random walk process noise (RWPN) modeling	89
Table 5.7	New simulation features	92

Table 5.8	Height and zenithal wet delay (ZWD) average standard deviation results for data resolution study	92
Table 5.9	Average standard deviation increase in Global Positioning System (GPS)-only case	93
Table 5.10	Average biases for different antenna movements and corrections	94
Table 5.11	Impact of the antenna movement implementation on the average standard deviation	95
Table 5.12	Impact of the latitude on the average standard deviation	96
Table 5.13	Height and zenithal wet delay (ZWD) average standard deviation results for study at high latitudes (80°).	96
Table 6.1	Amount of rejections in the French Oceanographic Fleet (FOF) precipitable water vapor (PWV) dataset	106
Table 6.2	Number of days in the French Oceanographic Fleet (FOF) precipitable water vapor (PWV) dataset	107
Table 6.3	Amount of precipitable water vapor (PWV) comparisons between French Oceanographic Fleet (FOF) and 5th ECMWF ReAnalysis (ERA5)	108
Table 6.4	Amount of precipitable water vapor (PWV) comparisons between the French Oceanographic Fleet (FOF) and satellite-based microwave radiometer (SMWR)	110
Table 6.5	Amount of precipitable water vapor (PWV) comparisons between the French Oceanographic Fleet (FOF) and ground-based Global Navigation Satellite System (GNSS)	111
Table 6.6	French Oceanographic Fleet (FOF) research vessels (R/Vs) crossings information	112
Table 6.7	Statistics of the differences between the French Oceanographic Fleet (FOF) dataset and the reference datasets	113
Table 6.8	Statistics of the differences between the research vessels (R/Vs) when crossings occur	118
Table 7.1	Correlation coefficients between precipitable water vapor (PWV) and sea surface temperature (SST)	132
Table A.1	Root mean squared error (RMSE) of the difference between the survey vessel height and tide gauge	142
Table A.2	Root mean squared error (RMSE) of the difference between survey vessel and BRST precipitable water vapors (PWVs)	143
Table B.1	Statistical results of the height estimation for each processing model	145
Table B.2	Statistical results of the zenithal wet delay (ZWD) estimation for each processing model	149
Table C.1	French Oceanographic Fleet (FOF) campaigns	153

LIST OF ALGORITHMS

Algorithm 2.1	KalmanFilter	33
---------------	------------------------	----

LIST OF ACRONYMS

AGU	American Geophysical Union
AIRS	atmospheric infrared sounder
AMMA	African Monsoon Multidisciplinary Analysis
AMSL	above mean sea level
AMSR-2	Advanced Microwave Scanning Radiometer 2
AROME	Applications de la Recherche à l'Opérationnel à Méso-Echelle
AS-ECV	AMSR-2 Air-Sea Essential Climate Variable
ARP	antenna reference point
BDS	BeiDou Navigation Satellite System
CMR	Calibration Microwave Radiometer
CNES	Centre National d'Études Spatiales
CNRS	Centre National de la Recherche Scientifique
CSUM	Centre Spatial Universitaire de Montpellier
doy	day of year
ECMWF	European Center for Medium-range Weather Forecasts
EGM	Earth Gravitational Model
EGU	European Geosciences Union
E-GVAP	EUMETNET GPS Water Vapour Programme
EKF	extended Kalman filter
ENC	electronic navigational charts
ENSTA Bretagne	École Nationale Supérieure de Techniques Avancées Bretagne
ERA5	5th ECMWF ReAnalysis
ERA1	ECMWF ReAnalysis-Interim
ERP	Earth rotation parameters
ESA	European Space Agency
EU	European-Union
EUMETNET	European Meteorological Network

FES	Finite Element Solution
FOF	French Oceanographic Fleet
GIEC	Groupe d'experts intergouvernemental sur l'évolution du climat
GLONASS	GLObalnaïa NAvigatsionnaïa Spoutnikovaïa Sistéma
GMF	Global Mapping Function
GNSS	Global Navigation Satellite System
GNSS-M	GNSS for meteorology
GNSS-C	GNSS for climatology
GNSS-RO	GNSS radio occultation
GNSS ₄ SWEC	Advanced Global Navigation Satellite Systems tropospheric products for monitoring severe weather events and climate
GPM	Global Precipitation Measurement
GMI	Global Precipitation Measurement (GPM) Microwave Imager
GPS	Global Positioning System
GPT	Global Pressure and Temperature
HAS	high accuracy service
Hy-2A	Hai Yang 2A
IAG	International Association of Geodesy
IERS	International Earth Rotation and Reference Systems Service
IF	ionosphere-free
IFREMER	Institut Français de Recherche pour l'Exploitation de la MER
IGS	International GNSS Service
IMU	inertial measurement unit
IPCC	Intergovernmental Panel on Climate Change
IPEV	Institut polaire français Paul-Émile Victor
IPO	Integrated Program Office
IR	infrared
IRD	Institut de Recherche pour le Développement
ITCZ	intertropical convergence zone
IWV	integrated water vapor
JPL	Jet Propulsion Laboratory

LC	linear combination
LEO	low Earth orbit
LHCP	left-hand circularly polarized
Lidar	laser imaging detection and ranging
MEO	medium Earth orbit
MM5	Fifth Generation National Center for Atmospheric Research (NCAR)/Penn State Mesoscale Model
MODIS	Moderate Resolution Imaging Spectroradiometer
MSL	mean sea level
MW	microwave
NASA	National Aeronautics and Space Administration
NCAR	National Center for Atmospheric Research
NCEP	National Centers for Environmental Prediction
NGL	Nevada Geodetic Laboratory
NGS	National Geodetic Survey
NMF	Niell Mapping Function
NOAA	National Oceanic and Atmospheric Administration
NPOESS	National Polar-orbiting Operational Environmental Satellite System
NRT	near real-time
NWM	numerical weather model
NWP	numerical weather prediction
PCO	phase center offset
PCV	phase center variation
pdf	probability density function
PPP	precise point positioning
PRN	pseudorandom noise
PWV	precipitable water vapor
RH	relative humidity
RHCP	right-hand circularly polarized
RMS	root mean squared coefficient
RMSD	root mean squared difference

RMSE	root mean squared error
ROC	rate of change
RS	radiosonde
RSS	Remote Sensing Systems
RT	real-time
RTS	real-time service
RTK	Real Time Kinematic
R/V	research vessel
RWPN	random walk process noise
SARAL	Satellite with ARgos and ALtiKa
SHOM	Service Hydrographique et Océanographique de la Marine
SMWR	satellite-based microwave radiometer
SWVR	satellite-based water vapor radiometer
SNR	signal to noise ratio
SPP	single point positioning
SSH	sea surface height
SSM/I	Special Sensor Microwave Image
SSMIS	Special Sensor Microwave Image Sounder
SST	sea surface temperature
STD	standard deviation
SWD	slant-path wet delay
SWV	slant-path water vapor
TCWV	total column water vapor
TEC	total electron content
TEQC	translation, editing and quality check
TUV	Technische Universität Wien
USA	United States of America
UTC	coordinated universal time
VLBI	very long baseline interferometry
VMF	Vienna Mapping Functions

WV	water vapor
WVR	water vapor radiometer
ZHD	zenithal hydrostatic delay
ZTD	zenithal troposphere delay
ZWD	zenithal wet delay

LIST OF NOTATIONS AND SYMBOLS

LIST OF NOTATIONS

Notation	Description
CO	cut-off angle of the elevation
WG	weighting function of the elevation
RW	random walk process noise on the ZWD
CO (1) - WG (2) - RW (3)	processing model with (1) of cut-off angle, (2) as a weighting function of the elevation, and (3) of random walk process noise on the ZWD
\mathbf{x}	vector
$\hat{\mathbf{x}}$	a priori solution of \mathbf{x} vector
\mathbf{X}	matrix
\mathbf{X}^T	transpose matrix
\mathbf{X}^{-1}	inverse matrix

LIST OF SYMBOLS

G	GPS constellation (USA)
R	GLONASS constellation (Russia)
E	Galileo constellation (Europe)
Q	QZSS constellation (Japan)
p	GNSS pseudo-range observable
Φ	GNSS carrier phase observable
φ	phase observable
Φ_n	narrow-lane carrier phase observable
e	residual pseudo-range errors
ε	residual phase errors
d^i	satellite instrumental delay
d_r	receiver instrumental delay
az	azimuth of the satellite
el	elevation of the satellite
γ	zenithal angular direction of the signal path
θ	latitude
λ	carrier wavelength
c	light celerity in vacuum
v	light velocity in the medium
δt	time resolution of the Global Navigation Satellite System (GNSS) processing
x	Global Navigation Satellite System (GNSS) solution variable

X	X point coordinate
Y	Y point coordinate
Z	Z point coordinate
E	East component of the projection of the location on Earth
N	North component of the projection of the location on Earth
U	Up component of the projection of the location on Earth
C	Clock-induced length delay
h	height of the antenna above sea level
I	ionospheric propagation delay
$IF1$	ionosphere-free (IF) coefficient for the first Global Navigation Satellite System (GNSS) signal carrier
$IF2$	ionosphere-free (IF) coefficient for the second Global Navigation Satellite System (GNSS) signal carrier
F_1	frequency band of the first Global Navigation Satellite System (GNSS) signal carrier
F_2	frequency band of the second Global Navigation Satellite System (GNSS) signal carrier
T	tropospheric propagation delay
ZTD	zenithal troposphere delay (ZTD)
ZHD	zenithal hydrostatic delay (ZHD)
ZWD	zenithal wet delay (ZWD)
G_{NS}	horizontal tropospheric delay gradient in the zonal direction
G_{EW}	horizontal tropospheric delay gradient in the meridional direction
\mathcal{M}	mapping function
IWV	integrated water vapor (IWV)
PWV	precipitable water vapor (PWV)
h_{MSL}	geoid height
dt	receiver clock error
σ_{ZWD}^2	zenithal wet delay (ZWD) variance
σ_C^2	clock variance
σ_X^2	X position variance
σ_Y^2	Y position variance
σ_Z^2	Z position variance
σ_E^2	east position variance
σ_N^2	north position variance
σ_U^2	up position variance
σ_{Φ_n}	narrow-lane uncertainty
σ_G^2	gradients variance
δt^{rel}	relativistic corrections
N_ϕ	integer number of cycles of phase ambiguity
ω	phase wind-up
Φ_{mp}	multipath error
a	amplitude of the reflected signal
α	attenuation of the amplitude of the reflected signal
H_0	vertical distance between the reflection location of the signal and the antenna phase center
Γ	rate of change of the antenna gain
g_r	reflected antenna gain

g_d	direct antenna gain
S	surface roughness
ξ	phase center offset (PCO)
pcv	phase center variation (PCV)
η	white noise measurement
τ	random walk process noise (RWPN)
cst	constant function of elevation
sin	sine function of elevation
\sqrt{sin}	square-root of a sine function of elevation
cos^{-4}	Hadas-proposed function of elevation
\mathbf{I}	identity vector
\mathbf{x}	state vector
$\boldsymbol{\mu}$	mean of the state vector
$\boldsymbol{\Sigma}$	covariance matrix
\mathbf{A}	model state matrix
$\boldsymbol{\alpha}$	random noise vector of state transition
$\boldsymbol{\Sigma}_\alpha$	variance-covariance matrix of the noise vector
\mathbf{y}	vector of observations
\mathbf{C}	observation matrix
$\boldsymbol{\beta}$	measurement Gaussian noise vector
$\boldsymbol{\Sigma}_\beta$	variance-covariance matrix of the observation vector
\mathbf{K}	Kalman filter gain matrix
\mathbf{p}	probability density function (pdf)
b	bias value
SST	sea surface temperature (SST)
RH	relative humidity (RH)
H_{wv}	atmospheric water vapor scale height
H	atmosphere scale height
T_{MSL}	temperature at the mean sea level (MSL)
p_{MSL}	pressure at the mean sea level (MSL)
g_{atm}	approximated gravity of the atmosphere mass center
g_{MSL}	gravity at mean sea level (MSL)
n	refraction index of the medium
N	refractivity of the medium
N_d	dry part of the refractivity
N_w	wet part of the refractivity
ξ_{NS}	zonal horizontal refractivity
ξ_{EW}	meridional horizontal refractivity
N_e	electron density
R	Fresnel coefficient
R_S	Fresnel coefficient for an electric field perpendicular to the plane of incidence
R_P	Fresnel coefficient for an electric field parallel to the plane of incidence
R_v	gas constant of the water vapor
T_m	mean temperature of the troposphere
S	length of the true bended signal
B_0	average geomagnetic field modulus

θ_0	average angle between the Global Navigation Satellite System (GNSS) signal propagation direction and the geomagnetic field
ρ	geometric range
g	geometrical path from the antenna to the top of the atmosphere the GNSS signal would take in the absence of atmosphere
δL	excess path length
ρ_v	mean liquid water density

LIST OF SUBSCRIPTS

i	i -th satellite
r	receiver
s	simulated
S	slant path from the antenna to the top of the atmosphere
LC	ionosphere-free (IF) linear combination
$F_{1,2}$	first or second carrier

GENERAL INTRODUCTION

CONTENT

1.1	Motivation	1
1.1.1	Water Vapor Observation Techniques for Troposphere Monitoring	1
1.1.2	Water Vapor Observation Gap above the Oceans	4
1.2	Objectives	6
1.3	Methodology	6
1.4	Structure of the Thesis	7

1.1 MOTIVATION

Water vapor is the main role player in the hydrological cycle, carrying water and energy from one place to another via the troposphere [Bev 92]. The hydrological cycle is the global process followed by the water that evaporates from the Earth's surface, travels the atmosphere in the form of water vapor until it condenses into clouds, and returns to the ground as precipitation. This process drives the energy provided by the Sun which infrared rays are absorbed by atmospheric gases, thus warming the Earth's surface, by transferring this energy to the atmosphere. There, this energy will move to new places thanks to the atmospheric circulation. The atmosphere then stores and delivers a high amount of energy all around the Earth through water vapor. The Intergovernmental Panel on Climate Change (IPCC) underlines in its Sixth Assessment Report on Climate Change [Lee 23] that the amount of water vapor in the atmosphere can be increased by 7% for each supplementary degree of atmospheric temperature. Then, the atmosphere can store more water vapor and more energy in the context of global warming. High concentrations of water vapor in the atmosphere can result in intense weather events. Thus, we understand here that water vapor is of great significance for climate and weather studies.

1.1.1 *Water Vapor Observation Techniques for Troposphere Monitoring*

Most of the water vapor contained in the atmosphere is located in the troposphere, which is between the Earth's surface and until 10 km above. It is continuously monitored all around the world by meteorological organizations such as *Météo France* in France. From models and measurements, they are able to make numerical weather prediction (NWP) and alert the populations in advance when violent weather phenom-

ena will occur, lowering the number of deaths and the damages, such as in France during the recent Ciaran storm on November 1st, 2023 [Mur].

The atmosphere monitoring of the water vapor currently relies on several common techniques measuring what we call the precipitable water vapor (PWV), for climate study and weather forecast purposes [Rev 03]. Such as displayed in Figure 1.1 most of them are deployed over the land.

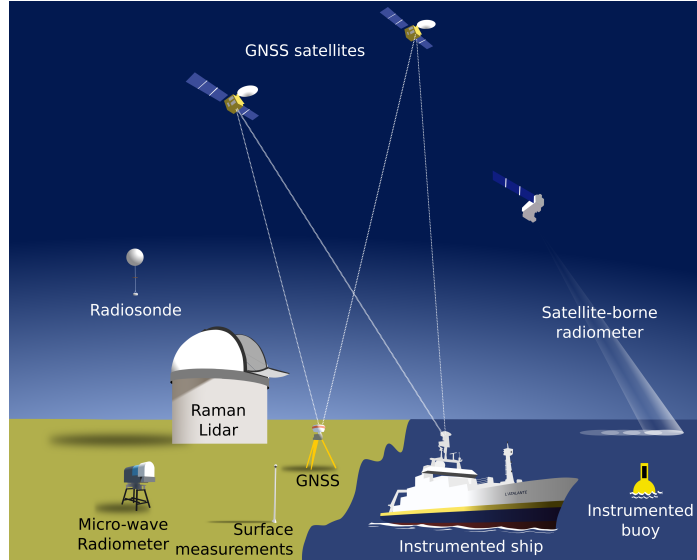


Figure 1.1: Schematic of different atmospheric water vapor measurement techniques.

1.1.1.1 Radiosondes

The radiosonde (RS) is the most famous water vapor measurement technique, as it has existed since 1930 and provides cost-effective measurements [Ell 91]. It consists of a balloon launched from a meteorological station around twice a day. The balloon is instrumented with a humidity sensor, a pressure sensor, a Global Positioning System (GPS) receiver, and a temperature sensor. It will record the water vapor at different altitudes in the whole atmosphere air column, while the balloon soars. The resulting dataset is then composed of a series containing the relative humidity, pressure and temperature measured for every 5 m of altitude of measurement.

The specific humidity profile is retrieved from the RS measurements following Miloshevich et al. (2006) [Mil 06]. Then the specific humidity profile is integrated on the whole atmosphere height to get the PWV information [Boc 21].

The common weakness of the RS is that they are following the air currents, then they are not elevating straight in the atmosphere, but the profile is variable. Moreover, it takes around one hour to ascend the whole troposphere, and two to 2.5 hours before the balloon explodes at 20 – 30 km to fall back to Earth, generally. Only two balloons per day are launched, which means that the time resolution of the measurement is quite low. However, it permits us to have a good knowledge of the distribution of water vapor in the atmosphere column. It is the only in situ measurement method of the atmospheric column water vapor. Other long-time series of daily in-situ measurements of the water vapor exist, but they remain surface measurements involving psychrometers and dew point hygrometers [Mid 53].

1.1.1.2 *Water Vapor Radiometers*

The atmospheric water vapor is remotely measured thanks to infrared (IR) or microwave (MW) radiometers called water vapor radiometer (WVR), providing highly accurate data [Bev 92].

Its advantage compared to the RS is that it is a continuously measuring instrument scanning an entire cone above the location of the WVR [Win 76; Elg 82]. However, the sensor is expensive and does not provide satisfying spatial horizontal resolution because they are sparsely spread [Bev 92].

Raman laser imaging detection and rangings (Lidars) also measures water vapor with high temporal accuracy from nighttime measurements of the atmosphere perturbation of an emitted wave from the Lidar [Boso8]. It provides an accurate vertical profile such as for the RS [Eng 92].

WVRs can be embarked onboard a satellite to observe the Earth's surface in the infrared band at its nadir, such as Atmospheric infrared sounder (AIRS) and Moderate Resolution Imaging Spectroradiometer (MODIS) (National Aeronautics and Space Administration (NASA)), and Satellite with ARgos and ALtiKa (SARAL) (Centre National d'Études Spatiales (CNES)). Special Sensor Microwave Image Sounder (SSMIS) (National Oceanic and Atmospheric Administration (NOAA)), Windsat (Integrated Program Office (IPO)), National Polar-orbiting Operational Environmental Satellite System (NPOESS)), are some of the many WVR currently orbiting the Earth onboard satellites, scanning the Earth's surface along their path to retrieve the water vapor content from microwave radiometer. However, both satellite-based water vapor radiometer (SWVR) techniques are providing measurements along their path only, meaning twice a day for each location on Earth at most, and some regions such as the poles are not covered [Smi 19].

1.1.1.3 *Numerical Weather Models*

numerical weather models (NWMs) have also been developed, taking into account the atmosphere dynamics and assimilating measurements such as the ones cited previously. One of the most famous global NWM is called 5th ECMWF ReAnalysis (ERA5) for 5th European Center for Medium-range Weather Forecasts (ECMWF) reanalysis. It provides meteorological and oceanography grid datasets all over the globe, computed from multiple data sources. ERA5 is a global reanalysis provided by the ECMWF, containing several atmospheric information including the atmospheric water vapor through the total column water vapor (TCWV) product, equivalent to the Global Navigation Satellite System (GNSS) retrieved PWV. ERA5 covers the whole globe on a 0.25° grid, on a hourly basis. The ERA5 TCWV is displayed by the Copernicus website. Its ancestor is the ECMWF ReAnalysis-Interim (ERA-Interim), and other NWM exist as well.

1.1.1.4 *Global Navigation Satellite Systems*

Since Bevis et al. (1992) [Bev 92] has introduced the water vapor measurement technique through ground-based GNSS, numerous studies have been conducted on this subject. Indeed, GNSS appears to be a cost-effective and continuous measurement technique, as it relies on ground-based GNSS networks that sometimes already exist, providing long-term datasets in many countries. Ground-based GNSS datasets provide accurate water vapor measurements [Wan 07], permitting to perform meteorology and climate study [Off 10]. GNSS main advantages are that its near real-time processing

can be automated, and measurements are available within all weather conditions [Roc 93].

More than 20 000 GNSS stations currently permit to monitor the troposphere above land areas worldwide through the Nevada Geodetic Laboratory (NGL) time series, with denser networks mainly in developed countries [Sim21].

The main GNSS network used for troposphere monitoring in Europe is currently the EUMETNET GPS Water Vapour Programme (E-GVAP) from the European Meteorological Network (EUMETNET) [Ved 20] whose European network is shown in Figure 1.2. The

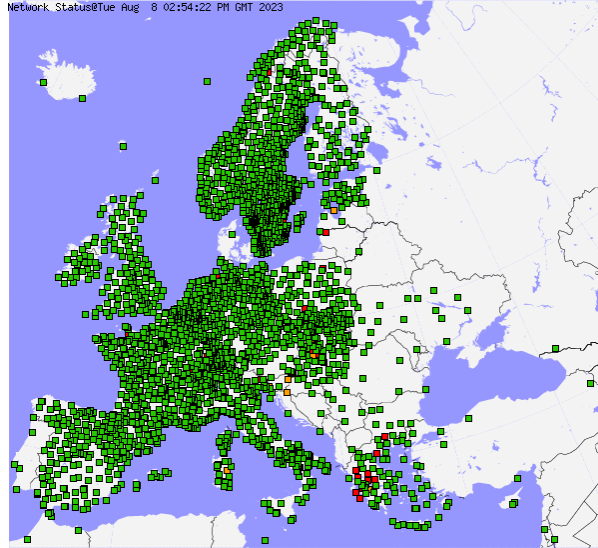


Figure 1.2: E-GVAP network stations over Europe. The green squares correspond to the stations providing data from 11 h to 14 h, orange stations have provided data from 8 h to 11 h on August 8th, and red stations have provided data between August 6th, 14 h and August 8th, 8 h. (Retrieved from egvap.dmi.dk (Accessed August, 8th, 2023))

E-GVAP program stated that a PWV accuracy of 3 mm is essential for climate study, while 5 mm is sufficient for NWP and now-casting applications [Off 10]. This program aims at providing daily PWV measurements through routine measurements and processing. The reprocessing of such dataset permits to get long lasting water vapor time series on a global scale, which would be useful for climate studies.

Several campaigns have studied atmospheric processes using precise GNSS post-processing products on a limited period and location, such as African Monsoon Multidisciplinary Analysis (AMMA) [Boc 08], Hymex [Boc 16], and EUREC⁴A [Bon 17; Boc 21]. These studies showed the possibilities with global scale study of the climate with GNSS, as they ended up to a satisfying accuracy to study the key processes [Off 10; Boc 13].

1.1.2 Water Vapor Observation Gap above the Oceans

As we can see in Figure 1.1, the land segment is relatively well covered by several different means of measurement of atmospheric water vapor, especially in developed countries. On the other hand, the oceans are sparsely covered as it is difficult and expensive to deploy specific platforms for measuring the atmosphere from the ocean surface. The satellites are a good alternative, such as the satellite-based microwave radiometers (SMWRs) [Smi 19], because they can cover the entire Earth within half a

day thanks to their rapid displacement and their large swath, but they provide sparse resolution as they are covering the same location twice a day and provide data mapped on a large spatial resolution basis. Also, clouds and heavy rain appear as obstacles to the radiometer, and they cannot provide data less than 25 km from the coast as the land is spoiling the swath observation [Ali 90].

As far as 70.8 % of the Earth's surface is covered by the oceans and strong events can form there, measuring the atmospheric water vapor above the oceans appears unavoidable. Indeed, the most severe weather events originate at sea and can hit the coastal areas, such as Cevenol episodes – fast heavy precipitations occurring in South of France, creating floodings – or hurricanes in tropical areas [Kat 05; Sho 09; Jul20]. Fortunately, many different ships are constantly sailing across the oceans. By instrumenting these ships, the oceans would be constantly monitored, but this can seem quite expensive. For now, they are mainly provided with surface measurement instruments, that are useful but not giving information on the atmospheric column water vapor.

Most of these ships carry GNSS antennas for navigation, which could be compatible with tropospheric monitoring. As mentioned at the beginning of this introduction, GNSS antennas are already used for atmospheric water vapor monitoring above land. Indeed, the signal path and velocity are altered by the water vapor contained in the atmosphere it passes through, such as seen in Figure 1.3.

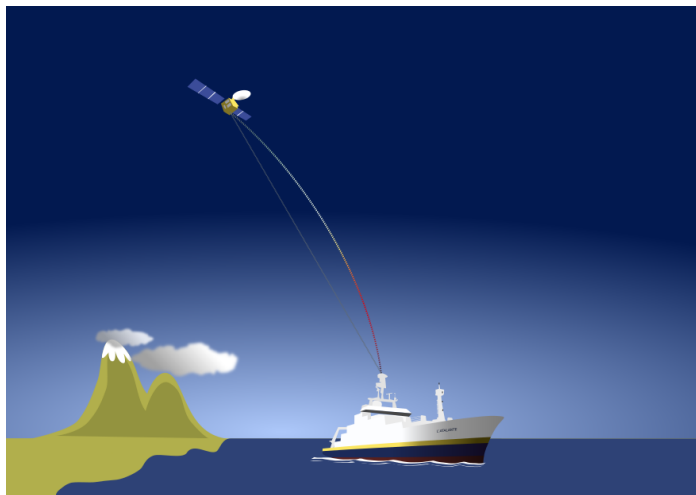


Figure 1.3: Schematic of the delay in GNSS signal due to atmospheric water vapor.

The signal arriving at the receiver at the Earth's surface is then delayed. This delay, when properly estimated during the GNSS data processing, is directly proportional to the total amount of water vapor contained in the troposphere above the observing antenna. Bevis et al. (1992) [Bev 92] was the first to mention the possibility of measuring water vapor through GNSS. Since then, it has become a very typical issue as demonstrated by the number of publications on troposphere water vapor retrieval from ground-based GNSS stations [Roc 93; Dav 93; Kou 01; Lu 15; Boc 16; Gue 16; Sim21]. Nowadays, networks of ground-based GNSS stations are routinely used for the purpose of monitoring water vapor [Pac 09], and some even intend to use them for other instruments assessment [Zha 17] or weather forecasting [Ved 04; Pac 09].

In that respect, some research teams have studied the possibility of applying water vapor measurement from GNSS technology to shipborne antennas, in order to broaden its potential to the whole Earth's surface. The first idea of mounting a geodetic

GNSS antenna on a ship for atmospheric measurements was proposed by Rocken et al. (2005) [Roc 05]. Since then, several studies have been published on this matter, but this movement gained further momentum following [Wan 19] that showed the possibility of retrieving atmospheric water vapor amount during cruises with an accuracy respecting the maximum threshold of 2 – 3 mm necessary for climate study [Off 10].

1.2 OBJECTIVES

Shipborne GNSS is a widespread cost-effective technology that can monitor continuously and efficiently the atmospheric water vapor above the ocean, to complement the SMWR as well as other sparse and expensive techniques. Long-term shipborne water vapor retrieval, such as proposed by Wu et al. (2022) [Wu 22b], permits us to study offshore climate changes and to better understand the role of the ocean-atmosphere exchanges. Routine measurement implementation such as proposed by Bosser, Van Baelen, and Bousquet (2022) [Bos 22b] should further permit the feeding of weather forecasting models for numerical prediction [Pol 07].

The overall goal is to be able to automatically process shipborne GNSS data from any raw dataset, and retrieve water vapor information from GNSS processing as accurately as possible. Here we focus on the post-processing of the data using the precise point positioning (PPP) technique in a kinematic way. This method is useful for a single antenna located offshore because no reference dataset is needed. However, the method can be tricky as several processing parameters can affect the estimation result and accuracy.

The zenithal wet delay (ZWD) may be highly correlated to height estimate during the GNSS data processing [Dod 96], especially in kinematic processing [Wan 19] where each time step provides a position estimate at the same time as the troposphere delay. A static positioning relies on the estimation of the position of the antenna only once a day, thus reducing the correlation between height and the ZWD estimated at each time step of the processing.

The GNSS processing strategies for atmospheric water vapor retrieval have been assessed several times for ground-based GNSS stations [Sel 16; Kač 19]. However, this kind of study has not been performed for shipborne antennas, even if shipborne GNSS water vapor retrieval is becoming a widely studied issue. Three processing parameters can be tuned to decorrelate the height and the atmospheric water vapor delay, for example: the cut-off to filter the observations coming from lower-elevation satellites, the weighting function of the observed satellite elevation applied to the uncertainty of the measurement, and the random walk process noise (RWPN) to model the atmospheric delay variations, that are unstable and unpredictable.

All these processing configuration parameters tuning would also depend on other aspects such as the constellations considered, the time resolution of the process, the movement and location of the ship during the acquisition, etc. All these aspects are addressed in this thesis, along with their assessment.

1.3 METHODOLOGY

First, a study of the GNSS processing strategy and the atmospheric water vapor retrieval has been performed, along with the state-of-the-art of shipborne GNSS retrieval

of the water vapor. The comparison to the usual water vapor measuring techniques they performed led to statistical results that serve as the baseline for expected results for shipborne antenna processing. Although the processing strategies for GNSS water vapor retrieval has been assessed from ground-based antennas, none has been performed concerning the application to offshore antennas such as the ones carried on vessels. Also, only one of the studies of the state-of-the-art performs the processing of long-lasting shipborne dataset [Wu 22b], encountering many different situations expected offshore.

To apply the most suitable processing strategy to another more diverse and longer-lasting shipborne GNSS dataset to retrieve the water vapor information above the oceans, a second part is dedicated to the assessment of a set of processing configurations. To this end, two simple shipborne GNSS datasets have been used:

- a month of data from the survey vessel of the École Nationale Supérieure de Techniques Avancées Bretagne (ENSTA Bretagne);
- a simulated dataset from a homemade simulator.

The survey vessel dataset permitted us to confirm that the processing strategy has an impact on the GNSS processing quality. Indeed, the comparison to other nearby measurements of sea surface height (SSH) and atmospheric water vapor led to significant discrepancies among the processing configuration estimates.

The built simulator has been conceived for the purpose we are interested in. We have carefully dealt with the way of modeling the simulated signal, and the number of simulations needed for statistical significance. Besides the processing configuration, the modeling of the simulated signal has been examined to best estimate the GNSS variables in different configurations. The estimation errors have been confronted for the different processing strategies, leading to the highlight of a recommended processing configuration.

In the third part, the recommended processing configuration has been applied to a bunch of five vessels from the French Oceanographic Fleet (FOF) operated by Institut Français de Recherche pour l'Exploitation de la MER (IFREMER), whose dataset runs for over eight consecutive years. The estimated water vapor content along the trajectories is then compared to external datasets such as for the other shipborne GNSS studies from the state of the art, permitting us to compare our resulting differences.

The statistical differences being satisfying with regard to the results highlighted in the state of the art, we then explore the remaining water vapor content dataset under different climate study angles such as the latitude-dependency, the seasonality, and the correlation to the sea surface temperature (SST).

1.4 STRUCTURE OF THE THESIS

This thesis is divided into three main parts, namely the theory, the processing strategy assessment, and the application to long-term shipborne GNSS processing.

The theory part deals with GNSS generalities from existing constellations to the signal processing method, and application to atmospheric water vapor observation in Chapter 2. Chapter 3 is detailing the major shipborne GNSS studies published from Rocken et al. (2005) [Roc 05] until today by providing the campaign setup, the processing configuration used, and the assessment of the water vapor delay quality by comparison to conventional water vapor retrieval techniques.

The processing strategy assessment part is split into two chapters. [Chapter 4](#) is a preliminary study based on a 49-day dataset from the research vessel of [ENSTA Bretagne](#) mainly used for a hydrography class training course. This vessel mainly stays docked in the Brest harbor. Its [GNSS](#) data have been processed using several combinations of processing parameters. The results have been assessed by comparison to nearby reference datasets. [Chapter 5](#) presents a wider study of processing parameters assessment relying on simulated shipborne [GNSS](#) dataset. The home-made simulator permitted the simulation of several different sets of [GNSS](#) data, to test processing configurations on diverse datasets. These tests permit us to draw recommendations on the best strategy to post-process shipborne [GNSS](#) data in kinematic [PPP](#), based on our results.

The third part contains two chapters. [Chapter 6](#) is the application of the processing strategy recommended after [Chapter 5](#) to the data made available by [IFREMER](#) from five of their offshore research vessels ([R/Vs](#)) from 2015 to 2022. This dataset represents a great opportunity to test the highlighted processing configuration, because it is huge, diverse, and represents all the sea states, weather conditions, and a wide range of locations possible on Earth's oceans. To assess their quality, the resulting time series of water vapor retrieved along their path is compared to various other sources of water vapor measurement. Then, [Chapter 7](#) gives a first look at the possibilities offers by such [PWV](#) dataset for climate study.

Finally, [Chapter 8](#) concludes this thesis by summarizing the outcomes of the two last parts, and drawing further prospects for application to near-real-time retrieval for weather prediction.

GNSS TOOLS AND THEIR APPLICATION TO WATER VAPOR RETRIEVAL AT SEA

This part relies on the theory about GNSS measurement, processing and the application for atmospheric water vapor monitoring. It is composed of two chapters.

First, the generalities about GNSS measurements as well as their processing is detailed. Then, it deals with the application of GNSS technique to atmospheric water vapor monitoring.

Secondly, a detailed state-of-the-art of the literature assessing shipborne GNSS water vapor retrieval permits to highlight the current advances as well as the incoming prospects in the field of study.

This thesis addresses some of the issues that have been arisen in this state-of-the-art.

 PRINCIPLES OF GNSS

CONTENT

2.1	GNSS Systems and Services	11
2.2	GNSS Positioning Principles	14
2.2.1	Observation Equations	14
2.2.2	Processing Methods of GNSS Data	15
2.3	Sources of Errors and Delays in the GNSS Signal	16
2.3.1	Satellite-Induced Delays	17
2.3.2	Ionosphere Effect	18
2.3.3	Neutral Atmosphere Effect	20
2.3.4	Multipath Effect	24
2.3.5	Antenna Phase Center Effect	27
2.4	Kalman Filtering for GNSS	28
2.4.1	Prediction Model	28
2.4.2	Correction Model	30
2.4.3	Processing Strategies to Manage the Errors in the Kalman Filter	31
2.4.4	Kalman Filter Implementation for PPP	33
2.5	GNSS Atmospheric Water Vapor Observation Principle	33
2.5.1	PWV Derived from GNSS ZWD Estimates	33
2.5.2	GNSS for Climate	34
2.5.3	GNSS for Meteorology	34
2.6	Conclusion on GNSS Principles	35





Global Navigation Satellite System ([GNSS](#)) refers to all global Earth covering systems providing positioning, navigation, and timing services with high accuracy in all weather conditions.

2.1 GNSS SYSTEMS AND SERVICES

The [GNSS](#) positioning relies on the measurement of the time of propagation at the speed of light of an electromagnetic signal emitted by at least four orbiting satellites around the Earth and received by a [GNSS](#) receiver located at the Earth's surface on land, at sea, and in the air, or even onboard low Earth orbit ([LEO](#)) satellites [[Seeo3](#)]. [GNSS](#) signals are composed of harmonic waves with a wavelength of about 0.2 m, along with a pseudorandom noise ([PRN](#)) code. A [GNSS](#) receiver can operate different types of signal measurements such as pseudo-range measurement: the *pseudo* distance between the satellite and the receiver, carrier phase measurement, and Doppler effect measurement.

Pseudorange measurement relies on the difference between the receiver's internal clock at the signal reception and the satellite clock at signal transmission. This is possible thanks to the atomic clocks equipping the GNSS satellites with precisions reaching the highest existing standards with a 30 ns stability, and its replica generated more or less synchronously by the receiver [HW 13]. Time propagation measurement can be converted into a distance between the emitting satellite and the receiver by using the light celerity. Apart from the clocks' asynchronicity and other delays, this method achieves a meter-level accuracy satellite-receiver distance measurement. Carrier-phase measurement relies on the number of phase beats of the received signal over time and its instantaneous phase difference with the receiver's internal phase at the time of reception. Although this measurement technique needs long-lasting satellite tracking – that is interrupted into cycle slips whenever the receiver loses sight of the observed satellite – to converge, it could achieve a millimeter-level accuracy satellite-receiver distance measurement. Doppler measurement relies on the change in frequency over time of the received signal due to the relative speed between the emitting satellite and the receiver. This measurement method will not be studied in this manuscript.

Currently, four different governments have developed their own GNSS system:

-  the United States of America (USA) operated Global Positioning System (GPS) in service since 1995 with currently 32 satellites operating as a 27-slots constellation orbiting on six near-circular medium Earth orbit (MEO) planes 20 180 km high with an orbital repetition of revolution of one day [Heg17];
-  the Russian GLObalnaïa NAVigatsionnaïa Spoutnikovaïa Sistéma (GLONASS) fully operational since 2015 with currently 24 satellites constellation orbiting on 3 near-circular MEO planes 19 100 km high with a period of revolution of eight days [Rev 17];
-  the European-Union (EU)-operated Galileo that is available since 2016 and will be fully deployed in 2024 and currently counts 26 operating satellites on three circular MEO planes 23 222 km altitude with an orbital repetition of ten days [Fal 17];
-  the Chinese BeiDou Navigation Satellite System (BDS) providing global services since 2018 and fully completed in 2020 with currently 27 satellites on three MEO 21 155 km high and 8 other satellites on four orbital planes 35 786 km high with an orbital repetition of seven days [Yan 17].

By launching GNSS satellites at medium Earth orbit (MEO) such as shown in Figure 2.1, the number of satellites required in the constellation to be visible from any point on the surface of the Earth is reduced compared to low Earth orbit (LEO) [Gue 22]. As a result, only a minimum of 24 satellites are needed to cover the entire Earth's surface with a sufficient number of satellites for positioning and navigation purposes. The orbital inclination of all satellites is around 55°, except for GLONASS that is 10° higher, permitting to cover higher latitudes.

Each GNSS constellation emits in several frequencies within the L-band, between 1 and 2 GHz, such as described in Table 2.1. GNSS satellite systems emit only in frequencies of Table 2.1 for each given band, identifying the different emitting satellites thanks to their characteristic PRN. However, there is an exception with GLONASS constellation that uses a set of channels separated by about 0.5 MHz to distinguish the

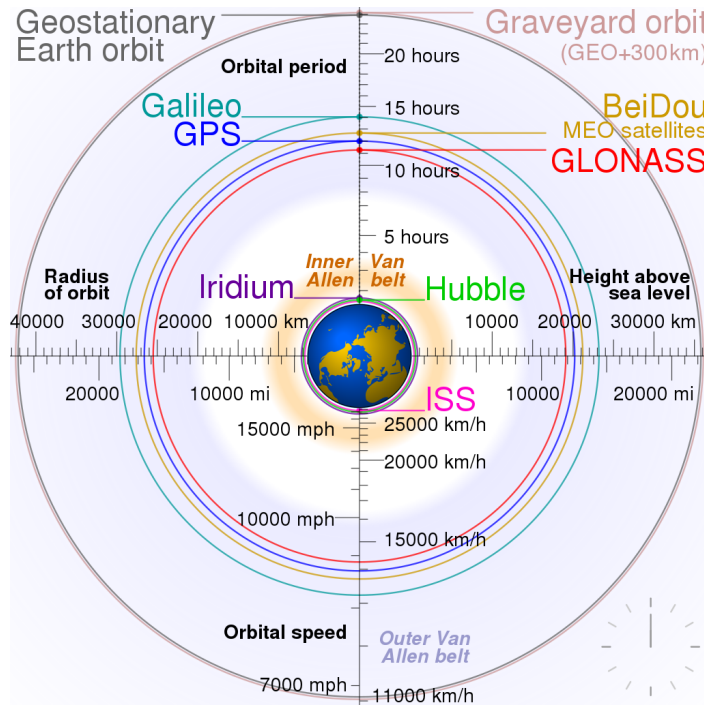


Figure 2.1: Schematic representation of satellites orbits around the Earth: GNSS constellations occupy MEO between 18 000 km and 24 000 km of altitude (right hand side of horizontal axis), giving them orbital periods of 10 to 14 h (top of vertical axis). (Comparison satellite navigation orbits. Retrieved July 21, 2023, from [wikimedia.org](https://commons.wikimedia.org/wiki/File:Comparison_satellite_navigation_orbits.png).)

different satellites in view for the L1 and L2 bands. These channels are numbered $k = -7, \dots, +6$ so that the 12 to 14 satellites together in view can always be distinguished.

The use of L-band is particularly adapted to GNSS application because it allows precise measurement with low impact of the atmosphere on the signal. Indeed, lower frequencies would have been entirely reflected on the ionosphere towards space, preventing it from reaching the receiver station at the Earth’s surface. L-bands also limit the signal attenuation when it travels through the troposphere compared to higher frequencies, thus permitting to get higher signal to noise ratio (SNR). All GNSS systems provide signals in two narrow frequency bands: several signals in a lower L-band between 1.1 and 1.3 GHz and a single signal in an upper L-band between 1.55 and 1.65 GHz. The availability of these two bands permits the cancellation of most of the ionospheric effect affecting the signal path (see Section 2.3.2.1).

GNSS	Main available L-band frequencies [MHz]			
GPS	L1: 1575.420	L2: 1227.600	L5: 1176.450	
GLONASS	L1: $1602.0 + k \cdot 0.5625$	L2: $1246.0 + k \cdot 0.4375$	L3: 1205.025	
Galileo	E1: 1575.420	E6: 1278.750	E5a: 1176.450	E5b: 1207.140
BDS	B1C: 1575.420	B2a: 1176.450	B2b: 1207.140	B3: 1268.520

Table 2.1: Name and frequency in MHz of main available L-band frequencies of the four GNSS constellations [Teu 17]. k is the channel number for each different satellite for GLONASS L1 and L2 bands.

The GNSS positioning is subject to several error sources. They are addressed in Section 2.3. Before, the principle of GNSS data processing is assessed in following Section 2.2.

2.2 GNSS POSITIONING PRINCIPLES

The pseudorange and carrier phase observation equations must be correctly modeled to accurately position the receiver. Sources of error detailed in Section 2.3 must also be correctly identified and estimated as best as possible.

Several common data processing methods exist for positioning an antenna using GNSS. All of these methods have different accuracies, ranging from tens of meters for standard positioning using single-frequency pseudo-range, to a few millimeters for post-processed precise point positioning (PPP) and Real Time Kinematic (RTK) positioning techniques relying on carrier-phase measurements.

2.2.1 Observation Equations

The pseudo-range observation equation, taking into account all signal code transmission mechanisms, can be written as follows [Gue 22]:

$$p_r^i = \rho_r^i + \zeta_r^i + c(d_r + d^i) + c(dt_r - dt^i + \delta t^{rel}) + T_r^i + I_r^i + e_r^i \quad (2.1)$$

where p_r^i denotes the GNSS pseudo-range observable between the i -th satellite and the receiver, ζ_r^i denotes the antenna phase center offsets of the satellite and the receiver, c denotes the light celerity in vacuum, d_r and d^i denote the receiver and satellite instrumental delays, dt_r , dt^i and δt^{rel} denote respectively for the receiver and i -th satellite receiver clock bias, and the relativity effect, T_r^i and I_r^i denote respectively for the tropospheric propagation delay and the ionospheric propagation delay due to the propagation of the signal in the atmosphere between the i -th satellite and the receiver, and e_r^i denotes the remaining effects such as satellite and receiver noise, and multipath effect. ρ_r^i denotes the geometric range between the i -th satellite and the receiver and is defined with the satellite and receiver coordinates such as in Equation (2.2).

$$\rho_r^i = \sqrt{(X^i - X_r)^2 + (Y^i - Y_r)^2 + (Z^i - Z_r)^2} \quad (2.2)$$

The carrier phase observation in Equation (2.3) is similar to the pseudorange in Equation (2.1):

$$\Phi_r^i = \rho_r^i + \zeta_r^i + c(dt_r - dt^i + \delta t^{rel}) + \lambda_r^i(-N_{\phi_r}^i + \omega_r^i) + T_r^i - I_r^i + \varepsilon_r^i \quad (2.3)$$

where $\Phi_r^i = \lambda \cdot \varphi_r^i$ denotes the GNSS carrier phase observable in meters between the i -th satellite and the receiver, with φ_r^i the phase observable in cycles and λ the carrier wavelength, $N_{\phi_r}^i$ is the integer number of cycles of phase ambiguity i.e. the number of complete wave phase cycles between its transmission by satellite emission and its reception by the antenna, ω_r^i denote the phase wind-up between the receiver and the i -th satellite, i.e. the relative orientation between the antennas of the transmitting satellite and the receiver, and ε_r^i denotes the residual phase errors such as phase biases, receiver noise, and multipath effect. The observation Equations terms are detailed along with their units in Table 2.2. As seen in Table 2.2 and Equation (2.3), the phase difference is measured in meters by multiplying the phase φ in cycles by the wavelength of the GNSS signal. Clock delay terms can also be converted to meters by multiplication with the speed of light in space c .

Notation	Description	Unit
p	GNSS pseudo-range observable	m
ρ	satellite - receiver geometric range	m
ζ	PCO	m
c	light celerity in vacuum	$\text{m} \cdot \text{s}^{-1}$
d_r	receiver instrumental delay	s
d^i	satellite instrumental delay	s
dt	receiver clock bias	s
δt^{rel}	relativistic corrections	s
T	tropospheric propagation delay	m
I	ionospheric propagation delay	m
e	residual pseudo-range errors	m
Φ	GNSS carrier phase observable	m
φ	phase observable	cycles
λ	carrier wavelength	m
N_φ	integer number of cycles of phase ambiguity	cycles
ω	phase wind-up	cycles
ε	residual phase errors	m

Table 2.2: Description and units of the terms of the observation Equations (2.1) and (2.3).

2.2.2 Processing Methods of GNSS Data

Pseudo-range-based, real-time (RT) or near real-time (NRT) processing, or kinematic measurement, provide less accuracy than carrier-phase-based, post-processing, or static measurement. Relative positioning against a reference ground-based GNSS antenna or network is also more accurate than absolute positioning methods. However, the most accurate techniques are not available to most users because they can be substantially more expensive, so they are limited to scientific and high-accuracy applications. Here, only the carrier-phase-based post-processing methods will be developed, as it is more precise than pseudo-range-based processing.

Differential carrier-phase processing has been developed since the 1980s [Lan 17]. It can remove unknown terms from the observation equations. This is done in several stages:

- single differencing: one satellite is observed by two receivers at the same time. Differencing the observations permits the removal of delays due to the satellite such as clock, orbits, and instrumental phase delay.
- double differencing: differencing the single difference computed from two separate satellites observed at the same time permits to remove also receiver delays such as clock, and instrumental phase delay so that the ambiguity becomes an integer.

- triple differencing: differencing the double difference computed for two successive time slots permits to also identify ambiguities and cycle slips.

This method utilizes a nearby network of reference ground GNSS stations. The stations in this network perform a truly accurate positioning and estimation of all of the parameters in Equation 2.3, allowing the antenna under study to be positioned with millimeter accuracy in a post-processing scheme.

While applied to RT kinematic positioning with GNSS antennas, this processing method is called RTK. The antenna is then located in real time thanks to the calculation of the baseline that separates its reference point from the ground-based reference GNSS antenna.

Another positioning technique is the PPP processing [Zum 97]. PPP uses carrier-phase measurement along with pseudo-range measurement to a lesser extent. It is an extended version of the single point positioning (SPP) that uses pseudo-range measurement only, providing an accuracy of tens of meters. The difference with differential carrier-phase processing is that it is an absolute positioning method: no network is required, but this technique still provides good results with a positioning accuracy of tens of millimeters for static processing. This accuracy is achieved by modeling all the delays affecting the signal and its measurement, even the smallest ones, and by correcting some effects affecting the GNSS signal during the process [Kou 01]. The main weakness of PPP processing relies on the fact that these aspects must be estimated during the processing. Thus, the solution needs additional product availability such as phase biases and satellite ephemeris. The integer ambiguity fixing can currently be done in a period of less than 1 minute before converging to centimeter accuracy positioning [Lau 18]. The main advantage of PPP is to eliminate the corrections coming from nearby reference stations, allowing precise positioning in remote regions, and lowering the computation time compared to differential positioning.

2.3 SOURCES OF ERRORS AND DELAYS IN THE GNSS SIGNAL

Different effects affect the GNSS signal accuracy, from the satellite emission to the receiving of the signal by the antenna, including environmental reflections and atmospheric delays. These delays are taken into account in the GNSS data processing detailed in Section 2.2.

GNSS signals propagate in media of different characteristics and can be affected by the nearby environment before reaching the receiver, thus creating multipath effect - addressed in Section 2.3.4, as well as the noise due to the antenna measurement - addressed in Section 2.3.5. Typically, the atmospheric effects - further detailed in Section 2.3.2 and Section 2.3.3 - are responsible for 0.2 m and up to 5 m of the positioning variability from the tropospheric and ionospheric delays respectively when it is not corrected [Lan 17].

All these delays together account for 0.5 to 6 m of the standard deviation of the antenna position [Lan 17]. Then, to accurately position the receiver, these effects must be taken into account besides the signal range corresponding to the time propagation needed for the signal to travel along the geometrical path from the observed satellite to the receiver.

Other effects that are not addressed in the following Sections affect the GNSS processing result, such as:

Type	Products	Time	Accuracy
RTS	orbits, clocks, code and phase biases	RT	2.00 m
ultra-rapid	orbits, clocks and ERP	every 6 h	0.10 m
rapid	orbits, clocks, and ERP	17 h after end of day	0.05 m
final	orbits, clocks, and ERP	after 14 days	< 0.05 m

Table 2.3: Types of ephemeris products from the IGS. Real-time service (RTS) products are currently under testing [IGSb]. IGS products are a combination of solutions from several analysis centers [IGSa]. Accuracy denotes for the accuracy of the product positioning (retrieved from <https://rgp.ign.fr>)

- the satellite constellation geometry: they have to be spread through the entire sky map of the antenna to get useful correction, so the use of multi-GNSS observations is supposed to improve the processing compared to GPS-only [Xia 19];
- the mapping function used to map the tropospheric delay to the zenithal direction;
- the code and phase biases available in the ephemerid products;
- the satellite positioning errors that are limited thanks to the use of the ephemerids,
- the antenna orientation bias,
- the relativistic effects.

2.3.1 Satellite-Induced Delays

As seen in Section 2.1, the GNSS receiver is positioned against the observed satellites. To position the receiver against the Earth, it is then necessary to know the location of the satellites against the Earth.

To this extent, it is necessary to provide the orbit and clock offsets of the observed constellations of satellites when processing the GNSS data. The International GNSS Service (IGS) provides such products from the reanalysis of several analysis centers such as the Jet Propulsion Laboratory (JPL) after the occurrence, such as shown in Table 2.3.

For NRT processing, the ultra-rapid products of Table 2.3 can be applied. However, they rely on 24 h observations and 24 h of prediction, so their accuracy is much lower than rapid products, which are available only the day after the occurrence. The highest quality is provided by the final products, but the post-processing must be achieved after their release more than 14 days after the occurrence.

RT solutions are currently under testing through the real-time service (RTS) [IGSb]. Although the RT broadcast products coming from the satellites are still flawed, implying errors in the RT positioning of a receiver at the Earth's surface of about 1 – 25 m [Bra17], European Space Agency (ESA) provides since January 2023 high accuracy service (HAS) broadcast ephemeris with an accuracy of 20 cm for Galileo [ESA].

2.3.2 Ionosphere Effect

The ionosphere is the highest part of the Earth's atmosphere from 50 km up to 1 000 km above mean sea level (AMSL). It is composed of gas ionized by the interaction of atmospheric molecules such as nitrogen and oxygen with high-energy particles or photons coming from the Sun and cosmic rays. This interaction transforms neutral molecules into cations and produces free electrons, which are found mostly 200 to 400 km AMSL with diurnal variations due to changing Sun exposure as the Earth rotates.

This ionized environment affects the signal path all along its travel through the ionosphere between the satellite and the receiver. This signal is refracted, traveling a longer path through the ionosphere, resulting in a signal pseudorange delay such as modeled by the added term I_r^i in Equation (2.1). As shown in Equation (2.3), the ionosphere affects the carrier phase by advancing it. These impacts on the GNSS signal are useful to remotely study the ionosphere, as they are proportional to the total electron content (TEC). Then, GNSS can be a useful tool for ionosphere remote sensing [Jak17; Haj 98] such as TEC mapping [Jak 11; Li 23], scintillation monitoring affecting GNSS measurements [Kin 07; Luo 23], or space weather [Bil18], and ionosphere tomography applications [Mei 23].

2.3.2.1 Ionosphere-Free Linear Combination

However, it is also possible to use several of the available GNSS multi-frequency measurements from each observed satellite to remove the ionospheric effect when it is not under study. Indeed, it appears that as shown in both Equation (2.1) and (2.3), the ionosphere impact I_r^i on pseudorange and carrier phase only differ in sign. Moreover, the ionospheric impact is frequency dependent, as it appears to be proportional to the inverse of the squared signal frequency (cf Equation (2.21) of Jin, Cardellach, and Xie (2014) [Jin 14]). The most famous ionosphere removal operation is called ionosphere-free (IF) linear combination (LC). The aim is to combine two given GNSS variables from two different frequency measurements such as in Equation (2.4).

$$x^{LC} = IF1 \cdot x_1 - IF2 \cdot x_2 \quad (2.4)$$

where:
$$IF1 = \frac{F_1^2}{F_1^2 - F_2^2} \quad IF2 = \frac{F_2^2}{F_1^2 - F_2^2}$$

where x^{LC} denotes the IF linear combination of the GNSS solution variable, F_1 and F_2 denote two different frequencies, and x_1 and x_2 denote the GNSS solution variable for both signal frequencies F_1 and F_2 . The frequencies depend on the observed GNSS constellation (cf Table 2.1) and the available frequency measurements within the receiving device. The use of a double-frequency device or more is mandatory to be able to perform the IF LC. As an example, Equation (2.4) could be applied to the pseudorange of Equation (2.1) and carrier-phase of Equation (2.3) to get the IF pseudo-range and carrier-phase, that would remove the I_r^i term of their observation equations at the first order.

The IF LC of Equation (2.4) removes the ionosphere effect on the GNSS signal to the first order using its proportional dependency into frequency. The first order ionosphere

removal of Equation (2.4) accounts for 99.9 % of the ionospheric effect on the GNSS signal propagation [HP 14].

As far as the IF combination produces real ambiguity values, the ambiguity estimation consists of applying the narrow lane combination from Equation (2.5) after correcting the phase cycle biases.

$$\Phi_n = \frac{\lambda_2}{\lambda_2 - \lambda_1} \Phi_1 - \frac{\lambda_1}{\lambda_2 - \lambda_1} \Phi_2 \quad (2.5)$$

where Φ_n denotes the narrow-lane carrier phase observable, λ_i denotes the i -th satellite carrier wavelength, and Φ_i denotes the i -th satellite GNSS carrier phase observable.

This combination permits to get the narrow lane wavelength:

$$\lambda_n = \frac{\sqrt{\lambda_1^2 + \lambda_2^2}}{\lambda_2 + \lambda_1} \quad (2.6)$$

where λ_n denotes the narrow lane carrier wavelength, and the narrow lane integer ambiguity:

$$N_{\phi_n} = N_{\phi_1} + N_{\phi_2} \quad (2.7)$$

where N_{ϕ_n} denotes the narrow lane integer number of cycles of phase ambiguity, and N_{ϕ_i} denotes the i -th satellite integer number of cycles of phase ambiguity, with an uncertainty σ_{Φ_n} of:

$$\sigma_{\Phi_n} = \frac{\sqrt{\lambda_1^2 + \lambda_2^2}}{\lambda_1 + \lambda_2}. \quad (2.8)$$

2.3.2.2 Second Order Ionosphere Correction

Although the IF LC is precise enough for most GNSS applications, it might be necessary to work on the remaining 0.1 % of error for precise positioning purpose [Jak17]. Higher-order ionospheric corrections are then available, that rely on models. We will describe only the second-order ionospheric correction.

According to Hernández-Pajares et al. (2014) [HP 14], the second order ionospheric correction can be approximated by

$$-\frac{7527\lambda^3}{2c^2} \cdot B_0 \cdot \cos \theta_0 \cdot \int_s N_e ds_0 \quad (2.9)$$

where B_0 denotes the average geomagnetic field modulus, θ_0 denotes the average angle between the GNSS signal propagation direction and the geomagnetic field, and N_e denotes the electron density along the path of geometric distance s_0 .

From their results, Hernández-Pajares et al. (2014) [HP 14] have shown that applying second-order ionosphere correction can improve by twice the estimation of the GNSS variables, and provide even better troposphere estimation. These results were obtained by directly computing the slant TEC instead of using mapping functions (see Section 2.3.3.2) to map vertical TEC to the signal path, which appears to reduce the computing accuracy.

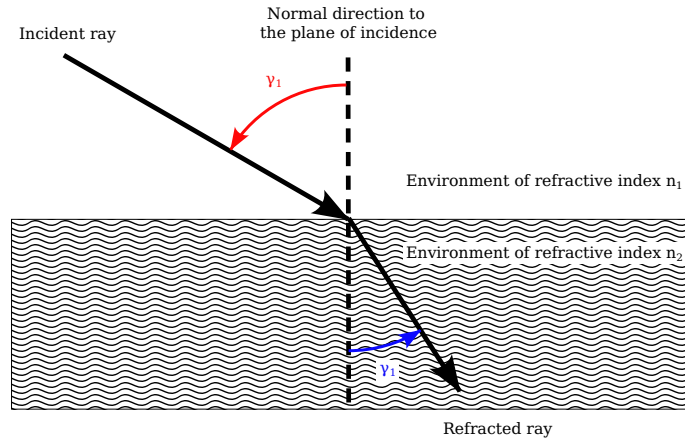


Figure 2.2: Illustration of the Snell's law of Equation (2.10).

2.3.3 Neutral Atmosphere Effect

The lower part of the atmosphere is electrically neutral and non-dispersive, it is then impossible to remove its effects on the signal propagation with a simple linear combination, as opposed to the ionosphere. The neutral atmosphere is divided into the upper stratosphere up to 50 km AMSL separated from the lower troposphere by the tropopause at 9 – 16 km AMSL. The neutral atmosphere is composed of a dry part with 78 % of nitrogen, 21 % of oxygen, and 1 % of other gases such as argon, or the commonly-known greenhouse effect gas carbon dioxide. Water vapor amounts for 0.25 % of the total atmosphere weight besides the dry atmosphere, and is a much more largely unknown greenhouse effect gas than carbon dioxide. However, its horizontal distribution is heterogeneous and its amount varies significantly locally. It accounts for 0.01 % of the air mass at the Poles to up to 3 % at the Equator where the temperature is higher. Its vertical distribution is decreasing with altitude, reaching an average of 1 % at sea level.

As far as the troposphere accounts for 80 % of the whole atmosphere mass as well as most of its water vapor [Hob 17], the neutral atmosphere will be assimilated to the troposphere throughout this thesis dissertation; hence the troposphere effect T_r^i modeled in observation Equation (2.1) and (2.3). However, still 25 % of this delay is due to gases that are located above the troposphere in the neutral atmosphere.

2.3.3.1 Tropospheric Delay

The troposphere density increases with a decrease in altitude. This change in density creates a signal bending and speed decrease. The bending is due to the changing refractive index when traveling into a changing density medium, following Snell's law:

$$n_1 \sin \gamma_1 = n_2 \sin \gamma_2 \quad (2.10)$$

where n_1 and n_2 denote the refraction index of the medium of layers 1 and 2 respectively, and γ_1 and γ_2 denote the zenithal angular direction of the signal path in layers 1 and 2 respectively such as illustrated by Figure 2.2. Indeed, the troposphere can be

divided into several layers of different densities, each modeled by its refractive index such as in Equation (2.11):

$$n = \frac{c}{v} \quad (2.11)$$

where n denotes the refraction index of the medium, c denotes the light celerity in vacuum, and v denotes the light velocity in the medium. When the signal passes from one layer number 1 to another layer number 2, its direction is changed following Equation (2.10). This law has to be integrated all over the atmosphere column crossed by the signal, following the Fermat principle of Equation (2.12):

$$S = \int_s n(h)dh \quad (2.12)$$

where S denotes the optical length of the true bended signal, s denotes the slant path from the antenna to the satellite, and n denotes the refraction index of the medium.

The tropospheric delay T_r^i of observation Equation (2.1) and (2.3) is defined as the difference between the optical length of the true bended signal and the geometrical distance between the satellite and the receiver antenna resulting in (2.13):

$$T_r^i = \int_s n(s)ds - \int_g dg \quad (2.13)$$

where s denotes the slant path from the antenna to the satellite and g denotes the geometrical path from the antenna to the top of the atmosphere the GNSS signal would take in the absence of atmosphere. By defining the refractivity N from the refraction index following Equation (2.14) [Smi 53], we obtain a quantity defining the deviation of the fraction of Equation (2.11) from the unity.

$$N = (n - 1) \cdot 10^6 \quad (2.14)$$

Equation (2.13) can thus be rewritten into Equation (2.15):

$$T_r^i = 10^6 \cdot \int_s N \cdot ds + \underbrace{\left(\int_s ds - \int_g dg \right)}_{\delta L} \quad (2.15)$$

This is leading to Equation (2.16) when separating the refractivity of the medium into dry N_d and wet N_w parts.

$$T_r^i = 10^6 \cdot \left(\int_s N_d \cdot ds + \int_s N_w \cdot ds \right) + \delta L \quad (2.16)$$

The dry part N_d is due to the neutral gas listed at the beginning of Section 2.3.3. The bending of the signal excess path length δL of Equation (2.15) is commonly considered to be part of the hydrostatic delay [Nil 13]. Water vapor is the only component of the wet part of the atmosphere, highly unpredictable. These slant path dry and wet delays can be mapped to the zenith direction of the antenna in order to characterize the troposphere delay above the GNSS antenna, affecting the GNSS signal paths in all directions. To this end, mapping functions are proposed.

2.3.3.2 Tropospheric Mapping Functions

A tropospheric mapping function $\mathcal{M}(el)$ is used to map the tropospheric delay from the slant path to the zenithal direction of the antenna leading to the zenithal troposphere delay (ZTD) quantity ZTD [Jin 14].

$$T_r^i(el) = \mathcal{M}(el) \cdot ZTD(el) \quad (2.17)$$

It allows us to characterize the delay observed in the satellite elevation direction by the delay observed at antenna zenith:

$$\mathcal{M}(el) = \frac{T_r^i(el)}{T_r^i(el = 90^\circ)} \quad (2.18)$$

This makes it possible to retrieve the state of the troposphere at the time of measurement independently of any observation angle. The simplest mapping function is obtained under the assumption of a plane Earth with a horizontally stratified atmosphere. This way, the bending effect is ignored and the mapping function becomes a simple cosecant function of the elevation:

$$\mathcal{M}(el) = \csc el = \frac{1}{\sin el} \quad (2.19)$$

Although this simple mapping function leads to an error of approximately 1 % equivalent to 2 cm on the tropospheric estimation for an elevation angle of 20°, it is not sufficient for precise positioning. Marini (1972) [Mar72] then proposed a mapping function of the continuous fraction form such as in Equation (2.20):

$$\mathcal{M}(el) = \frac{1}{\sin el + \frac{a}{\sin el + \frac{b}{\sin el + \frac{c}{\sin el + \dots}}}} \quad (2.20)$$

Equation (2.20) takes the bending into account, and many values have been proposed for the coefficients a , b , c , and so on, depending on surface NWM components such as pressure, temperature, the height of troposphere, etc [Hob 17]. However, using surface measurements still introduces errors to the tropospheric estimation. Thus, Niell (1996) [Nie96] proposed a function with coefficients involving only measurement date, latitude, and measurement height, such as in Equation (2.21):

$$\mathcal{M}(el) = \frac{\frac{1}{1 + \frac{a}{1 + \frac{b}{1 + c}}}}{\sin el + \frac{a}{\sin el + \frac{b}{\sin el + c}}} \quad (2.21)$$

Today, people mainly use the Global Mapping Function (GMF) that derives from the purely geometrical Niell mapping function with b and c taking empirical values and a following Equation (2.22) [Böh 06]:

$$a = a_0 + A \cos \left(\frac{d - 28}{365} 2\pi \right) \quad (2.22)$$

where a_0 and A denote the global grids of mean values and amplitudes of dry and wet coefficients respectively, and d denotes the day of the year.

Contrary to the Niell mapping function, GMF is based on atmospheric properties, determining its coefficients a , b , and c from ECMWF models for a fixed period [Böh

o6]. The Vienna Mapping Functionss (VMFs) is a similar mapping function to GMF but relies on ECMWF NWM ray-tracings, providing a gridded and site-wise mapping function [Boe 06]. The last versions of the discrete VMF and the climatological GMF are VMF3 and Global Pressure and Temperature (GPT)₃ [Lan 18]. Both provide dry and wet mapping functions that can be applied separately to N_d and N_w parts of Equation (2.16). The zenithal direction tropospheric delay thus obtained is in meters, with values from 1.5 to 3 m.

2.3.3.3 Zenith Total Delay

Using a mapping function of previous Section 2.3.3.2, we map the tropospheric propagation delay T_r^i of observation Equations (2.1) and (2.3) to the zenith direction. We thus obtain the ZTD following Equation (2.17). The ZTD corresponds to the quantity estimated within the PPP processing, through an a priori value coming from NWMs, and a correction from the process.

As far as the troposphere delay is composed of a dry and a wet part, we can separate Equation (2.16) into dry $T_{r,dry}^i$ and wet $T_{r,wet}^i$ terms such as in Equation (2.23):

$$T_r^i = T_{r,dry}^i + T_{r,wet}^i \quad (2.23)$$

We can then separate the ZTD of Equation (2.17) into a dry and a wet part as well:

$$ZTD = ZHD + ZWD \quad (2.24)$$

where ZTD, ZHD, and ZWD denote the ZTD, zenithal hydrostatic delay (ZHD), and ZWD respectively.

The hydrostatic part ZHD accounts for the major part of ZTD with 2.0 – 2.2 m at sea level while ZWD accounts for 0.01 – 0.8 m [Gue 22]. The ZHD is due to atmospheric density [Saa72], due to the neutral gas contained in the troposphere, and can be easily computed at mean sea level (MSL) from Equation (2.25) thanks to its low variability and dependence only on surface pressure.

$$ZHD(h) = 0.0022768 \frac{p_h}{1 - 0.00266 \cos(2\theta) - 0.00028h} \quad (2.25)$$

where p_h denotes the pressure at the antenna height, h denotes the height of the antenna above sea level, and θ denotes the latitude. Equation (2.25) comes from dry refractivity defined in Hobiger and Jakowski (2017) [Hob 17] and hydrostatic balance.

Then, we can extrapolate the ZHD from the antenna height to the MSL following the formula of [Ste 09] in Equation (2.26), adapted to our shipborne measurements as the antenna height is lower than 50 m AMSL such as explained by Bosser et al. (2021) [Bos 21a]:

$$ZHD(h_{MSL}) = ZHD(h) - 10^{-6} \cdot k_1 \cdot \frac{p_{MSL}}{T_{MSL}} \cdot \frac{g_{MSL}}{g_{atm}} \cdot (h - h_{MSL}) \quad (2.26)$$

where h and h_{MSL} denote the shipborne antenna and the geoid height corresponding to MSL, p_{MSL} and T_{MSL} denote the pressure and temperature at the MSL, $g_{MSL} = 9.806 \text{ 2 m.s}^{-2}$ denote the gravity at MSL, $g_{atm} = 9.784 \text{ 0 m.s}^{-2}$ denote the approximated gravity of the atmosphere mass center [Saa72], and $k_1 = 0.776 \text{ 43 K} \cdot \text{Pa}^{-1}$ is a refractivity constant [Tha74].

On the contrary, ZWD is highly variable and unpredictable, so it is computed from the GNSS estimated ZTD after removing the ZHD at the antenna height:

$$ZWD = ZTD - ZHD. \quad (2.27)$$

2.3.3.4 Tropospheric Gradients

The *ZTD* as described in Section 2.3.3.3 is ignoring the tropospheric change in azimuth.

Indeed, at a given time, two satellites at the same elevation angle but at different azimuths will transmit signals that pass through different troposphere states before reaching the GNSS antenna. When using mapping functions to map the slant path delays to the zenith direction, only the elevation of the satellite is considered. Thus, a second tropospheric parameter has been added and is estimated in the processing filter along with all other parameters: the tropospheric gradients. These gradients describe the horizontal change in the troposphere, eastward with G_{EW} and northward with G_{NS} . They are defined from the meridional ζ_{EW} and zonal horizontal refractivity ζ_{NS} thanks to a dedicated gradient mapping function \mathcal{M}_{az} [Che 97] as described in Section 2.3.3.2, to map it to the zenith direction of the antenna such as for the *ZTD* component, leading to Equation (2.28) :

$$\begin{pmatrix} \zeta_{EW} \\ \zeta_{NS} \end{pmatrix} = \begin{pmatrix} 10^{-6} \cdot \mathcal{M}_{az}(el) \cdot \frac{\sin(az)}{\tan(el)} \cdot G_{EW} \\ 10^{-6} \cdot \mathcal{M}_{az}(el) \cdot \frac{\cos(az)}{\tan(el)} \cdot G_{NS} \end{pmatrix} \quad (2.28)$$

The meridional and zonal horizontal refractivity come from the first order Taylor expansion of the refractivity of the medium N [Dav 93].

2.3.4 Multipath Effect

The multipath effect is an error created by the GNSS signals that are received by the antenna after diffraction or reflections on nearby surfaces, thus creating longer signal paths. This effect can highly deteriorate the measurement accuracy when it is too important. Because of its nearby environment dependency, the multipath effect is hardly removable from the measurement. It affects differential corrections and precise positioning and increases the ambiguity resolution time. These applications then require to reduce the effect of multipath thanks to multipath mitigation [Bra17].

GNSS electromagnetic signal is right-hand circularly polarized (RHCP). This means that the electromagnetic wave carrying the signal is turning clockwise around the propagation direction axis as seen by the receiver, such as shown in Figure 2.3.

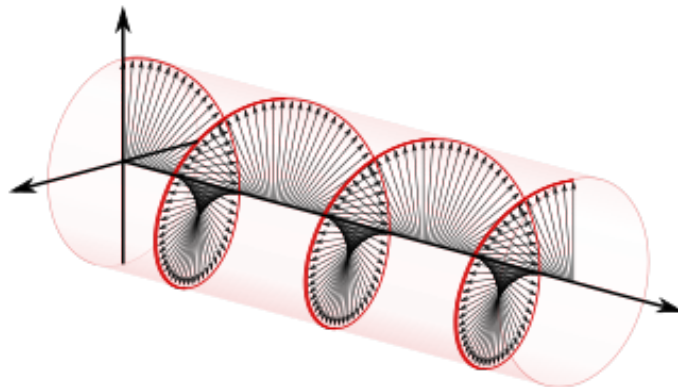


Figure 2.3: Schematic of the propagation of an RHCP GNSS electromagnetic wave. (Circular polarization. Retrieved July 23, 2023, from Dave3457 - Own work, Public Domain, [wikimedia.org](https://commons.wikimedia.org/wiki/File:Right-hand_circular_polarization.svg))

Using RHCP prevents phase shifting into the propagation signal. It also allows for filtering the left-hand circularly polarized (LHCP) L-band signals that could reach the receiver after being reflected once by the antenna environment. Multipath effect due to multiple reflections in the environment before reaching the antenna, added to the antenna noise measurement addressed in Section 2.3.5 can be responsible for up to 1 m of the positioning standard deviation of the antenna. Thus this error has to be mitigated for precise positioning application.

2.3.4.1 Multipath Mitigation

The receiving antenna must be placed as wisely as possible so that it reduces the multipath sources in the environment. The aim is to approach an ideally multipath-free environment, which is not fully possible. The antenna will ideally be placed higher than other surrounding objects.

As far as multipath will still occur in any situation, it is also possible to play with the antenna type for multipath mitigation. Ground-based reference GNSS antennas are ideally positioned in an obstacle-free area, so the main multipath source comes from the ground below the antenna. Thus, they are negative elevation signals as seen by the antenna, contrary to the direct paths coming from positive elevations. Then, dedicated technologies have been developed to keep the positive angle observations and remove the paths coming from negative elevations: radio-frequency absorbing ground-planes that are preventing the unwanted elevation angle paths from reaching the antenna mounted above; and the choke-ring antenna. The latter consists of a set of concentric conductive rings surrounding the antenna canceling the signals coming from low and negative elevation angles. These antennas are mainly used in ground-based GNSS applications because they are quite unwieldy. However, choke-rings antennas attenuate direct signals of elevations lower than 15° , so low elevation angle measurements are noisy. Dual systems can then be used to counterbalance this effect at low-elevation angles [Bra17].

Finally, it is possible to attenuate the multipath effect during the data processing. To this end, the covariance matrix of the measurement Gaussian noise $\Sigma_{\beta k}$ of Equation (2.43) is weighted according to the elevations of the corresponding observed satellite, providing greater confidence in high elevation measurements compared to those taken at low elevations. An elevation angle cut-off is applied as well to prevent the filter from considering measurements made from satellites between the horizon and this cut-off angle, which may be too spoiled by the multipath effect. Indeed, the multipath effect is usually raised with the decrease in elevation, because the obstructions should not be above the antenna. This principle is also true for ionosphere and troposphere effects because low-elevation paths are passing through a wider portion of the atmosphere than zenithal signals. Thus, the variance in processing least squares or Kalman Filter will be divided by a weighting function of elevation angle, producing an increase in low-elevation variance [Had 20]. The usual weighting functions provided by GNSS processing tools and software are cst , \sin , and $\sqrt{\sin}$. The cst function is the equivalent of unweighting measurements with elevation angle.

On the other hand, antennas are capable of selecting RHCP from all the signals arriving at the antenna. This allows to remove multipath signals that would have been reflected an odd number of times because such signals should be LHCP when observed by the antenna.

2.3.4.2 Multipath Effect Analytic Model

Elosegui et al. (1995) [Elo 95] detailed a first simple multipath contribution to the phase presented in Young, Neilan, and Bletzacker (1985) [You 85] and Georgiadou and Kleusberg (1987) [Geo 87]:

$$\Phi_{mp} = \frac{\lambda}{2\pi} \arctan \left(\frac{\alpha \sin \left(4\pi \frac{H_0}{\lambda} \sin el \right)}{1 + \alpha \cos \left(4\pi \frac{H_0}{\lambda} \sin el \right)} \right) \quad (2.29)$$

where Φ_{mp} denotes the multipath error, α denotes the attenuation of the amplitude of the reflected signal, H_0 denotes the vertical distance between the reflection location of the signal and the antenna phase center, el denotes the elevation of the satellite. The $\frac{\lambda}{2\pi}$ coefficient allows the multipath phase error to be converted from cycles to meters to be consistent with the Table 2.2 residual phase errors ε unit to which the multipath phase error is added.

Equation (2.29) assumes that the received GNSS signal is linearly polarized and that the signal is reflected on a horizontal plane surface at a distance H_0 below the antenna phase center in the far field, allowing the use of geometrical beam optics.

Later, King and Watson (2010) [Kin 10] proposed a new model as an upgraded version of the simplified model proposed by Elosegui et al. (1995) [Elo 95]. They aimed at proposing a model for radiating near field, where geometric beam optics do not apply, as well as taking the antenna gain into account such as in Equation (2.30).

$$\Phi_{mp} = \frac{\lambda}{2\pi} \arctan \left(\frac{a \sin \left(4\pi \frac{H_0}{\lambda} \sin el \right)}{g_d + a \cos \left(4\pi \frac{H_0}{\lambda} \sin el \right)} \right) \quad (2.30)$$

In Equation (2.30), the attenuation of the amplitude of the reflected signal α is replaced by the amplitude of the reflected signal $a = S \cdot g_r \cdot R$, where S and R denote respectively for the surface roughness depending on the reflecting surface material and Fresnel coefficient. The terms g_d and g_r denote the direct and reflected antenna gains for a rate of change of the antenna gain of $\Gamma = 1.1$:

$$g_d = \cos \left(\frac{90 - el}{\Gamma} \right) \quad g_r = \cos(90/\Gamma)(1 - \sin el) \quad (2.31)$$

To implement the right-hand circular polarization of the GNSS signal, the following Fresnel equation is introduced:

$$R = \sqrt{R_S^2 + R_P^2} \quad (2.32)$$

where:

$$R_P = \frac{n_1 \sqrt{1 - \left(\frac{n_1}{n_2} \cos el \right)^2} - n_2 \sin el}{n_2 \sin el + n_1 \sqrt{1 - \left(\frac{n_1}{n_2} \cos el \right)^2}} \quad (2.33)$$

denotes the Fresnel coefficient for an electric field parallel to the plane of incidence, and:

$$R_S = \frac{n_1 \sin el - \sqrt{n_2^2 - (n_1 \cos el)^2}}{n_1 \sin el + \sqrt{n_2^2 - (n_1 \cos el)^2}} \quad (2.34)$$

denotes the Fresnel coefficient for an electric field perpendicular to the plane of incidence, where $n_1 = 1$ is the refractive index of air and $n_2 = 1.33$ is the refractive index of salt water.

The resulting multipath from seawater reflection (with $S = 0.811$ for an elevation angle of 90° [Bra17]) of the GPS L1 band as seen by an antenna over 24 h is shown in Figure 2.4. It shows the need for a sufficiently high cut-off elevation angle, as multipath is most prevalent in low-elevation observations.

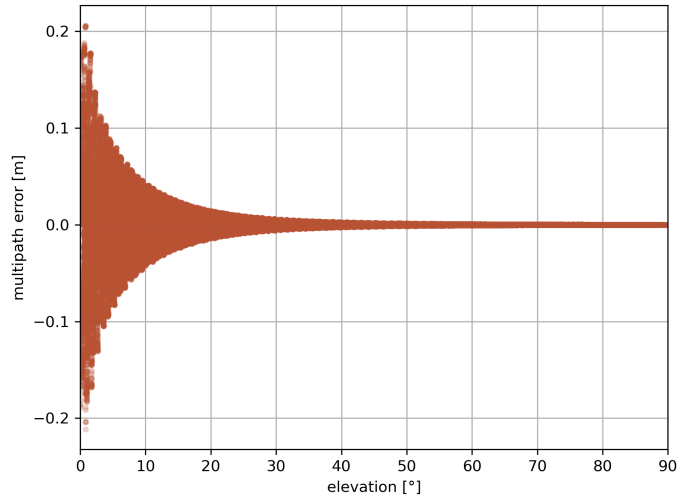


Figure 2.4: Multipath error for a 1.5 m high Trimble TRM105 000.10 antenna. The plot is for GPS, GLONASS and Galileo constellations

2.3.5 Antenna Phase Center Effect

The receiver antenna is measuring the GNSS signal with respect to an internal reference point named phase center, showing a constant offset ζ from the geometrical antenna center in Equation (2.1). However, the antenna phase center also varies around a fixed phase center given by the antenna manufacturer. This phenomenon, called antenna phase center variation (PCV), amounts to 1 – 2 cm [HW 13]. As seen in Figure 2.5, PCV depends on azimuth and elevation of the observed satellite as well as the GNSS signal wavelength, and is different for each model of antenna.

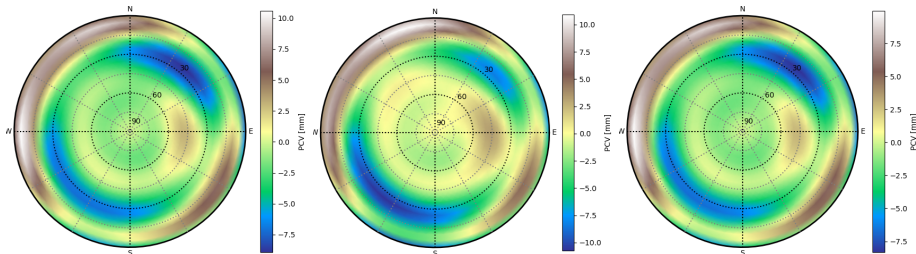


Figure 2.5: Trimble TRM105 000.10 antenna PCV calibration maps for GPS L1 (left), GLONASS L1 (center), and Galileo E5a (right), from (ngs14.atx).

Antenna PCV is evaluated by test series on each antenna type, resulting in antenna PCV maps for each observable wavelength. All antenna PCV maps are gathered in antenna calibration files searchable online such as in ngs20.atx.

2.4 KALMAN FILTERING FOR GNSS

The carrier-phase observable is fed to a stochastic linear regression such as Kalman filter or least squares method to solve for the remaining positioning parameters in the case of differential positioning, and for the clock delays, positioning, and atmospheric terms in the case of PPP. Because it is used in Chapter 5, we will focus on the Kalman filter technique, that has first been introduced by Kalman (1960) [Kal60].

The Kalman filter is a statistical filter implementation for a continuous space. It relies on the hypothesis that the problem is Gaussian and linear. It uses the density of the state variables that are defined with its moments representation: the mean and the covariance of their normal distribution. The state variables at a given time step are gathered into a multivariate normal distribution X of mean a vertical state vector \mathbf{x} of mean $\boldsymbol{\mu}$ of the same size than \mathbf{x} and covariance matrix $\boldsymbol{\Sigma}$ that is a quadratic matrix, symmetric and positive-semidefinite, of size the state vector size squared. Its diagonal displays the variance of each state variable of \mathbf{x} , while the rest displays the covariance of each couple of state variables. The Gaussian and linear hypotheses in continuous space lead to the following probability density function (pdf) of X :

$$\mathbf{p}(X = \mathbf{x}) = \mathbf{p}(\mathbf{x}) = \frac{1}{\sqrt{\det(2\pi\boldsymbol{\Sigma})}} \exp\left(-\frac{1}{2}(\mathbf{x} - \boldsymbol{\mu})^T \boldsymbol{\Sigma}^{-1}(\mathbf{x} - \boldsymbol{\mu})\right) \quad (2.35)$$

The Kalman filter is a fast filter that provides the best estimation, that corresponds to the minimum variance estimate.

The initial stage of the state vector \mathbf{x}_0 must be normally distributed, so the Equation (2.35) must be true at the initial step, to ensure the Gaussian behavior of the state vector in the following time steps of the filtering.

The Kalman filtering is a recursive estimation method that proceeds in two steps for each iteration:

1. the *prediction* of the a priori state $\hat{\mathbf{x}}_k$ at a given time step k from the previous time step $k - 1$;
2. the *correction* \mathbf{x}_k of the predicted state at time step k by the assimilation of the measurements made at time step k .

2.4.1 Prediction Model

We suppose here that we are at a given time step $k > 0$, and we know the state of the system at the time step $k - 1$. We can compute the a priori state k from the state $k - 1$, given by the state equation:

$$\hat{\mathbf{x}}_k = \mathbf{A}_k \mathbf{x}_{k-1} + \boldsymbol{\alpha}_k \quad (2.36)$$

The model state matrix \mathbf{A}_k at the time step k is a squared matrix of the squared size of the state vector. $\boldsymbol{\alpha}_k$ denotes the random noise vector of state transition of the same size than $\hat{\mathbf{x}}_k$, that has a zero mean and a covariance denoted $\boldsymbol{\Sigma}_{\alpha k}$.

The multivariate normal distribution of $\hat{\mathbf{x}}_k$ knowing \mathbf{x}_{k-1} has a mean of $\mathbf{A}_k \mathbf{x}_{k-1}$ and a covariance of $\boldsymbol{\Sigma}_{\alpha k}$. The associated linear Gaussian state transition probability is then expressed by:

$$\mathbf{p}(\hat{\mathbf{x}}_k | \mathbf{x}_{k-1}) = \frac{1}{\sqrt{\det(2\pi\boldsymbol{\Sigma}_{\alpha k})}} \exp\left(-\frac{1}{2}(\hat{\mathbf{x}}_k - \mathbf{A}_k \mathbf{x}_{k-1})^T \boldsymbol{\Sigma}_{\alpha k}^{-1}(\hat{\mathbf{x}}_k - \mathbf{A}_k \mathbf{x}_{k-1})\right)$$

$$(2.37)$$

As far as the ionospheric effect is considered as removable through the [IF LC](#), we do not model it in the Kalman filtering so far. [ZHD](#) is well known from the antenna height and composes the major part of the [ZTD](#), its value is computed prior to performing the filtering. The remaining atmospheric effect to model in the Kalman Filter for each visible satellite i is the wet part:

$$T_{r,wet}^i = ZWD \cdot \mathcal{M}_w(el^i). \quad (2.38)$$

Thus, the estimated variables in the Kalman filter for the [PPP](#) processing are then the location of the receiver $(X_r \ Y_r \ Z_r)$, the [ZWD](#), the tropospheric gradients, the receiver clock delay dt_r , and the integer ambiguity $N_{\phi_r}^i$, so the state vector would be as follows:

$$\mathbf{x}_k = \left[X_r \ Y_r \ Z_r \ ZWD \ G_{EW} \ G_{NS} \ dt_r \ N_{\phi_r}^i \right]^T, \quad (2.39)$$

The constraints applied to the state vector variables will serve to define the possible variations of the prediction model by implementing them in the random noise vector of state transition covariance matrix, simply noted Σ_α as it does not depend on the time step k :

$$\Sigma_\alpha = \begin{bmatrix} \sigma_X^2 & 0 & 0 & 0 & 0 & 0 & 0 & 0 \\ 0 & \sigma_Y^2 & 0 & 0 & 0 & 0 & 0 & 0 \\ 0 & 0 & \sigma_Z^2 & 0 & 0 & 0 & 0 & 0 \\ 0 & 0 & 0 & \sigma_{ZWD}^2 & 0 & 0 & 0 & 0 \\ 0 & 0 & 0 & 0 & \sigma_G^2 & 0 & 0 & 0 \\ 0 & 0 & 0 & 0 & 0 & \sigma_G^2 & 0 & 0 \\ 0 & 0 & 0 & 0 & 0 & 0 & \sigma_C^2 & 0 \\ 0 & 0 & 0 & 0 & 0 & 0 & 0 & 0 \end{bmatrix}, \quad (2.40)$$

where σ_X^2 , σ_Y^2 and σ_Z^2 denote for the positioning estimation variance, σ_{ZWD}^2 denotes for the [ZWD](#) variance, σ_G^2 denotes for tropospheric gradients variance, and σ_C^2 denotes for the clock delay estimate variance. The variation σ_G^2 of the meridional and zonal horizontal refractivity in the processing filter is usually defined as a hundred times smaller than the [ZWD](#) variation [[Gra 00](#)].

$$\sigma_G^2 = 10^{-2} \cdot \sigma_{ZWD}^2 \quad (2.41)$$

To define the model state matrix for [PPP](#) processing, we suppose that the prediction of a given state of some variables at time step k is the same as the time before. In the case of kinematic processing, the position is supposed to stay the same as the previous step $k - 1$ a priori, as well as the clock delay, but the covariance matrix Σ_α will be set with high uncertainty for these terms' variance, as opposed to the static processing. The ambiguity is supposed to be the same as the previous time step $k - 1$. This leads to the following model state matrix, simply noted \mathbf{A} as it does not depend on the time step k either:

$$\mathbf{A} = \mathbf{I}_8 \quad (2.42)$$

2.4.2 Correction Model

We now know the a priori state $\hat{\mathbf{x}}_k$ at time step k from the prediction equation. We correct the predicted state at time step k by using the vector of the measurements \mathbf{y}_k made at time step k :

$$\mathbf{y}_k = \mathbf{C}_k \hat{\mathbf{x}}_k + \boldsymbol{\beta}_k \quad (2.43)$$

\mathbf{C}_k denotes the observation matrix at time step k with size the size of the state vector $\hat{\mathbf{x}}_k$ times the size of the observation vector \mathbf{y}_k - corresponding to the number of measurement variables. $\boldsymbol{\beta}_k$ is the measurement Gaussian noise vector of time step k with zero mean and a covariance denoted $\boldsymbol{\Sigma}_{\boldsymbol{\beta}_k}$, of size the square of the size of the observation vector \mathbf{y}_k .

The multivariate normal distribution of \mathbf{y}_k has a mean of $\mathbf{C}_k \hat{\mathbf{x}}_k$ and a covariance of $\boldsymbol{\Sigma}_{\boldsymbol{\beta}_k}$. The associated linear Gaussian measurement probability is then expressed by:

$$\mathbf{p}(\mathbf{y}_k | \hat{\mathbf{x}}_k) = \frac{1}{\sqrt{\det(2\pi\boldsymbol{\Sigma}_{\boldsymbol{\beta}_k})}} \exp\left(-\frac{1}{2}(\mathbf{y}_k - \mathbf{C}_k \hat{\mathbf{x}}_k)^T \boldsymbol{\Sigma}_{\boldsymbol{\beta}_k}^{-1} (\mathbf{y}_k - \mathbf{C}_k \hat{\mathbf{x}}_k)\right) \quad (2.44)$$

In practice, the observation vector \mathbf{y}_k is composed of the carrier-phase measurements coming from each of the visible satellites described in Equation (2.3) at the time step k . Its size is then equal to the number of visible satellites n_{sat} at time step k :

$$\mathbf{y}_k = \left[\Phi_{rk}^1 \quad \Phi_{rk}^2 \quad \dots \quad \Phi_{rk}^{n_{sat}} \right]^T. \quad (2.45)$$

Kalman filtering needs the dynamics and measurement equations to be linear. However, Equation (2.3) still has one term that is not linear, the geometric range ρ_r^i showing the squared unknown receiver position coordinates in Equation (2.2), the satellite position being known in double differences, or thanks to the ephemerids in case of PPP processing. To linearize the coordinates terms, we split X_r in an assumed approximate value X_{r0} and an unknown part ΔX_r , as well as the two other coordinates, such as described in Equation (2.46).

$$\begin{aligned} X_r &= X_{r0} + \Delta X_r \\ Y_r &= Y_{r0} + \Delta Y_r \\ Z_r &= Z_{r0} + \Delta Z_r \end{aligned} \quad (2.46)$$

Then, it is possible to expand Equation (2.2) into a Taylor series, leading at the first order to the linearized Equation (2.47) concerning the unknown parts of the receiver coordinates.

$$\begin{aligned} \rho_r^i &= \rho_{r0}^i - \frac{(X^i - X_{r0})}{\rho_{r0}^i} \cdot \Delta X_r - \frac{(Y^i - Y_{r0})}{\rho_{r0}^i} \cdot \Delta Y_r \\ &\quad - \frac{(Z^i - Z_{r0})}{\rho_{r0}^i} \cdot \Delta Z_r \end{aligned} \quad (2.47)$$

where $\rho_{r0}^i = \sqrt{(X^i - X_{r0})^2 + (Y^i - Y_{r0})^2 + (Z^i - Z_{r0})^2}$.

In the case of PPP processing, for a given timestamp k and each observed satellite i , the approximated receiver distance to the satellite ρ_{r0}^i is considered as known, as well as the satellite clock delay dt^i and the phase wind-up ω_r^i that are already taken

into account in the ephemerides, and the relativistic corrections δt^{rel} that is modeled. By shifting all the known terms to the left, Equation (2.3) can be rewritten as the following linear equation used in the extended Kalman filter (EKF):

$$\begin{aligned}
\Phi_r^i = & -\frac{(X^i - X_{r0})}{\rho_{r0}^i} \cdot \Delta X_r - \frac{(Y^i - Y_{r0})}{\rho_{r0}^i} \cdot \Delta Y_r - \frac{(Z^i - Z_{r0})}{\rho_{r0}^i} \cdot \Delta Z_r \\
& + \mathcal{M}_w(el_k^i) \cdot ZWD + 10^{-6} \cdot \mathcal{M}_{az_k^1}(el_k^1) \cdot \frac{\sin(az_k^1)}{\tan(el_k^1)} \cdot G_{EW} \\
& + 10^{-6} \cdot \mathcal{M}_{az_k^1}(el_k^1) \cdot \frac{\cos(az_k^1)}{\tan(el_k^1)} \cdot G_{NS} + c \cdot dt_r + \lambda \cdot N_{\phi_r}^i \\
& + \rho_{r0}^i + c(\delta t^{rel} - dt^i) + \lambda \cdot \omega_r^i + \varepsilon_r^i.
\end{aligned} \tag{2.48}$$

The remaining terms in the last line of Equation (2.48) are known from the ephemerid products of the satellites that are fed to the filter and are then removed before moving to the correction step of the filtering. Then, the observation matrix is defined as:

$$\mathbf{C}_k^T = \begin{bmatrix} -\frac{(X^1 - X_{r0})}{\rho_{r0}^1} & \dots & -\frac{(X^{n_{sat}} - X_{r0})}{\rho_{r0}^{n_{sat}}} \\ -\frac{(Y^1 - Y_{r0})}{\rho_{r0}^1} & \dots & -\frac{(Y^{n_{sat}} - Y_{r0})}{\rho_{r0}^{n_{sat}}} \\ -\frac{(Z^1 - Z_{r0})}{\rho_{r0}^1} & \dots & -\frac{(Z^{n_{sat}} - Z_{r0})}{\rho_{r0}^{n_{sat}}} \\ \mathcal{M}_w(el_k^1) & \dots & \mathcal{M}_w(el_k^{n_{sat}}) \\ 10^{-6} \cdot \mathcal{M}_{az_k^1}(el_k^1) \cdot \frac{\sin(az_k^1)}{\tan(el_k^1)} & \dots & 10^{-6} \cdot \mathcal{M}_{az_k^{n_{sat}}}(el_k^{n_{sat}}) \cdot \frac{\sin(az_k^{n_{sat}})}{\tan(el_k^{n_{sat}})} \\ 10^{-6} \cdot \mathcal{M}_{az_k^1}(el_k^1) \cdot \frac{\cos(az_k^1)}{\tan(el_k^1)} & \dots & 10^{-6} \cdot \mathcal{M}_{az_k^{n_{sat}}}(el_k^{n_{sat}}) \cdot \frac{\cos(az_k^{n_{sat}})}{\tan(el_k^{n_{sat}})} \\ c & \dots & c \\ \lambda & \dots & \lambda \end{bmatrix} \cdot \tag{2.49}$$

2.4.3 Processing Strategies to Manage the Errors in the Kalman Filter

This filtering is equally applied with some constraints on the observation data assimilated in the correction step of the processing. These constraints have to be tuned to be adapted to the situation.

Several processing features can be tuned in order to mitigate multipath affecting the GNSS signal observation. For example, the setup of a wise cut-off angle is important. It has to be suitable to prevent the use of the observations coming from satellites with low elevation above the horizon that are highly affected by multipath effect [Mek 10]. Also, the cut-off angle has to be tuned wisely to decorrelate ZWD and height in the GNSS processing [Kač 19]. Contrary to the multipath mitigation, it has to be as low as possible, because low-elevation angle satellite observations can be more useful to separate the ZWD from the height estimate.

The implementation of a weighting function increasing the weight of the variance of the low-elevation satellite observations is a variant of the cut-off angle permitting to keep the low-elevation information and data while giving them lower credit than the high-elevation observations. Elevation cut-off and weighting techniques can be applied together while processing the GNSS data.

A third processing feature, the random walk process noise (RWPN) has to be tuned wisely in order to get rid of the correlation between the ZWD and the positioning,

especially the antenna height, affecting the GNSS processing. It is used to constrain the ZWD variance over time:

$$\sigma_{ZWD}^2 = \tau^2 \cdot \delta t \quad (2.50)$$

where δt denotes the time resolution of the GNSS processing. The ZWD variance σ_{ZWD}^2 is introduced into the ZWD corresponding slot of the variance-covariance matrix of the noise vector Σ_α .

Too loose RWPN will let the ZWD absorb some of the change in height over time, which could be considered as noise by the filter in kinematic processing; whereas an RWPN too tight will prevent the system from delivering the right ZWD variations over time, thus smoothing the estimation. Considering that, the variance-covariance matrix of the noise vector Σ_α of Equation (2.40) becomes:

$$\Sigma_\alpha = \begin{bmatrix} \sigma_X^2 & 0 & 0 & 0 & 0 & 0 & 0 & 0 & 0 \\ 0 & \sigma_Y^2 & 0 & 0 & 0 & 0 & 0 & 0 & 0 \\ 0 & 0 & \sigma_Z^2 & 0 & 0 & 0 & 0 & 0 & 0 \\ 0 & 0 & 0 & \tau^2 \cdot \delta t & 0 & 0 & 0 & 0 & 0 \\ 0 & 0 & 0 & 0 & 10^{-2} \cdot \tau^2 \cdot \delta t & 0 & 0 & 0 & 0 \\ 0 & 0 & 0 & 0 & 0 & 10^{-2} \cdot \tau^2 \cdot \delta t & 0 & 0 & 0 \\ 0 & 0 & 0 & 0 & 0 & 0 & \sigma_C^2 & 0 & 0 \\ 0 & 0 & 0 & 0 & 0 & 0 & 0 & 0 & 0 \end{bmatrix} \quad (2.51)$$

where τ denotes the RWPN, and δt denotes the time resolution of the GNSS processing. σ_X^2 , σ_Y^2 , σ_Z^2 can be high when the processing is dynamical without constraint, low when the dynamical processing is constrained, and tends to zero when the processing is in static mode; and σ_C^2 is high, being modeled as a white noise.

Another method to decorrelate ZWD and height estimates is to run the processing by iteration:

1. a priori horizontal position is estimated (eventually with a high cut-off angle to mitigate multipath),
2. height and ZWD are estimated separately using previous horizontal results (eventually with a low cut-off angle to estimate ZWD more accurately),
3. a posteriori positioning components are estimated taking into account the ZWD value computed at the previous step.

Dodson et al. (2001) [Dod 01] showed that this PPP processing method increases the accuracy of the ZWD estimation to up to 1 mm, which is equivalent to a ground-based GNSS static PPP processing accuracy.

Bar-Sever and Kroger (1996) [BS 96] has actually studied the RWPN tuning effect on the ZWD retrieval accuracy, while Selle and Desai (2016) [Sel 16] showed the link between RWPN and weighting function on the elevation. The latter actually showed that the suitable RWPN value providing the best estimation accuracy will depend on the weighting function used for processing the GNSS data. Finally, Kačmařík et al. (2019) [Kač 19] has shown by testing different processing strategies that 3° of cut-off angle provides the best accuracy on the estimation of the tropospheric gradients.

2.4.4 Kalman Filter Implementation for PPP

The implementation of the [EKF](#) for [PPP GNSS](#) processing follows [Algorithm 2.1](#).

Algorithm 2.1 KalmanFilter

Input: \mathbf{x}_{k-1} , Σ_{k-1} , Σ_α , \mathbf{A} , \mathbf{y}_k , $\Sigma_{\beta k}$, \mathbf{C}_k

Output: \mathbf{x}_k , Σ_k

- 1: $\hat{\mathbf{x}}_k \leftarrow \mathbf{A}\mathbf{x}_{k-1}$
 - 2: $\hat{\Sigma}_k \leftarrow \mathbf{A}\Sigma_{k-1}\mathbf{A}^T + \Sigma_\alpha$
 - 3: $\mathbf{K}_k \leftarrow \hat{\Sigma}_k\mathbf{C}_k^T (\mathbf{C}_k\hat{\Sigma}_k\mathbf{C}_k^T + \Sigma_{\beta k})^{-1}$
 - 4: $\mathbf{x}_k \leftarrow \hat{\mathbf{x}}_k + \mathbf{K}_k (\mathbf{y}_k - \mathbf{C}_k\hat{\mathbf{x}}_k)$
 - 5: $\Sigma_k \leftarrow (\mathbf{I} - \mathbf{K}_k\mathbf{C}_k) \hat{\Sigma}_k$
 - 6: **return** \mathbf{x}_k , Σ_k
-

2.5 GNSS ATMOSPHERIC WATER VAPOR OBSERVATION PRINCIPLE

2.5.1 PWV Derived from GNSS ZWD Estimates

A water vapor value defined as the integrated water vapor ([IWV](#)) is closely linked to the [ZWD](#). It is defined from the water vapor density in the atmosphere column ρ_v as follows:

$$IWV(h) = \int_h^\infty \rho_v(z) dz \quad (2.52)$$

where h denotes the height of the antenna above sea level.

[ZWD](#) estimation from ground-based [GNSS](#) dataset permits to compute the [IWV](#) in $\text{kg}\cdot\text{m}^{-2}$ as in [Equation \(2.53\)](#):

$$IWV = \frac{10^6}{\left(\frac{k_3}{T_m} + k'_2\right) R_v} \cdot ZWD \quad (2.53)$$

where T_m denotes the mean temperature of the troposphere following [Equation \(2.54\)](#) [[Bev 92](#)], k'_2 and k_3 are refractivity coefficients of the water vapor determined empirically locally [[Tha74](#)], and $R_v = 461.51 \text{ J} \cdot \text{kg}^{-1} \cdot \text{K}^{-1}$ is the gas constant of the water vapor.

$$T_m = \frac{\int \frac{P_v}{T} dz}{\int \frac{P_v}{T^2} dz} \quad (2.54)$$

The [IWV](#) thus computed is directly proportional to the [PWV](#) [PWV](#) through mean liquid water density $\rho_v = 1000 \text{ kg} \cdot \text{m}^{-3}$ following [Equation \(2.55\)](#):

$$PWV = \frac{1}{\rho_v} \cdot IWV \quad (2.55)$$

Thus, $1 \text{ kg} \cdot \text{m}^{-2}$ equals to 1 mm of [PWV](#). As a rule of thumb, it is widely agreed that 1 mm of [PWV](#) causes a delay of approximately 6.5 mm on the [GNSS](#) signal.

Methods used for surface pressure and moisture-weighted mean temperature (T_m) computation have uncertainties in themselves that are added to the [GNSS ZTD](#) estimation uncertainty when computing the [PWV](#) such as explained above.

The retrieved *PWV* can then be used for atmosphere water vapor monitoring purposes through *GNSS* measurements. The *PWV* content amounts from 0 to 70 mm, with values between 40 and 70 mm near the Equator, and less than 20 mm near the Poles [Wu 22b].

As far as the retrieved *PWV* depends on the remaining atmosphere above the *GNSS* antenna, this quantity will change for two antenna measurements at the same location but distinct heights. The *PWV* retrieved at the antenna height can be extrapolated to another height for comparison to other products for example. To this end, we will adjust the *PWV* to the height difference Δh , for a vertical distance of less than 100 m, by using the empirical formula proposed by Bock et al. (2005) [Boc 05]:

$$\Delta PWV = -4 \cdot 10^{-5} \cdot PWV \cdot \Delta h \quad (2.56)$$

2.5.2 *GNSS for Climate*

GNSS for climatology (*GNSS-C*) corresponds to the long-term variations study of the atmospheric water vapor content using *GNSS* measurements. It is mainly done thanks to ground-based *GNSS* networks datasets that can be post-processed with the more accurate final ephemerid products and then give long-term troposphere monitoring, such as the products from the Nevada Geodetic Laboratory (NGL) (<http://geodesy.unr.edu/>). Bock et al. (2013) [Boc 13] showed that an accuracy of 1 to 2 mm can be achieved on ground-based *GNSS* retrieved *PWV*, showing a very good agreement with other water vapor measurement methods. *GNSS* post-processing enables the study of climate change and the hydrological cycle and fills a gap due to the sparsity and heterogeneity of global tropospheric monitoring [Boc 20].

In a context of global warming and climate change, a temperature change will influence the amount of water vapor in the atmosphere, changing the regional balance and raising the global water vapor amount. On one side, the increase in global atmospheric water vapor content will heat the Earth because of its strong greenhouse effect, eventually entering a vicious circle of atmospheric heating. On the other side, the increase of water vapor that can be involved in weather events can lead to stronger meteorological phenomena. Studying climate trends is definitely relevant and essential nowadays. Climate studies allow for predicting future living conditions, the impact on ecosystems and migrations, and planning land use accordingly. This makes *GNSS-C* very valuable [Bia 16].

2.5.3 *GNSS for Meteorology*

GNSS for meteorology (*GNSS-M*) stands for the use of *GNSS* data for *NWP* [Pol 07]. *GNSS-M* needs *RT* or *NRT* products for rapid update, which is possible thanks to the development of highly accurate ephemerid products [Ge 02; Liu 02].

The *NRT GNSS* data availability over a long time and under a thin time resolution permits the immediate capture of water vapor content variation in the atmosphere [Bev 94]. Indeed, *RSs* launched twice a day does not permit to see some fast occurring events, while *GNSS* monitoring of the atmosphere does. Since water vapor is an important but highly variable parameter in meteorology, the benefit of *GNSS-M* for accurate weather forecasting is particularly important for preventing severe weather events such as flash floods or strong storms, and for issuing appropriate weather warnings. Indeed, the assimilation of *GNSS* data has been shown to improve weather forecasting [Kar

11; Ben 12; Iku 21], especially during heavy rain events [Ved 04]. The fact that GNSS measurement is possible in all weather conditions contributes to this improvement.

The deployment of dense ground-based GNSS networks makes it possible to capture spatial water vapor variations as well as local variations in time. The COST Action ES1206 developed Advanced Global Navigation Satellite Systems tropospheric products for monitoring severe weather events and climate (GNSS4SWEC), the "advanced global navigation satellite systems tropospheric products for monitoring severe weather events and climate" project, from 2013 to 2017. The aim was to provide nowcasting thanks to GNSS products from ground-based antennas, especially for severe weather events NWP, such as fog, heavy rain, flooding, and Foehn [DH 20]; and climate study. In the framework of GNSS4SWEC, a state-of-the-art of ground-based GNSS has been established by [Gue 16]. They underline the new research interests of the field of atmospheric monitoring through ground-based GNSS stations. They can prove useful for severe weather forecasting, of high interest in Europe; nowcasting with real-time processing of the data; and multi-GNSS combination expected to improve tropospheric products. GNSS data assimilation in NWP and climate study were other aims of this project.

The idea of assimilating water vapor measurements to NWP models from GNSS antennas carried out on ships around Japan has been investigated by Ikuta, Seko, and Shoji (2021) [Iku 21], providing encouraging results both in general and during heavy rainfall episodes.

2.6 CONCLUSION ON GNSS PRINCIPLES

GNSS has taken a central place in today's life. Although it is used for positioning and navigation under different processing methods that can achieve accuracies up to the millimeter range for the most expensive instruments and advanced techniques, the most precise applications need to take into account the instrumental delays and environmental impact of the signal during the measurement. Among them, the multipath is a big issue affecting the signal.

The troposphere also has an impact on the GNSS signal, and its effect has to be evaluated in case of precise positioning. To deal with all error sources, several features must be wisely tuned during the estimation process. Among others we will be interested in the cut-off angle on the elevation of the satellites, the weighting function of the elevation of the satellite applied to the variance of the observations, and the constraint over the tropospheric component variations.

The enhancement of GNSS processing accuracy permits the development of new applications of this technology. Indeed, several ground-based GNSS networks have spread out over the continents, with the denser networks found in developed countries. They permit the study of long-term variability in several aspects requiring positioning accuracy such as continental drift, or atmosphere monitoring. They are also used as reference stations for precise RT or post-processed positioning of moving or static GNSS antennas. The ground-based RT products can currently be assimilated to NWP models [Kar 11; Ben 12].

As far as numerous vessels are sailing the oceans all around the world at any time of day and night, carrying GNSS antennas for positioning on their electronic navigational charts (ENC), it could be interesting to gather their GNSS data for troposphere monitoring at sea. This has been first studied by Rocken et al. (2005) [Roc 05], and

more democratized since [Wan 19] that showed an accuracy of 2 to 3 mm sufficient for troposphere study purposes. Since then, more and more studies about shipborne GNSS PWV retrieval have been pursued. The major studies covering this topic that have already been released are gathered and detailed in Chapter 3.

SHIPBORNE GNSS FOR PRECIPITABLE WATER VAPOR
RETRIEVAL

CONTENT

3.1	Offshore Precise Point Positioning Issues	37
3.2	Litterature on Shipborne GNSS for Precipitable Water Vapor Retrieval	38
3.3	Studies Features	40
3.3.1	Multi-GNSS Performance	41
3.3.2	Processing Features	41
3.4	Assessment of Shipborne GNSS PWV Quality	43
3.4.1	Ground-Based GNSS Stations	45
3.4.2	Numerical Weather Models	46
3.4.3	Satellite Water Vapor Radiometers	47
3.4.4	Radiosondes	48
3.4.5	Compared Datasets Correlation	50
3.5	Conclusion on the Shipborne GNSS Litterature	50
3.5.1	Contributions and Limitations in the Framework of this Thesis	51
3.5.2	Future Prospects Arisen by these Studies	52

3.1 OFFSHORE PRECISE POINT POSITIONING ISSUES

Precisely positioning a vessel with a GNSS antenna cannot be done with differential positioning, and absolute methods provide an accuracy of centimeter-level [Bor 94; Spi 98]. Indeed, although a network of reference ground-based GNSS stations is available in coastal areas, there are none in the open sea. Then, only PPP positioning is relevant in this case, as it provides absolute positioning. To this end, many parameters have to be estimated along with the positioning, such as clock biases and tropospheric delay, as explained in Section 2.2.

Collecting shipborne GNSS PWV permits ocean data covering a larger scale than using a few expensive sensors located in specific areas. Indeed, many ships are constantly sailing the oceans, especially along maritime routes where millions of commercial vessels are carrying GNSS antennas to track their course. It is complementary to the completeness of atmospheric water vapor provided by satellite radiometers, which continuously cover the globe and sound much of the oceans twice a day at relatively low spatio-temporal resolution locally.

However, contrary to the ground GNSS stations, shipborne antennas are moving, so the position and ZWD have to be estimated simultaneously at each time step, contrary

to the ground stations that are considered static and have their location estimated only once a day. On the other side, the sea reflects greatly the L-band waves in different ways depending on the sea state, so multipath error can be high in the marine environment. Appropriate modeling of the processing is then crucial, as we will demonstrate in [Part 3.5.2](#).

Early studies have shown great promises, providing [PWV](#) estimation from simple offshore platforms such as buoys with an accuracy of 1 to 2 mm [[Cha 01](#); [Dod 01](#)].

3.2 SHIPBORNE GNSS WATER VAPOR RETRIEVAL FOR ATMOSPHERIC WATER VAPOR STUDY AT SEA: STATE OF THE ART

Since the first study of Chadwell and Bock (2001) [[Cha 01](#)], it has been demonstrated that [PWV](#) retrieving from offshore platforms [GNSS](#) antennas is of great interest for troposphere monitoring over seas. The field of research has reached more interest since the publication of Wang et al. (2019) [[Wan 19](#)] where it has been demonstrated that the 2 to 3 mm accuracy of [PWV](#) retrieved from antennas aboard big vessels with complex movements is achievable. All the published works about [PWV](#) retrieval from shipborne [GNSS](#) antennas until mid-2023 are listed in [Table 3.1](#) along with their publication date, number of shipborne antennas involved, date span and duration of the acquisition, and its location.

Of course, these studies have different purposes, the most singular being detailed in the following sections.

Long-Term Study

Contrary to the other studies of [Table 3.1](#), Wu et al. (2022) [[Wu 22b](#)] achieved a study over a longer period, covering several years with six [R/V](#) campaigns carried out by an [R/V](#) across the Oceans during which geodetic measurement were acquired. They interestingly carried out a shipborne [GNSS](#) retrieved [PWV](#) error budget by evaluating the errors from the different variables involved in the [PWV](#) computation. This error budget led to the conclusion that [PWV](#) has an uncertainty of 2.70 mm over their whole dataset. They are therefore able to determine the accuracy of numerous other measurement methods by comparing it to their long-term shipborne [PWV](#).

Slant-Path Water Vapor

Fan et al. (2016) [[Fan 16](#)] aims at getting slant-path water vapor ([SWV](#)), meaning the water vapor amount along the ray path through the troposphere when it is traveling between the satellite and the receiving antenna, for 3D water vapor tomography application at sea. This quantity can be derived from [GNSS PWV](#) that accounts for zenith-direction-only water vapor information. Thus, they used a modest-sized [R/V](#) compared to Rocken et al. (2005) [[Roc 05](#)] and Fujita et al. (2008) [[Fuj 08](#)] to get an experimental behavior of the platform close to that of a buoy that might further be used for tomography purposes.

Multi-Antennas Performance

Wei et al. (2023) [[Wei 23](#)] proposes to use several [GNSS](#) antennas onboard a ship in order to get more accurate [PWV](#) than with one antenna, using the inter-antennas baseline. They found out that using the baseline constraint between the two antennas permits almost instant convergence, compared to dozens of minutes with a conventional kinematic [PPP](#) processing. Large jumps observed in conventionally retrieved shipborne [GNSS PWV](#) are due to cycle slips in the satellite observation when the solution

Work	Year	N	Start	End	Avail.	Region
[Roc 05]	2005	1	2002/07	2003/08	2*1 weeks	Greater Antilles
[Roc 08]	2008	1	2006/10	2006/12	3 months	Indian Ocean
[Fuj 08]	2008	1	2006/10	2006/12	2 months	Indian Ocean
[Bon 12]	2012	1	2008/09	2009/01	4 months	NW Mediterranean coastal Sea
[Kea 12]	2012	1	2011/02	2011/02	10 days	Hawaiian Islands
[Fuj 14]	2014	1	2013/04	2013/05	1 month	NW Pacific Ocean
[Fan 16]	2016	1	2010/11	2010/11	2 days	Chinese Bohai Sea
[Sho 16]	2016	4	2015/01	2015/12	1 year	NW Pacific Ocean
[Sho 17]	2017	1	2016/10	2017/08	10 months	NW Pacific Ocean
[Wan 19]	2019	1	2016/08	2016/09	20 days	Fram Strait
[Liu 19]	2019	1	2014/03	2014/05	2 months	Indian Ocean
[Soh 20]	2020	1	2018/08	2018/09	23 days	Pacific Ocean
[Wu 20]	2020	1	2014/04	2014/05	56 days	Indian Ocean
[Bos 21a]	2021	3	2020/01	2020/02	34 days	W Atlantic Ocean
[Gon 21]	2021	1	2017/06	2017/08	77 days	Pacific Ocean
[Män 21]	2021	1	2019/09	2020/10	15 months	Central Arctic
[Bos 22b]	2022	1	2020/10	2021/06	9 months	Indian Ocean
[Wu 22a]	2022	1	2021/08	2021/09	16 days	Bohai and Yellow Sea
[Wu 22b]	2022	1	2014/04	2018/05	2 years	World Oceans
[Sho 23]	2023	3	2019/03	2021/04	1 months	N Pacific Ocean
[Wei 23]	2023	2	2019/07	2019/07	4 days	E China coast

Table 3.1: Summary of studies on shipborne GNSS PWV retrieval. Column **Work** is the reference number of the study in the Bibliography, and **Year** is the publication year. **N** is the number of R/Vs involved. **Start** and **End** mark the period considered in the study, in year-month format. **Avail.** is the length of time when the data is available during the period of study. **Region** is the location where the shipborne measurement takes place.

convergence needs to be achieved, and are smaller in the case of baseline-constrained processing PWV.

Performance of Low-Cost GNSS

The majority of studies presented in Table 3.1 used high-precision geodetic antennas, sometimes involving choke-rings to reduce the multipath effects on the GNSS measurements, and be able to provide a better ZWD accuracy during the processing. Ships that are not R/Vs such as commercial ships will not carry geodetic antennas, so their retrieved PWV might be degraded compared to these studies. As a result, Sohn et al. (2020) [Soh 20] studied the accuracy of a low-cost GNSS antenna retrieved PWV such as the antennas that could be used by non-specific ships.

Wu et al. (2022) [Wu 22a] also discussed this issue, but adding the *RT* topic to the equation, such as explained further in Section 3.3.2.1.

3.3 STUDIES FEATURES

Each one of the 21 studies about shipborne GNSS PWV retrieval has chosen particular processing models and features that are described in Table 3.2. This confrontation of

Work	co °	wg	rw mm·h ^{-0.5}	cst	dt s	mf
[Roc 05]	12	<i>sin</i>	–	–	1	Niell
[Roc 08]	3	–	–	–	5	GMF
[Fuj 08]	3	–	–	G	5	GMF
[Bon 12]	3	–	–	G	5	GMF
[Kea 12]	–	–	12	G	1	–
[Fuj 14]	3	–	–	G R Q	5	GMF
[Fan 16]	10	<i>cos</i> ⁻¹	0.8	G	1	–
[Sho 16]	5	–	6	G R Q	5	GMF
[Sho 17]	3	–	6	G R Q	5	GMF
[Wan 19]	7	–	4	G R E	30	GMF
[Liu 19]	7	<i>f</i>	20	G R	1	GMF
[Soh 20]	10	<i>sin</i>	–	G	30	GMF
[Wu 20]	7	–	5	G R	30	GMF
[Bos 21a]	7	<i>cst</i>	5	G	30	VMF1
[Gon 21]	3	–	–	G R E	30	–
[Män 21]	3	<i>sin</i> ²	–	G R E	30	VMF1
[Bos 22b]	3	$\sqrt{\sin}$	–	G	30	VMF1
[Wu 22a]	7	–	5	G R E	30	GMF
[Wu 22b]	–	–	5	G R E	30	GMF
[Sho 23]	3	–	1.8	–	2	GMF
[Wei 23]	10	–	–	G	30	–

Table 3.2: Modeling of shipborne GNSS PPP processing for the studies listed in Table 3.1. Column **Work** is the reference number of the study in the Bibliography, **co** is the cut-off on elevation angle, **wg** is the weighting function of elevation angle, noted as *f* when they used a weighting function without specifying it, **rw** is the *RWPN* on *ZWD*, **cst** is the constellations used, **dt** is the time resolution of the processing, and **mf** stands for the mapping function to map the slant-path wet delay (*SWD*) to the zenith direction. Missing information is marked as "–". All the GNSS processing presented in this listing ave been performed in post-processing, the reference post-processing being used here when the study aims at qualifying *RT* processing with post-processing results.

the configurations used by the different studies highlights the inhomogeneity in the

configurations chosen for processing GNSS data. Indeed, they draw a large range of cut-off angle values, weighting functions and random walk values, and sometimes they do not precise the configuration they have chosen, making one feel that it is not relevant information. Then, it appears that there is no agreement in the GNSS processing strategy, and most of the time, the chosen configuration remains vague and unjustified.

These studies all aimed at studying different aspects of shipborne PWV retrieval with GNSS antennas, the most singular being developed in the sections below.

3.3.1 Multi-GNSS Performance

Fujita et al. (2014) [Fuj 14] performed two studies to compare the efficiency of PWV retrieval with GPS only and the multi-GNSS combination GPS + GLONASS + QZSS.

Wang et al. (2019) [Wan 19] underlined a 10 % improvement when using multi-GNSS instead of GPS only, due to the higher number of satellites observed and the geometry refinement. They obtained a correlation coefficient between ERAI and shipborne GNSS of 96.74 %, and of 98.4 % with regard to the RS.

Wu et al. (2022) [Wu 22a] is simultaneously assessing the multi-constellations, RT, and low-cost issues with shipborne GNSS antennas. The aim of this study is actually to assess the quality of RT PWV retrieval from low-cost shipborne GNSS measurements. They embarked an expensive geodetic GNSS receiver together with a cheap U-Blox GNSS antenna to compare the real-time played back GNSS PWV retrieval from the low-cost antenna to the post-processed shipborne geodetic antenna PWV retrieval. They also compared both datasets with ERA5, the geodetic antenna resulting statistics of which are presented in Table 3.4. The RT processing of the geodetic antenna taking into account only G E constellations, against G R E constellations for post-processing, results in a decrease of the accuracy with a root mean squared error (RMSE) increased by +0.24 mm. As expected, using the low-cost antenna into an RT processing including also G E constellations occurred to a greater drop in retrieved PWV accuracy with a resulting RMSE reaching 4.01 mm compared to ERA5. RT PWV products from geodetic and low-cost shipborne antennas provide 2.48 mm of root mean squared difference (RMSD) and a correlation coefficient of 99 % [Wu 22a]. The multi-GNSS low-cost resulting PWV from RT processing shows a correlation coefficient of 97 % and an RMSD of 3.28 mm when comparing to the post-processing PWV of this same low-cost antenna dataset. Here, they showed that using G E constellations improves the accuracy and correlation between RT and post-processed PWV time series with low-cost antenna, compared to the RT/post-processed comparison with only one constellation (G or E).

The constellations marked for Wu et al. (2022) [Wu 22b] in Table 3.2 include Galileo even if this constellation dataset was used together with GPS and GLONASS only from 2017. This three-constellation acquisition setup accounts for 37 % of available measurement days.

3.3.2 Processing Features

Contrary to many studies, Fujita et al. (2008) [Fuj 08] uses a forward filter without backward smoothing. To remove side effects, Rocken et al. (2008) [Roc 08] has processed the GNSS data with a Kalman Filter over 8 days with one overlapping day, which

changes from the 24-hour usual processing strategies. They did not take into account the first day of each processed window as well. For the same reason, [Bos 22b] has processed the GNSS data over 30 h windows centered on noon, and then considered only the 00 : 00 - 24 : 00 time interval for each day under study.

As far as it is specified in all these studies, they are using IF linear combination to get rid of the first-order ionospheric effect such as explained in Section 2.3.2.1. Some of them are also using the second-order ionosphere removing, such as in Bosser et al. (2021) [Bos 21a].

Wu et al. (2022) [Wu 22b] and Wu et al. (2022) [Wu 22a] have used elevation-dependent-only antenna PCV map to overcome the fact that the angular bearing of the boat to the North is unknown.

Among everything, the two main points addressing processing strategies were about RT and ultra-rapid processing instead of post-processing, and RWPN modeling on ZWD.

3.3.2.1 Real-Time and Rapid Processing

Some studies about PWV retrieving from shipborne antennas are focusing on the accuracy of RT or NRT processing estimates, to get PWV information for NWP or nowcasting, requiring an accuracy of at most 5 mm such as said in Section 2.5.

Rocken et al. (2008) [Roc 08] aimed to study RT PWV retrieval for nowcasting purposes, but they first evaluated their GNSS dataset by post-processing it and comparing it the their shipborne RS, resulting in the RMSD presented in Table 3.4. Indeed, the post-processing uses the final products providing the most accurate information about the satellite orbits and clock errors, while RT processing uses played-back real-time products that are of weaker precision such as detailed in Table 2.3, thus degrading the estimation accuracy. Comparing the post-process estimates to the RT solution permits to assess the loss of accuracy due to the use of rapid satellite ephemerides. However, their idea was to combine RTK for the precise estimation of satellite clock errors in RT, and PPP. By this way, they obtained a degraded PWV accuracy of $(0.25 \pm 1.4 \text{ mm})$ compared to the regular post-processed PPP results presented in Table 3.4. This leads to a PWV accuracy of less than the required 5 mm. They highlighted that the PPP RTK solution converges faster than the PPP solution thanks to a quicker resolution of the ambiguities, and that PPP RTK solution is more stable. However, this solution requires a nearby ground reference GNSS network, which is not always the case in the open ocean. In this study, the R/V is sailing 2 000 km off the coastal stations at most.

Bosser, Van Baelen, and Bousquet (2022) [Bos 22b] original idea was to develop a routine processing of a shipborne GNSS antenna for daily offshore PWV retrieval. Three types of processing have then been performed to assess its precision:

- ultra rapid involving 300 s time resolution JPL products available at day + 1;
- rapid involving 30 s time resolution JPL products available at day + 3;
- post-processing involving final 30 s time resolution JPL products that are more accurate than both previous products (see Table 2.3) and are available at day + 14.

The statistical results displayed in Table 3.4 for [Bos 22b] are about the post-processing PWV retrieving over the 9-month cruise of the R/V, which provides better results than the two other techniques. Ultra rapid and rapid shipborne GNSS retrieved PWV solutions

have 1.03 mm and 0.73 mm of **RMSD** respectively with regards to post-processed shipborne **GNSS PWV** statistics presented in [Table 3.4](#).

3.3.2.2 Random Walk Process Noise and Time Resolution

To reduce shipborne **GNSS** retrieved **PWV** process-induced variations and negative bias observed during strong events **RT** processing, Shoji et al. (2023) [[Sho 23](#)] proposed a setup recommendation concerning **ZWD RWP**, analysis time width and processing time resolution, by testing different modelings in their shipborne **GNSS** dataset processing involving **RT** satellite products. They evaluated four different **RWP** values from $0.6 \text{ mm} \cdot \text{h}^{-0.5}$ to $6 \text{ mm} \cdot \text{h}^{-0.5}$ as well as nine processing time lengths from 0.5 h to 8.5 h and 15 different time resolutions from 0.1 s to 30 s. Unfortunately, the computational load prevented them from performing statistical study on all the processing option combinations they carried out. They compared only one of their test results to a nearby ground **GNSS** station, an **SMWR**, and a nearby ground-launched **RS** resulting in suitable **RMSDs** of less than 2 mm such as seen in [Section 3.4](#). The processing strategy of this **GNSS** dataset is provided by the **Work** line [[Sho 23](#)] in [Table 3.2](#): $\text{co3}^\circ - \text{rw}1.8 \text{ mm} \cdot \text{h}^{-0.5}$ and a resolution of 2 s. Among many things, Shoji et al. (2023) [[Sho 23](#)] assessed the anti-correlation between height and **ZTD** biases.

Fan et al. (2016) [[Fan 16](#)] discussed the impact of **ZWD RWP** modeling on the shipborne **GNSS PWV** retrieving as well. [Table 3.3](#) lists the comparison statistics of **PWV** resulting from all different processing modelings with the Fifth Generation National Center for Atmospheric Research (**NCAR**)/Penn State Mesoscale Model (**MM5**) model. [Table 3.3](#) depicts that setting up a too loose constraint on **ZWD** estimation creates

RWP	Bias	RMSD
$\text{mm} \cdot \text{h}^{-0.5}$	$\text{kg} \cdot \text{m}^{-2}$	$\text{kg} \cdot \text{m}^{-2}$
0.2	0.4	1.5
0.5	0.3	1.4
0.8	0.2	1.4
1	0.2	1.5
2	0.3	1.8
5	0.6	3.3
10	0.9	4.7
15	1.0	5.2

Table 3.3: Statistical results of **GNSS ZWD** retrieval from Fan et al. (2016) [[Fan 16](#)] compared to **MM5** water vapor (**WV**) model for each tested processing **RWP** value.

a noisy output probably because the acquisition errors such as multipath effect are assimilated to the **ZWD** during estimation. In this case, it seems that the most suitable **RWP** value is tight between $0.2 \text{ mm} \cdot \text{h}^{-0.5}$ and $1 \text{ mm} \cdot \text{h}^{-0.5}$.

3.4 ASSESSMENT OF SHIPBORNE GNSS PWV QUALITY

All the studies of [Table 3.1](#) provide comparison of the retrieved **PWV** from the **GNSS** antennas carried out by the ships they are studying to external sources of data, such

as ground-based GNSS antennas, NWMs, SMWRs, and RSs. Table 3.4 presents the biases and RMSDs for all comparisons provided by the different studies. The figures presented

Work	GNSS		NWM		SWVR		RS	
	<i>b</i>	RMSD	<i>b</i>	RMSE	<i>b</i>	RMSD	<i>b</i>	RMSD
[Roc 05]	-	-	-	-	-	-	-1	1.5
[Roc 08]	-	-	-	-	-	-	-	3.2
[Fuj 08]	+0.28	0.42	-	-	-	-	+1.34 [▲]	3.02 [▲]
[Bon 12]	-	-	-	2.63	-	3.43 [▽]	-	-
[Kea 12]	-	-	-	-	-	-	-1.2	2.16
[Fuj 14]	-	-	-	-	-	-	+0.17 [▲]	2.22 [▲]
[Fan 16]	-	-	-	1.4	-	-	-	-
[Sho 16]	-	-	-	-	-	-	-0.42	-
[Sho 17]	-	-	-	-	-	-	-0.72	1.71
[Wan 19]	-	0.95	+0.31	1.09	-	1.90	-	1.12
[Liu 19]	-	-	-	-	-0.6	0.8	-	-
[Soh 20]	-	-	-	-	0.21 [▽]	8.97 [▽]	-1.48	5.22
[Wu 20]	-	-	-	-	-0.01	1.53	-	-
[Bos 21a]	+0.81	1.54	+0.65	2.44	-2.25 [▽]	4.81 [▽]	-	-
[Gon 21]	-	-	-0.7	2.1	-0.4	1.5	-	-
[Män 21]	+1.03	2.18	+0.17	1.57	-	-	+8.08	1.47
[Bos 22b]	-1.13	2.71	-0.21	2.79	-	-	-2.54	4.29
[Wu 22a]	-	-	+0.68	2.78	-	-	-	-
[Wu 22b]	-0.17	2.64	+0.43	2.96	+0.38	2.29	+0.28	2.98
[Sho 23]	+0.25	1.49	0.11	0.2	+1.04	2.17	-0.48	1.75
[Wei 23]	-	-	-	2.15	-	-	-	4.54

Table 3.4: Statistics of the shipborne GNSS PWV retrieval comparison to external datasets for the studies listed Table 3.1. All figures are in mm. For simplification purposes, the statistical values presented in studies as ZWD are converted to PWV by multiplying them by a rough factor of 6.5 (see Section 2.3.3.3). IWV statistical values are transformed into PWV using Equation (2.55). When several results are available for a type of instrument reference, the best statistical result is presented here. Column **Work** is the reference number of the study in the Bibliography, and each other item is the comparison of shipborne GNSS PWV retrieval to the corresponding external source of PWV data : GNSS standing for ground-based antenna, NWM, SWVR that could be SMWR or satellite infrared radiometers when marked with a [▽], and RS. While comparing to RS, the values are given for all available ground stations except when the statistics are marked as [▲], meaning the RS balloon is launched from the GNSS carrying ship. The columns *b* and RMSD stand for the bias for the reference PWV value removed from the shipborne GNSS retrieved PWV value, and the RMSD and the RMSE, respectively. Unavailable comparisons are marked as "-".

in Table 3.4 are given for the reference PWV value removed from the shipborne GNSS retrieved PWV value. This means that a positive bias indicates that the GNSS is over-

estimating the *PWV* and a negative bias reveals a dryer atmosphere retrieval from the shipborne *GNSS* compared to the reference dataset.

3.4.1 Ground-Based GNSS Stations

Comparing shipborne *GNSS* retrieved *PWV* permits to assess the quality of kinematic processing in any sea state compared to the proven solution from ground-based *GNSS* antennas (see [Section 2.5](#)).

Männel et al. (2021) [[Män 21](#)] presents an evaluation of the shipborne water vapor (*WV*) retrieval with different ground *GNSS* stations. Statistical results of 2.18 mm of *RMSD* presented in [Table 3.4](#) among other ground *GNSS* station statistics corresponds to the longest period of comparison that has been corrected for antenna height difference. The *R/V* was cruising less than 200 km from the ground *GNSS* station. Additionally to their ground *GNSS* stations comparisons with the shipborne *PWV*, Männel et al. (2021) [[Män 21](#)] proposed several comparisons to very long baseline interferometry (*VLBI*) measurements from which the largest sample statistical results provided an *RMSD* of 2.54 mm (not shown in [Table 3.4](#)).

Bosser et al. (2021) [[Bos 21a](#)] have obtained an *RMSD* as low as 1.54 mm by comparing its shipborne *GNSS PWV* retrievals to nearby ground-based *GNSS* antennas. Moreover, they have studied the comparison during the *R/V* crossings, with the corresponding *RMSD* reaching 5.80 mm. The *RMSD* of the intra-ship comparison is higher than expected because they all involved *R/V Maria S. Merian*. Indeed, all statistical results from *R/V Maria S. Merian* (not displayed in [Table 3.4](#)) are degraded because the antenna was located under the main radar during this cruise, thus disturbing the *GNSS* measurements. A change in the antenna location showed that the antenna must be located suitably on the carrying vessel to be able to efficiently acquire data for atmospheric study purposes.

Bosser, Van Baelen, and Bousquet (2022) [[Bos 22b](#)] shipborne *PWV* comparisons to ground-based *GNSS* stations provides and *RMSDs* of about 2.71 mm. Although it is higher than Männel et al. (2021) [[Män 21](#)], this may be due to the survey zone (Indian Ocean vs Arctic Ocean such as seen in [Table 3.1](#)) and still provides sufficient accuracy for climate study. Indeed, the Arctic region provides lower *PWV* values and weaker variations [[Had 17](#)].

The *PWV* presented in [Table 3.4](#) for [[Sho 23](#)] showing an *RMSD* of 1.49 mm corresponds to the best-performing dataset among the three available shipborne *GNSS* antennas presented in [Table 3.1](#), but the change in *RMSDs* is less than 12 % in the two other cases. The statistical results of [Section 3.4](#) involve only one *R/V* for the Tokyo harbor ground-based *GNSS* comparison, and the two others were separately involved in the *SMWR* and *RS* comparisons.

Overall, whenever such *GNSS* solutions are compared, it relies on the fact that the vessel is sailing near the coast. This is not representative of any open sea conditions. Moreover, the distance between the two stations, which can reach a couple of hundred kilometers, might influence the bias because they might not be observing the same air column at a given time when the ship is far from the land station.

3.4.2 Numerical Weather Models

Another solution providing water vapor information is the *NWM*. There exists several *NWM* providing gridded datasets over time, either locally or globally, thanks to the assimilation of remote and in situ observations made from different types of instruments into weather models for temperature, pressure, water, etc. Most of the time, the comparison is made by interpolating the model to the *GNSS* antenna location, and to the time of *GNSS* measurement that can occur more often (several per minute) than the model (hourly).

Most studies providing comparisons to *NWM* used *ERA5* of the *ECMWF* as reference dataset, except [Wan 19] that used their previous *ECMWF NWM ERAI* that was available until August 2019. However, Wu et al. (2022) [Wu 22b] used the *CFSv2* model provided by National Centers for Environmental Prediction (*NCEP*), Boniface et al. (2012) [Bon 12] compared their shipborne *GNSS* data with a French *NWP* model called *ALADIN* and found a *PWV RMSE* of 2.63 mm,

The comparison of Bossier, Van Baelen, and Bousquet (2022) [Bos 22b] shipborne *PWV* with respect to *ERA5* provides an *RMSE* of 2.79 mm. Then it might seem that the *NWM* is not so accurate offshore in the Indian Ocean, because the statistics are equivalent to the comparison to the ground-based *GNSS* that is expected to be flawed because of the spacing between the ground coastal *GNSS* and the *R/V*.

In Wu et al. (2022) [Wu 22b], the *PWV* comparison *RMSE* between the shipborne *GNSS PWV* and the *CFSv2* fully coupled *NWM* provided by the *NCEP* of *NOAA* is of 2.96 mm. They show that the tropical areas have the greatest difference in *PWV* retrieval between shipborne *GNSS* and the *NWM CFSv2* with an *RMSE* of 3.06 mm (not shown in Table 3.4) whereas the polar areas are the less impacted zones. This is probably due to the high *PWV* range values from 40 mm to 70 mm that can be found in the Equatorial region, compared to the 20 mm *PWV* and weaker temporal variations occurring in highest latitudes.

By comparing different *RWPN* processed results to a Japanese mesoscale analysis, Shoji et al. (2023) [Sho 23] found that the *PWV RMSE* decreased with *RWPN* but it also creates a positive bias in the height estimation and an overestimation of *PWV* when it is lower than 40 mm, and an underestimation for higher values.

To stay consistent with the other studies, the comparison of Wei et al. (2023) [Wei 23] with *ERA5* in Table 3.4 [Wei 23] is provided for the best agreement with conventional *PPP* processing *PWV* during one day of the study, as they provided *RMSE* for separate days instead of the whole period. Except for the first day of study, the three others show *RMSEs* higher than 4.5 mm for both shipborne antennas, which is significant compared to the 3 mm that should be expected at a maximum for climate study. The baseline-constrained method generally shows an improvement, but the *RMSE* is still over 4.5 mm.

However, these models are not perfect either, especially at sea where the lack of in situ data produces very sparse and poor time resolution data assimilation. This gives another facet of the shipborne *GNSS PWV* retrieval : their usefulness in increasing *NWM* accuracy at sea.

3.4.3 Satellite Water Vapor Radiometers

As far as some *SMWRs* have been designed especially for offshore water vapor retrieving, it appeared obvious to some studies to compare their shipborne *GNSS PWV* to the equivalent dataset remotely retrieved from radiometers embarked onboard dedicated satellites.

Boniface et al. (2012) [Bon 12] compared its shipborne retrieved *PWV* with *MODIS* dataset, and found a *PWV RMSD* higher 3 mm. They were able to find a signature corresponding to mistral wind and high precipitation events into the shipborne *GNSS ZWD* signal. Thus, they concluded that *GNSS* is a suitable tool for atmospheric data acquisition at sea. Bosser et al. (2021) [Bos 21a] have also studied the comparison to *MODIS*, reaching at least 4.81 mm of *RMSD* and a correlation coefficient of 89.6 % at most with the best-fitting *R/Vs* - that appear to not be the same for *RMSD* and correlation coefficient.

Wang et al. (2019) [Wan 19] performed a comparison of the *PWV* to the *SARAL SMWR* along with the ground-based *GNSS*, *NWM*, and *RS* comparisons. They obtained an *RMSD* of 1.90 mm such as displayed in the *SMWR* column, and a correlation coefficient of 85.2 %.

Liu et al. (2019) [Liu 19] and Wu et al. (2020) [Wu 20] evaluated the ability of *PPP* shipborne *GNSS* to calibrate Hai Yang 2A (*Hy-2A*) Calibration Microwave Radiometer (*CMR*) over seas. The *SMWR* statistics presented in Table 3.4 then refer to the comparison of shipborne *GNSS* to *Hy-2A* in this particular case. Wu et al. (2020) [Wu 20] obtained a correlation coefficient of 94.4 % with the *CMR*. Moreover, they are providing several space scale results for the *CMR* comparison, and the 100 km distance to pixel threshold has been selected to be presented in Table 3.4. However, the 200 km and 150 km thresholds resulted in positive *PWV* biases of respectively 0.22 mm and 0.20 mm, whereas the 50 km threshold results in a negative bias of -0.30 mm. Then, it seems that the choice of a 100 km threshold provides a balance between closest *CMR* soundings with wet bias compared to the shipborne *GNSS PWV* retrieval and farthest soundings with dry bias, leading up to the presented low bias value of Table 3.4 for [Wu 20].

Sohn et al. (2020) [Soh 20] have compared the shipborne *GNSS PWV* to the *SWVR AIRS*, obtaining a low bias of 0.21 mm but a quite high *RMSD* value of 8.97 mm compared to other *RS* comparison *RMSDs* presented in Table 3.4 and a poor agreement with a correlation coefficient of 56 % only. However, Sohn et al. (2020) [Soh 20] underline that *PWV* measurements from *AIRS* has already performed worse statistical results [Hen 19] than the comparison of shipborne *GNSS* to *RS* showing an *RMSD* of 5.22 mm in Table 3.4 for [Soh 20]. In addition, Sohn et al. (2020) [Soh 20] presents a comparison of three ground *GNSS* stations *PWV* retrieval with nearby *RS*, leading to 1.27 mm to -4.13 mm of bias and 2.47 mm to 4.40 mm of *RMSD*, whereas the best performing comparison between the same three ground *GNSS* stations and *AIRS* provides -2.64 mm of bias and 4.38 mm of *RMSD*, denoting for a poor *AIRS PWV* retrieving accuracy compared to *GNSS* performance. These figures also highlight the best performance of ground *GNSS PWV* retrieving against the low-cost shipborne *GNSS* performances with respect to *RS* displayed in Table 3.4 for [Soh 20]. However, the obtained results show that although low-cost shipborne antennas accuracy is weaker than geodetic antennas for *PWV* retrieving, they are still providing *RT* errors of less than 5 mm suitable for meteorology purposes, in comparison to *RS*.

The aim of Gong, Liu, and Foster (2021) [Gon 21] was to use shipborne GNSS IWV retrieval to evaluate SMWR IWV measurements over the open oceans. They found an RMSD of 1.5 mm between the two techniques, showing how close their accuracy is. The main advantage of shipborne GNSS is that the fitting SMWR footprint is spatially closer to the GNSS antenna and not spoiled by the land effect that can occur in coastal areas where the other SMWR evaluation techniques occur.

Wu et al. (2022) [Wu 22b] compared the shipborne GNSS PWV dataset to four SWVR: Hy-2A, Jason-2, Jason-3 and SARAL. They decided to set up a distance of the SWVR sounding from the R/V measurement for the comparison. The statistical results of the 50 km distance threshold are presented in Table 3.4 displaying an RMSD of 2.29 mm, which is degraded up to 2.53 mm, 2.95 mm, and 3.32 mm when increasing the distance threshold to 100 km, 150 km, and 200 km respectively (not shown in Table 3.4). The corresponding correlation coefficients varies from 99 % for 50 km to 97 % for 200 km and the bias is 0.38 mm and 1.07 mm respectively. All these results are suitable for meteorology and climatology purposes.

However, SWVR dataset is sparse, providing a gridded dataset from which each point is covered by the satellite swath twice a day at most, except for high latitudes. This reduces the number of exact matching data to two per day and per satellite at most, which can be not statistically representative when speaking of short studies. Moreover, it is important to note that SMWR swath is spoiled by land detection whenever it partially covers coastal areas or islands. 25 km of data from the coast is removed from the released dataset because of this effect, so a coastal route might not have SMWR corresponding data next to the ship's position.

3.4.4 Radiosondes

Radiosonde (RS) is commonly assumed to be the reference for PWV retrieval. In that respect, two-thirds of the studies presented in Table 3.4 provide comparisons of their shipborne GNSS retrieved PWV to nearby RS.

Although the GNSS signal span through the troposphere is nearly instant, the RS needs some time to ascend the whole troposphere and reach the tropopause, and provides water vapor measurements for several height values. The main idea to compare both datasets is to integrate the whole RS data over the air column, and to average the GNSS PWV over a time laps corresponding to the ascending of the RS into the air. However, the latter time is not fully determined. This is how Shoji et al. (2016) [Sho 16] decided to average their GNSS data over 30 min while Fujita et al. (2008) [Fuj 08] have chosen 1 h. The RS follows a profile driven by the winds while elevating through the troposphere, while the GNSS scans the troposphere in a cone above the antenna defined by the cut-off angle. The resulting PWV is then broader with the GNSS than the RS measurement, explaining the potential discrepancy.

Although most of the RS values in Table 3.4 comparisons to shipborne GNSS PWV come from nearby ground-launched RS when the vessel is near the coast, Fujita et al. (2008) [Fuj 08] and Fujita et al. (2014) [Fuj 14] directly used RS launched from the same boat carrying the GNSS antennas. This permits us to get comparisons to this type of instrument even in the open sea.

Rocken et al. (2008) [Roc 08] has found a larger mean bias during nighttime compared to daytime, which they attributed to the daytime-due error in RS data. During

nighttime, the **RMSD** value with the **RS** is reduced to 2.2 mm, which is sufficient for climate study.

Shoji et al. (2017) [Sho 17] has evaluated the impact of several effects on the **GNSS ZTD** measurement, such as wave height, shipborne **GNSS** antenna height estimation above the sea surface, multipath effect, vessel movements, speed and direction, and wind in case the pressure used to compute the **ZHD** was measured onboard the vessel. They concluded that less than 5 m height waves sea state does not strongly affect **GNSS** measurements. The vessel and wind speeds also appeared to not correlate with the **GNSS ZTD** estimation errors. Shoji et al. (2017) [Sho 17] shows a better agreement of the **PWV** retrieved from its **GNSS** antenna located up on the mast than the other located on the same boat's deck, showing **RMSEs** of 1.71 mm and 3.15 mm respectively, with an increase in the negative bias of 0.10 mm and a rejection rate going from 3.6 % to 15.7 %. They concluded that the antenna must be placed in a cleared area to get less multipath effect spoiling the measurement, providing accuracies that fill the climate study requirements.

The Bosser, Van Baelen, and Bousquet (2022) [Bos 22b] post-processing **PWV** is resulting in an **RMSD** of 4.29 mm when comparing to ground-based **RS**. This is one to four times the **RS** comparisons **RMSDs** of other studies presented in Table 3.4, except for Sohn et al. (2020) [Soh 20] study providing an **RMSD** 0.93 mm higher while using a low-cost antenna. Although such error is quite high for climate study, they obtained better results when comparing to other techniques such as seen in Table 3.4 and above sections. This leads us to think that the **RS** was quite spoiled, the study thus underlined that strong deviations were observed occasionally, and that they interestingly obtained wet biases while this technology is known to have dry bias usually when compared to ground-based **GNSS** stations. Indeed, the other **RS** comparison in another drier location near the South Pole showed a lower **RMSD** value of 3.59 mm. The statistical results of Bosser, Van Baelen, and Bousquet (2022) [Bos 22b] were slightly higher than statistical values encountered in other shipborne **GNSS PWV** presented in Table 3.4 [Fuj 14; Wan 19; Män 21]. However, the antenna location has been changed after five months of the study (2021/03) from an intermediate deck of the vessel up to its crow's nest. Then, during the second part of the study, the root mean squared coefficients (**RMSs**) of Table 3.4 decreased by 0.39 mm, 0.28 mm, 1.11 mm for ground **GNSS**, **RS**, and **ERA5** comparisons respectively. Consequently, the location of the antenna at the highest point of the vessel appears to be a really important factor for shipborne **GNSS** measurement accuracy. A badly positioned antenna could reduce the accuracy of the retrieved **PWV** and affect the atmosphere study feasibility with such a shipborne **GNSS** antenna.

The comparison of Sohn et al. (2020) [Soh 20] shipborne **PWV** to **RS** being worse than those of Bosser, Van Baelen, and Bousquet (2022) [Bos 22b] while the **GNSS** antenna was suitably located up on the mast, it can be suspected that using a low-cost antenna degrades the estimation at least as much as placing a geodetic antenna in an inappropriate location.

Wu et al. (2022) [Wu 22b] performed comparisons to ship-launched **RSs** as well, resulting in a **PWV RMSD** of 2.54 mm better than the ground-launched **RS** comparison of 2.98 mm of **RMSD** presented in Table 3.4. The better fit of the ship-based dataset than the ground-based **RS** is explainable by the fact that the launch of **RSs** from the **R/V** occurred on the same carrying platform than the **GNSS** measurement whereas the ground-launched **RS** comparison where carried out when the **R/V** was sailing in coastal

areas but the length scale was set up to 100 km. It underscores the importance of the proximity of the two data sources in any comparison.

Such as for the ERA5 comparison, the daily Wei et al. (2023) [Wei 23] comparison with RS PWV shows a high RMSD value of 4.54 mm and 6.44 mm for both conventionally PPP processed antennas, with an improvement up to 4.27 mm and 4.40 mm of RMSD respectively speaking of baseline-constrained processed antennas.

It is interesting to note that when the new processing strategy proposed by Shoji et al. (2023) [Sho 23] yields a slightly higher RMSD than with the processing strategy used by Shoji et al. (2017) [Sho 17], the negative bias is almost halved.

Except for the cases where the RSs are launched from the R/V, comparison of shipborne GNSS PWV to ground-launched RS is affected by the same issues of distance to the station than the ground-based GNSS comparison detailed in Section 3.4.1.

3.4.5 Compared Datasets Correlation

Some studies also present the correlation between the shipborne GNSS PWV and the external comparison dataset. Although this information is interesting to qualify the ability of the shipborne GNSS to compute the PWV, it is not presented in Table 3.4 as they are really dependent in measurement duration and PWV variability. However, they are listed here.

Sohn et al. (2020) [Soh 20] obtained a correlation coefficient of 85 % between shipborne GNSS and shipborne RS.

Bosser et al. (2021) [Bos 21a] has provided the correlation coefficients of 95 % and 90 % at most for comparison with ERA5 and MODIS respectively.

Gong, Liu, and Foster (2021) [Gon 21] obtained a correlation coefficient of more than 99 % between shipborne GNSS and SMWR PWV values.

Männel et al. (2021) [Män 21] provides correlation coefficients of 97 % with both ERA5 and RS comparisons.

The Bosser, Van Baelen, and Bousquet (2022) [Bos 22b] post-processing study provides correlation coefficients of 98 %, 92 %, and 97 % with regards to ERA5, ground-based GNSS station, and ground-based RS comparisons respectively.

Besides the provided statistical differences between shipborne GNSS and various reference datasets summarized in Table 3.4, Wu et al. (2022) [Wu 22b] reported a correlation coefficient of 98 % and 97 % with the ground-launched and ship-launched RS PWV respectively. They also provided a correlation coefficient of 95 % between the shipborne GNSS PWV and the CFSv2 fully coupled NWM provided by the NCEP of NOAA.

3.5 CONCLUSION ON THE ALREADY-RELEASED SHIPBORNE GNSS STUDIES FOR WATER VAPOR RETRIEVAL

As of mid-year 2023, twenty additional studies about shipborne GNSS PWV retrieval have been published since the first one in 2005. They all carried out comparisons of their datasets to more conventional or coastal instruments permitting to retrieve PWV. Most of these studies provide RMS of less than the maximal error in climate study requirement of $3 \text{ kg} \cdot \text{m}^{-2}$. All but one study using a low-cost antenna in RT [Soh 20] provide RMS of less than $5 \text{ kg} \cdot \text{m}^{-2}$ sufficient for NWP and now-casting applications in meteorology [Off 10], if we consider that the usual techniques the dataset is compared to are flawless - which is not the case.

3.5.1 Contributions and Limitations in the Framework of this Thesis

The reference dataset to assess the quality of the shipborne GNSS PWV are of several different types: NWM, RS, SMWR, ground-based GNSS. They do not provide the same differences when the shipborne estimate is compared to several of these measurement techniques. This proves that the reference datasets are flawed. [Bos 22b] is the only study providing an inter-ship comparison permitting to assess the inherent accuracy of the process.

Furthermore, Bosser et al. (2021) [Bos 21a] showed that the shipborne antenna surrounding can affect the PWV retrieval. Indeed, by comparing the three available R/V datasets to ERA5, they have obtained substantially different RMSE values, which is more than doubled for one R/V compared to the others. A further investigation showed that the GNSS antenna was placed under the radar of the R/V, preventing the antenna from measuring accurately the signals coming from the satellites. Thus, the antenna positioning is fundamental for shipborne GNSS PWV retrieval and should be placed at the highest point of the vessel as possible to prevent multipath effect. Other factors seem to be affecting the measurement to a lesser extent, as the two well-placed antennas R/Vs are showing disparate statistical differences to ERA5 from one another.

The limitation of the observations from low-elevation satellites to limit the multipath effect can be tuned as well when processing GNSS data. The worst RMS of the shipborne GNSS studies is provided by [Soh 20], which has used a sine weighting function. Many different weighting functions are displayed through the different studies. Bosser et al. (2021) [Bos 21a] gets higher RMS values when they use a square of the sine function than Bosser, Van Baelen, and Bousquet (2022) [Bos 22b], where they are not applying the weighting function. In terms of cut-off angle, the worst performing study [Soh 20] used a 10° such as Wei et al. (2023) [Wei 23] that showed discrepancies with the RS. Thus one could conclude that a low cut-off angle would be helpful, but [Fan 16] gets excellent results with the same cut-off. We should then assess the link between the cut-off and the RWPN values in the shipborne GNSS estimation accuracy. 7° is widely used in ground-based processing and seems to perform well here as well, especially for [Wan 19]. 3° provides among the best fitting estimates to the reference dataset as well, except for the RS comparison of [Män 21]. Through all the adopted strategies, none of them seems to be outstanding in shipborne GNSS data processing.

The processing modeling is assessed in a few studies only [Fan 16; Sho 23], considering the different elements individually. Fan et al. (2016) [Fan 16] has tested several RWPN values on ZTD, showing the impact of the different methods by comparing them to reference measurements. They showed that a tight constraint provides better results than a loose one, even if a constraint too tight ($0.2 \text{ mm} \cdot \text{h}^{-0.5}$ in this case) degrades the solution. However, Liu et al. (2019) [Liu 19] still gets very good fitting with SMWR while they use a very loose constraint ($20 \text{ mm} \cdot \text{h}^{-0.5}$ in this case).

It has been shown that the processing modeling aspect can highly affect the estimation accuracy of the ground-based GNSS position and PWV retrieval [Sel 16; Kač 19]. We will then study in this thesis the processing modeling and its impact on the estimated GNSS parameters accuracy. To this end, we will consider a set of several configuration parameters, and tune them together to study their individual and combined effects on the accuracy of processing results.

Furthermore, different temporal resolutions have been proposed, with at most 30 s of resolution, but none assesses the contribution of using 1 s instead, which can be a

big deal for data transmission and record from remote places such as the middle of the ocean.

A long-term study such as [Wan 19; Sho 17; Män 21] permits to assess the sea state, weather condition, and location impact on the data processing result, but all the other studies are punctual with at most a few months long, such as seen in Table 3.1.

The studies proposing an elevation-dependent correction of the antenna PCV provide results with a low bias, but the RMS values are intermediate compared to the studies, while they do not assess the intake of such a model.

Some studies discuss the multi-GNSS contribution [Fuj 14] and other acquisition setting issues [Wan 19]. They showed that using several GNSS constellations provides better results than GPS-only.

We will then address all these issues by testing several configurations in this thesis, and process a long-lasting dataset over several years.

3.5.2 Future Prospects Arisen by these Studies

Other issues are being addressed in the studies of Table 3.1. They will not be addressed in this thesis but are of great interest for future work.

Some studies were released about the impact of assimilating PWV data from shipborne GNSS antennas in NWP. Ikuta, Seko, and Shoji (2021) [Iku 21] thus found that adding shipborne GNSS PWV assimilation to NWP models permits to increase in the PWV prediction overseas and improves the precipitation distribution and amount forecast during rainfall events in coastal areas compared to the NWP without shipborne measurement assimilation. The NWP models both assimilated GNSS radio occultation (GNSS-RO) and ground-based GNSS retrieved PWV, satellite clear-sky brightness temperature, rainfall amounts distribution analysis called Radar/Raingauge-Analysed Precipitation, and microwave-retrieved precipitation measurements. They used the same shipborne GNSS processing and PWV retrieval as in Sohn et al. (2020) [Soh 20] for their assimilation experiment. Seko, Koizumi, and Shoji (2020) [Sek 20a] and Seko and Shoji (2020) [Sek 20b] also found that shipborne GNSS PWV retrieval improves the detection of coastal rainfall occurrence even with a low amount of shipborne data assimilation, however the intensity of rainfalls might be over-estimated and they concluded that rising the overseas data assimilation by increasing the size of shipborne GNSS dataset assimilation would solve this issue.

All these studies have proved the RT to be possible, but using played back RT products. An issue to address here would be the data transmission from the vessel to an inland computation center. The Robusta-3A project from the Centre Spatial Universitaire de Montpellier (CSUM) of Université de Montpellier has built a dedicated nano-satellite that aims at transferring the acquired data from commercial ships between Corsica and mainland France in the Mediterranean Sea. These ships are equipped with a GNSS antenna, a data logger, and a data transmission antenna, to retrieve GNSS data along the trajectory of the ship, send it to the satellite when it passes through, the data being transmitted to a computation center in Université de Montpellier for NRT processing. The goal of this project is to get data over the Mediterranean Sea to forecast cévenol episodes: flash floods caused by heavy rain coming from the sea and hitting the South of France regularly. Routine processing of shipborne GNSS data is already assessed [Bos 22b].

The low-cost aspect of shipborne GNSS antenna that is assessed by a couple of studies [Soh 20; Wu 22a] is also of great interest to develop the PWV retrieving from ships on a large scale. This type of receiver could be easily - or is even already - installed onboard numerous commercial ships. The assessment of their data quality for water vapor monitoring would then be interesting, but this issue is not assessed in this thesis.

INFLUENCE OF THE PROCESSING MODELING ON THE PRECISE POINT POSITIONING OF SHIPBORNE GNSS ANTENNAS

Previous part has highlighted the lack of processing strategy assessment applied to shipborne GNSS.

This second part is about the influence of the GNSS PPP processing strategy on the quality of retrieved position, especially the vertical component, and troposphere delay. It relies on an ENSTA Bretagne owned survey vessel GNSS dataset processed under different modelings, followed by a broader study on a self-made simulation shipborne GNSS dataset.

The aim of this part is to recommend a suitable processing strategy for shipborne GNSS water vapor retrieval, that will be applied to a diverse long lasting dataset in the last part of this thesis.

 GNSS PPP PROCESSING MODELING ON REAL DATASET

CONTENT

4.1	Data and Processing Method	57
4.1.1	Panopée: a Hydrographic Survey Vessel Carrying a GNSS Antenna	57
4.1.2	Quality of the GNSS Dataset	58
4.1.3	GIPSY-OASIS II: a GPS Data Processing Software Package	59
4.1.4	Processing Models: Three Parameters under Study	60
4.1.5	Retrieving PWV from the Shipborne ZTD Estimate	63
4.1.6	Comparison Datasets	64
4.2	Assessment of Survey Vessel Processing Models	67
4.2.1	Qualification of Survey Vessel GNSS Solutions with the References	67
4.2.2	Comparison of the Best Performing Processing Model Retrieved PWV to Usual PWV Data Sources	72
4.3	Conclusion on the Real Dataset Processing Strategy Assessment	73

This preliminary study permits to test several combinations of processing configurations while PPP processing the GNSS data of the antenna carried out onboard the ENSTA Bretagne hydrographic vessel.

This study led to a poster presentation at the International Association of Geodesy (IAG) symposium in June 2021, supplemented by a publication in the proceedings of the conference [Pan 22b].

4.1 DATA AND PROCESSING METHOD

4.1.1 *Panopée: a Hydrographic Survey Vessel Carrying a GNSS Antenna*

Panopée is an eight-meter-long hydrographic survey vessel such as in Figure 4.1, equipped with different systems such as GNSS antennas, bathymetric sounders and an inertial measurement unit (IMU). It is operated in the Bay of Brest by ENSTA Bretagne for teaching hydrography and robotic engineering students and for oceanography, hydrography, robotic, and marine biology research projects.

The GNSS antenna located on a pole above the moonpool is a Septentrio PolaNt* MC designed for high-precision, multi-frequency, and multi-constellation positioning. This antenna is well adapted to the marine environment, so it was chosen to be mounted on the Panopée survey vessel. The receiver is integrated in the IMU of the

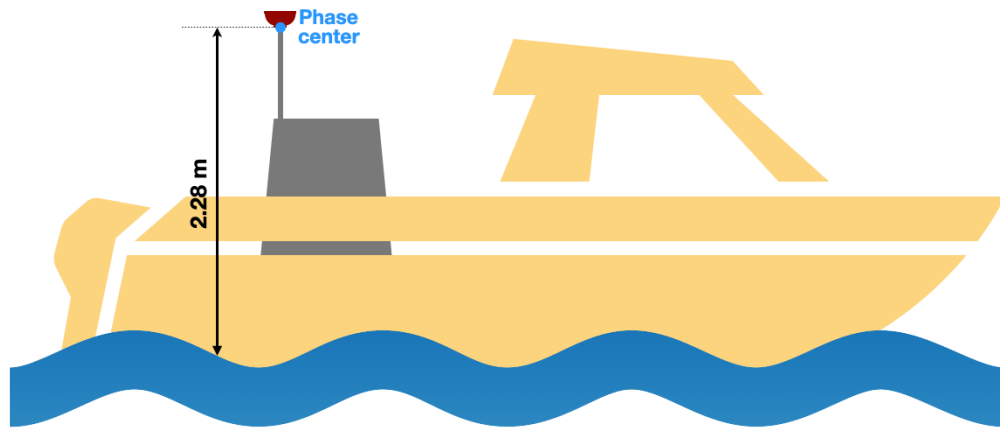


Figure 4.1: Panopée survey vessel schematic. The GNSS antenna is located on the moon pool at the back of the vessel, and its phase center is located 2.28 m above the sea surface.

vessel. The vertical lever arm of the antenna reference point (ARP) is of 2.28 cm above the sea surface. It is known with an accuracy of 1 to 2 cm, depending on the loading of the vessel and its speed.

This study is based on 49 days of survey vessel GNSS data from March, 30th (day of year (doy) 89) to June, 18th (doy 137) in 2018. During this period, the vessel was docked around 90 % of the time in the Marina du Chateau harbor. Some surveys have been made in the Bay of Brest for a couple of hours straight otherwise, as seen in Figure 4.2. This period has been chosen because there are no missing data during the whole 49-day period.

For a data size issue, we have chosen to process only the GPS constellation data acquired from the survey vessel antenna.

4.1.2 Quality of the GNSS Dataset

Three indicators displayed in Figure 4.3 are used to assess the quality of the survey vessel GNSS dataset and BRST reference station. These indicators have been computed using the translation, editing and quality check (TEQC) software [Est 99].

MP1 and MP2 indicators are empirical estimation of the multipath error computed from the pseudorange received by the antenna. They provide information on the multipath effect affecting respectively the first and second frequencies of the GNSS signal. This indicator is the lowest possible when the signal is not affected by multipath. As we can see in Figure 4.3, the first frequency is less affected by multipath. As expected, the low elevation signals are highly affected by multipath contrary to the higher elevation signal. Indeed, the multipath indicators worsen while the elevation cut-off is lowered for the survey vessel dataset, going from (0.53 ± 0.03) for MP1 with a 10° elevation cut-off to (0.66 ± 0.04) with a 3° elevation cut-off for both MP1 and MP2.

The third indicator ROS corresponds to the ratio of the number of observations to the number of phase cycle slips, which means that the higher the ROS indicator, the greater the cycle length, resulting in a better signal processing resolution as the ambiguities are solved for each cycle slip. Here as well, the cut-off angle seems to play a key role in the quality of the dataset, as we can see in Figure 4.3 that considering



Figure 4.2: Map of the Bay of Brest with the Panopée course between days 89 and 137 of 2018 (red), and the locations of Brest ground-based GNSS station (green), nearby Penfeld tide gauge (purple), and RS station of Météo France in Guipavas (orange). Panopée is docked in the Marina du Chateau (red star) most of the time, which is next to the tide gauge and the ground-based GNSS antenna. This map was created thanks to QGIS.

lower observations implies more cycle slips and then fewer observations in each of them.

The figures for the nearby reference BRST ground station also displayed in Figure 4.3 provide reference values for these three indicators of the quality of the survey vessel dataset. We can see that the fact that the antenna is onboard a moving vessel in an uncleared area, as opposed to the BRST antenna, decreases the GNSS data quality, with an especially high-quality decrease in the low elevation observations.

4.1.3 GIPSY-OASIS II: a GPS Data Processing Software Package

GIPSY-OASIS II v.6.4 (GNSS-Inferred Positioning System and Orbit Analysis Simulation Software, hereafter GIPSY) is a software product provided by NASA JPL and maintained by the Near Earth Tracking Applications and Systems groups. Among the multiple features, GIPSY provides PPP GNSS-based positioning for moving platforms with centimeter-level precision, particularly terrestrial positioning for geophysical research, such as climate studies by observation of the troposphere. It also provides dry and wet troposphere mapping functions (VMF1, GMF, Niell Mapping Function (NMF)), and the ability to set up the filter.

These GIPSY tools are used in the PPP processing codes implemented by Pierre Bosser. The dataset from the survey vessel has been post-processed using GIPSY through these codes. They provide the user with the ability to implement the modeling for each aspect of the processing such as the cutoff angle for the elevation of the observed satellites, the weighting function applied to this elevation, and the RWPN value to constrain the ZWD variations during the estimation process. However, GIPSY kinematic PPP processing with ambiguity resolution is handled only for GPS

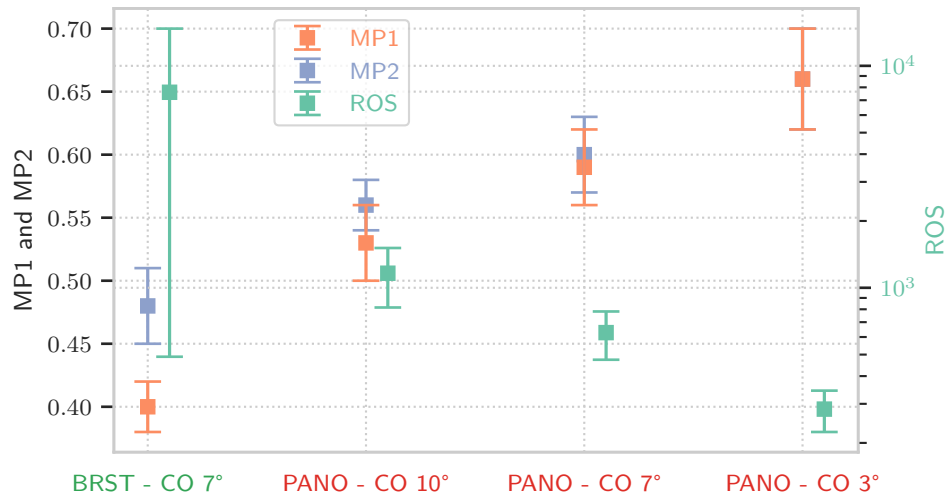


Figure 4.3: Indicators for shipborne antenna (red) and nearby reference ground-based GNSS station BRST (green) datasets from days 89 to 137. The survey vessel indices are given for different cut-off angle values: 10°, 7°, and 3°. The orange and purple indicators MP1 and MP2 represent the impact of the multipath effect from the first and second GNSS frequencies respectively. The green indicator ROS represents the average length of observation for each cycle slip.

constellation. For this reason, we have processed only the GPS data from the survey vessel.

The GIPSY features used to process the survey vessel data are:

- VMF1 as a mapping function for ZWD,
- a priori ZTD derived from VMF1 ZTD grid,
- 30 s high resolution final JPL products,
- kinematic mode,
- 30 s resolution of the solution,
- International Earth Rotation and Reference Systems Service (IERS) conventions for solid Earth tide model,
- tide model Finite Element Solution (FES)2014 for ocean tide loading effects.

The processing was done over a 30-hour window centered on noon for each day of study, to reduce edge effects.

4.1.4 Processing Models: Three Parameters under Study

As explained in Section 2.4.3, the processing modeling can be tuned by the software user, and can have an impact on the quality of the GNSS solution, especially in kinematic PPP processing. The tuning of a cut-off angle as well as the use of a weighting function on the elevation of the observed satellites can help mitigate the multipath, and implementing an RWPN on the ZWD variations can help decorrelate height and ZWD, especially along with a low cut-off angle.

Parameter	Tested models		
cut-off angle	3°,	7°,	10°.
weighting function	cst ,	sin ,	\sqrt{sin} .
RWPN	$3\text{ mm} \cdot h^{-0.5}$,	$5\text{ mm} \cdot h^{-0.5}$,	$10\text{ mm} \cdot h^{-0.5}$.

Table 4.1: PPP processing modeling tested on the survey vessel dataset. We studied here the parameters detailed in Section 2.4.3. cst is the uniform function that does not depend on elevation, sin is the sine function applied to elevation, and \sqrt{sin} is the latter function with the square root applied.

We have selected a few parameter values to study, all combinations of which would be tested on the survey vessel dataset. The selection of three values for three different parameters, as described in Table 4.1. Table 4.1 lists the studied parameters upon the survey vessel dataset processing, along with all the values tested for each of them. It results in the testing and analysis of 27 processing model combinations. The choice of the values of Table 4.1 is explained in the following Sections 4.1.4.1 to 4.1.4.3.

4.1.4.1 Cut-off applied to the satellite elevation angle

7° of cut-off angle is a commonly used intermediate value for processing GNSS datasets [Bos 22b]. 3° is a relatively low cut-off angle that has been recommended by Kačmařík et al. (2019) [Kač 19] to process the ship-based GNSS data, permitting to get more satellites in the antenna scope by integrating the low-elevation satellites that are useful for decorrelating height and ZWD parameters in the filter process. It is also compared to the intermediate cut-off angle of 7° in Kačmařík et al. (2019) [Kač 19]. To the contrary, 10° of cut-off angle might be chosen as a relatively high cut-off angle, eliminating all low-elevation observations but effectively limiting the multipath effect contrary to the 3° cut-off angle. The choice of the elevation cut-off angle value has an effect on the number of removed satellites at a given time. As expected, Figure 4.3 shows that the low elevation angle observations are more affected by the multipath, as the MP1 and MP2 indices are better for high cut-off angles.

4.1.4.2 Weighting function of the elevation of the satellites applied to the measurement uncertainty

$wg=cst$ consists in giving the same weight to all the observation uncertainties, so that there is no discrimination in the phase measurement between low and high-elevation observations. $wg=sin$ consists in dividing the phase uncertainty by the sine of the elevation, meaning that low elevation observations will be applied a higher uncertainty than the high elevation observations, following the curvature of a reverse sine function such as in Figure 4.4. The \sqrt{sin} weighting function consists of applying a square root to the previous sin function of the elevation. It results in the weighting of the phase measurement uncertainty drawn in Figure 4.5.

As we can see here, $wg = sin$ gives less credit to all the observations than $wg = \sqrt{sin}$. In particular, $wg = \sqrt{sin}$ permits to efficiently increase of the uncertainty of very low elevation measurement, while rapidly lowering the weighting impact for the half-lower observations, compared to $wg = sin$. Thus, it is expected that $wg = sin$ would be more efficient for processing data very affected by multipath;

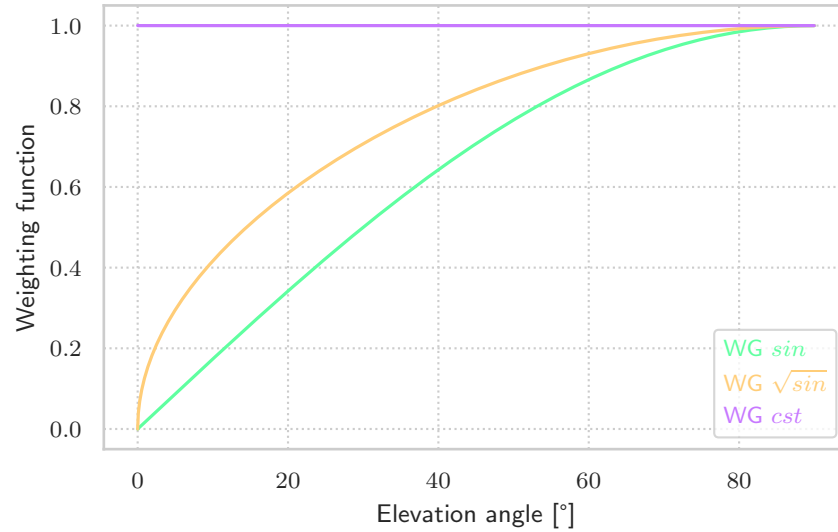


Figure 4.4: Weighting effect of the measurement variance as a function of the elevation of the satellites. The three tested values for WG modeling are shown here: the flat weighting function is represented in purple, the sine function of the elevation in green and $\sqrt{\sin}$ of the elevation is in orange.

whereas $wg = \sqrt{\sin}$ should be better at decorrelating height and ZWD estimates, by giving more weight to lower elevation observations.

4.1.4.3 Random walk process noise applied to the ZWD estimate

A low RWPN value constrains a lot the ZWD variations in order to stabilize the system [Dac 15], but Kouba and Héroux (2001) [Kou 01] recommends to use $RW = 5 \text{ mm} \cdot \text{h}^{-0.5}$ whereas Pacione, Vespe, and Pace (2009) [Pac 09] applied $RW = 20 \text{ mm} \cdot \text{h}^{-0.5}$. Many of the studies provide RWPN values they used to PPP process their GNSS data [Lu 15; Bos 22b], but they do not justify their choice, and sometimes they do not provide any RWPN value they used [Oli 16]. Fortunately, Hadas et al. (2017) [Had 17] has quantified the ZWD RWPN all around the globe, using historical ZWD time series. They created optimal ZWD RWPN global maps yearly between 2012 and 2015, or according to the seasons in 2015 to study the seasonal effect as the years were nearly identical with differences below $1 \text{ mm} \cdot \text{h}^{-0.5}$. It appears that the ZWD RWPN varies spatially and seasonally, with a mean value of $5.0 \text{ mm} \cdot \text{h}^{-0.5}$ over the four studied years. The lowest value of $0.1 \text{ mm} \cdot \text{h}^{-0.5}$ is found around the poles above land, and the highest value is found above the oceans, around 40°N and 40°S of latitude. Most of all, it appears that the seasonal effect is wider over the oceans, with a maximum value of $16.4 \text{ mm} \cdot \text{h}^{-0.5}$ around 40°N and 40°S of latitude in the oceans. The maximum RWPN difference between two seasons is $7.3 \text{ mm} \cdot \text{h}^{-0.5}$ over the Atlantic Ocean at a latitude around 40°S , $4.8 \text{ mm} \cdot \text{h}^{-0.5}$ between 45°N and 45°S , and $2.0 \text{ mm} \cdot \text{h}^{-0.5}$ elsewhere. This study highlights a mean RWPN of $5 \text{ mm} \cdot \text{h}^{-0.5}$ on the ZWD over the year and around the globe.

Such as detailed in Table 4.1, we have tested the values $3 \text{ mm} \cdot \text{h}^{-0.5}$ that represents a tight RWPN, $5 \text{ mm} \cdot \text{h}^{-0.5}$ that corresponds to the mean found by Hadas et al., and $10 \text{ mm} \cdot \text{h}^{-0.5}$ that represents a loose RWPN value, chosen as the double of the mean value. These values would result in differently noisy ZWD time series.

Indeed, the graph of Figure 4.5 shows how the tightness of the *RWPN* impacts the *ZTD* variations. First, it appears that as expected, a looser *RWPN* provides a noisier

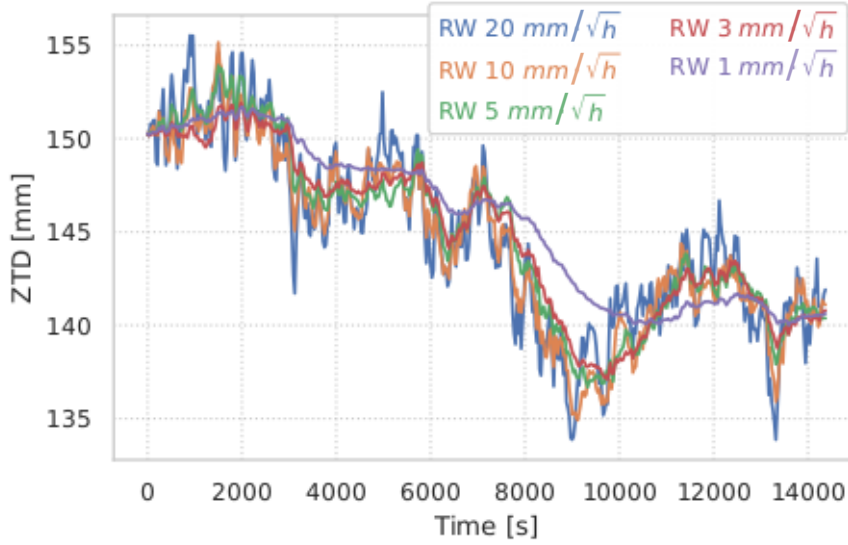


Figure 4.5: *RWPN* effect on the estimated *ZWD* variations. Five different values have been tested here, from a very tight value of $1 \text{ mm} \cdot \text{h}^{-0.5}$ (purple) to a very loose constraint of $20 \text{ mm} \cdot \text{h}^{-0.5}$ (blue). The values tested on the survey vessel dataset were $\text{RW} = 3 \text{ mm} \cdot \text{h}^{-0.5}$ (red), $\text{RW} = 5 \text{ mm} \cdot \text{h}^{-0.5}$ (green), and $\text{RW} = 10 \text{ mm} \cdot \text{h}^{-0.5}$ (orange).

result, such as seen in the high variations of the blue ($\text{RW} = 20 \text{ mm} \cdot \text{h}^{-0.5}$) and orange ($\text{RW} = 10 \text{ mm} \cdot \text{h}^{-0.5}$) curves; compared to the purple ($\text{RW} = 1 \text{ mm} \cdot \text{h}^{-0.5}$) and red ($\text{RW} = 3 \text{ mm} \cdot \text{h}^{-0.5}$) curves. Second, it appears that a very tight constraint produces a phase shift, especially apparent in the $\text{RW} = 1 \text{ mm} \cdot \text{h}^{-0.5}$ result. The fact is that the constraint is too tight, so the estimation cannot follow the measurement as it should, creating a delay in the resulting *ZTD*. In contrast, a constraint too loose such as $\text{RW} = 10 \text{ mm} \cdot \text{h}^{-0.5}$ and $\text{RW} = 20 \text{ mm} \cdot \text{h}^{-0.5}$ produces artifacts in a very noisy *ZTD* estimate, because of the impact of other signal perturbations in the *ZTD* estimate than the actual water vapor.

4.1.5 Retrieving *PWV* from the Shipborne *ZTD* Estimate

To compute the *PWV* from the *GNSS* estimation of the shipborne *ZTD* estimate, we first compute *ZHD* from *ERA5* *MSL* pressure fields following Equation (2.25).

Then, we correct the *ZHD* from the antenna height following the formula of [Ste 09] in Equation (2.26), adapted to our shipborne measurements as the antenna height is lower than 50 m *AMSL* which permits to not over-extrapolates the values, such as explained by Bosser et al. (2021) [Bos 21a].

Then we subtract the *ZHD* from the *ZTD* such as in Equation (2.27), to obtain the *ZWD*.

Finally, we compute the *IWV* following Equation (2.53), and then deduce the *PWV* following Equation (2.55) such as described in the case of ground-based antennas in Section 2.5.1.



Figure 4.6: Photo of the Penfeld tide gauge. (Retrieved from refmar.shom.fr - Accessed October, 25th, 2023).

4.1.6 Comparison Datasets

Several types of data coming from Brest standing instruments have been selected to assess the height and *ZWD* estimates from the shipborne antenna processing under different modelings.

First, the resulting shipborne antenna height quality is assessed for the different processing configurations by comparing it to the nearby tide gauge sea surface measurement.

Because of the high reliability of a nearby ground-based *GNSS* antenna processing, and the nature of the dataset comparable to the shipborne *GNSS* dataset, the assessment of the shipborne processing models will be made by comparing all configuration *ZWD* results to the nearby reference ground station *ZWD*, such as described in Section 4.1.6.2. The highlighting of a better-performing processing model for *ZWD* will lean on the comparison of the *RMSD* between the shipborne and the ground-based *GNSS* antennas, for all the processing configurations. The shipborne *ZWD* time series best fitting the reference station *ZWD* will then be considered the best-performing processing model.

Thereafter, the best-performing processing modeling shipborne *ZWD* will be compared to other external atmospheric water vapor data. The comparisons are described in Sections 4.1.6.3 and 4.1.6.4. As far as these datasets directly provide information on the survey vessel, the assessment of shipborne processing modeling will rely on both *GNSS* antenna *PWVs* that are computed from the corresponding *ZWDs* following the method detailed in Section 2.3.3.3.

4.1.6.1 Tide Gauge

The Brest harbor is equipped with a *RONIM* digital tide gauge such as displayed in Figure 4.6 since February 1993, located in the Penfeld estuary, marked as a purple star (partially covered by the green star) in Figure 4.2. The Service Hydrographique et Océanographique de la Marine (*SHOM*) manages the observatory and publishes the data on data.shom.fr. They provide almost 300 years of observation of the sea level in Brest, making it one of the longest sea level time series in the world [Pou08].



Figure 4.7: Photo of the BRST antenna located in the Penfeld estuary. (Retrieved from igs.org - Accessed October, 25th, 2023).

The dataset is provided with a 10 minutes time resolution. To compare the 30 s resolution survey vessel height dataset to this sea surface height dataset, we use the nearest time method, and we remove the mean vertical lever arm of the survey vessel antenna to bring the height measurement down the sea surface. This means that any tide gauge data will be removed from the nearest-in-time height data from the GNSS dataset. The RMSD will then be computed thanks to the means bias resulting from the mean of the latter difference, and its standard deviation. This will be applied to all the many processing strategies height estimates, that will then be compared to one another.

4.1.6.2 Ground-Based GNSS station BRST

The tide gauge is collocated with the ground-based GNSS antenna BRST, located 292 m away, in place since 1998. Its current equipment is a Trimble antenna TRM 57 971.00 - NONE, and a receiver Trimble ALLOY - 5.45 installed in November 2018. The previous receivers were a Septentrio PolaRx5 as of June 18th, 2018, and a Trimble NetR9 since October 2011. The ground-based GNSS BRST receiver has then been changed once from Trimble NetR9 to Septentrio PolaRx5 during the period of study, after 20 days.

The survey vessel is sailing next to the Brest harbor, staying within a 10 km radius from the BRST ground station. This means that we can compare both GNSS-derived ZWD estimates, as they are observing the same satellites and the same portion of the atmosphere.

The BRST GNSS station is providing multi-GNSS data, but only the GPS constellation is used to stay coherent with the survey vessel processing strategy and be able to compare them accurately. For the same reason, a time resolution of 30 s is applied to the process, using high-resolution final satellite products. However, contrary to the shipborne antenna, the BRST dataset is fixed on the ground so we consider here a static processing as opposed to the kinematic processing of the shipborne antenna.

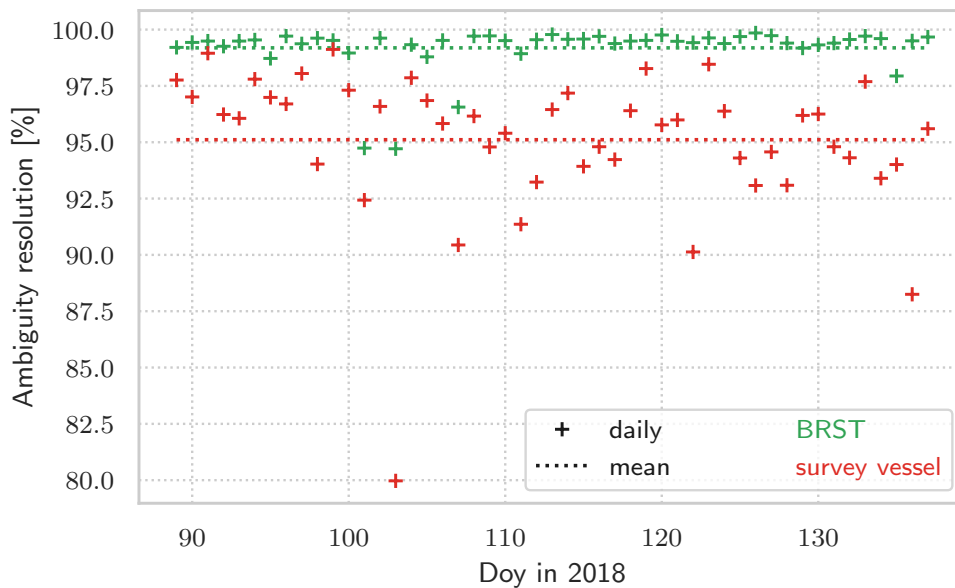


Figure 4.8: Daily ambiguity resolution percentage for the BRST GNSS antenna (green crosses) and the shipborne GNSS antenna (red crosses) and the associated means over the period in 2018 (purple line), in the case of uncertainty of less than 20 % of the cycle narrow lane length. This length corresponds to 20 mm.

This kind of processing permits estimating only one position per day of study, which is supposed to be highly accurate with an accuracy that can reach the millimeter scale. The ZWD being still estimated at each processing step, the static positioning permits us to decorrelate the position and the troposphere delay, so that we can get a more accurate estimate of the ZWD.

BRST antenna mean position is near the Penfeld river, as seen in Figure 4.2 where it is marked under the green star, located with an uncertainty of 5 mm.

As for the ground-based GNSS PPP processing in Bosser and Bock (2021) [Bos 21b], Bock et al. (2016) [Boc 16], and Bock et al. (2021) [Boc 21], the ground-based GNSS dataset is processed using a modeling of $\text{CO} = 7^\circ - \text{WG} = \sqrt{\sin} - \text{RW} = 5 \text{ mm} \cdot h^{-0.5}$. This processing strategy results in an amount of daily ambiguity resolution presented in Figure 4.8.

Here we consider the ambiguity as solved when the uncertainty is less than 20 % of a narrow lane cycle of length of about 10 cm. The ambiguities considered as fixed in Figure 4.8 may differ from the float ambiguities of less than 2 cm (see Equation (2.8)). Under this rule, an average of 99 % of the ambiguities are fixed over the study for BRST ground-based antenna. The average ambiguity resolution is of 95 % for the shipborne antenna.

The resulting formal error is of less than 1 mm. The ZWD estimated from BRST GNSS antenna measurements at 30 s of resolution will be compared to all the survey vessel ZWD retrievals by subtracting the former from the latter at the corresponding time datum. The statistics of bias, standard deviation and RMSD on ZWD will be computed from the resulting difference for each survey vessel processing strategy.

The indicators are represented in Figure 4.3, where it is interesting to note that the reference station BRST is less affected by multipath than the shipborne antenna. Also, the number of observations between two cycle slips is greater for BRST than for any of the survey vessel datasets represented here. This shows the relevance of the

BRST dataset for being a reference to assess the survey vessel processing quality for all configurations.

4.1.6.3 ERA5

As ERA5 delivers hourly atmospheric parameters such as the TCWV on a 0.25° grid on a global scale such as explained in Section 1.1.1.3, data are extracted at the survey vessel location.

Here we apply the comparison method from [Bos 21a]. the ERA5 TCWV values from the four surrounding points of the shipborne antenna location are extrapolated to the survey vessel antenna height by using Equation (2.56). The ellipsoidal height estimated during the GNSS processing is reduced to the MSL thanks to the Earth Gravitational Model (EGM)2008 geoid model, to match the ERA5 height reference.

The resulting four TCWV values at the shipborne antenna height are then bilinearly interpolated to the antenna location.

The times are matched using the nearest GNSS time datum for each of TCWV timestamps.

4.1.6.4 Radiosonde

A meteorological station managed by Météo France is located in Guipavas, less than 20 km from the Brest Harbor, since 1966. It launches a balloon carrying a RS twice a day at midday and midnight coordinated universal time (UTC), every day, providing another source of information for the survey vessel ZWD retrieval assessment.

As far as the RS provides the amount of water vapor at different heights while ascending the atmosphere, the PWV is computed by integrating the RS water vapor measurements all over the atmosphere column. Each RS datum is compared to the matching date at midday or midnight from the shipborne ZWD, and statistics are computed from the resulting difference dataset.

Here, we chose to compare both PWV datasets by matching the times of the shipborne GNSS PWV retrieval with the time of launch of the RS. This choice might induce some bias as the RS needs about one hour to travel the whole troposphere column, such as underlined in some of the studies presented in Chapter 3.

4.2 ASSESSMENT OF SURVEY VESSEL PROCESSING MODELS

As explained in Chapter 2, height is less accurate than the horizontal positions in GNSS solution, and ZWD is correlated to height in the GNSS processing. As we are studying the ZWD estimation here, we will then focus on qualifying the height and ZWD results from the survey vessel by comparing the corresponding time series in all processing modeling with external data.

4.2.1 Qualification of Survey Vessel GNSS Solutions with the References

4.2.1.1 Antenna height

The antenna height is qualified thanks to the Penfeld tide gauge, by comparing the tide gauge sea surface measurement to the survey vessel height dataset reduced to the vertical lever arm of the antenna. The standard deviation and RMSD for each processing

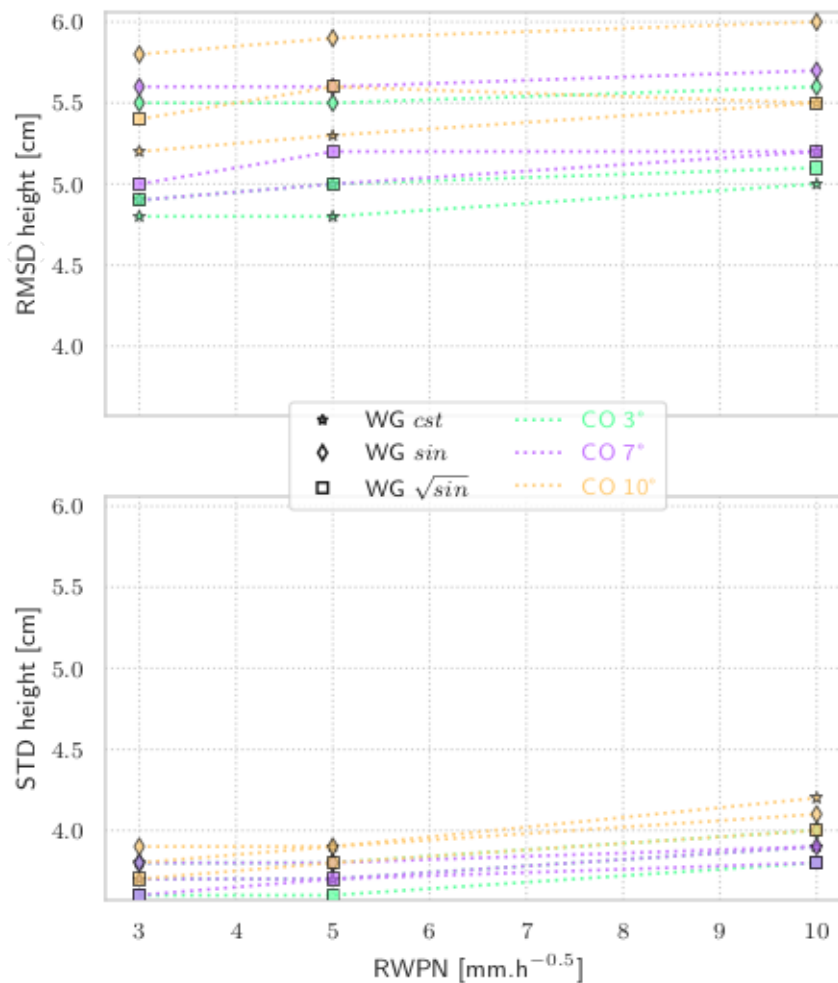


Figure 4.9: RMSD (top) and standard deviation (STD, bottom) of the difference between sea surface measurements from the survey vessel and Penfeld tide gauge in centimeters, as a function of the RWPN model, over the 49 days. Different colors represent the cut-off angle models: green is for $co = 3^\circ$, blue is for $co = 7^\circ$, and orange is for $co = 10^\circ$. Different markers represent the weighting function models: square is for $wg = cst$, triangle down is for $wg = sin$, and star is for $wg = \sqrt{sin}$.

model height result are given in Figure 4.9. The statistics represented in this Figure are detailed in Table A.1 of Appendix A.

A Fisher test has been performed to assess whether the height difference standard deviations computed for each processing model are significantly different with respect to the length of the dataset.

To this end, we suppose here that the height estimates follow a Gaussian law and are independent from one another. Then we consider the null hypothesis stating that "their variances are identical" and we test this hypothesis at a level of 0.05. We compute the statistical p-value for the degree of freedom of our problem linked to the quantile $1 - \frac{0.05}{2}$. For the comparison between the shipborne antenna and ERA5, the degree of freedom is 479, giving a p-value of 0.99. Finally, we compute the quotient of the highest variance into the smallest. If the quotient is lower than the statistical p-value, the null hypothesis is rejected, and the variances are considered as significantly different.

In our case, it results that all the height differences were significantly different, so it is relevant to compare the different results to assess the best-performing processing modeling in terms of height estimation. However, the main limitation of this test is that it is significantly sensitive to the non-normality.

It appears here that the maximum **RMSD** between the survey vessel antenna height and the Penfeld tide gauge sea surface height time series during the 49 days of study is of 6.0 cm. It is obtained with the processing model $co = 10^\circ - wg = sin - rw = 10 \text{ mm} \cdot h^{-0.5}$. The best **RMSD** is obtained with a processing modeling of $co = 3^\circ - wg = cst - rw = 3 \text{ mm} \cdot h^{-0.5}$ or $5 \text{ mm} \cdot h^{-0.5}$, both giving an **RMSD** of 4.8 cm.

However, the survey vessel **GNSS** antenna height above the sea surface is inaccurate because of the changing loading and the speed of the vessel that can be more or less sunk into the water by a couple of centimeters (see [Section 4.1.1](#)). This can impact the bias between the survey vessel and tide gauge height time series. Then, it is essential to also study the standard deviation of the differences between the survey vessel height and the tide gauge to assess the quality of the survey vessel height estimate.

Focusing on the cut-off angle modeling, it appears that:

- a low cut-off angle permits to better estimate the height of the antenna, as the **RMSD** values are systematically rising proportionally to the cut-off, regardless of the weighting function and random-walk modeling;
- according to the standard deviation results, the effect is less obvious, as $co = 3^\circ$ and $co = 7^\circ$ give equivalent results;
- $co = 10^\circ$ systematically gives a worse statistical difference between shipborne antenna height and the tide gauge.

A higher amount of low elevation observations then seems to be a leading cause of accuracy for the height estimation, more than the limitation of the multipath effect. This is true even taking into account that the survey vessel was mostly docked next to a rocky dyke higher than the **GNSS** antenna, whose height difference to the antenna depends on the tide, which can show a tide range over 7 m.

The **RWPN** impact on the height estimation quality seems to be closely linked to the cut-off and the weighting function modeling:

- a tight **RWPN** value of $rw = 3 \text{ mm} \cdot h^{-0.5}$ provides better height fitting to the tide gauge for $wg = cst$ and $wg = sin$ than other **RWPN** values;
- $rw = 5 \text{ mm} \cdot h^{-0.5}$ provides equal statistical results than $rw = 3 \text{ mm} \cdot h^{-0.5}$ for $co = 3^\circ$ and $co = 7^\circ$;
- $rw = 10 \text{ mm} \cdot h^{-0.5}$ systematically worsens the standard deviation and the **RMSD**.

Then, it mainly seems that in the survey vessel study case, a loose **RWPN** should be avoided.

In terms of weighting function configuration:

- $wg=cst$ provides better **RMSDs** than $wg=sin$ and $wg=\sqrt{sin}$;
- $wg=\sqrt{sin}$ systematically gives the best standard deviations;

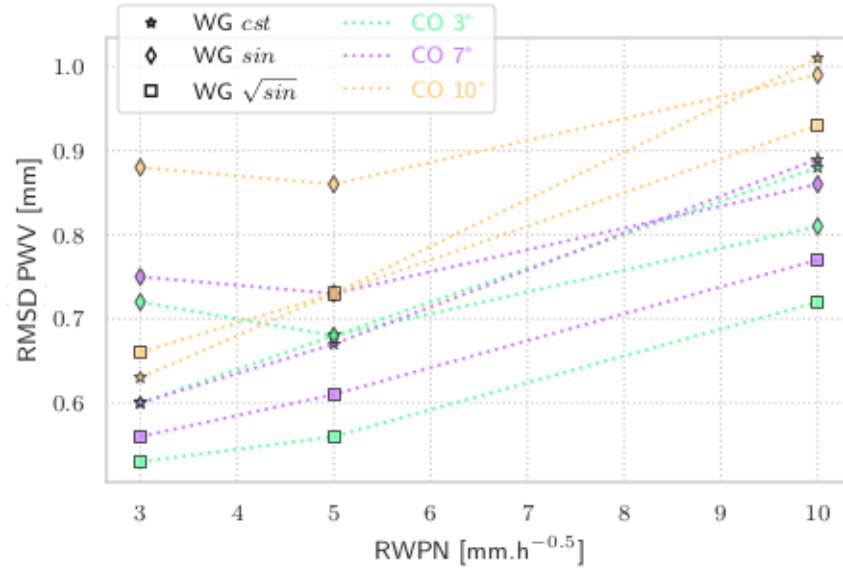


Figure 4.10: **RMSD** between the survey vessel and BRST ground-based GNSS station in centimeters, as a function of the RWPV model. Different colors represent the cut-off angle models: green is for $co = 3^\circ$, blue is for $co = 7^\circ$, and orange is for $co = 10^\circ$. Different markers represent the weighting function models: square is for $wg = cst$, triangle down is for $wg = sin$, and star is for $wg = \sqrt{\sin}$.

- $wg=sin$ provides the worst **RMSD**;

The height bias, from 3.0 cm to 4.4 cm, might have been affected by the vertical lever arm uncertainty that is not due to the processing. It is possible that the 0.4 cm separating both $wg=\sqrt{\sin}$ and $wg=cst$ bias results is because $wg=\sqrt{\sin}$ better estimated the antenna height, that is 0.4 cm higher than the $wg=cst$ estimation. The resulting **RMSD** would be affected in consequence. Otherwise, it is also interesting to note that the $wg=\sqrt{\sin}$ resulting biases are systematically higher than those of $wg=cst$ and lower than for $wg=sin$.

As the height is correlated to the **ZWD** in the kinematic GNSS processing, it is interesting to investigate further by studying the **ZWD** estimates, which is also interesting to study **PWV**.

4.2.1.2 Retrieved **PWV**

We study here the **RMSD** between the survey vessel and BRST **PWV**s computed from their respective **ZWD** to assess the survey vessel processing modeling. The results are displayed in Figure 4.10. The statistics represented in this Figure are detailed in Table A.2 of Appendix A.

As for the height estimate, it appears here that the maximum **RMSD** of 1.0 mm between the survey vessel and BRST **PWV** time series is for the configuration $co = 10^\circ - wg = sin - rw = 10 \text{ mm} \cdot \text{h}^{-0.5}$. This shows a ground-based-GNSS-quality fitting to the BRST **PWV** of less than 1 mm.

This high accuracy is explainable by the fact that the vessel is docked most of the time, behaving as a moored buoy more than a sailing ship. Also, inside the Marina du Chateau, the sea surface is mostly flat. The **PWV RMSD** displayed in Figure 4.10

can reach 0.5 mm at the minimum with a processing configuration $co = 3^\circ - wg = \sqrt{\sin} - rw = 3 \text{ mm} \cdot h^{-0.5}$.

Although the statistics show results better than expected, a Fisher test has been performed here as well, showing that all the **PWV** difference statistics are significantly different, except in the case of $co = 3^\circ$ and $co = 7^\circ$ that show standard deviations that are not always significantly different, depending on the weighting function modeling. Indeed, the variances are both equal to 0.66 mm^2 when using these cut-off angles with the $\sqrt{\sin}$ weighting function, so their quotient equals 1, being higher than the statistical p-value of the test. Changes in the other processing parameters provide significantly different **RMSDs** as well as in the previous case of the height.

It seems that the cut-off angle and the weighting function configurations impact are closely linked:

- apart from a modeling involving $co = 10^\circ - rw = 10 \text{ mm} \cdot h^{-0.5}$, $wg = cst$ provides the same **RMSD** whatever the cut-off angle modeling, for each of the **RWPN** values tested;
- for the other weighting function configurations $wg = \sin$ and $wg = \sqrt{\sin}$, it appears that the **RMSD** is raising with the cut-off angle value, whatever the **RWPN** configuration.

We can then state that in the case of the survey vessel study, a low-elevation cut-off angle is the best modeling.

As of **RWPN** modeling,

- $rw = 10 \text{ mm} \cdot h^{-0.5}$ systematically provides the worse **RMSD** values;
- $rw = 3 \text{ mm} \cdot h^{-0.5}$ gives either same or better **RMSD** values than $rw = 5 \text{ mm} \cdot h^{-0.5}$, except for $co = 7^\circ - wg = \sin - rw = 5 \text{ mm} \cdot h^{-0.5}$ that is better than $co = 7^\circ - wg = \sin - rw = 3 \text{ mm} \cdot h^{-0.5}$.

The previous conclusion of avoiding a loose **ZWD** constraint for the height estimation in [Section 4.2.1.1](#) is reached concerning the **PWV** as well. However, $rw = 3 \text{ mm} \cdot h^{-0.5}$ and $rw = 5 \text{ mm} \cdot h^{-0.5}$ do not particularly stand out from one another.

The **PWV RMSDs** results concerning the weighting function modeling corroborates the standard deviation results from the height estimate comparison to the tide gauge in [Section 4.2.1.1](#):

- $wg = \sqrt{\sin}$ systematically provides the best **PWV** fitting between the survey vessel and BRST
- $wg = \sin$ appears to be the worst weighting function model.

This might be because with $wg = cst$, all the satellite observations are given the same uncertainty even if the lower ones are more affected by multipath on the one hand and that $wg = \sin$ is however providing too high uncertainty to the lowest observations on the other hand. $wg = \sqrt{\sin}$ appears to be a good agreement by giving less uncertainty than $wg = \sin$ for the intermediate elevation observations, providing them more credit in the Kalman Filter.

We can then suppose that the vertical lever arm of the survey vessel antenna is better estimated with the model $wg = \sqrt{\sin}$ than $wg = cst$, and it could be adjusted by +0.4 cm, then providing an even better **RMSD** for $wg = \sqrt{\sin}$ and $wg = \sin$ by decreasing the bias, while $wg = cst$ resulting **RMSDs** could worsen.

Therefore, we would recommend using $wg = \sqrt{\sin}$ in light of this study.

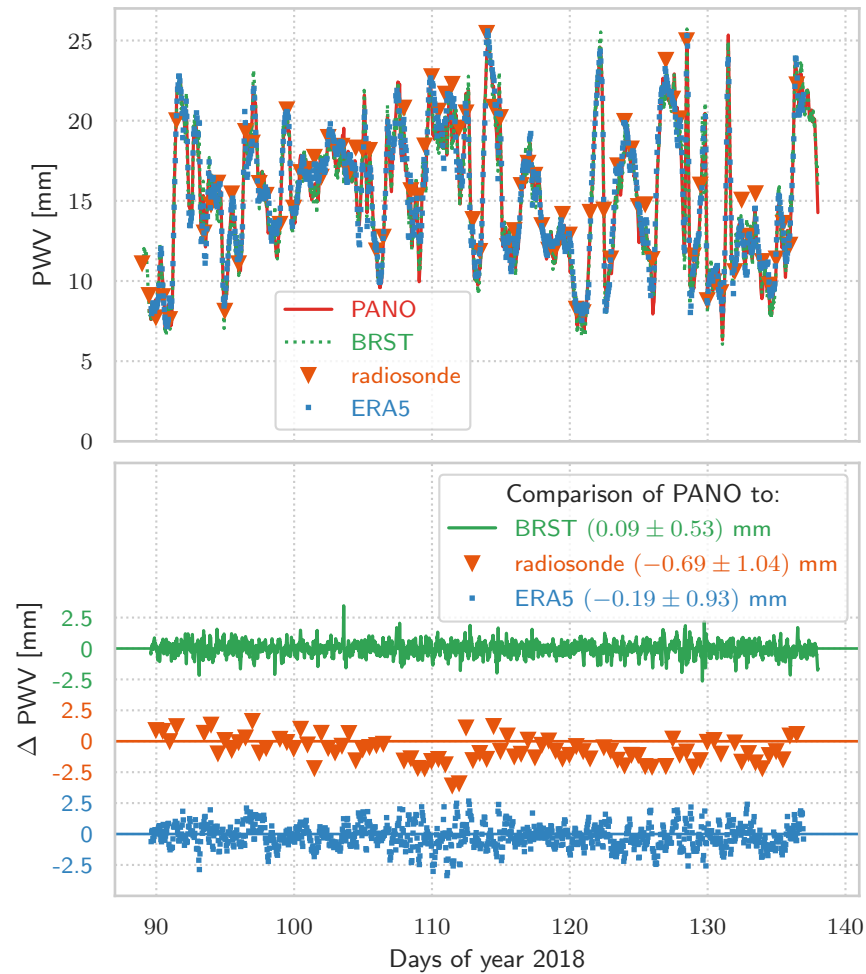


Figure 4.11: *PWV* time series from different measurement techniques (top) and difference time series between the survey vessel and usual water vapor measuring techniques, between days 89 and 137 of the year 2018 (bottom). Red plot corresponds to *PWV* retrieved from the survey vessel with a processing model $co = 3^\circ - wg = \sqrt{\sin} - rw = 3 \text{ mm} \cdot \text{h}^{-0.5}$, green is the BRST *GNSS PWV* retrieval, orange is the RS *PWV* retrieval, and blue is the ERA5 *TCWV* product.

4.2.2 Comparison of the Best Performing Processing Model Retrieved *PWV* to Usual *PWV* Data Sources

The time series of the survey vessel *PWV* dataset during the period of study resulting from the best-performing processing model $co = 3^\circ - wg = \sqrt{\sin} - rw = 3 \text{ mm} \cdot \text{h}^{-0.5}$, as well as the reference *PWV* datasets from BRST ground-based *GNSS* station, ERA5 of the ECMWF, and RS of Guipavas are displayed on the top graph of Figure 4.11. It shows a good agreement of all the time series, to a lesser extent for some data points coming from the RS.

The bottom graph of Figure 4.11 displays the time series resulting from the subtraction of the ground-based reference *PWV* to the survey vessel *PWV* time series. They are providing a very good agreement with a mean difference of $(+0.09 \pm 0.53) \text{ mm}$ for the comparison to the BRST ground-based *GNSS* station, $(-0.19 \pm 0.93) \text{ mm}$ for the comparison to the ERA5-provided *TCWV* product, and $(-0.69 \pm 1.04) \text{ mm}$ for the comparison to the RS. These biases are small, and show a dry bias for the *GNSS* retrieved

PWV compared to the other classical techniques ERA5 and the RS. This is observed as well for some shipborne GNSS studies of Table 3.4. Indeed, 7 of the 9 studies that compared to ground-launched RSs have found a dry bias of the shipborne GNSS, as well as 2 out of the 7 studies that compared it to ERA5. In the three comparisons, the statistic on the differences show a very well-fitting shipborne GNSS retrieved PWV time series, that would be suitable for meteorology and climate study.

The comparison to the RS integrated content has been made at the time of launch of the balloon, which not really corresponds to the reality. Indeed, the balloon needs thirty minutes to one hour to ascend the atmosphere, so comparing to a mean value of survey vessel PWV retrieving over 30 minutes or more could have brought to better accordance between both datasets. This can explain some part of the RS higher difference compared to the other dataset comparisons. Other clues are the distance between the shipborne antenna and the RS station such as seen in Figure 4.2; and the RS horizontal deflection mostly towards East due to the wind that is usually coming from the West in Brest.

4.3 CONCLUSION ON THE REAL DATASET PROCESSING STRATEGY ASSESSMENT

The survey vessel dataset studied here has been processed under different processing models, permitting highlighting the impact of the modeling on the GNSS solution accuracy.

The results developed in Section 4.2.1 highlight that the processing modeling does have an impact on the GNSS solution. Indeed, a Fisher test has been made and shows that the statistics of the differences with the references are significantly different for both the height and PWV estimates. Comparing the statistics of the difference between the survey vessel height and the tide gauge, and the survey vessel and BRST PWVs for each of the testing processing models, we have enlightened the poor performance in our case of study of a high cut-off angle $co = 10^\circ$, $wg = \sin$, or a high RWPN $rw = 10 \text{ mm} \cdot h^{-0.5}$ compared to other processing models tested. Among the other models tested, the best performing in terms of height and PWV estimates accuracy is $co = 3^\circ - wg = \sqrt{\sin} - rw = 3 \text{ mm} \cdot h^{-0.5}$ or $co = 3^\circ - wg = \sqrt{\sin} - rw = 5 \text{ mm} \cdot h^{-0.5}$. The main points are that it seems better to use a low cut-off angle, and $wg = \sqrt{\sin}$ provides a better PWV estimation and lowers the height difference standard deviation. Also, a constraint too loose applied to the ZWD estimate provides a worse result, because the filter does not correctly decorrelates the ZWD to the height.

The focus on the comparison with the ground-based GNSS antenna to qualify the shipborne antenna processing configuration results does not permit to highlight biases that could be common to GNSS measurements. Such biases would have been enlightened by studying the comparison to the other sources such as ERA5 and the radiosonde.

The survey vessel dataset is a little bit simple because it is located near the coast, in a sheltered area: the Brest harbor. Also, the period of study relies on a mainly docked vessel, with two navigation parts of a few hours only, which is not sufficient to perform statistically significant difference study. Thus, it may not be representative of the general situation in which we could process shipborne GNSS data for water vapor retrieving. Indeed, the main goal would be to get data overseas, where the coastal weather stations and GNSS antennas cannot be used to get this information and the only data available is from SMWRs.

While we have shown that processing modeling impacts the height and ZWD estimation from a relatively simple case study of shipborne GNSS antenna, the next chapter will permit to assess how the processing configuration impacts the GNSS results while working on simulated GNSS dataset, to highlight a general-case best-performing processing model to PPP process shipborne GNSS data.

PROCESSING MODELING ASSESSMENT OF SIMULATED
SHIPBORNE GNSS SIGNAL

CONTENT

5.1	Simulation of a GNSS Signal Acquisition	76
5.1.1	Strengths and Weaknesses of Simulated Shipborne GNSS Dataset	76
5.1.2	Simulation Features	77
5.2	Processing Methods for the Estimation	80
5.2.1	Parameters Estimation	80
5.2.2	Kalman Filter Tuning	81
5.3	Results and Comparison of the Processing Models	82
5.3.1	Sensitivity of Correlation Coefficient to Processing Modeling	82
5.3.2	Sensitivity of Height Estimation to Processing Modeling . . .	83
5.3.3	Sensitivity of ZWD Estimation to Processing Modeling	84
5.4	Discussion on a Suitable Processing Modeling	86
5.4.1	Elevation Weighting Function	86
5.4.2	RWPN on ZWD	89
5.4.3	Cut-Off Angle	90
5.4.4	Recommended Modeling	91
5.5	Impact of Simulation Features on Processing	91
5.5.1	Summary of the Studied Features	91
5.5.2	Data Sampling	91
5.5.3	GNSS Constellations	92
5.5.4	Antenna Phase Center Variation	93
5.5.5	Latitude	95
5.6	Conclusion on the Simulated Shipborne GNSS Processing Modeling .	97

This study relies on home-made simulated shipborne GNSS signals, permitting to test several combinations of processing configurations while PPP processing the GNSS. The accuracy of the retrieved ZWD from the processing of this simulated signal will be assessed by comparing the estimated ZWD to the initial simulated ZWD. This is a complementary study to the previous chapter, permitting to extend to a more general case the real dataset study, in order to highlight a relevant reference processing modeling for general shipborne antenna GNSS processing.

This study led to an oral presentation at the European Geosciences Union (EGU)²² in Vienna in May 2022 [Pan 22a], supplemented by a scientific paper publication in *Sensors* [Pan 23].

This chapter is inspired by Panetier, Bossier, and Khenchaf (2023) [Pan 23].

5.1 SIMULATION OF A GNSS SIGNAL ACQUISITION

Before processing the GNSS dataset and assessing the result quality, the current first section details the implementation of the homemade simulated shipborne GNSS signal.

5.1.1 *Strengths and Weaknesses of Simulated Shipborne GNSS Dataset*

Using real GNSS dataset to study processing methodology can prove challenging when it comes to getting an absolute reference to assess the quality of the GNSS solutions, although real sensing captures any event that could occur during the acquisition, affecting either the positioning, clock errors or atmospheric parameters. On an open sea area, the available datasets such as tide gauge for height reference, or radiosonde and ground-based GNSS antennas for ZWD reference are not available, contrary to the previous case of the Panopée vessel that was evolving in a coastal area, providing all these facilities. Moreover, the models and other measurement techniques available offshore provide atmospheric water vapor information that is biased as well.

The idea is here to rely on a well-known simulated shipborne GNSS dataset from a homemade simulator, to assess the processing configuration efficiency. Several signals will then be simulated in different acquisition situations simply by changing a few parameters such as the vessel location, its behavior, the troposphere water vapor content, the model of the antenna, etc. The impact of these acquisition settings and configuration on the processing model performance will be addressed in the second part of this study.

The simulated phase observable is directly built from a set of simulated GNSS solutions such as antenna position, troposphere water vapor above the antenna, and receiver clock error. From this, we will investigate the performance of different GNSS processing models. Indeed, the quality of the estimates will be assessed directly by comparing them to the simulated quantities.

The sky map of the satellites as seen by the simulated GNSS antenna comes from real broadcast ephemerides. This provides a real geometry as it would be for a real case, thus implying effects that would exist in real life.

This simulator does not provide ambiguities, that are considered fixed, so there will be no need for time convergence for the solution in the estimator.

It is important to notice, however, that signal simulation cannot account for the complexity of phenomena that can affect the troposphere, or the behavior of vessel carriers that could be very wide, depending on boat handling instructions as well as vessel size, sea state, and weather conditions.

Tide and swell phenomena are modeled by simple sinusoidal signals, the carrier's course is assumed to be fixed, and initially, the boat's heading is assumed to be fixed towards the North. Furthermore, the multipath model is quite simple, as it assumes that the antenna is located at the highest point of the carrier, and that there are no masks around. The only multipath reflectances modeled are therefore off the sea surface and do not take into account possible deformation by waves. In a concrete case of acquisition using a shipborne antenna, these conditions may hardly be verified, and thus have a major impact on the quality of the measurement, such as in Bosser, Van Baelen, and Bousquet (2022) [Bos 22b], where the recorded data proved unusable due to the positioning of the antenna under the ship's radar.

The impact of this simple simulation in the scope of our study is that the processing modeling highlighted as the best performing over these simulated GNSS signals might not be the best performing over a specific real case of study. However, it gives a general solution that could be applied in any case as a suitable solution for processing shipborne GNSS datasets.

5.1.2 Simulation Features

Different GNSS-derived estimates over time are simulated at first, such as antenna position, ZWD, and receiver clock delay, as well as some noises affecting the measurement such as antenna PCV, multipath error, and white measurement noise. The simulation does not take into account the interaction of the GNSS signal with the ionized particles during its propagation into the ionosphere. To this end, we assume that the ionospheric effect has been removed by using the IF LC, such as explained in Section 2.3.2.1, applying Equation (2.4) to all the simulated variables. All these signals, detailed in Sections 5.1.2.1 and 5.1.2.2, are next added together to form the simulated carrier-phase signal used thereafter, to test different processing models.

IGS GNSS satellite orbits are used for this study. Using multi-GNSS has been shown to improve the troposphere water vapor content retrieval, so we use three different GNSS constellation ephemerides: GPS, GLONASS, and Galileo.

The resulting final carrier-phase is simulated following Equation (5.1) that is a simplification of Equation (2.3) following Elosegui et al. (1995) [Elo 95], King and Watson (2010) [Kin 10], and Teunissen and Montenbruck (2017) [Teu 17]:

$$\varphi_s^{i LC} = c \cdot dt_s + h_s \cdot \sin(el^i) + \frac{ZWD_s}{\sin(el^i)} + \varepsilon_s^{i LC} \quad (5.1)$$

where the error term is expressed as

$$\varepsilon_s^{i LC} = pcv_s^{LC}(az^i, el^i) + \Phi_{mp,s}^{LC}(az^i, el^i) + \eta_s^{LC} \quad (5.2)$$

where i denotes the i -th satellite, and az^i and el^i denote the azimuth and elevation of the i -th satellite, and the different terms are described in Table 5.1.

Parameter	Description
$\varphi_s^{i LC}$	IF linear combination of the simulated phase observable
c	light celerity in vacuum
dt_s	simulated receiver clock bias
h_s	simulated height of the antenna above sea level
ZWD_s	simulated ZWD
$\varepsilon_s^{i LC}$	simulated residual phase errors
pcv_s^{LC}	IF linear combination of the simulated PCV
$\Phi_{mp,s}^{LC}$	IF linear combination of the simulated multipath error
η_s^{LC}	IF linear combination of the simulated white noise measurement

Table 5.1: Description of the simulated carrier-phase signal terms of Equation (5.1).

The main interesting features of this simulation are summarized in Table 5.2.

Parameter	Value
Constellations	GPS, GLONASS, Galileo
Time resolution	30 s
Location	Mid-latitudes
Antenna height	30 m above MSL + tide + heave
ZWD RWPN	$5 \text{ mm} \cdot \text{h}^{-0.5}$
Antenna PCV	Perfectly corrected

Table 5.2: Setup for the shipborne GNSS measurement simulation.

For significance purposes, many troposphere signals have been simulated, leading to as many simulated carrier-phase signals permitting to assess the estimation quality through significant statistical study. The amount of simulated signals has been fixed to 200. This value has been assessed by testing different amounts of simulated tropospheres on the resulting mean difference biases. 200 appeared to provide a significant reduction of the statistical errors compared to a lower amount of tropospheres, while a higher number of simulations did not provide significant change.

5.1.2.1 Simulation of GNSS-Derived Estimates

The longitude and latitude of the carrying vessel are considered as fixed for the study and have been set to 0° and 45° N respectively. This latitude corresponds to mid-latitudes, like those of France, where the dataset from Chapter 4 was collected to study whether the processing modeling has an impact on ZWD retrieved from a shipborne GNSS antenna. In reality, this point corresponds to a land area, but here we consider a planet entirely covered with water, an approximation that is consistent when the R/V sails offshore. The problem is independent in longitude thanks to the GNSS constellation orbital planes around the rotating Earth. For simplification purposes, the ship is considered as not moving horizontally, so no horizontal movement has been added to the simulated carrier-phase.

The mean altitude of the carrying vessel has been set to MSL. The antenna is supposed ship-mounted 30 m above the sea surface. The height is then simulated with a mean value of 30 m. A heavy tide is added, modeled with a 12 m peak-to-peak amplitude sine signal of 12 h period. A heave signal is also added as a 40 cm peak-to-peak amplitude sine signal of 16 s period. These two signals permit the modeling of both fast and slow height changes that could impact a shipborne GNSS antenna. This simulated height h_s corresponds to a zenithal direction movement of the antenna, represented in the top graph of Figure 5.1. It is mapped to the slant path direction of the signal by using the sine function of the elevation el of the observed satellite before being added to the simulation of carrier-phase signal: $h_s \cdot \sin el$.

The troposphere water vapor effect has been simulated by creating a 24 h 30 s resolution ZWD signal with an initial value following the normal distribution $\mathcal{N}(0.150 \text{ m}, 0.100 \text{ m})$ and a RWPN of $5 \text{ mm} \cdot \text{h}^{-0.5}$. One of the 200 ZTD simulated result in the bottom graph of Figure 5.1. We have chosen the simple mapping function of Equation (2.19) to map the simulated ZWD ZWD_s to the slant path direction, which means that it is divided by

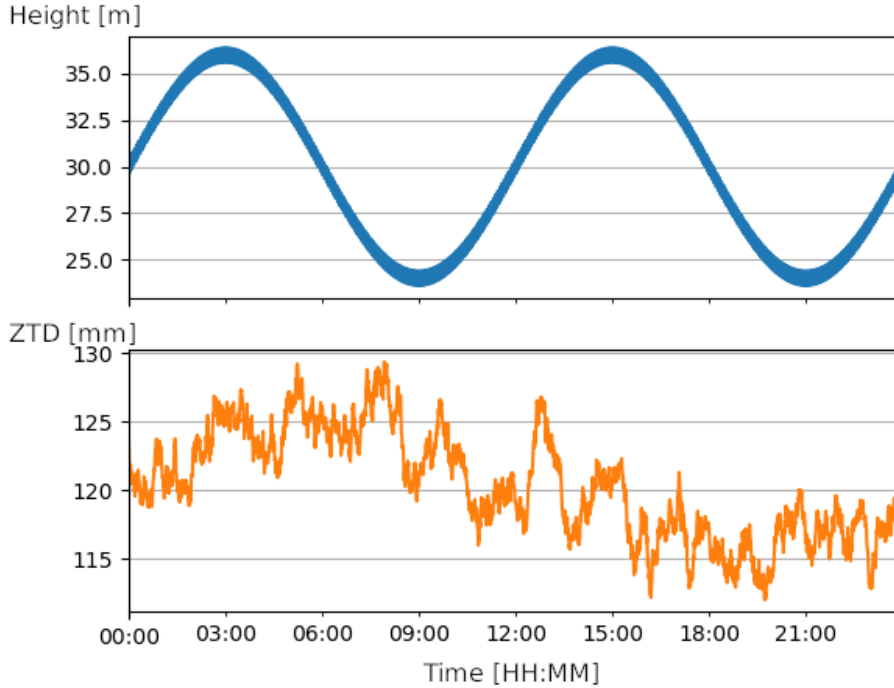


Figure 5.1: Simulated height (top) and ZWD (bottom) time series. The simulated height and one over 200 simulated ZWD signals with a $5 \text{ mm} \cdot \text{h}^{-0.5}$ $RWPN$ value are represented here.

the sine of satellite elevation before being added to the carrier-phase signal simulation [Elo 95]: $\frac{ZWD_s}{\sin e}$.

The simulated clock error C_s is in length unit, corresponding to the term $c \cdot dt_r$ of Equation (2.3). Then, the simulated clock delay is directly added to the simulated carrier-phase signal. As for King and Watson (2010) [Kin 10], the clock and orbit errors of the observed satellites are assumed known and free of error. In this study, no receiver clock error has been simulated either, so dt_r has just been set to a zero-meter constant signal.

5.1.2.2 Simulation of Error Sources

In terms of orientation, the antenna is supposed to be in the horizontal plane and to face the North direction all the time, as if it were a static ground-based antenna. The PCV effect is supposed perfectly corrected. To this end, no PCV effect has been added to the simulated signal.

The simulated multipath follows Equation (2.30) with a height $H_0 = 30 \text{ m}$.

The simulated measurement noise $\eta_s^{F_{1,2}}$ has been modeled as a white noise of standard deviation of $\frac{\lambda}{100}$. The FLC is directly applied to the standard deviation here.

All these simulated errors are in length units and added as is to the simulated carrier-phase.

5.2 PROCESSING METHODS FOR THE ESTIMATION

5.2.1 Parameters Estimation

A Kalman Filter such as described in Section 2.4 has been implemented to process the simulated shipborne GNSS dataset. From now on, the ambiguity is considered fixed, so its impact is omitted in the equations so far.

Placing the satellite in the local frame of the receiving antenna, we reformulate the measurement equation with E_r , N_r , and U_r denoting the Cartesian coordinates of the receiver at the surface of the Earth, the Prime meridian, the Equator, and the ellipsoid constituting the origin of the coordinates.

The remaining parameters to be estimated at a resolution of 30 s here are:

- 3D positioning mapped to a local frame as of Cartesian coordinates,
- receiver clock error equivalent in meters,
- ZWD as described in Equation (2.38),
- tropospheric gradients as described in Equation (2.28),

so the state vector of Equation (2.39) now becomes:

$$\mathbf{x} = \left[E_r \quad N_r \quad U_r \quad ZWD \quad G_{EW} \quad G_{NS} \quad dt_r \right]^T. \quad (5.3)$$

The covariance between the estimated variables is supposed to be zero at first, and the standard deviation of all the variables is arbitrarily set to 10^{-3} m, leading to the following covariance state matrix:

$$\Sigma_{k0} = 10^{-6} \cdot \mathbf{I}_7. \quad (5.4)$$

Using the trigonometry formulas, the resulting IF LC observation equation to be implemented to the Kalman Filter Equation (2.48) when gathering all the satellite observations at each time step, is then:

$$\begin{aligned} \Phi_r^{iLC} = & E_r \cdot \cos(el^i) \sin(az^i) + N_r \cdot \cos(el^i) \cos(az^i) + U_r \cdot \sin(el^i) \\ & + C + \frac{ZWD}{\sin(el^i)} + \frac{G_{NS} \cdot \cos(az^i) + G_{EW} \cdot \sin(az^i)}{\sin(el^i) \tan(el^i)}. \end{aligned} \quad (5.5)$$

The observation matrix from Equation (2.49) is now entirely defined thanks to the elevation and azimuth of the observed satellites at the given time step k :

$$\mathbf{C}_k = \begin{bmatrix} \cos(el_k^1) \sin(az_k^1) & \dots & \cos(el_k^{n_{sat}}) \sin(az_k^{n_{sat}}) \\ \cos(el_k^1) \cos(az_k^1) & \dots & \cos(el_k^{n_{sat}}) \cos(az_k^{n_{sat}}) \\ \sin(el_k^1) & \dots & \sin(el_k^{n_{sat}}) \\ \mathcal{M}(el_k^1) & \dots & \mathcal{M}(el_k^{n_{sat}}) \\ 10^{-6} \cdot \mathcal{M}_{az_k^1}(el_k^1) \cdot \frac{\sin(az_k^1)}{\tan(el_k^1)} & \dots & 10^{-6} \cdot \mathcal{M}_{az_k^{n_{sat}}}(el_k^{n_{sat}}) \cdot \frac{\sin(az_k^{n_{sat}})}{\tan(el_k^{n_{sat}})} \\ 10^{-6} \cdot \mathcal{M}_{az_k^1}(el_k^1) \cdot \frac{\cos(az_k^1)}{\tan(el_k^1)} & \dots & 10^{-6} \cdot \mathcal{M}_{az_k^{n_{sat}}}(el_k^{n_{sat}}) \cdot \frac{\cos(az_k^{n_{sat}})}{\tan(el_k^{n_{sat}})} \\ c & \dots & c \end{bmatrix} \quad (5.6)$$

where \mathcal{M} denotes for the mapping function of ZWD and tropospheric gradients.

The measurement noise defined in Section 5.1.2.2 permits to define the variance-covariance matrix of the observation vector:

$$\Sigma_{\beta} = \frac{\lambda^2}{100} \cdot \mathbf{I}_{n_{sat}} \quad (5.7)$$

5.2.2 Kalman Filter Tuning

The simulated dataset is processed through different models of elevation cut-off angle, *RWPN* value on the *ZWD*, and weighting function of the elevation as for the processing study in Chapter 4. The models previously applied to this preliminary study and detailed in Table 4.1 have been tested here as well. More *RWPN* values have been tested as well with several *RWPN* values in range $1 \text{ mm} \cdot \text{h}^{-0.5}$ to $20 \text{ mm} \cdot \text{h}^{-0.5}$.

An alternative to $\text{WG} = \sqrt{\sin}$, such as presented by the red curve in Figure 5.2 providing more weight to high elevation and less to intermediate elevation observations, will be tested as well. This function has been proposed among others by Hadas,

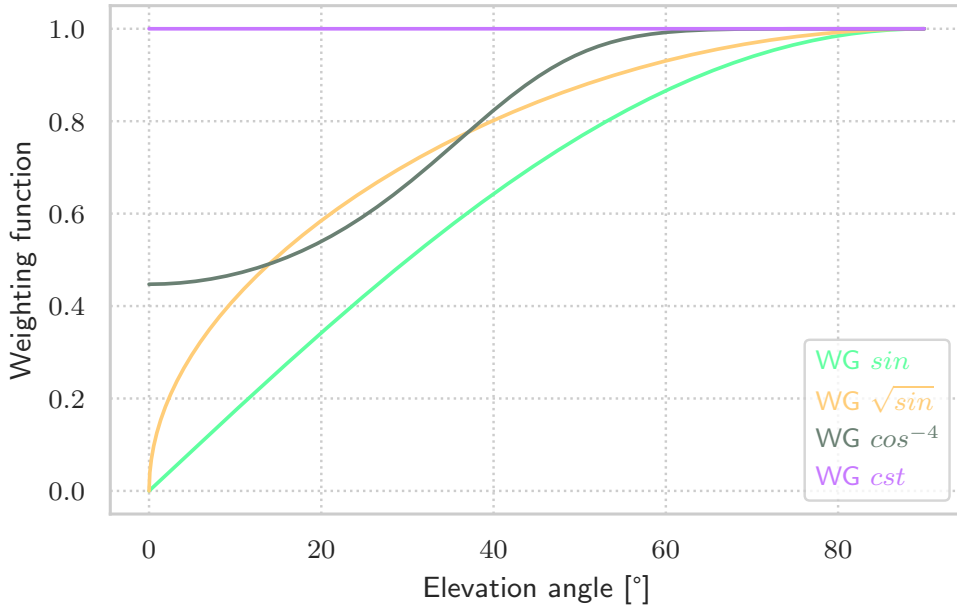


Figure 5.2: Weighting function of the elevation of the observed satellites tested to process the simulated shipborne GNSS dataset. The grey curve \cos^{-4} stands for the new tested weighting function proposed by Hadas, Hobiger, and Hordyniec (2020) [Had 20]. This function permits giving more weight to the high elevation observation measurements, and less weight to the observation of satellites between 14° and 37° compared to $\text{WG} = \sqrt{\sin}$.

Hobiger, and Hordyniec (2020) [Had 20], following

$$\text{WG} = \frac{1}{\sqrt{1 + 4 \cos^8(el)}}.$$

Then, the standard deviation of the measurement will be multiplied by the elevation-dependent function $\sqrt{1 + 4 \cos^8(el)}$ in the Kalman Filtering. For simplification purposes, this weighting function will later be named \cos^{-4} .

The tested modelings for each of the parameters under study are detailed in Table 5.3. The testing of all processing combinations detailed in Table 5.3 leads to 108 studies to

Parameter	Tested models
cut-off angle	3°, 7°, and 10°.
weighting function	cst , sin , \sqrt{sin} , and cos^{-4} .
RWPN	1, 3, 5, 7, 8, 10, 12, 15, and 20 mm · h ^{-0.5} .

Table 5.3: PPP processing modeling tested on the simulated dataset described in Section 5.1. We studied here the parameters detailed in Section 2.4.3. More values of RWPN have also been added to be tested.

compare to each other, to highlight unfavorable or more suitable processing models for ZWD retrieval at sea.

The RWPN value is used to define the ZWD and tropospheric gradients variances, such as in Equations (2.50) and (2.41) respectively.

The antenna being in movement during the acquisition, the processing is done in kinematic mode. Then, the 3D position and the clock error are given a high a priori variance in Equation (2.40) of the Kalman Filter, compared to the ZWD variance in Equation (2.50):

$$\sigma_C^2 = \sigma_E^2 = \sigma_N^2 = \sigma_U^2 = 10^2 \text{ m}^2 \quad (5.8)$$

5.3 RESULTS AND COMPARISON OF THE PROCESSING MODELS

First, the average correlation coefficient between height and ZWD over the 200 GNSS signals estimation has been computed for each of the processing models. The results are presented in Section 5.3.1

Second, the bias and standard deviation of the differences between the estimation and the simulation on height and ZWD have been calculated for all the GNSS signals processed in each configuration. From these 200 differences, the RMSEs of the biases and the standard deviations of the height difference and ZWD have been computed for each of the processing models and are presented in Sections 5.3.2 and 5.3.3.

5.3.1 Sensitivity of Correlation Coefficient to Processing Modeling

The correlation coefficient between the estimates of height and ZWD has been calculated for each of the GNSS signal processing models, for the 200 different carrier phase simulations. The mean correlation coefficient was then calculated from the 200 correlation coefficients, for each processing model. The standard deviations of the correlation coefficients are all lower than 1 %, so we will focus on the mean correlation coefficient between ZWD and height, presented in Figure 5.3.

Figure 5.3 shows a mean correlation coefficient ranging from 16 %, obtained for $co = 3^\circ - wg = sin - rw = 1 \text{ mm} \cdot h^{-0.5}$, to 78 % for $co = 10^\circ - wg = cst - rw = 20 \text{ mm} \cdot h^{-0.5}$.

The mean correlation coefficient increases with the RWPN value. This might be due to the difficulty of the ZWD estimate to aggregate temporal variability when using a tighter RWPN, so it tends to behave differently from the other variables. In contrast, a loose constraint will allow any temporal variation, so the ZWD will resemble the other estimates.

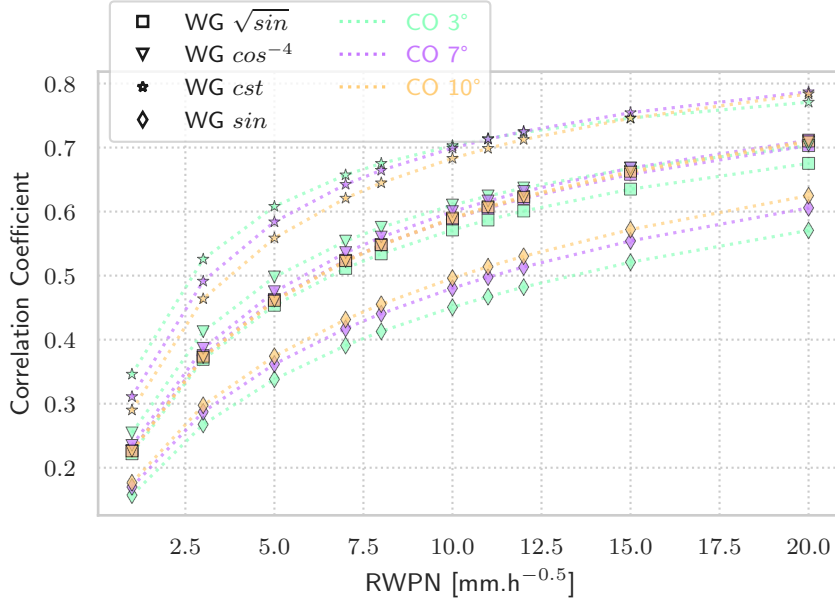


Figure 5.3: Mean correlation coefficient between height and ZWD as a function of $RWPN$ for each cut-off angle for the elevation weighting functions $WG = cst$ (top left), $WG = sin$ (top right), $WG = \sqrt{sin}$ (bottom left), and $WG = cst$ (bottom right).

Also, the best-performing weighting function in terms of decorrelation is $WG = sin$, whereas $WG = cst$ proves to be the worst. $WG = \sqrt{sin}$ is very slightly better than $WG = cst$, showing the same result when using $co = 10^\circ$.

As expected, the mean correlation coefficient increases with the cut-off angle when using $WG = sin$ and $WG = \sqrt{sin}$, which corroborates the fact that height and ZWD are better decorrelated when embedding the signals coming from low elevation satellites. However, we observe the opposite behavior with $WG = cst$ and $WG = cst$. As shown in Figure 5.2, both weighting functions give more weight to very low elevation measurements than $WG = sin$ and $WG = \sqrt{sin}$. Then, it seems that giving too much credit to low elevation observations, that are more affected by multipath effect, might induce artifacts affecting the height and ZWD estimates, thus raising the correlation coefficient.

Interestingly, with $WG = cst$ and $WG = cst$, the cut-off has more impact at the lower $RWPN$ values. This might be because the multipath effect is entirely assimilated to the ZWD estimation when the $RWPN$ is loose. On the contrary, $WG = sin$ and $WG = \sqrt{sin}$ show more cut-off-related impact at high $RWPN$ values, probably because the troposphere-induced delay is better-estimated thanks to low-elevation satellite measurements, and can be more taken into account by the filter when the ZWD variation is loose enough.

5.3.2 Sensitivity of Height Estimation to Processing Modeling

The $RMSEs$ of the height bias and of the standard deviation have been computed for each of the processing models and are presented in Figures 5.4 and 5.5.

Figure 5.4 shows that, despite the amplitude of the simulated vertical movements, the height estimates are still of good quality. Indeed, the height bias $RMSE$ is 37 mm at most, with (-3 ± 37) mm such as seen in Table B.1 of Appendix B of height bias

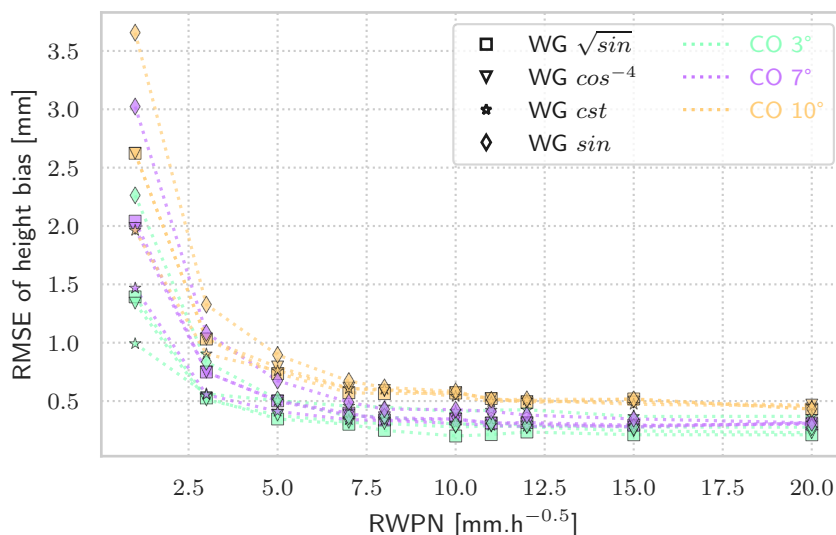


Figure 5.4: **RMSE** of the estimated height biases for each processing modeling applied on simulated signals, as a function of **RWP** for each weighting function and each cut-off angle.

obtained for $co = 10^\circ - wg = sin - rw = 1 \text{ mm} \cdot h^{-0.5}$. The major part of the highest **RMSE** values on height bias is due to the dispersion of the biases rather than its average. Average height biases range from 0 mm to 2 mm when using $co = 3^\circ$ or $co = 7^\circ$, except when using $wg = cst$ occurring at a maximum height bias average of 4 mm with $co = 3^\circ$. For $co = 10^\circ$, the average height biases range from 3 mm to 6 mm, depending on the weighting function and **RWP** modeling. These values are marginal compared to the dispersion of the height bias.

Increasing the **RWP** decreases the height bias **RMSE** for any given cut-off angle and weighting function modeling.

Decreasing the cut-off angle produces a decrease in the height bias and standard deviation **RMSEs**, which is logical because a low cut-off angle permits better height and **ZWD** decorrelation. However, the multipath effect is quite low in the shipborne antenna simulation, requiring a well-placed antenna, for example, at the very top of the vessel.

$wg = sin$ appears to give the worst height bias **RMSE**, while $wg = cst$ and $wg = \sqrt{sin}$ provide similar results to one another in height bias. The use of $wg = cst$ always induces a higher height standard deviation than $wg = \sqrt{sin}$. Although $wg = cst$ systematically gives the best height bias such as seen in Figure 5.4, it appears in Figure 5.5 that the height standard deviation is up to two times worse than when using the other weighting functions.

5.3.3 Sensitivity of **ZWD** Estimation to Processing Modeling

The **RMSEs** of the **ZWD** bias and standard deviation have been computed for each of the processing models and are presented in Figures 5.6 and 5.7.

Figure 5.6 shows that the **ZWD** estimate is also of good quality for all the processing models. As for the height bias in Section 5.3.2, the processing modeling $co = 10^\circ - wg = sin - rw = 1 \text{ mm} \cdot h^{-0.5}$ also gives the highest **ZWD** bias **RMSE**, reaching 1.3 mm, with (-0.1 ± 1.3) mm such as seen in Table B.2 of Appendix B. It appears that

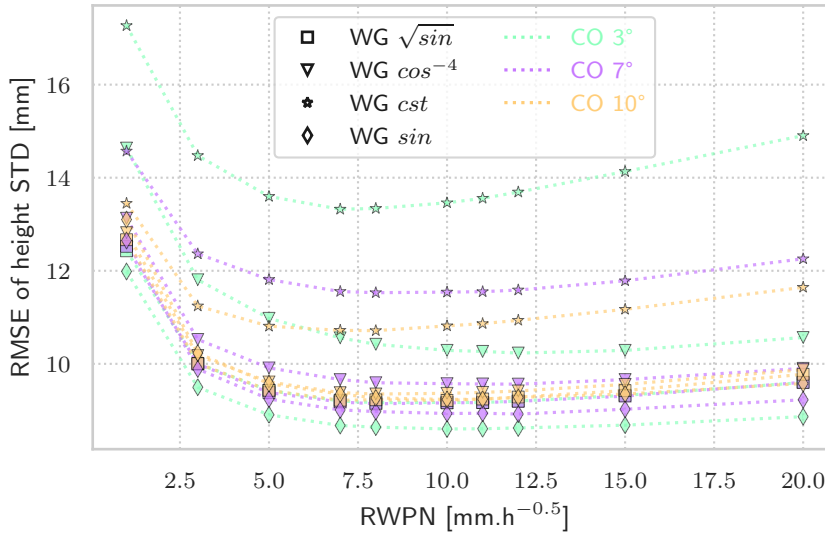


Figure 5.5: **RMSE** of the estimated height standard deviations for each processing modeling applied on simulated signals, as a function of **RWPN** for each weighting function and each cut-off angle.

the average bias is negligible compared to the bias dispersion in the **ZWD** estimation, being less than 0.1 mm, except when using $CO = 10^\circ$, which occurs with an average **ZWD** bias of at most 0.2 mm for all weighting functions but $wg = sin$.

As for the height, increasing the **RWPN** decreases the **ZWD** bias **RMSE** for any given cut-off angle and weighting function modeling. This shows that releasing the constraint on the **ZWD** provides more precision on the height and **ZWD** biases. It corroborates the observations made on ground antennas real data by Young, Blewitt, and Kreemer (2022) [You 22], recommending the use of at least $rw = 6 \text{ mm} \cdot \text{h}^{-0.5}$ to process **GNSS** data.

Decreasing the cut-off angle also produces a decrease in the **ZWD** bias and standard deviation **RMSEs**, corroborating the previous conclusions made on height.

Although $wg = cst$ and $wg = \sqrt{sin}$ provide similar results to one another, the two other weighting functions show different behaviors for the **ZWD** estimation performance from what was seen for the height standard deviation in Figure 5.5. Figure 5.6 shows **ZWD** bias variations according to weighting function and **RWPN** similar to the height biases of Figure 5.4, but the weighting function and the **RWPN** appear closely related in the **ZWD** standard deviation represented in Figure 5.7. While $wg = sin$ performs better in **ZWD** standard deviation than the other weighting functions with high **RWPN** values, the **ZWD** standard deviation is up to twice the others' when the **RWPN** is loosened. $wg = \sqrt{sin}$ and $wg = cst$ proves better with intermediate **RWPN** values to estimate the **ZWD** in terms of standard deviation, with $wg = cst$ being slightly better from around $rw = 8 \text{ mm} \cdot \text{h}^{-0.5}$ especially with $CO = 3^\circ$. $wg = cst$ performs better at very low **RWPN** values, then skyrocketing the **ZWD** standard deviation when the **RWPN** value is loosened.

Table B.2 of Appendix B details the dispersion figures of the standard deviations of the differences between the estimation and the simulation of height and **ZWD**. We can see there that apart from when using modeling implying $rw = 1 \text{ mm} \cdot \text{h}^{-0.5}$ or $wg = sin$, the standard deviation dispersions presented in Table B.2 of Appendix B are very low, most of the time lower than 1 mm, and even lower than 0.5 mm on

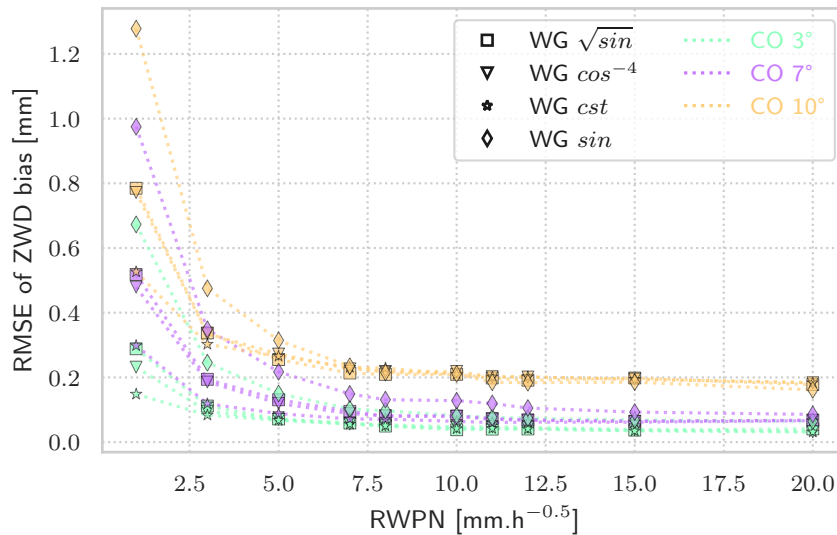


Figure 5.6: RMSE of the estimated ZWD biases for each processing modeling applied on simulated signals, as a function of RWPN for each weighting function and each cut-off angle.

ZWD. It appears that using low RWPN values or increasing the processing cut-off angle increases the variability of the standard deviations on height and ZWD differences, for any elevation weighting function. Although $wg = \sqrt{\sin}$ usually provides lower ZWD standard deviation than $wg = cst$ as for the height estimate, in the case of a RWPN lower than $3 \text{ mm} \cdot \text{h}^{-0.5}$ the weighting function $wg = cst$ achieves a better estimation of ZWD than $wg = \sqrt{\sin}$.

5.4 DISCUSSION ON A SUITABLE PROCESSING MODELING

In light of the observations made in Section 5.3, we will highlight a suitable processing modeling to apply to the shipborne GNSS antenna dataset for atmospheric water vapor study.

5.4.1 Elevation Weighting Function

As depicted later in Section 5.4.3, the effect of the elevation weighting function is closely related to the applied cut-off angle. Taking into account Figure 5.3, $wg = cst$ shows significant deterioration of the height at $co = 3^\circ$ compared to $co = 7^\circ$ and $co = 10^\circ$; the fact that there is almost no change in height precision when changing the cut-off angle, $co = 3^\circ$ even providing the best estimation precision in both cases; and the fact that in Figure 5.3, $wg = cst$ appears to systematically degrade height estimation compared to $wg = \sin$ and $wg = \sqrt{\sin}$ and that $wg = cst$ is even worse in estimating height and ZWD; we can then conclude that if the low elevation data are useful for precisely processing the GNSS measurements, weighting them with an appropriate elevation function is a key processing modeling to obtain better height and ZWD estimations.

Figure 5.3 shows that $wg = cst$ and $wg = cst$ both have the expected increase in the correlation coefficient with the cut-off angle only for $rw = 20 \text{ mm} \cdot \text{h}^{-0.5}$, but curiously show the contrary for the lower RWPN. Therefore, and especially at a low

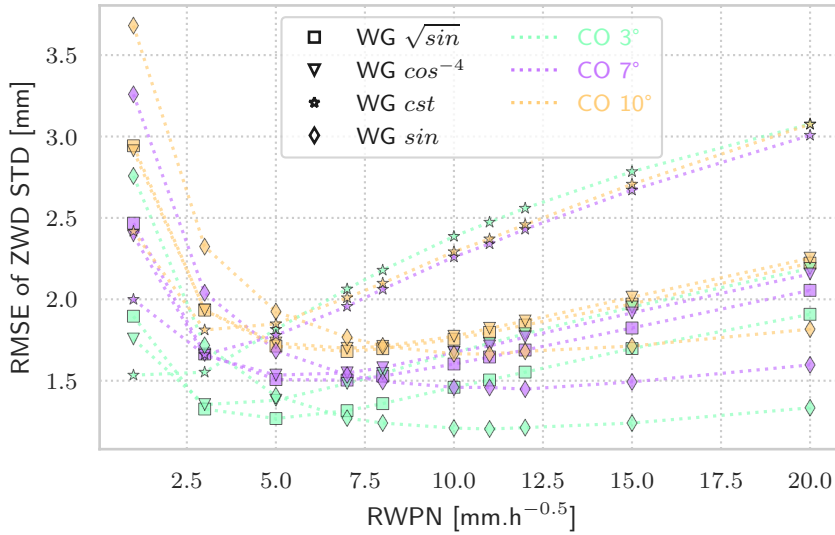


Figure 5.7: RMSE of the estimated ZWD standard deviations for each processing modeling applied on simulated signals, as a function of RWPN for each weighting function and each cut-off angle.

cut-off angle, $wg = \sin$ or $wg = \sqrt{\sin}$ will be preferred to correctly process the data despite the effect of the multipath during the estimation process.

Concerning the height and ZWD estimations, as far as a very low RWPN value decreases the quality of both height and ZWD, we will not focus on $wg = cst$ because it is identically or slightly worse performing than $wg = \sqrt{\sin}$, nor $wg = cst$ that is worse performing than the three other weighting functions for intermediate and higher RWPN values. Therefore, we hereafter focus on the impact of $wg = \sqrt{\sin}$ and $wg = \sin$ on height and ZWD estimation.

Table 5.4 shows the minimum values of the average standard deviation for ZWD and height differences for the three tested cut-off angles, and $wg = \sqrt{\sin}$ and $wg = \sin$.

It is noticeable that all the standard deviation minima presented in Table 5.4 are not obtained with the same RWPN. Therefore, the last column of Table 5.4 presents the RWPN values that provide the minimum standard deviation on ZWD and height for each pair of modeling on the cut-off angle and weighting function.

At a given cut-off angle, the minimum average standard deviation in ZWD is obtained using $wg = \sin$ instead of $wg = \sqrt{\sin}$. However, the differences remain very low, in the 0.1 mm range, and tend to decrease when the cut-off angle increases. For $co = 3^\circ$, the minimum standard deviation obtained by using $wg = \sqrt{\sin}$ is +5.3% higher than when using $wg = \sin$. At $co = 7^\circ$, the rate of change of $wg = \sqrt{\sin}$ is +3.8% higher than $wg = \sin$ and decreases to +0.9% at $co = 10^\circ$. The same conclusion is reached when considering the height estimates. A +6% increase in the average standard deviation of the difference is obtained when using $wg = \sqrt{\sin}$ compared to $wg = \sin$ for $co = 3^\circ$ and +2.5% at $co = 7^\circ$. $wg = \sqrt{\sin}$ even provides a +0.3% better average standard deviation minima than $wg = \sin$ for $co = 10^\circ$. It appears that the choice between $wg = \sin$ and $wg = \sqrt{\sin}$ mainly affects the low-elevation satellite signals; then it decreases with increasing cut-off angle [Had 20].

Table 5.5 further details the ZWD estimate for each of these RWPN values. The three last columns of Table 5.5 show that $wg = \sqrt{\sin}$ is +9.8% better at estimating ZWD than $co = 3^\circ - wg = \sin - rw = 5 \text{ mm} \cdot \text{h}^{-0.5}$. At the minimum, obtained with

Estimate	co	wg	Average STD	ROC	Associated RWPN
	[°]		[mm]	[%]	[mm·h ^{-0.5}]
ZWD	3	<i>sin</i>	1.2		11
		$\sqrt{\sin}$	1.3	+5.3	5
	7	<i>sin</i>	1.4	+20.3	12
		$\sqrt{\sin}$	1.5	+24.9	7
	10	<i>sin</i>	1.7	+38.2	11
		$\sqrt{\sin}$	1.7	+39.5	7
height	3	<i>sin</i>	8.6		10
		$\sqrt{\sin}$	9.2	+6.6	8
	7	<i>sin</i>	8.9	+3.7	12
		$\sqrt{\sin}$	9.1	+6.3	8
	10	<i>sin</i>	9.2	+7.4	10
		$\sqrt{\sin}$	9.2	+7.1	10

Table 5.4: Minima on ZWD and height average standard deviations (STD) for each cut-off and two weighting functions, with the associated RWPN. The rate of change (ROC) is calculated by comparing to the best average standard deviation presented on the first line of both ZWD and height parts.

$co = 3^\circ - wg = \sin - rw = 11 \text{ mm} \cdot \text{h}^{-0.5}$, changing $wg = \sin$ by $wg = \sqrt{\sin}$ degrades the estimate of ZWD by +28.2%. In general, the rate of change between $wg = \sqrt{\sin}$ and $wg = \sin$ decreases when the cut-off angle increases, but the ZWD standard deviations also increase compared to $co = 3^\circ$.

The use of $wg = \sin$ implies the need to use a model that doubles the simulation used RWPN for a better estimation. $wg = \sqrt{\sin}$ appears to work well with lower RWPN, such as $rw = 5 \text{ mm} \cdot \text{h}^{-0.5}$ for $co = 3^\circ$ and $rw = 7 \text{ mm} \cdot \text{h}^{-0.5}$ for higher cut-off angles, instead of $rw = 11 \text{ mm} \cdot \text{h}^{-0.5}$ to $rw = 12 \text{ mm} \cdot \text{h}^{-0.5}$ for obtaining the minimum standard deviation with $wg = \sin$. As ZWD was simulated with a $5 \text{ mm} \cdot \text{h}^{-0.5}$ RWPN, $rw = \sqrt{\sin}$ seems to remain consistent with the temporal variability of atmospheric water vapor compared to $wg = \sin$. Indeed, Table 5.6 shows that for the three cut-off angle values tested, $wg = \sqrt{\sin}$ performs around +10% better in estimating the ZWD than $wg = \sin$ when using $rw = 5 \text{ mm} \cdot \text{h}^{-0.5}$. The height estimation with $wg = \sqrt{\sin}$ at $rw = 5 \text{ mm} \cdot \text{h}^{-0.5}$ does not change with the elevation cut-off angle. However, $wg = \sin$ performs better at low elevation cut-off angle, showing an improvement of +5.9% at most for $co = 3^\circ$. Both weighting functions give similar results to the rate $\pm 1.5\%$ for the other two cut-off angles.

As far as the weighting function performance depends on the RWPN model, it is necessary to study further the RWPN impact on the height and ZWD estimation.

Estimate	co [°]	RW [mm·h ^{-0.5}]	Average STD [mm]		ROC
			<i>sin</i>	$\sqrt{\sin}$	
ZWD	3	11	1.2	1.5	+28.2%
		5	1.4	1.3	-9.8%
	7	12	1.4	1.7	+16.6%
		7	1.5	1.5	-1.9%
	10	11	1.7	1.8	+8.0%
		7	1.8	1.7	-4.8%

Table 5.5: Average ZWD standard deviations obtained for $wg = \sin$ and $wg = \sqrt{\sin}$ for each of the underlined configurations of Table 5.4. The rate of change (ROC) of the ZWD estimate obtained with $wg = \sqrt{\sin}$ compared to $wg = \sin$ is given in the last column.

Estimate	co [°]	Average STD [mm]		ROC
		<i>sin</i>	$\sqrt{\sin}$	
ZWD	3	1.4	1.3	-9.8%
	7	1.7	1.5	-10.4%
	10	1.9	1.7	-11%
height	3	8.9	9.4	+5.9%
	7	9.2	9.4	+1.5%
	10	9.5	9.4	-1.5%

Table 5.6: ZWD and height average standard deviations for each cut-off and two weighting functions, for $rw = 5 \text{ mm} \cdot \text{h}^{-0.5}$. The rate of change is calculated by comparing $wg = \sqrt{\sin}$ to $wg = \sin$.

5.4.2 RWPN on ZWD

As seen in Section 5.3.1, the correlation coefficient for $co = 3^\circ$ and $rw = 5 \text{ mm} \cdot \text{h}^{-0.5}$ is 0.45 with $wg = \sqrt{\sin}$, while it is as low as 0.33 when using $wg = \sin$. However, $wg = \sin$ also shows a correlation coefficient of 0.45 as the previous $rw = \sqrt{\sin}$ with its nominal RWPN of $rw = 10 \text{ mm} \cdot \text{h}^{-0.5}$ at $co = 3^\circ$.

The minimum value of the ZWD standard deviation RMSE in Figure 5.7 is obtained with $wg = \sin$ from $rw = 10 \text{ mm} \cdot \text{h}^{-0.5}$ to $rw = 12 \text{ mm} \cdot \text{h}^{-0.5}$, depending on the cut-off angle, such as seen in Table 5.4. Then it appears that the ZWD average standard deviation is better when loosening the RWPN compared to the simulation value. As an approximation, we can state that $wg = \sin$ needs to loosen the RWPN twice to minimize the standard deviations of the differences to be best performing.

Young, Blewitt, and Kreemer (2022) [You 22] have observed that processing GPS PPP data with GipsyX software (JPL, NASA [Ber 20]) requires increasing the RWPN to at least $rw = 6 \text{ mm} \cdot \text{h}^{-0.5}$ from the default $rw = 3 \text{ mm} \cdot \text{h}^{-0.5}$. This could be explained by the fact that the data were processed using $wg = \sin$, which requires a

higher *RWPN* to detect the variability of *ZWD*, according to the above results. The same study could then be conducted using $wg = \sqrt{\sin}$ to validate the simulation results and to try to acquire a suitable *GPS* positioning through a more accurate physical model.

Selle and Desai (2016) [Sel 16] have presented a similar observation. They recommend $rw = 8.4 \text{ mm} \cdot \text{h}^{-0.5}$ when using $wg = \sin$, whereas $rw = 5.4 \text{ mm} \cdot \text{h}^{-0.5}$ is needed when processing with $wg = \sqrt{\sin}$ for the same ground *GNSS* antenna dataset. Then it seems that the shipborne simulation of the *GNSS* antenna corroborates these ground antenna observations with a rise in processing the *RWPN* needed when using $wg = \sin$.

Table B.2 of Appendix B shows that the standard deviation of the 200 differences between estimation and simulation for each processing model is low on average, but its variation is significant and shows a convex shape shown in Figure 5.3 for the height and *ZWD* estimates as a function of *RWPN*. This means that there is a nominal *RWPN* modeling to process the *GNSS* data passing through a $5 \text{ mm} \cdot \text{h}^{-0.5}$ *ZWD* varying simulated troposphere.

Figures 5.4 and 5.6 also show that $wg = \sin$ degrades the accuracy of height and *ZWD* estimation compared to $wg = \sqrt{\sin}$ and $wg = \text{cst}$. $wg = \text{cst}$ appears to be the best performing weighting function model, except with a low cut-off angle of $co = 3^\circ$, where it results in the worst height estimation for *RWPN*s higher than $5 \text{ mm} \cdot \text{h}^{-0.5}$, and it is the worst performing model according to the height standard deviation in Figure 5.5. On the face of it, to accurately estimate height and *ZWD* we recommend favoring $wg = \text{cst}$ or $wg = \sqrt{\sin}$ when using *GNSS* measurements at low elevation angles with a *RWPN* around $rw = 5 \text{ mm} \cdot \text{h}^{-0.5}$ or above. This is also consistent with the best resulting processing of real dataset case study of Chapter 4, obtained for a *RWPN* model of 3 to $5 \text{ mm} \cdot \text{h}^{-0.5}$.

To conclude on the weighting function modeling in light of the *RWPN* study, $wg = \sqrt{\sin}$ then seems to be a decent compromise to achieve the best *ZWD* possible for meteorology purposes while staying coherent with the physical process. It is important to keep in mind that at low elevation cut-off angles, this weighting function does not provide the optimal height as with $wg = \sin$ which will likely provide a slightly better height estimate.

5.4.3 Cut-Off Angle

The average standard deviation shown in the fourth column of Table 5.4 shows that the configuration that gives the closest *ZWD* and height estimates to the reference is $co = 3^\circ - wg = \sin - rw = 11 \text{ mm} \cdot \text{h}^{-0.5}$. The rate of change shows that the increase in the cut-off angle induces an increase in the standard deviation of the *ZWD* differences up to +20.3 % for $co = 7^\circ$ and +38 % for $co = 10^\circ$. The height results also show that increasing the cut-off angle decreases the resulting minimum in the average standard deviation of the height difference, with a change rate of +3.7 % for $co = 7^\circ$ and +7.4 % for $co = 10^\circ$.

Regarding the cut-off angle, Figure 5.3 shows that in the case of $wg = \sin$ or $wg = \sqrt{\sin}$ modelings, decreasing the cut-off angle decreases the correlation between height and *ZWD*. This is consistent with the real data study giving the best results when using low cut-off angles in Section 4.2.1.

On the other hand, Figures 5.4 and 5.3 show that the increase in cut-off angle significantly degrades the accuracy of the height and ZWD estimations and the precision of the ZWD estimation, for any weighting function. Figure 5.3 shows in turn that interestingly the height precision is improved for high cut-off angles with $wg = cst$ and $wg = cst$, whereas the height precision is very slightly improved for low cut-off angles with $wg = sin$ and is not affected by the cut-off angle choice with $wg = \sqrt{sin}$.

5.4.4 Recommended Modeling

For the rest of the study, we then selected $co = 3^\circ - wg = \sqrt{sin} - rw = 5 \text{ mm} \cdot h^{-0.5}$ as a configuration to process GNSS data of a shipborne antenna placed at the highest point of the vessel. This processing provides an RMSE of the difference between the estimates and the simulation of 9.4 mm on the height and 1.3 mm on the ZWD.

5.5 IMPACT OF SIMULATION FEATURES ON PROCESSING

To assess the impact of the simulation features on the shipborne GNSS data processing, we have simulated new signals different from the previous study. The new simulated carrier phase signals were processed using the strategy recommended from Section 5.4.4, and the statistics of the difference between the estimation and the simulation of these new signals were compared to the statistical results of the reference dataset presented above.

5.5.1 Summary of the Studied Features

This study would not be complete unless we study the impact of the acquisition features on the solution. This is why more simulations have been created, with one feature in each new simulation that is different from the previous one, now referred to as *reference simulation*, whose features are recalled in Table 5.7 along with the new tested feature.

These simulations lead to 13 new studies, that will involve the features described in Sections 5.5.2 to 5.5.5. For each of them, we performed the processing on 200 new datasets before computing the statistics of the difference with the simulated quantities, as we did for the reference simulation.

5.5.2 Data Sampling

For purposes of data management and storage, or processing time reduction, we studied as well the impact of lower time resolution processing. Then we processed the reference simulated dataset by taking into account only one datum out of ten. This leads to a study of the difference in results between a relatively high time resolution of 30 s and a high time resolution of 5 minutes.

This reduction in processing resolution might produce a decrease in the processing estimation accuracy.

We investigate the impact of data sampling on the estimation of ZWD and height. Thus, we consider downsampling GNSS raw data to 300 s instead of 30 s previously. This lower-resolution PPP processing leads to a degradation of the estimates. In fact,

Parameter Investigated	Reference Simulation Features	New Feature	Section
Constellations	GPS, GLONASS, Galileo	GPS only	5-5.3
Time resolution	30 s	300 s	5-5.2
Location (ZWD RWPN)	Mid-latitudes ($5 \text{ mm} \cdot \text{h}^{-0.5}$)	1. latitude ($2 \text{ mm} \cdot \text{h}^{-0.5}$) 2. latitude ($10 \text{ mm} \cdot \text{h}^{-0.5}$)	80° 10° 5-5.5
Antenna orientation	None	1. North-oriented 2. Oriented to 45° 3. Runs in a circle	5-5.4
PCV correction	Perfectly corrected	1. None 2. Regular 3. Azimuthal mean	5-5.4

Table 5.7: New simulation features tested with regards to the reference simulation.

with the recommended modeling of $\text{co} = 3^\circ - \text{WG} = \sqrt{\sin} - \text{RW} = 5 \text{ mm} \cdot \text{h}^{-0.5}$, the average standard deviation of the difference between estimates and simulation increased by +11.9 % in height and +43.9 % in ZWD as shown in Table 5.8.

Estimate	30 s ref [mm]	300 s [mm]	ROC
ZWD	1.3	1.8	+43.9 %
Height	9.4	10.5	+11.9 %
Correlation	0.45	0.62	+37 %

Table 5.8: Height and ZWD average standard deviation results for data sampling study. Ref. stands for the reference simulation.

Table 5.8 also shows that the decrease in resolution creates an increase of +37 % in the correlation coefficient for the selected processing configuration. It appears that using thinner time resolution also provides better decorrelation between the two estimates in the GNSS processing.

We can then conclude that using high-resolution data sampling is important for obtaining better results on a PPP processing of shipborne antennas.

5.5.3 GNSS Constellations

Managing a high amount of data might be eventually challenging at sea, involving costly voluminous storage boxes or sending devices to ground-based storage. Indeed, it might be impossible to log all the available constellations raw GNSS data. It is then possible to record only one constellation dataset. Also, this is sometimes mandatory as older receivers provide GPS-only measurements. By processing the reference dataset taking into account only the GPS-provided observations, we will be able to assess the

impact on the **ZWD** and height accuracy compared to the reference multi-constellation simulation.

This change will affect the satellite geometry and the number of observations will significantly decrease. This reduction of available observations might produce a drop in the processing estimation accuracy.

Unlike the reference simulation performed with three constellations (**GPS**, **GLONASS**, and **Galileo**), we are considering only **GPS** observations here. Using only **GPS** satellites induces a degradation of the estimation, as shown in **Table 5.9**. Indeed, the average

Estimate	Multi-GNSS ref [mm]	GPS-Only [mm]	ROC
ZWD	1.3	1.9	+51.1 %
Height	9.4	15.1	+59.8 %
Correlation	0.45	0.40	-12.8 %

Table 5.9: Height and **ZWD** average standard deviation results for **GNSS** constellation study.

standard deviation increases by +59.8 % for the height estimate and +51.1 % for the **ZWD**.

However, **GPS**-only height bias is almost twice better than multi-constellation with $wg = cst - RW = 5 \text{ mm} \cdot h^{-0.5}$ but is still not better than the reference simulation with the recommended processing model. The multi-constellation processing is better at estimating the **ZWD** than the **GPS**-only processing in all the configurations tested.

Then, if several constellations are available, it might be very important to use all of them to reduce the estimation error, with an improvement that can reach a factor of two. On the other hand, the mean correlation coefficient between **ZWD** and height is slightly better when using only **GPS**, with an improvement of +12.8 % compared to multi-**GNSS** processing. This effect seems to be contrary to common sense, so it might be the first evidence of some weaknesses of our simulation.

5.5.4 Antenna Phase Center Variation

The **PCV** antenna effect is under study in another new simulation dataset. Previously, we simulated the **PCV** error affecting each visible satellite while the **R/V** was operating within three different behaviors:

- an antenna that is always well oriented to the North, thus corresponding to the reference simulation dataset;
- an antenna that has a constant bias of orientation from the North, such as a constant heading vessel;
- an antenna that is moving through time, such as the boat turning around, performing a 360° over 24 h.

The simulated **PCV** error has been modeled as a Trimble antenna TRM 105 000.10 - NONE, illustrated in **Figure 2.5** for each of the three studied **GNSS** constellations. This noise is given to the **PCV** term of the carrier-phase error $pcv_s^{LC}(az^i, el^i)$ in Equation (5.2).

This study involved a second aspect, concerning the way of correcting the **PCV** effect on the measurement. Three different means have been tested on each of the datasets from the three **R/V** routes listed above:

- no **PCV** correction is applied at all;
- the **PCV** correction is applied considering that the antenna is always pointing toward the North;
- the azimuthal mean of the **PCV** has been computed, resulting in an elevation-dependent correction only.

The **PCV** correction is applied to the simulated dataset before performing the Kalman filtering.

The first simulated **R/V** route behavior toward the North, along with the second correction applied considering a North-oriented antenna, corresponds to the reference simulation with a perfectly corrected **PCV** effect. Then these new simulations with the different correction methods led to eight new studies about the impact of **PCV** effect and its correction.

The impact of the **PCV** of the receiver antenna added to the reference simulation of **GNSS** observation is studied here.

Table 5.10 summarizes the average **ZWD** and height biases obtained with each of the **PCV** antenna configurations. The displayed values correspond to the difference with the reference simulation results that provided near zero average biases such as seen in Appendix B. The North correction of the antenna **PCV** when heading North does

Mvmt	To North		45° North		Turning	
	Height	ZWD	Height	ZWD	Height	ZWD
Avg Bias [mm]						
No correction	-8.5	-1.1	+6.2	+1.3	+9.0	+1.8
North correction	<i>ref.</i>	<i>ref.</i>	-1.8	-0.2	+1.0	+0.3
Azimuthal mean	-0.9	-0.2	+2.7	+0.4	+0.1	+0.1

Table 5.10: Average height and **ZWD** biases for different antenna movements (Mvmt) over 24 h, processed with different antenna correction methods. The reference simulation is annotated as *ref.* in the table.

not apply as it corresponds to the reference simulation, marked as *ref.* in Table 5.10.

The absence of antenna correction induces a height bias of almost 10 mm depending on the horizontal movement of the **R/V**. The bias on **ZWD** is lower, around 1 mm. The application of the North correction reduces these biases by dividing them by 10, with a decrease in the bias to around 1 mm on height and 0.2 to 0.3 mm on **ZWD**. The North correction is slightly better than the azimuthal mean correction when the heading is constant, whatever the direction. This means that the heading of the vessel affects the estimation in the case of a linear path with an azimuthal correction. However, the

azimuthal mean correction performs well in correcting the bias of the PCV antenna for more complicated vessel displacements, such as when the R/V is constantly turning around over 24 h. The biases are then decreased to 0.1 mm on both height and ZWD, which is two orders of magnitude better than with no correction.

Table 5.11 shows the change in the average standard deviations of height and ZWD for each antenna configuration and correction, compared to the reference simulation, using the recommended modeling configuration.

Mvmt STD	To North		45° North		Turning	
	Height	ZWD	Height	ZWD	Height	ZWD
No cor- rection	+7.6 %	+10.6 %	+5.4 %	+11.7 %	+9.9 %	+22.0 %
North correc- tion	<i>ref.</i>	<i>ref.</i>	+4.1 %	+10.0 %	+6.1 %	+16.6 %
Azimuthal mean	+3.3 %	+6.1 %	+2.4 %	+3.9 %	+4.3 %	+8.4 %

Table 5.11: Height and ZWD average standard deviation increase rate compared to reference processing, for different antenna movements (Mvmt) over 24 h, processed with different antenna correction methods in the selected configuration.

Without correction of the antenna effect, the average standard deviation increases by less than +10 % on height up to +22 % on ZWD for the turning antenna. Applying a correction using a North-oriented PCV map lowers the average standard deviation in height and ZWD. Contrarily to the bias, in all the cases both average standard deviations improve when applying an azimuthal mean correction.

The azimuthal mean correction then appears to be a good alternative to correct the antenna PCV to balance the unknown changing horizontal orientation of the antenna through time.

5.5.5 Latitude

A change in latitude would have an impact on the satellite geometry. This would result, at high latitudes, to a lack of satellites near the zenith of the antenna. This can have two effects:

- most of the observation data are more affected by the multipath effect, and they are given less weight in the Kalman Filter, lowering the availability of highly reliable observed information;
- the cut-off angle is removing a large part of the observations that are too low above the horizon, thus limiting the number of available data at each time step.

To study this effect on the processing accuracy, we have made new simulations with two new antenna positions:

- In the polar region (80° N);
- In the Tropical region (10° N).

Moreover, the change in latitude implies a change in the **ZWD** variations as well [Had 17]. The reference simulation has been made at mid-latitude ($45^\circ N$) with a medium variability, using a simulation **RWPN** of $5 \text{ mm} \cdot \text{h}^{-0.5}$. Thus, the above-mentioned new simulations have been performed with different **RWPN** values, taking into account that the variability in water vapor content must be lower in Polar regions ($2 \text{ mm} \cdot \text{h}^{-0.5}$), and can be higher in Equatorial regions ($10 \text{ mm} \cdot \text{h}^{-0.5}$). This change in simulation **RWPN** might have an impact mainly on the best-performing **RWPN** model within the processing.

Here, we study the impact of the change in the latitude of the **R/V** while acquiring the data.

Estimating the **ZWD** and height at these latitudes increases the average standard deviation of height of $+29.2\%$ and $+9.7\%$ for latitudes of 10° and 80° , respectively, as shown in Tables 5.12 and 5.13. The **ZWD** average standard deviation increases by $+48\%$ at 10° of latitude and decreases by -10.9% at 80° of latitude.

Estimate	Mid-Latitudes [mm]	Equatorial reg [mm]	ROC
ZWD	1.3	1.9	$+48.0\%$
Height	9.4	12.2	$+29.2\%$
Correlation	0.45	0.46	$+1.7\%$

Table 5.12: Height and **ZWD** average standard deviation results for study at low latitude (10°).

Estimate	Mid-Latitudes [mm]	Polar reg. [mm]	ROC
ZWD	1.3	1.1	-10.9%
Height	9.4	10.3	$+9.7\%$
Correlation	0.45	0.45	-0.1%

Table 5.13: Height and **ZWD** average standard deviation results for study at high latitudes (80°).

It is worth noting that the estimation of the 10° of latitude signal with $\text{rw} = 10 \text{ mm} \cdot \text{h}^{-0.5}$ instead of the recommended $\text{rw} = 5 \text{ mm} \cdot \text{h}^{-0.5}$ gives an increase in the **ZWD** average standard deviation of only $+23\%$ compared to the reference simulation with the recommended model. This is half the increase with processing at $\text{rw} = 5 \text{ mm} \cdot \text{h}^{-0.5}$. The decrease at latitude 80° hits -31% with processing at $\text{rw} = 3 \text{ mm} \cdot \text{h}^{-0.5}$ instead of the recommended $\text{rw} = 5 \text{ mm} \cdot \text{h}^{-0.5}$. Then it appears that using a suitable **RWPN** for the region of study allows for better results than keeping a medium value by default. However, it may be difficult to adapt the **RWPN** processing to the region where the vessel operates, as it is moving all the time, and the mean **RWPN** depends on seasons and years and is not uniform at a given latitude [Had 17].

Changing the latitudes does not appear to have a significant effect on the mean correlation coefficient. Then, the geometry of the satellites does not seem to be a major issue for the **GNSS** processing.

A more chaotic *ZWD* is more difficult to catch. This may explain why the results are better for low *RWPN* simulated *GNSS* signals. It is relevant to use a *RWPN* as close as possible to the *ZWD* variations at the location of the study. If possible, models or reanalysis could be used to determine an approximate value of the *RWPN* at the antenna location. However, $5 \text{ mm} \cdot h^{-0.5}$ still gives suitable results for all latitudes, so this mean value can be an adequate compromise for processing shipborne datasets coming from vessels that are sailing all around the world, at all latitudes.

5.6 CONCLUSION ON THE SIMULATED SHIPBORNE GNSS PROCESSING MODELING

In this chapter, we simulated shipborne *GNSS* measurements to assess the impact of the modeling strategy on the estimation. We applied a Kalman filtering of the simulated *GNSS* measurements to highlight a standing-out processing configuration for *PPP* shipborne *GNSS*.

The use of a low cut-off angle such as $\text{CO} = 3^\circ$ is shown to provide rather conclusive results, since the use of low elevation measurements permits decorrelating *ZWD* and height estimates, then improving the whole estimation process. Although $\text{WG} = \sin$ gave good estimates of *ZWD* and height, it appears that $\text{WG} = \sqrt{\sin}$ better describes the physical behavior of the *ZWD*. Indeed with $\text{WG} = \sin$, the processing *RWPN* needs to be raised compared to the simulation *RWPN*, to obtain the best *ZWD* estimate. $\text{WG} = \sqrt{\sin}$ function then appears to be the best compromise between representing physical processes and obtaining a suitable estimation in *PPP* processing. Using an *RWPN* adapted to the *ZWD* variations in the zone under study will provide a better height and *ZWD* estimation. The use of $\text{WG} = \sqrt{\sin}$ will require the use of a mean value $\text{RW} = 5 \text{ mm} \cdot h^{-0.5}$ for a far-moving vessel, that still stays suitable under any latitudes. However, the use of $\text{WG} = \sin$ model will require doubling the *RWPN* to obtain a better estimation, according to the simulation results.

We also studied the impact of the data acquisition conditions on the solution. The processing of the simulated shipborne *GNSS* gives a +22 % better estimation of the *ZWD* when using *GPS*, *GLONASS*, and Galileo, instead of *GPS* only. It is worth processing all the available constellations to obtain a broader dataset and a wider satellite geometry, although *GPS* still gives satisfying results by itself. If the time-dependent orientation of the antenna is not known, we also recommend applying an azimuthal mean antenna *PCV* correction, that depends only on the elevation of the observed satellite. As the vessel does not face North, such as a ground *GNSS* antenna, this method allows adaptation of the antenna effect correction to any heading of the boat, improving the *ZWD* estimate of +7 % compared to a usual *PCV* correction. Finally, reducing the temporal resolution gives better results in the estimation. We would then recommend using at most 30 s of resolution for processing the shipborne *GNSS* data whenever possible.

The whole simulation relies on a simplified model of the shipborne *GNSS* carrier phase measurement. For example, no horizontal movement of the boat was simulated. This could be implemented for further study.

The recommended processing model will further be applied to long-lasting datasets from five of the *FOF R/Vs*, studied in [Chapter 6](#).

WATER VAPOR MONITORING DURING THE FRENCH OCEANOGRAPHIC FLEET CAMPAIGNS BETWEEN 2015 AND 2022

The results made on a the real dataset under the simple acquisition conditions of a teaching hydrographic vessel detailed in [Chapter 4](#) and those from the simulated dataset detailed in [Chapter 5](#) both indicate an actual possible effect on the estimation accuracy when tuning the processing model. The study on real dataset enlighten the best performance of low cut-off angle and [RWP](#) values, and disqualify the weighting function modeling with \sin . Meanwhile, the study on simulations allows us to reveal the same effect of the processing configuration for larger research vessels sailing in the middle of the sea. The recommended shipborne [GNSS PPP](#) processing modeling from these simulations is $\text{CO } 3^\circ - \text{WG } \sqrt{\sin} - \text{RW } 5 \text{ mm} \cdot \text{h}^{-0.5}$.

This Part is about the [PPP](#) processing of the [FOF GNSS](#) datasets from 2015 to 2022 of five open-sea research vessels: Alis, Antea, L'Atalante, Pourquoi Pas?, and Thalassa. We have processed these [GNSS](#) datasets using the recommended modeling from previous part, and retrieved the precipitable water vapor. We compared it to other sources of water vapor measurement, and finally studied the assessed long-term water vapor trend to the edge of climate changes.

The future prospects following the satisfying results obtained in this section would be to adapt the automated processing strategy of raw shipborne [GNSS](#) dataset to real-time issues.

ASSESSMENT OF THE FRENCH OCEANOGRAPHIC FLEET DATASET

CONTENT

6.1	Data and Methods	101
6.1.1	The French Oceanographic Fleet: A Diverse Shipborne GNSS Dataset	101
6.1.2	Shipborne GNSS PPP processing method	103
6.1.3	PWV Comparison Datasets	107
6.2	Evaluation of Shipborne GNSS PWV Results	112
6.2.1	External PWV Dataset Comparison	112
6.2.2	Result of Comparison between R/Vs	118
6.3	Conclusion on the FOF Processing	119

This chapter relies on the processing of five shipborne GNSS datasets from FOF R/Vs provided by IFREMER, from 2015 to 2022. The datasets have been processed using the recommended processing model after Chapter 5. The resulting ZWD time series quality is assessed by comparing it to other atmospheric water vapor measurement datasets.

The preliminary work from this study constituted an oral presentation at the American Geophysical Union (AGU)22 in Chicago (USA) in December 2022 [Pan 22c].

6.1 DATA AND METHODS

6.1.1 *The French Oceanographic Fleet: A Diverse Shipborne GNSS Dataset*

The FOF is the result of the unification of the R/Vs and underwater and surface vehicles for marine observation and study belonging to its four French founding research organizations: Centre National de la Recherche Scientifique (CNRS), IFREMER, Institut polaire français Paul-Émile Victor (IPEV), and Institut de Recherche pour le Développement (IRD). The FOF is operated by IFREMER for 80 % of the time, and the SHOM for 20 %. The research vessels are numerous and have different purposes. Among the deep sea R/Vs, we will focus on the GNSS datasets from Alis, Antea, L'Atalante, Thalassa, and Pourquoi Pas?. GNSS observation data from 242 campaigns cover a total of 3287 days and take place in four oceans of the globe from 2015 to 2022. More specifically, Alis has been involved in 51 campaigns with an antenna replacement at the end of year 2019, Antea has been involved in 49 campaigns for a total of 390 days, L'Atalante has been involved in 66 campaigns with an antenna replacement at the end of summer 2019,

Thalassa has been involved in 32 campaigns, and Pourquoi Pas? has been involved in 44 campaigns.

The trajectories of the R/Vs are drawn on the map of [Figure 6.1](#), while the campaigns are detailed in [Appendix C](#).

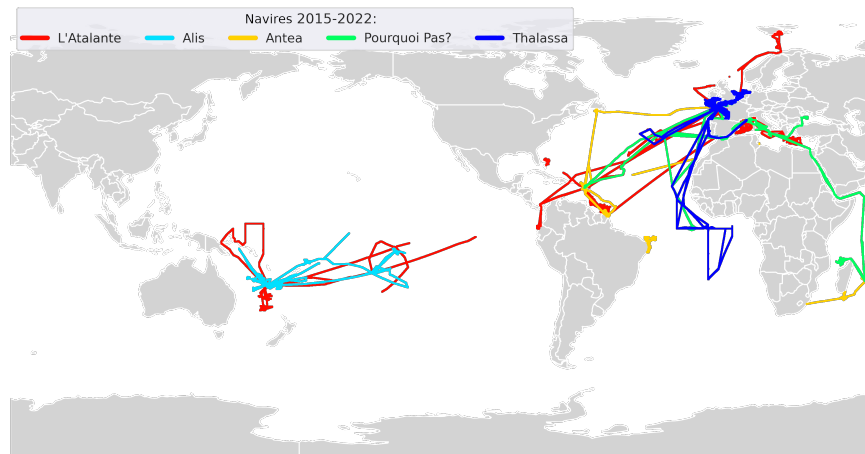


Figure 6.1: Map showing the trajectories of each of the FOF R/Vs recorded from 2015 to 2022. The red corresponds to L'Atalante, cyan corresponds to Alis, yellow corresponds to Antea, green corresponds to Pourquoi Pas?, and blue corresponds to Thalassa.

As we can see in [Appendix C](#), Thalassa mainly operates in the North Sea, the English Channel, the North-Western Mediterranean Sea, and the Eastern Atlantic Ocean, from the Azores to the middle of the South Atlantic Ocean passing by the African coast and mostly the Celtic Sea and the Bay of Biscay; Pourquoi Pas? operates from the Western Europe Coast to the Caribbeans and by the West African coast in the Atlantic Ocean, the Mediterranean Sea up to the Black Sea, and down to the Western Indian Ocean passing by the Red Sea; Antea operates in the Atlantic Ocean from France to the East to Saint-Pierre-et-Miquelon to the West, down to the West Indies by the Atlantic and the Caribbean Sea, off the Brazilian coast, the middle of the Atlantic Ocean from the Moroccan coast to the Caribbeans, and in the Western Indian Ocean from La Réunion to the South of the Mozambique canal to study the so called Agulhas current; Alis operates in the South Pacific Ocean, from New Caledonia to the French Polynesia; L'Atalante operates in the South Pacific Ocean like Antea, passing by the Panama canal, the Caribbean Sea and the West Indies, the North Atlantic Ocean, the Mediterranean Sea, the English Channel, the North Sea, and the Barents Sea up to Svalbard. The amount, variety, and length of the available dataset ensure a wide range of sea and weather conditions during the study and the originality of this study. This dataset is wide, rich, and very complete, giving access to many areas of study for the atmosphere water vapor.

The R/Vs are not operated continuously, and data from Pourquoi Pas? and Thalassa have been provided from 2019 only, compared to the three other R/Vs, as we can see in [Figure 6.2](#).

These graphs show for each of the five R/Vs, the time series availability of ZWD data from 2015 to 2022, after the screening detailed in [Section 6.1.2](#). Besides Thalassa and Pourquoi Pas?, the year 2017 is empty of data for L'Atalante, and Antea has no data in 2015, 2020, and 2022. The other years are not fully complete, with blocks of data acquisition spaced out with blank periods. For example, Alis has spent more

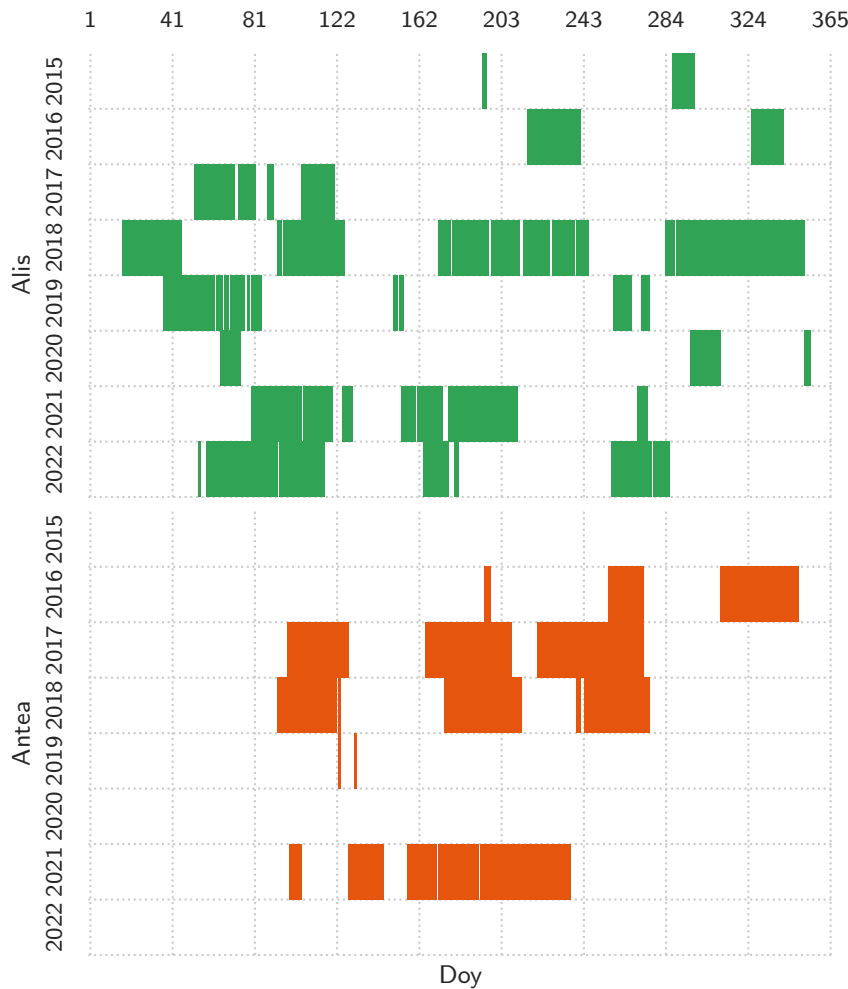


Figure 6.2: Time series of the FOF R/V records from 2015 to 2022 - [to be continued 1/3]. The green corresponds to Alis, orange corresponds to Antea. Antea has no dataset in 2015, 2020, and 2022. See the next pages for the following of the Figure, with other R/V time series.

time acquiring data in 2018 than the other years, and the years from 2015 to 2017, as well as 2020, have provided few campaigns. Also, Antea shows only two thin sets of acquisitions in 2019. 2016 and 2018 have been fruitful years for L'Atalante, and all five R/Vs show a major break in the middle of the Covid-19 year in 2020. Pourquoi Pas? and Thalassa show a high amount of data acquisition during the four years of the provided data.

The FOF dataset was full of GPS observations, but the other constellations were not provided. The study then relies on the GPS observations only.

6.1.2 Shipborne GNSS PPP processing method

As a following version of GIPSY-OASIS II (see Section 4.1.3), GipsyX was used to kinematic PPP process the FOF GNSS dataset. GipsyX provides GPS and GLONASS attitude models, and preliminary attitude models for Galileo and BDS. Its features include single receiver ambiguity resolution using JPL's orbit and clock products for GPS, and

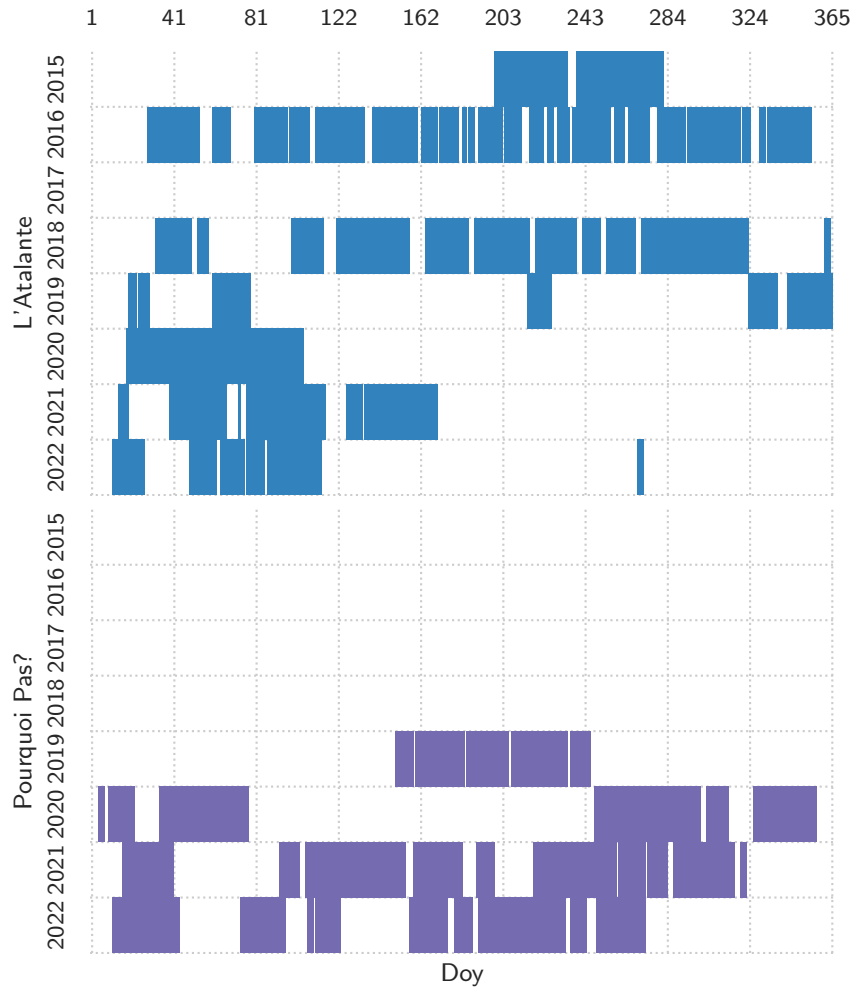


Figure 6.2: Timeseries of the FOF R/V records from 2015 to 2022. - [continued 2/3]. The blue corresponds to L'Atalante, purple corresponds to Pourquoi Pas?. L'Atalante has no dataset in 2017. Pourquoi Pas? has no dataset before 2019. See the previous and next page for the following of the Figure, with the other R/V time series.

sophisticated filter and smoother with flexible process noise modeling. The kinematic processing was performed on a 30 s-resolution basis.

The applied processing model follows the recommendations of Section 5.4.4: $co = 3^\circ - wg = \sqrt{sin} - rw = 5 \text{ mm} \cdot h^{-0.5}$. VMF1 is used to compute the tropospheric delay and the gradients.

The PCV correction has been made using an-elevation-dependent-only PCV map created from the National Geodetic Survey (NGS) PCV maps averaged over the azimuth.

The ocean load has been disabled because GipsyX does not handle its computation for a moving antenna, which is the case in the middle of the ocean. Then, the height measurement on the antenna might not correspond to other measurements of SSH. We will then focus here only on the study of the PWV derived from the shipborne GNSS retrieved ZWD following Equation (2.55) by comparing to other more conventional PWV datasets.

The ZWD is computed from the ZTD estimated during the processing of the shipborne GNSS dataset and the ZHD estimated by ERA5 of the ECMWF following Section 2.3.3.3. The PWV is derived from the resulting ZWD by using the mean temperature T_m from

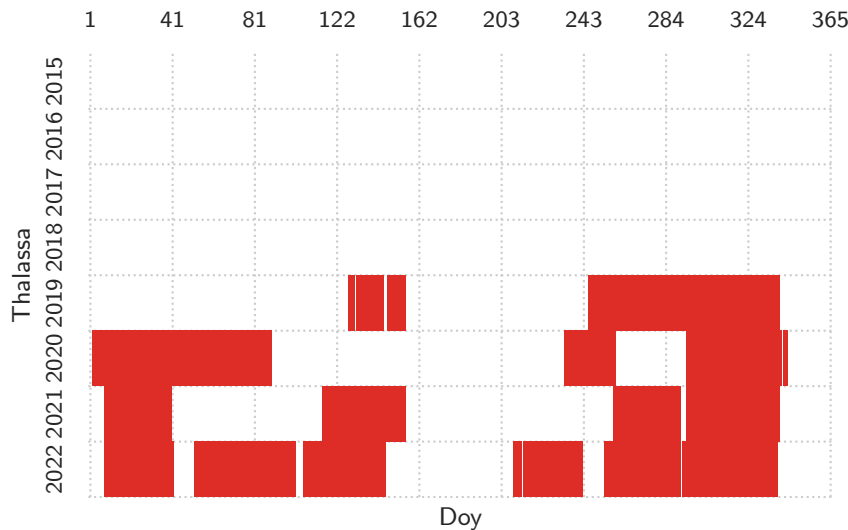


Figure 6.2: Timeseries of the FOF R/V records from 2015 to 2022. - [continued 3/3]. The red corresponds to Thalassa. Thalassa has no dataset before 2019. See the previous page for the following of the Figure, with the other R/V time series.

Technische Universität Wien (TUW). Moreover, following [Boc 20], a screening is performed to remove the outliers from the dataset, as they did in Bosser, Van Baelen, and Bousquet (2022) [Bos 22b]. The screening is performed through several steps:

1. a range-check is performed on the positioning GNSS formal error, removing the data with an error higher than 0.1 m;
2. a range-check is performed on the ZTD values that are removed when higher than 3 m and lower than 2 m;
3. a range-check is performed on the ZTD formal errors, removing the data corresponding to errors higher than 4 mm;
4. an outlier check is performed, with the screening of the ZTD values differing from the medium value by more than 0.5 m;
5. a second outlier check is performed on the ZTD formal errors, considering as outliers the standard deviation values diverging of more than three times the inter-quartile range from the median standard deviation value;
6. a data check is performed, removing the days that are filled with data on less than 25 % of the time after the screening, because the amount of data to perform the process would be too small.

The threshold values on position and ZTD standard deviations have been chosen considering the whole period distribution of formal errors.

The resulting 30 s PWV time series is composed of 8 582 065 points covering 3184 days in total, i.e. 95.2 % of the GipsyX estimates has been converted to PWV after the screening. The amount of rejected data per year and per R/V is given in Table 6.1. As displayed here, it seems that Alis provides data of poor quality compared to the other R/Vs, especially in 2017 where it shows a soaring rejection rate of 13 %. Thalassa has shown excellent results all over the years. 2015 and 2016 are the only years showing a

Year	Alis	Antea	L'Atalante	Pourquoi Pas?	Thalassa	TOTAL
2015	3 %	—	2 %	—	—	2 %
2016	3 %	0 %	2 %	—	—	2 %
2017	13 %	2 %	—	—	—	5 %
2018	4 %	6 %	1 %	—	—	3 %
2019	6 %	9 %	2 %	1 %	1 %	2 %
2020	8 %	—	2 %	3 %	1 %	2 %
2021	8 %	2 %	1 %	2 %	1 %	3 %
2022	9 %	—	8 %	2 %	2 %	4 %
TOTAL	7 %	3 %	2 %	2 %	1 %	3 %

Table 6.1: Amount of screened data in the FOF shipborne GNSS PWV dataset compared to the GipsyX estimation dataset, for each of the R/Vs (columns) and each year of the study (rows).

screening rate equivalent to the other R/Vs for Alis. Antea shows a high rejection rate in 2019, but it is because the dataset is really small with only two separate days of data such as seen in Figure 6.2. L'Atalante also shows a high rejection rate of 8 % in 2022. It can be interesting to further study the screening to understand what happened these years.

After having screened the position outliers, there are no ZTD outliers left, except for the Alis dataset in 2022 where four more points have been removed. The range check and data check accounts for around 25 % of the total screened values. L'Atalante in 2016 and Thalassa in 2022 show a higher range check screening than the others, each accounting for almost 5 % of the screened data. The high rejection rate observed on Antea in 2018 is due to both position range-check, and ZTD outliers and data check. It seems that the formal error on the position for this R/V is often quite poor, especially when compared to L'Atalante which accounts for more data acquisition than Alis on the period, as seen in Figure 6.2. Even if Alis accounts for less data than the other R/Vs, it accounts for almost half the screened data through the whole FOF dataset, most of them due to outliers in the position, accounting for one-third of the whole FOF rejected data. L'Atalante shows a higher global amount of screening compared to the other R/Vs, but it accounts for more data in total, so this is not surprising, contrarily to Antea showing the same amount of rejected data than Pourquoi Pas? and Thalassa, while it represents only two third of these two R/Vs dataset in total.

More specifically, Alis presents data in 355 days before and 247 days after the antenna replacement at the end of year 2019, Antea is present in 390 days, L'Atalante provides 612 days before and 321 days after the antenna replacement at the end of summer 2019, Thalassa provides 660 days, and Pourquoi Pas? provides 619 days of the FOF PWV total time series. The detail of the distribution of PWV data among the R/Vs and the years is given in several days in Table 6.2.

Year	L'Atalante	Thalassa	Pourquoi Pas?	Alis	Antea	TOTAL
2015	80	0	0	14	0	94
2016	269	0	0	45	58	372
2017	0	0	0	50	124	174
2018	222	0	0	168	104	494
2019	78	121	92	58	2	351
2020	88	162	156	31	0	437
2021	118	153	219	109	102	701
2022	78	224	152	107	0	561
TOTAL	933	660	619	582	390	3184

Table 6.2: Number of days in the FOF shipborne GNSS PWV dataset, for each of the R/Vs (columns) and each year of the study (rows). The R/Vs are ranked from the highest to the lowest number of days.

6.1.3 PWV Comparison Datasets

Several external sources of PWV information have been used to compare to the shipborne GNSS PWV, to assess its accuracy.

It is important to keep in mind that the reference datasets for the shipborne GNSS PWV evaluation have their uncertainty that is not taken into account for the evaluation of the shipborne GNSS PWV dataset.

6.1.3.1 ERA5

As for the survey vessel comparison in Chapter 4, the FOF PWV measurement is compared to hourly ERA5 by using the nearest GNSS time between both time series and by bilinearly interpolating the four nearest points to the R/V position such as explained in Section 4.1.6.3. The ERA5 TCWV product is brought to the GNSS antenna height using the EGM2008 geoid model using Equation (2.56).

This method of comparison led to an amount of 61 985 points of comparison such as detailed in Table 6.3, covering a total of 2 900 days including 887 days for L'Atalante, 667 days for Thalassa, 618 days for Pourquoi Pas?, 569 days for Alis, and 392 days for Antea.

6.1.3.2 Satellite-Borne Microwave Radiometer

SMWRs are directly measuring PWV over the sea surfaces of the globe.

Seven different satellite-carrying microwave radiometer datasets have been extracted from the Remote Sensing Systems website remss.com¹ on the period of study going from 2015 to the end of 2022. We used Special Sensor Microwave Image (SSM/I) that provides SMWR observations through the instrument f15, however, it is underlined to not use it after August 2006 for climate study. SSMIS provides SMWR through the

¹ SSM/I, GMI, AMSR2, and WindSat data are produced by Remote Sensing Systems and sponsored by NASA. Data are available at www.remss.com, visited 14 Nov. 2022.

Year	Alis	Antea	L'Atalante	Pourquoi Pas?	Thalassa	TOTAL
2015	270	---	1788	---	---	2058
2016	956	1269	5640	---	---	7865
2017	752	2744	---	---	---	3496
2018	3553	2087	4729	---	---	10369
2019	1246	39	1659	2039	2643	7626
2020	---	---	1964	3346	3598	8908
2021	---	2209	2536	4723	3466	12934
2022	---	---	568	3255	4906	8729
TOTAL	6777	8348	18884	13363	14613	61985

Table 6.3: Size of the [PWV](#) comparison dataset between the 30 s [FOF](#) and hourly [ERA5](#), for each of the [R/Vs](#) (columns) and each year of the study (rows).

instruments f16, f17, and f18 throughout the whole period. WindSat, Global Precipitation Measurement ([GPM](#)) Microwave Imager ([GMI](#)) and Advanced Microwave Scanning Radiometer 2 ([AMSR-2](#)) provide [SMWR](#) measurements during the whole period as well. Concerning [AMSR-2](#), the major update Remote Sensing Systems ([RSS](#)) version 8.2 released on May 2021, has been used to perform the best evaluation possible of the shipborne [GNSS PWV](#), as previous versions revealed drifts in the [AMSR-2 Air-Sea Essential Climate Variable \(AS-ECV\)](#) climate records containing the atmospheric columnar water vapor product of interest here.

Each one of these satellites performs a total Earth's surface coverage within half a day, which means that they cover the same location twice a day, except at low latitudes where the swaths are spaced out, such as seen in [Figure 6.3](#). Using all the satellites then ensures almost 14 crossings per day with any [R/V](#). There might be no data in certain regions, for reason of heavy rain or near land that could spoil the measurement. Considering the significant time length, we can consider that the amount of comparison dataset is statistically significant for shipborne [GNSS PWV](#).

The daily products, providing a 1°-grid [PWV](#) dataset for the morning and another for the afternoon for each [SMWR](#), are dated at Greenwich mean time, which means that we know the exact time of measurement for each point of the grid. The comparison is made for crossing points, which means that we use the [SMWR](#) data from the four nearest points from the shipborne as for [ERA5](#), within 15 s before and after the shipborne [GNSS](#) measurement date, as the [GNSS](#) dataset has a 30 s resolution.

This method led to an amount of 13 195 points of comparison covering 2 481 days including 811 days for L'Atalante, 566 days for Thalassa, 498 days for Pourquoi Pas?, 419 days for Alis, and 240 days for Antea, such as seen in [Table 6.4](#). The lower number of days of comparison with [SMWRs](#) compared to [Table 6.2](#), shows that the shipborne [GNSS](#) is effectively acquiring [GNSS](#) data in some regions and times where the [SMWR](#) is not available. This can be because of the near-land missing data less than 25 km from the coast, or heavy rain episodes, that prevent the [SMWR](#) from getting accurate data and are then missing in the provided [SMWR](#) dataset.

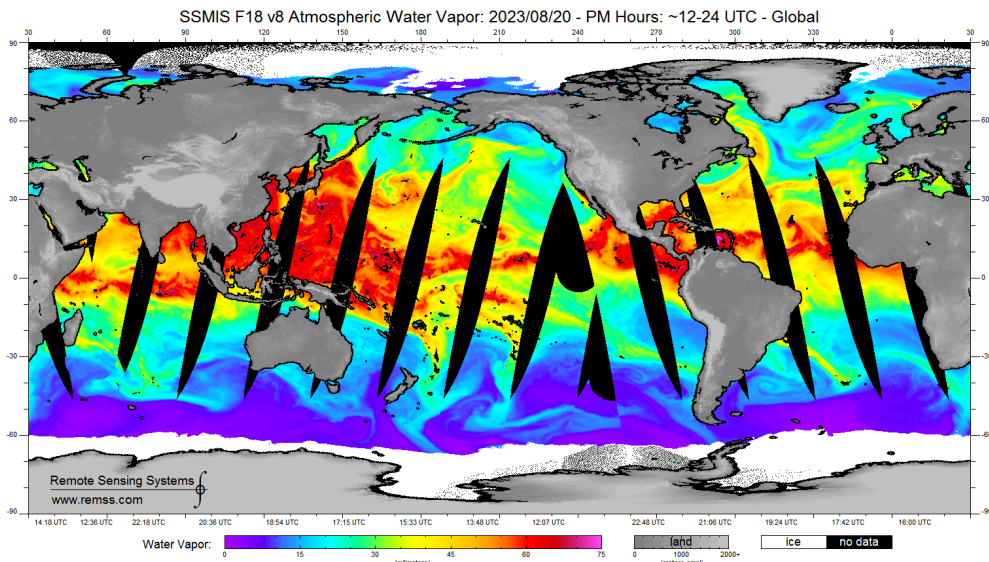


Figure 6.3: SSMIS f18 atmospheric water vapor on August 20th, 2023 afternoon. SMWR swaths are not overlapping at low latitudes, and data are missing especially in Polar areas that are covered with ice. Source: remss.com, visited 31 Oct. 2023

6.1.3.3 Ground-Based GNSS Stations

The world geodetic database from the NGL release over 18 600 ground-based GNSS station positions and tropospheric products from different world GNSS stations networks on their website: geodesy.unr.edu [Ble 18]. These products are computed by using a ZHD coming from the VMF1 model instead of ERA5, then they are supposed to be less accurate than the FOF dataset [Yua 23]. The remaining ZWD value is converted to the PWV that is provided by the NGL database. We used this provided PWV dataset to compare to our shipborne antennas PWV time series.

We have first compared the database of the stations and their position to the R/Vs paths to extract the ground stations that are within 100 km from a R/V path, and the time of crossing. A second time, the corresponding PWV product directly available from the NGL database has been downloaded for the given ground stations at the time of crossing. This means that the time-matching data are retrieved, taking into account that the PWV products from NGL are given on a 5 minutes resolution basis. Third, the shipborne GNSS PWV has been extrapolated to the ground-based GNSS station height following Equation (2.56), and the difference has been computed, so that we can compare them. However, the PWV values from stations higher than 100 m above the R/V antenna height are not considered for comparison, because the ERA5 extrapolation at this altitude to compute the ZWD is not relevant and leads to curious PWV results [Bos 21a]. Also, the error of ZHD retrieving from VMF1 must be limited while working near the MSL because of the VMF1 poor resolution. The screening value has been chosen to stay coherent with the screening applied to the FOF dataset, converting the ZWD outlier value into PWV outlier check by using a 6.5 coefficient as a rule of thumb (Equation 2.5.1). The resulting set of ground stations used for comparison appears in Figure 6.4. The colors used on this map correspond to the R/Vs that were compared to the displayed ground station PWV dataset. The ground stations that have been used for comparison with several R/Vs are depicted in the color of the R/V that has crossed the highest number of different years.

Year	Alis	Antea	L'Atalante	Pourquoi Pas?	Thalassa	TOTAL
2015	53	—	547	—	—	600
2016	194	329	1590	—	—	2113
2017	140	493	—	—	—	633
2018	511	227	1205	—	—	1943
2019	188	2	393	565	623	1771
2020	76	—	422	434	925	1857
2021	202	220	578	668	639	2307
2022	274	—	280	657	987	2198
TOTAL	1638	1271	5015	2324	3174	13422
N doys	419	240	811	498	566	1736

Table 6.4: Size of the *PWV* comparison dataset between the *FOF* and *SMWR*, for each of the *R/Vs* (columns) and each year of the study (rows). The last line **N doys** shows the corresponding number of days covered by the comparison dataset for each *R/V*.

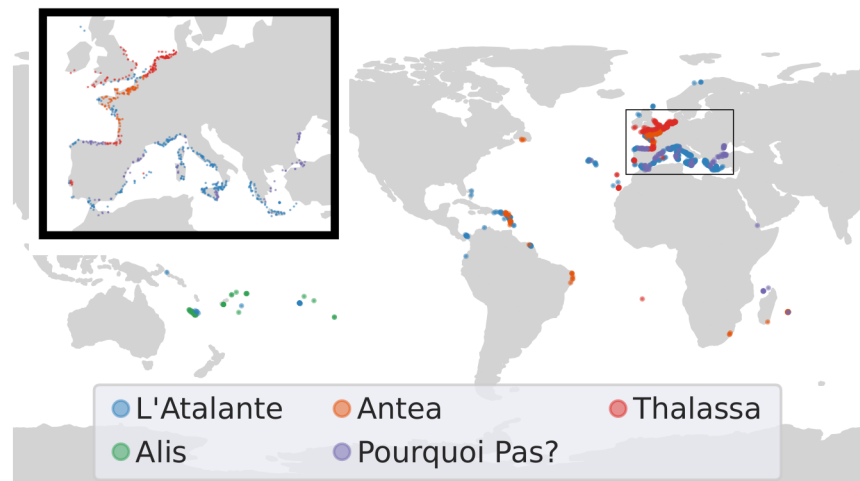


Figure 6.4: Map of the ground stations crossed by *FOF* *R/Vs* from 2015 to 2022. The colors correspond to the *R/V* that was compared to the ground station *PWV* dataset. The ground stations that have been used for comparison with several *R/Vs* are depicted in the color of the *R/V* that has crossed the highest number of different years.

This method led to 83 499 points of comparison for all the *R/Vs* from 2015 to 2022, covering a total of 1 027 days including 423 days for L'Atalante, 473 days for Thalassa, 367 days for Pourquoi Pas?, 349 days for Alis, and 288 days for Antea, such as detailed in Table 6.5.

We can see from the last line of Table 6.5 that most of the *R/Vs* are sailing in coastal areas less than half the time, by comparison to the total amount of available days of data in Table 6.2. However, the amount of comparison datasets is still high, as the

Year	Alis	Antea	L'Atalante	Pourquoi Pas?	Thalassa	TOTAL
2015	873	--	890	--	--	1763
2016	1557	1004	7752	--	--	10313
2017	3255	5584	--	--	--	8839
2018	8393	17717	11453	--	--	37563
2019	2032	120	1197	955	14488	18792
2020	1946	--	6391	11002	16221	35560
2021	8053	13588	3879	22061	25398	72979
2022	6225	--	2039	9728	27783	45775
TOTAL	32334	38013	33601	43746	83890	231584
N days	349	288	423	367	473	1341

Table 6.5: Size of the **PWV** comparison dataset between the **FOF** and ground-based **GNSS** tropospheric products from **NGL**, for each of the **R/Vs** (columns) and each year of the study (rows). The last line **N days** shows the corresponding number of days covered by the comparison dataset for each **R/V**.

coastal areas provide several ground-based antennas at the same time, on a 5 minute period basis.

The ground-based **GNSS** comparison also completes the **SMWR** comparison that is not available within 25 km from the coast.

6.1.3.4 Inter-Ship Comparisons

As the **R/Vs** are often sailing the same regions as seen in [Figure 6.1](#), and because they are attached to French harbors where they often resupply and face maintenance, their paths are sometimes crossing, such as seen in [Figure 6.5](#).

These maps show that in three cases, L'Atalante or Thalassa are docked in harbors, while Antea is entering the Toulon harbor where L'Atalante is docked in October 2018 in the first map, Thalassa is entering the Brest harbor in February 2021 in the third map, and Pourquoi Pas? is leaving the Brest harbor where Thalassa stands in January 2020 in the second map. In the fourth map, we can see that Thalassa is evolving offshore the Brest harbor while L'Atalante leaves the harbor in January 2022. The length of the crossings events is displayed in [Table 6.6](#).

Then, it is possible to compare **R/V** shipborne **GNSS PWV** time series to one another. We limit the crossing distance to 50 km for comparison. Within this radius, both datasets are compared by matching the times.

Applying this method of comparison leads to four crossings of 6 311 points in total including 1 511 points between L'Atalante and Antea, 2 936 points between Pourquoi Pas? and Thalassa, 568 and 1 296 points during two different crossings between L'Atalante and Thalassa.

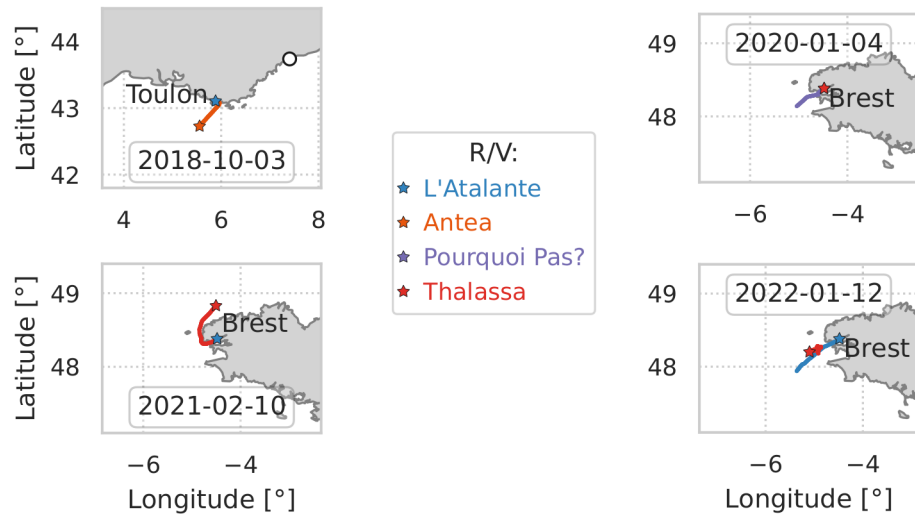


Figure 6.5: Maps of the crossings of the *R/Vs* showing the location and the date of the meeting when they are less than 50 km apart. The maps are displayed for each crossing (middle and bottom rows), with a star showing the start of the trajectory of each *R/V*. The date displayed on each map corresponds to the day of the star's location, UTC.

Crossing <i>R/Vs</i>		Date	Start (UTC)	Duration	N
L'Atalante	Antea	2018-10-03	16:24:30	12:35:00	1511
Pourquoi Pas?	Thalassa	2020-01-04	19:00:00	24:28:00	2936
L'Atalante	Thalassa	2021-02-10	10:16:00	4:43:30	568
L'Atalante	Thalassa	2022-01-12	13:45:30	10:47:30	1296
TOTAL				52:33:00	6311

Table 6.6: Name of the crossing *R/Vs* with the corresponding starting date and time (UTC), the length, and the involved number of points (N) of the crossing datasets.

6.2 EVALUATION OF SHIPBORNE GNSS PWV RESULTS

The evaluation of the *PWV* results is made through the comparison to usual *PWV* measuring techniques in Section 6.2.1, and then by comparing inter-FOF datasets in Section 6.2.2 when two *R/Vs* are crossing.

6.2.1 External *PWV* Dataset Comparison

The statical results of the comparison of the shipborne *GNSS PWV* to usual offshore and coastal *PWV* retrieval techniques are presented in Table 6.7. As seen in Table 6.7, ERA5 provides worse biases than the other comparisons, except for Thalassa that shows worse bias with ground-based *GNSS*, and Alis shows an equivalent bias than *SMWR* comparison. However, the standard deviation is higher for the ground-based *GNSS* comparisons than the others, possibly because the ground-based stations' accuracy is not the same depending on the stations considered, and because they can be as

R/V	ERA5 [mm]	SMWR [mm]	Ground GNSS [mm]
L'Atalante	+1.11 ± 1.61	+0.61 ± 1.57	+0.89 ± 2.28
Thalassa	+0.23 ± 1.43	-0.08 ± 1.30	+0.30 ± 1.72
Pourquoi Pas?	+0.90 ± 1.75	+0.04 ± 1.42	+0.60 ± 2.06
Alis	+0.52 ± 1.94	+0.54 ± 2.50	+0.38 ± 2.75
Antea	+0.86 ± 2.21	+0.14 ± 2.27	+0.31 ± 2.32
All FOF	+0.75 ± 1.76	+0.29 ± 1.73	+0.46 ± 2.15

Table 6.7: Bias and standard deviation of the differences of the R/Vs PWV compared to ERA5, SMWR, and ground-based GNSS. The difference statistics are shown for each of the five R/Vs, and the whole FOF dataset in the last line.

far as 100 km from the R/V, so the observed PWV can differ. In all comparison cases, the RMSE of the FOF comparison is less than 2.20 mm, with the best matching SMWR comparison providing an RMSE of 1.78 mm.

The comparison results will be detailed in Sections 6.2.1.1 to Section 6.2.1.3.

6.2.1.1 ERA5 Comparison Results

By comparing to the NWM ERA5, we can see in Table 6.7 that the overall bias is quite high compared to the other shipborne GNSS datasets, whereas the standard deviations are comparatively small. All the R/Vs are showing a wet bias compared to ERA5, and their comparison to ERA5 is shown as a scatter plot in Figure 6.6.

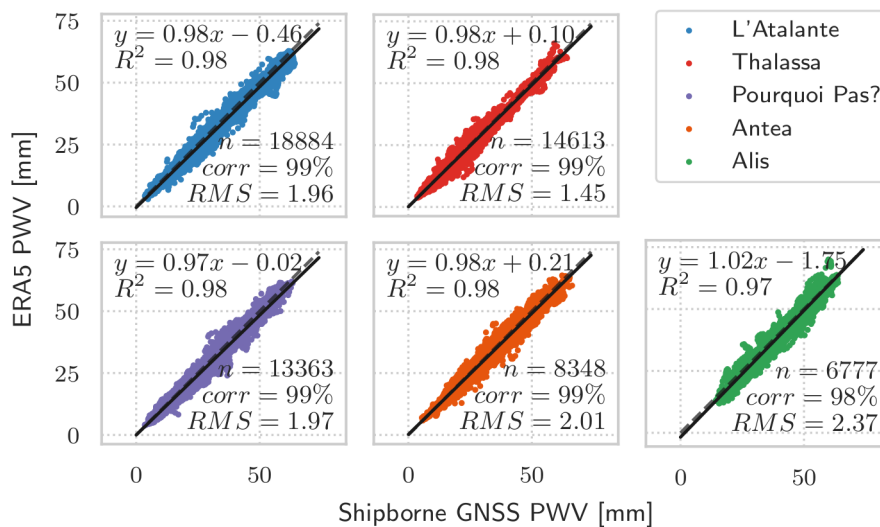


Figure 6.6: Scatter plot of ERA5 TCWV product as of the shipborne retrieved PWV from each R/V. The equation and the coefficient of determination (R^2) of the linear regression plot as a continued black line is displayed along with the number of points of comparison (n), the correlation coefficient ($corr$), and the RMSE between the datasets.

In [Table 6.7](#) Alis shows a quite usual bias value compared to all the state-of-the-art studies presented in [Chapter 3](#). L'Atalante, Pourquoi Pas? and Antea show a greater bias than these previous studies. To the contrary, Thalassa shows a relatively low bias, and its [RMSE](#) of 1.45 mm is also lower than all but two of these studies. Indeed, only Shoji et al. (2023) [[Sho 23](#)] and Wang et al. (2019) [[Wan 19](#)] have shown lower statistical values than the difference between Thalassa and [ERA5](#). Moreover, Wang et al. (2019) [[Wan 19](#)] compared to [ERA-Interim](#) which is the previous version of [ERA5 NWM](#). The other [R/Vs](#) shows statistical results of the difference with [ERA5](#) ranging from 1.94 mm to 2.21 mm, it appears that our results are all within the average, while Bossler, Van Baelen, and Bousquet (2022) [[Bos 22b](#)], Wu et al. (2022) [[Wu 22a](#)], and Wu et al. (2022) [[Wu 22b](#)] show higher [RMSE](#) values. Thus, our resulting standard deviations are lower than in these studies. The bigger variability in Wu et al. (2022) [[Wu 22a](#)] might be because they have used a low-cost [GNSS](#) receiver, as they provide the worst [RMSE](#) even if their bias is in the average, and it is a real-time study. We can also see that the amount of data involved in the comparison is correlated to the [RMSE](#) reducing, except for Thalassa which shows excellent matching with [ERA5](#).

As we can see on [Figure 6.1](#), Thalassa evolves most of the time near the Western European coast, where [ERA5](#) performs better than in areas covered with less atmosphere monitoring systems [[Bos 21b](#)]. On the contrary, L'Atalante, Pourquoi Pas?, and Antea spend a lot of time in diverse areas with less accurate [ERA5](#) because of the lack of atmosphere monitoring. Although L'Atalante is showing the highest bias with [ERA5](#) just before Thalassa, it is also the [R/V](#) providing the highest amount of data and the wider range of latitudes explored. The wide range of situations encountered permits us to explain the high bias between these [R/Vs](#) and [ERA5](#). However, Alis always sails the Pacific Oceans where few observations permit to feed the [NWM](#), but the bias is better than the other [R/Vs](#) except Thalassa. We can then suppose that this zone is relatively stable on a long-term basis, so it is well described by [ERA5](#), but high variations of [PWV](#) may occur briefly, then being captured by the shipborne [GNSS](#) whereas [ERA5](#) do not transmit these low-resolution variations, leading to the second highest standard deviation compared to the other [R/Vs](#).

6.2.1.2 SMWR Comparison Results

The comparison of the shipborne [GNSS](#) retrieved [PWV](#) to the crossing swath of [SMWRs](#) result in [Figure 6.7](#).

The histogram at the bottom of [Figure 6.7](#) shows that there is a slightly wet bias of the shipborne [GNSS PWV](#) estimation compared to the [SMWR](#). Most of the biases are less than 5 mm apart from the [SMWR](#), even with biases mainly grouped between -3 mm and 3 mm corresponding to accuracy suitable for climate study. But a couple of outliers appear to range from almost 20 mm down to -37 mm, which is highly significant with regard to the screening already performed on the shipborne dataset.

The comparison to [SMWR](#) is shown as a scatter plot in [Figure 6.8](#). The coefficients of determination show a good agreement between the linear regression and the scatter plots. The correlation coefficients show an excellent agreement between the [R/V](#) retrieved [PWV](#) and the [SMWR](#) measurement. However, the [RMSE](#) of the comparisons with Alis and Antea is quite high compared to the other [R/Vs](#). This is due to outliers that can be seen on the scatter plots, and the fact that these [R/Vs](#) are providing fewer points of comparison.

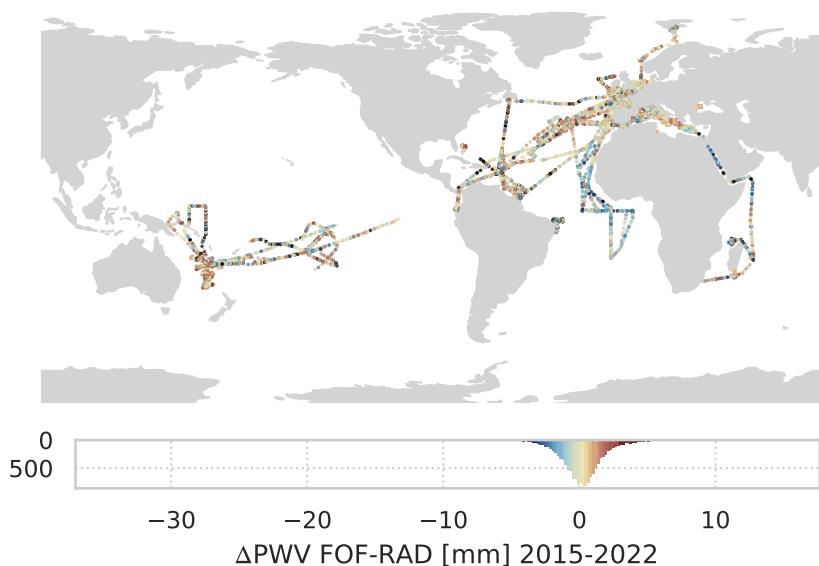


Figure 6.7: Map of the difference between the shipborne GNSS and SMWR PWVs along the R/Vs trajectories. The blue color shows a dry bias and the red a wet bias of the shipborne GNSS compared to the SMWR.

The retrieved PWV from GNSS better corresponds to SMWRs as seen in Table 6.7 than with ERA5, for all the R/Vs but Alis. The obtained biases are coherent with the ones of the previous shipborne GNSS PWV studies of Chapter 3 presented in Table 3.4. However, the RMSE values are quite worse in the case of Alis and Antea. The common point between these two R/Vs is that they are evolving mostly in the Equatorial region. In the Equatorial region, the amount of water vapor in the atmosphere is higher than in other parts. Many clouds can then cover the sky during the rainy season, and the SMWR might not be able to get data at these locations, or they could be altered by rainy conditions. Another thing is that many islands are in the Pacific Ocean where Alis moves, so the signal of the SMWR compared to Alis might have been polluted by little land areas under the swath of the SMWR, even if they are supposed to be removed.

The fact that L'Atalante, which is often sailing the open sea, is better corresponding to SMWR than ERA5 underlines how important it is to get more offshore data to enhance the accuracy of NWMs at sea, and that shipborne GNSS could be a great source of information for this.

All the comparisons show a wet bias of the shipborne GNSS PWV compared to the SMWR, except Thalassa which shows a dry bias, which is very low however. Thalassa provides the best RMSE of 1.31 mm, as for the ERA5 comparison. The provided differences agree well with the ground-based GNSS comparison to SMWR provided by Mears et al. (2015) [Mea 15], especially the behavior of higher difference in Alis and Antea comparisons. Indeed, they found out that the fitting of the dataset was weaker in case of higher PWV content in the atmosphere, whereas Alis and Antea are displaying less satisfying RMSEs than the other R/Vs while they are sailing the Equatorial region in the majority, where the PWV content is higher, corroborating this finding.

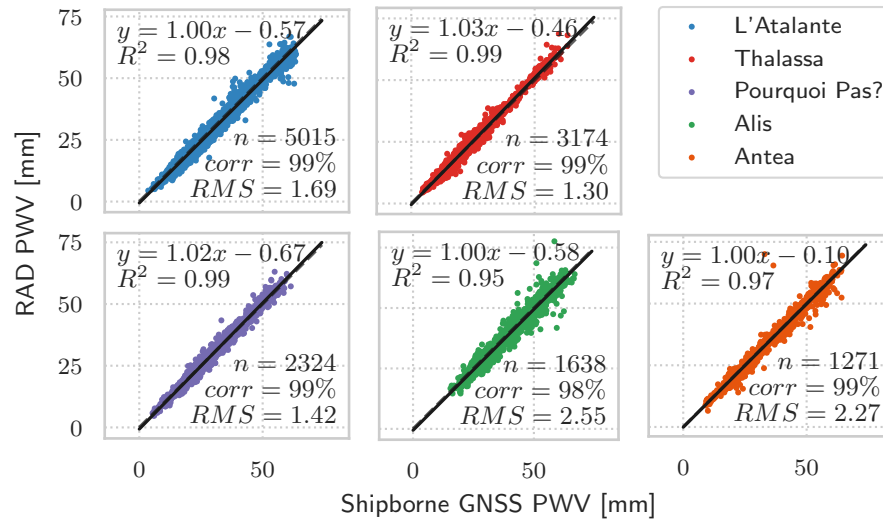


Figure 6.8: Scatter plot of SMWR PWV product as of the shipborne retrieved PWV from each R/V. The equation and the coefficient of determination (R^2) of the linear regression plot as a continued black line is displayed along with the number of points of comparison (n), the correlation coefficient ($corr$), and the RMSE between the datasets.

6.2.1.3 Ground-Based GNSS Comparison Results

The comparison with the ground-based GNSS station PWV provides biases similar to the biases of the previous shipborne GNSS PWV studies detailed in Table 3.4 of Chapter 3. Speaking of RMSE, the comparison to ground-based GNSS stations leads to a global RMSE of 2.19 mm, of equivalent quality than for any of the studies presented in Table 3.4, showing an RMSE up to 2.71 mm.

However, this result is altered by the poor results obtained with Alis, showing an RMSE of 2.77 mm such as seen in Figure 6.9 depicting the shipborne and ground stations time series drawn from one another. The other R/Vs show RMSEs up to 2.45 mm, the best result being obtained with Thalassa with an RMSE of 1.75 mm, which is a medium value compared to the studies of Table 3.4. Then, Alis requires further study to identify the high RMSE sources.

We can see in Figure 6.9 that the correlation between the FOF and the ground-based GNSS station retrieved PWVs is really good, with at least 97% depending on the considered R/V. In all cases, the comparison involves an important number of comparisons, with more than 32 334 comparisons for Alis up to 83 890 points for Thalassa. It is interesting to notice that compared to the total amount of data for L'Atalante, there are not that many comparisons to ground stations. This is due to its real offshore applications.

The Thalassa RMSE is almost 60% lower than for Alis, which could be explainable by the fact that, as seen on the corresponding scatter plots, the PWV values are higher for Alis than Thalassa, so the variations over the distance can be heavier for the first case where more water vapor is available. This is due to the location of the R/Vs: Alis is evolving in the Equatorial region all the time, while Thalassa is in the mid-latitudes regions most of the time.

The histogram of the differences in PWV between the R/Vs and the ground-based GNSS stations in Figure 6.10 shows that the deviation of the differences around the

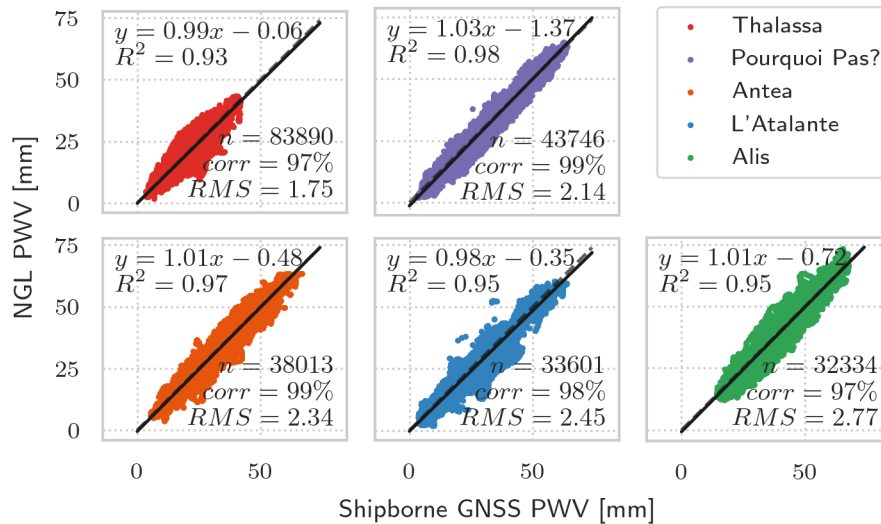


Figure 6.9: PWV scatter plot between shipborne GNSS antenna and coastal ground-based GNSS stations crossed less than 100 km away. The scatter plots are displayed for the different R/Vs, for the whole available dataset. The stations of more than 100 m above the R/V antenna height have been removed.

mean value is due to nearest crossed stations as much as the most remote occurrences.

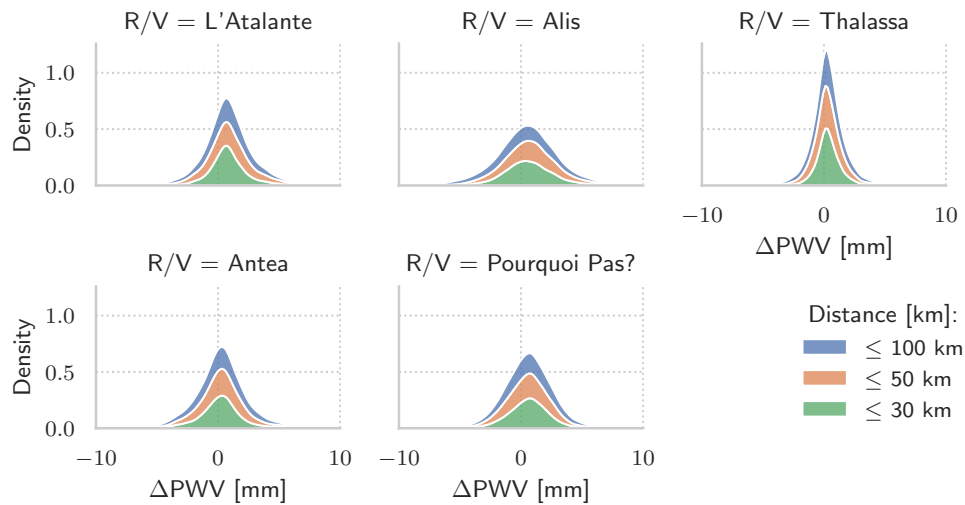


Figure 6.10: Histogram of the differences between the shipborne antennas and the ground-based GNSS stations crossed less than 100 km away. The colored areas are overlapping, letting the green area be the stations crossed less than 30 km away, while the orange area extending above the green corresponds to stations crossed between 30 km and 50 km away, and the blue extending area corresponds to stations crossed between 50 km and 100 km.

In the case of Alis, it is showing a flatter histogram, especially for comparison to ground-based GNSS located between 30 and 50 km away. However, the up to 100 km away ground station comparisons appear to be less represented in the case of Alis,

and still show a dry bias after all. Thus, the distance and the *PWV* quality might be both involved in the higher *RMSE* of the differences.

The errors are due either to the shipborne antenna or the crossed ground stations in some regions where *Thalassa* - the best-fitting antenna - is not evolving. To determine this, we can study the differences in the Western Europe region, where *Thalassa* is evolving most of the time. First, in all cases, a bad shipborne measurement can overaffect the differences if it is next to a lot of stations at the time of measurement. Indeed, this flawed measurement will be compared to many ground-based *GNSS* stations in this case. Second, it is interesting to note that in [Figure 6.9](#), *Thalassa* does not display *PWV* values higher than 45 mm, while *Alis* displays *PWV* values above 15 mm at least. As far as they represent respectively the best and worst fitting to ground stations, there seems to be a correlation between the *PWV* value and the efficiency of the *PPP* processing to accurately estimate the *ZWD*, or the accuracy of the *PWV* computing method from *ZWD*.

6.2.2 Result of Comparison between *R/Vs*

The results of the comparison between the *R/Vs*, when they are crossing at a distance of less than 50 km from one another, is detailed in [Table 6.8](#). The significant difference in the statistical results for the two crosses of *Thalassa* and *L'Atalante* is quite striking.

Year	Crossing <i>R/Vs</i>		N	Statistics [mm]
2018	<i>L'Atalante</i>	<i>Antea</i>	1511	-0.41 ± 0.37
2020	<i>Pourquoi Pas?</i>	<i>Thalassa</i>	2936	-0.37 ± 0.29
2021	<i>L'Atalante</i>	<i>Thalassa</i>	568	$+1.10 \pm 0.97$
2022	<i>L'Atalante</i>	<i>Thalassa</i>	1296	$+0.35 \pm 0.27$
	All <i>FOF</i> crossings		6311	-0.10 ± 0.63

Table 6.8: Bias and standard deviation of the differences of the *R/Vs PWV* compared to each other when they are crossing to less than 50 km. The differences in statistics are shown for each of the three occurring *R/V* crossings between *Pourquoi Pas?*, *Thalassa*, *L'Atalante*, and *Antea*, and for the whole *FOF* crossings in the last line, N being the number of points of comparison.

The *PWV* time series of the crossings are then displayed in [Figure 6.11](#).

We know from [Figure 6.5](#) that the first crossing occurs when *Thalassa* is docked at the Brest harbor while *L'Atalante* gets into port, arriving from the North on the other side of the point of *Finistère*. [Figure 6.11](#) shows that while *L'Atalante* comes closer to *Thalassa*, both time series appear to fit one another. We can then conclude that the difference in *PWV* here is due to the distance, and that the horizontal gradient of atmospheric water vapor was not negligible in this area at the time of crossing. Indeed, the second crossing time series appears to be fitting even when both *R/Vs* is 50 km away. The significant difference is due to the difference in weather that can be encountered between the Bay of Brest facing the Atlantic Ocean, and the Northern Coastal Bretagne that is located in the English Channel. Similarly, *L'Atalante* and *Antea*

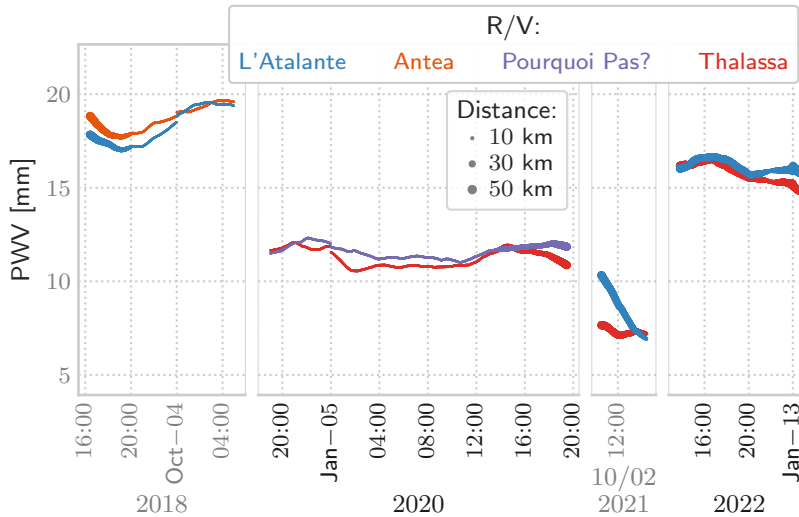


Figure 6.11: PWV time series of four R/Vs crossings less than 50 km away. The crossing R/V are L'Atalante (blue), Antea (orange), Pourquoi Pas? (purple), and Thalassa (red). The distance between R/Vs is represented by the line width. The crossings are mapped in Figure 6.5

show better fitting when they are closer. However, the crossing between Thalassa and Pourquoi Pas? shows a small discrepancy between midnight and 4 o'clock UTC on January 5th, 2020. The second crossing of L'Atalante and Thalassa appears to be quite far, but the time series are well fitting to one another. We can then state that the significant difference in 2021 is actually due to the distance and a significant gradient in PWV between the two starting positions.

6.3 CONCLUSION ON THE FOF PROCESSING

We focused here on the kinematic PPP post-processing of five R/Vs from the FOF datasets following the recommended modeling after Chapter 5, on the long term. Indeed, IFREMER has provided us with all the data they have been able to record on Atalante, Pourquoi Pas?, Alis, Antea, and Thalassa from 2015 to 2022. The resulting PWV time series have been confronted to other data sources for processing method evaluation.

The differences of the FOF dataset with ERA5 agree well with the results of the studies listed in Chapter 3.

This study brings out a first comparison with offshore SMWR on a long period (several years), showing encouraging results with a good agreement even if some outliers arise. The overall shipborne bias compared to SMWR appears to be wet.

Although the comparison to coastal ground-based GNSS station showed good results, it provides worse fitting than ERA5 and SMWR comparisons. This is probably due to the NGL method for conversion method of the tropospheric product into water vapor.

The crossings of the R/Vs permit highlighting a good fitting between the involved R/Vs of different shapes. One discrepancy arise, because of the weather conditions being different from one part of the peninsula to the other in North Finistère. This

study provides a preliminary value of the inherent uncertainty of the method with an [RMSE](#) of 0.64 mm on the [PWV](#).

In future work, the recommended processing modeling will be applied for the routine analysis of the [GNSS](#) raw data acquired by commercial ships. This analysis will likely result in an estimate of the [ZWD](#) over the course of the boat, suitable for studying the space and time distribution of atmospheric water vapor over open seas for weather forecasting, and other climate aspects, such as attempted in [Chapter 7](#).

FOF PWV DATASET FOR ATMOSPHERIC WATER VAPOR MONITORING

CONTENT

7.1	Impact of the Latitude on the PWV Comparisons	121
7.1.1	Zonal Impact on the Comparison with ERA5	121
7.1.2	Zonal Impact on the Comparison with SMWR	123
7.1.3	Zonal Impact on the Comparison with NGL	124
7.2	Impact of the Season on the PWV Comparisons	125
7.2.1	Seasonal Impact on the Comparison with ERA5	126
7.2.2	Seasonal Impact on the Comparison with SMWR	126
7.2.3	Seasonal Impact on the Comparison with NGL	127
7.3	Contribution of the FOF Dataset to the Climate Study	128
7.3.1	Latitude and PWV	128
7.3.2	Season and PWV in Mid-Latitudes Region	130
7.3.3	Correlation with Sea Surface Temperature	131
7.4	Conclusion on the Contribution of Shipborne PWV to Atmosphere Water Vapor Monitoring	133

7.1 IMPACT OF THE LATITUDE ON THE PWV COMPARISONS

As explained by Hadas et al. (2017) [Had 17], the PWV range and variation are impacted by the location on Earth, the changes being mainly due to the latitude. This section focuses on the impact of the latitude on the PWV differences presented in Section 6.2.

As far as the available datasets provide measurements above the Tropic of Capricorn, the different regions are defined through the latitudes of the Tropic of Cancer and the Arctic Circle parallels. Namely, "Equator" denotes the data between the two Tropics, "Pole" denotes the data North from the Arctic Circle, and "Mid-Latitude" denotes the data in between, in the rest of this Chapter.

7.1.1 Zonal Impact on the Comparison with ERA5

We deal with the study of the zonal location impact on the PWV differences with ERA5. The scatter plot is represented on Figure 7.1 for three different latitude regions: the mid-latitude regions, the Equatorial region, and the Polar region.

Only L'Atalante is going in the Polar region, above 60° of latitudes, when it is heading to the Svalbard. As the number of comparisons is very low in this region (317

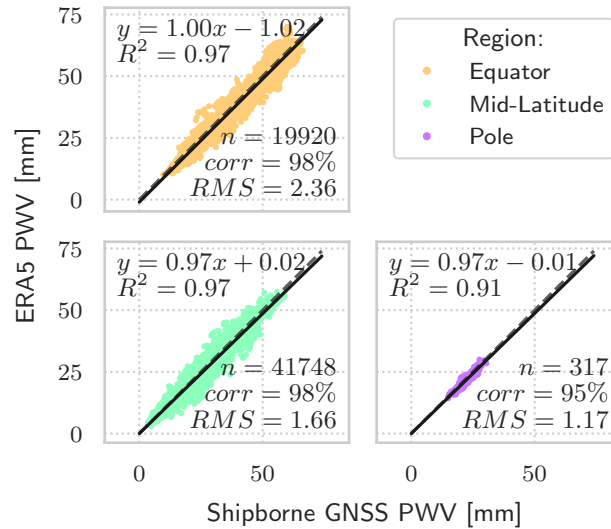


Figure 7.1: PWV scatter plot between shipborne GNSS antenna and ERA5 for three latitude regions: the Pole, the Equator, and the mid-latitudes regions.

points), the RMSE is low with 1.17 mm. However, the correlation is quite low with 95 % against 98 % for the other two regions. Accordingly, the coefficient of determination R^2 is quite low (0.91) compared to the other regions (0.97). This effect might be due to a dataset corresponding to the Polar region that is not representative because of its small size.

Although the mid-latitudes benefit from more than double the number of points of the Equatorial region, both regions show the same correlation coefficient and coefficient of determination of the linear regression. However, the RMSE is higher in the Equatorial region (2.36 mm) than in the mid-latitudes region (1.66 mm). This corroborates the effect observed on ground-based GNSS by Bosser and Bock (2021) [Bos 21b], which showed a difference of the PWV measurements with ERA5 of more than 2 mm at the Equator while it was less than 2 mm at the mid-latitudes. They showed that it was even weaker in the Polar region. Ding et al. (2023) [Din 23] has also compared to ERA5 ground-based GNSS stations PWV products, that were provided by the NGL such as our reference ground-based GNSS stations. They have found a latitude-dependent difference, with higher bias in the Equatorial and Polar region, and a standard deviation significantly decreasing from the Equator to the Poles.

Thus, we see that the Equatorial region is more noisy in terms of PWV retrieval. Two hypotheses can differently explain this phenomenon. First, the Equatorial region involves more atmospheric water vapor, and its variations can be more important in the same time lapse than in the mid-latitude region. The fact that ERA5 is smoothed compared to reality can explain the difference between the two results if the shipborne GNSS better manages the rapid changes in PWV, spatially and temporally. Second, the Equatorial region is composed of data-sparse regions that are mid-latitudes in our study (see Figure 6.1). The accuracy of ERA5 relies on the assimilation of diverse and accurate data acquired in the nearby region. Otherwise, the NWM is flawed. The observation of a difference in the comparison between both retrieved PWV datasets might be due to the lack of data assimilated in ERA5 in the Equatorial region, meaning that the mid-latitude region ERA5 products are better than in the Equatorial region.

The shipborne GNSS being an independent measurement technique, it can be used to validate ERA5 in the Equatorial region.

However, it is important to remember that there are more than double the number of comparisons in mid-latitudes than in the Equatorial region, as most R/Vs are sailing the North Atlantic Ocean and the Mediterranean Sea. Then, any bias in the Alis antenna that is the main R/V sailing in the Equatorial region might impact further the result in the Equatorial region. The higher RMSE at low latitudes might also be due to a flawed shipborne GNSS PWV as Alis has previously been pointed out as less accurate than the other R/Vs in Chapter 6. Even if the bias stays acceptable, it would be interesting to further study it to determine whether the bias is mainly due to a poor ERA5 product in the Tropics, a shipborne measurement that is flawed (we have only one ship going for a long time in this region), or the GNSS PWV retrieval that is generally not suitable for performing ERA5 validation in the Tropics.

Bock and Parracho (2019) [Boc 19] has highlighted a ± 1 mm variation in the bias with ERAI depending on the latitude. The Equatorial region appears to be drier in ERA5 while the mid-latitudes are wetter. The authors suggest that the differences might be due to high-frequency variability that ERAI do not detect because of its 6-hour time resolution. They also highlighted that the large discrepancies are due either to topographic change - which does not concern the FOF dataset located at sea, or the highly changing PWV behavior in the case of monsoon for example, or the season change.

7.1.2 Zonal Impact on the Comparison with SMWR

The scatter plot of the PWV differences with SMWR is represented Figure 7.2 for three different latitudes regions: the mid-latitudes regions, the Equatorial region, and the Polar region.

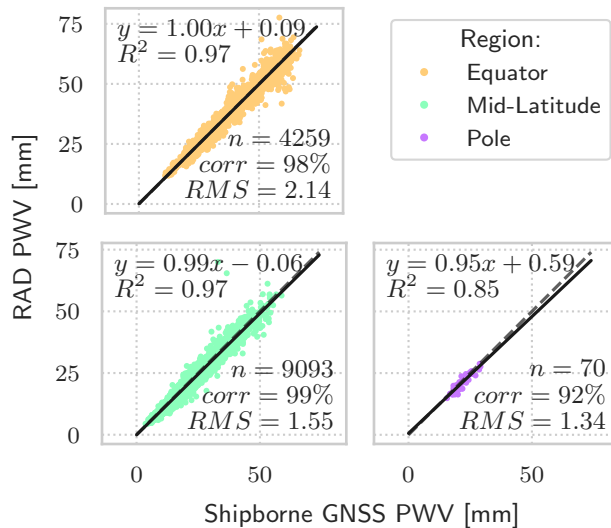


Figure 7.2: PWV scatter plot between shipborne GNSS antenna and SMWR for three latitude regions: the Pole, the Equator, and the mid-latitudes regions.

Concerning the Polar region, the number of comparisons between shipborne GNSS and SMWR is 70, which explains the low fitting coefficient in the linear regression. A

lower number of comparisons availability compared to the previous comparison to ERA5 was expected for all the latitudes, because ERA5 provides data on an hourly basis while the seven SMWRs provide data twice a day each at most. It is still interesting to notice that the RMSE is 0.17 mm higher than for the comparison with ERA5, and the correlation coefficient is degraded by 3 %.

Both Equatorial and mid-latitude regions display good-fitting linear regressions with a coefficient of determination of 0.97 such as for the ERA5 comparison. The correlation coefficients are equivalent to that of the ERA5 comparison, with a 1 % rise for the mid-latitude region. Still, the number of comparisons in the Equatorial region is half the mid-latitude region. Contrary to the observation made at high latitudes, RMSE values are quite better than for the ERA5 comparison, with a better fitting of 9 % in the Equatorial region and 7 % in the mid-latitude region. However, the shape of the scatter plots is different from ERA5. Indeed, they seem to better fit the linear regression line while the data is more spread for ERA5 in both regions, but the comparison to SMWR provides significant outliers, especially for higher PWV values. Mears et al. (2015) [Mea 15] has obtained the same behavior with a high standard deviation for higher PWV values, but they supposed that it was due to the difference in location between the offshore SMWR measurement and the coastal ground-based GNSS antenna. However, the same pattern appears in our data while directly comparing the PWVs when the SMWR is passing right above the R/V. The previous resulting comparison to ERA5 would encourage drawing the hypothesis that these outliers are due to an SMWR failure. Failures are explainable by the presence of heavy rain or large clouds on the SMWR swath path, that might have been forgotten during the data quality check carried out before the data release.

Some studies are using shipborne GNSS data to assess the quality of SMWR water vapor retrieving such as [Wan 19]. The above observation tends to confirm that shipborne GNSS is suitable for offshore SMWR assessment.

7.1.3 Zonal Impact on the Comparison with NGL

The scatter plot of the PWV differences with the ground-based GNSS antennas is represented Figure 7.3 for three different latitudes regions: the mid-latitudes regions, the Equatorial region, and the Polar region.

The number of comparisons being halved once more in the Polar region, we will not consider the linear regression of this graph. The RMSE and correlation coefficient of the comparison between shipborne and ground-based GNSSs in the Polar region are very slightly degraded compared to the comparison of the shipborne GNSS to the SMWR.

Although the difference between the shipborne GNSS and the NGL ground stations rely on many more points than the comparison to ERA5, the linear regression fit and the statistical results are significantly degraded. Indeed, the scatter plot displays a wider range around the linear regression line. However, the mid-latitudes seem to provide better fitting for the higher half of the PWV values. Some outliers are spotted as well, but they are not spread across the graph as for the comparison to SMWR.

The NGL products are flawed, as the ZHD is directly provided by the VMF1 for the water vapor estimation, involving possible bias. The only screening performed on the NGL PWV values was a threshold value on the standard deviation provided in the NGL tropospheric file, of the same value as for the FOF screening (see Section 6.1.2). Many

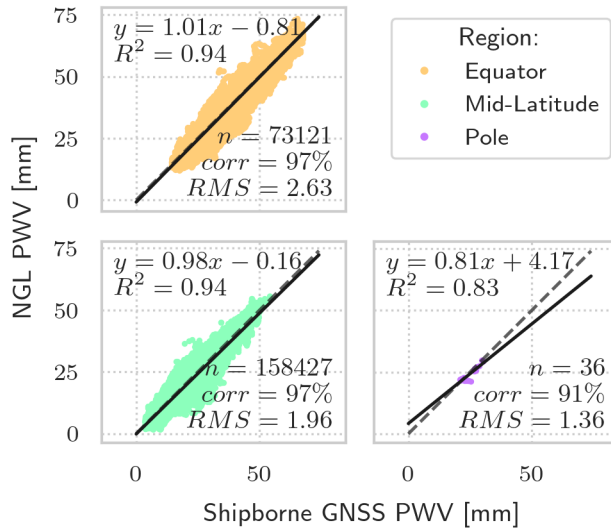


Figure 7.3: PWV scatter plot between shipborne GNSS antenna and nearby NGL ground stations for three latitude regions: the Pole, the Equator, and the mid-latitudes regions.

unsatisfying values are then still available in the comparison NGL dataset. The outliers are likely due to individual ground-based GNSS stations that provide inaccurate PWV compared to the other ground-based stations. This is all the more likely that many coastal ground stations are compared to the shipborne antenna at the same time, but only a few points are outliers.

As far as the datasets are equivalent - both coming from GNSS antennas - they should correspond more to one another than when compared to ERA5 or SMWR. However, it appears to provide the worst comparison. This is explainable by the fact that the PWV data from ground-based antennas is directly provided by the NGL website that provides international GNSS ground stations PWV products retrieved from ZWD by using VMF1 that is not well accurate for that application. Given the trajectory of the FOF R/Vs in Figure 6.1, we can state that the ground-based dataset used to compare to the shipborne GNSS PWV is heterogeneous.

In a nutshell, the higher scattering of the differences between the two GNSS datasets may be due to the inhomogeneity of the NGL dataset. Focusing on one region might help get better matching, as well as processing ground-based GNSS dataset with the same configuration and software as the FOF.

Globally, the zonal distribution presents difference patterns concerning the difference between the shipborne antenna PWV retrieval and external datasets.

7.2 IMPACT OF THE SEASON ON THE PWV COMPARISONS

It appears from the studies cited above that the seasons also have an impact on the PWV. This section will then focus on the seasonal impact on the PWV comparisons to the external datasets used in Chapter 6.

To this end, the FOF dataset has been limited to the mid-latitudes and split into four seasons:

- winter: from January to March;

- spring: from April to June;
- summer: from July to September;
- autumn: from October to December.

7.2.1 Seasonal Impact on the Comparison with ERA5

The scatter plot of the PWV differences with the ground-based GNSS antennas is represented Figure 7.4 for four different seasons in the mid-latitudes region.

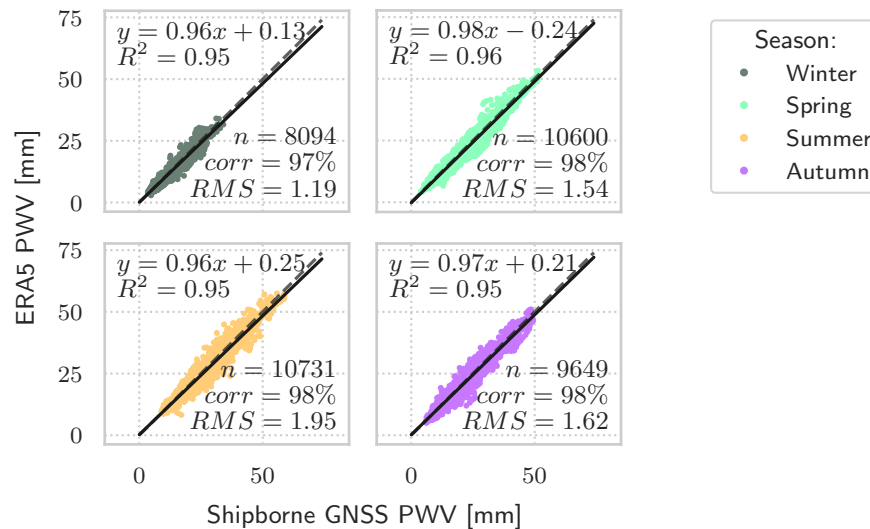


Figure 7.4: PWV scatter plot between shipborne GNSS antenna and ERA5 for three latitude regions: the Pole, the Equator, and the mid-latitudes regions.

The four seasons provide an equivalent size of comparison datasets between shipborne GNSS and ERA5.

The coefficients of determination of the linear regression are equivalent among the seasons, with the spring season being 1% better with $R^2 = 96\%$. The slope of the linear regression is slightly lower than 1 in all cases.

The differences result in RMSE values lower than the total RMSE value for the mid-latitude region of 1.66 mm displayed on Figure 7.1, except in summer where it reaches 1.95 mm. The best fitting between shipborne GNSS and ERA5 appears to be in winter when the PWV values are lower.

7.2.2 Seasonal Impact on the Comparison with SMWR

The scatter plot of the PWV differences with SMWR is represented Figure 7.5 for four different seasons in the mid-latitudes region.

The four seasons slicing provides comparison datasets of size going from simple (in winter) to double (in spring and summer). The R/Vs appear to spend less time offshore during autumn and winter, probably because it is cold and the sea state is too bad.

The coefficients of determination of the linear regression are also equivalent among the seasons, changing by at most 0.02 for the autumn season. Still, the slope of the linear regression is slightly lower than 1 in all cases.

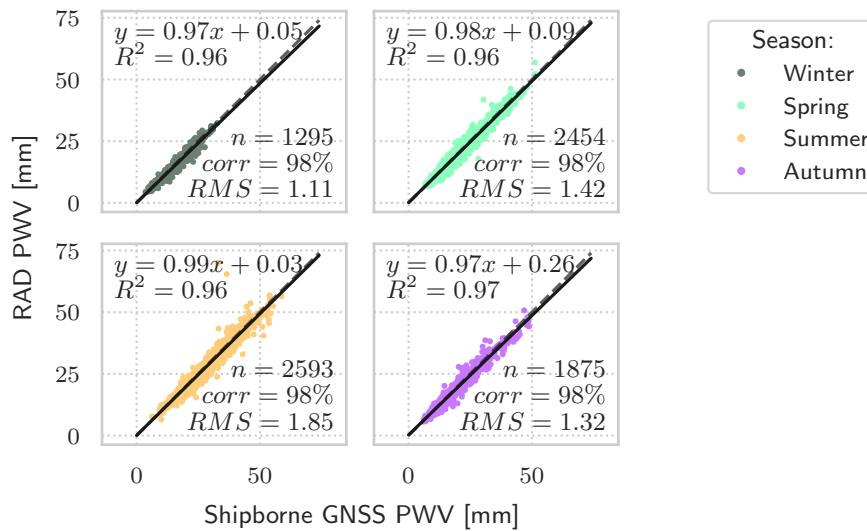


Figure 7.5: PWV scatter plot between shipborne GNSS antenna and SMWR for the different seasons in mid-latitude region.

All the four seasons comparisons are providing 98 % of correlation. As for the comparison to ERA5, the worst fitting season between shipborne GNSS and SMWR is summer, with the previously mentioned significant outliers being grouped in summer. This season provides the only RMSE above the total RMSE of 1.55 mm in Figure 7.2, with a rise of 0.30 mm. The best RMSE is also obtained in winter, but contrary to the comparison to ERA5, autumn provides a better RMSE than spring. This might be due to some outliers that can be seen on the spring season graph of the comparison to SMWR. These outliers are located in spring and summer, and always display a higher value for SMWR than for the shipborne GNSS, which might suggest an alteration of the GNSS or SMWR accuracy with the air temperature rises.

7.2.3 Seasonal Impact on the Comparison with NGL

The scatter plot of the PWV differences with the ground-based GNSS antennas from NGL is represented Figure 7.6 for four different seasons in the mid-latitudes region.

The mid-latitude region displayed an RMSE of 1.96 mm in Figure 6.9. As for the other seasonal studies above, the summer season displays the worst RMSE as high as 2.43 mm. However, the autumn season also has higher RMSE than the total mid-latitude region, with an RMSE increase of 9 %. The RMSE in spring is equivalent to the total mid-latitude region RMSE, while it is as low as 1.50 mm in winter.

Winter also displays the best coefficient of determination, but it is curiously lower than the global R^2 for mid-latitudes. Here also, the outliers displayed on the mid-latitude scatter plot of Figure 6.9 are essentially due to the summer.

The correlation coefficients are slightly degraded to 95 % in winter and autumn, and 94 % in spring and summer. This might also be due to the inhomogeneity of the NGL comparison dataset that might provide less consistency in the differences, which is even more obvious in seasonal cutting than in global study.

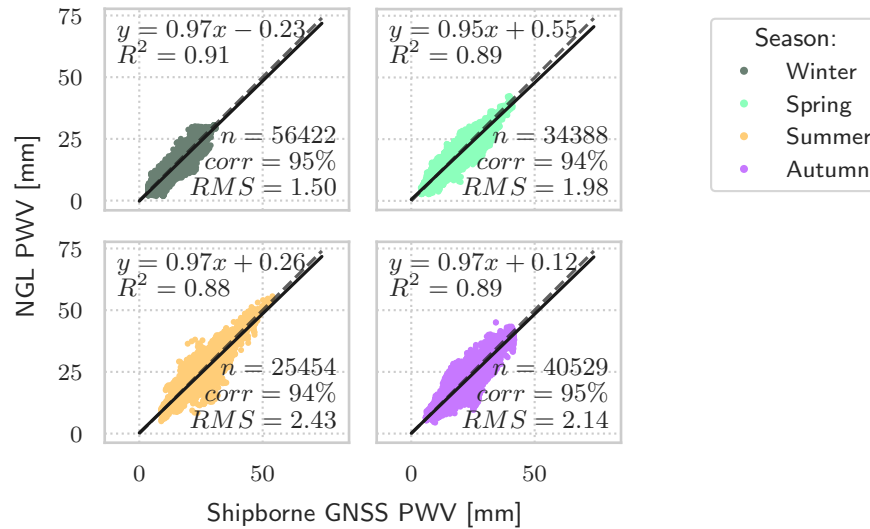


Figure 7.6: PWV scatter plot between shipborne GNSS antenna and NGL ground stations for the different seasons in mid-latitude region.

Contrary to the previous radiometer comparison per season, it appears that there are more comparisons in autumn and winter, showing that the R/Vs are indeed staying in coastal areas during the bad weather seasons.

7.3 CONTRIBUTION OF THE FOF DATASET TO THE CLIMATE STUDY

7.3.1 Latitude and PWV

We computed the mean of PWV values obtained for different latitudes on a 3° step, resulting in Figure 7.7.

Figure 7.7 shows that the mean water vapor content is higher in the Equatorial zone, and it decreases poleward. The standard deviation shows that the variations in PWV are lower at high latitudes, corroborating Hadas et al. (2017) [Had 17]. Considering the standard deviation represented with the blue frame in Figure 7.7, we can see that a curious effect occurs around 60° of latitude where a drop in standard deviation appears. This is an artifact because only a few points are available at the North of the Arctic Circle, so it is important to consider that the R/V did not stay long enough to capture all the trends that are occurring at these latitudes. The latitudes around 60° are covered only by L'Atalante while it is passing by its route to and from Svalbard (see Figure 6.1), so no R/V is staying a while in this zone.

From 0° to 30° , the standard deviation of the PWV measurements is quite stable, so it appears that even if the amount of available water vapor increases, their variations are steady.

We have separated the shipborne PWV dataset into three regional categories such as:

- Equatorial region between the Tropics of Cancer and Capricorn;
- mid-latitudes region between the Tropic of Cancer and the Arctic Circle;
- Polar region above the Arctic Circle,

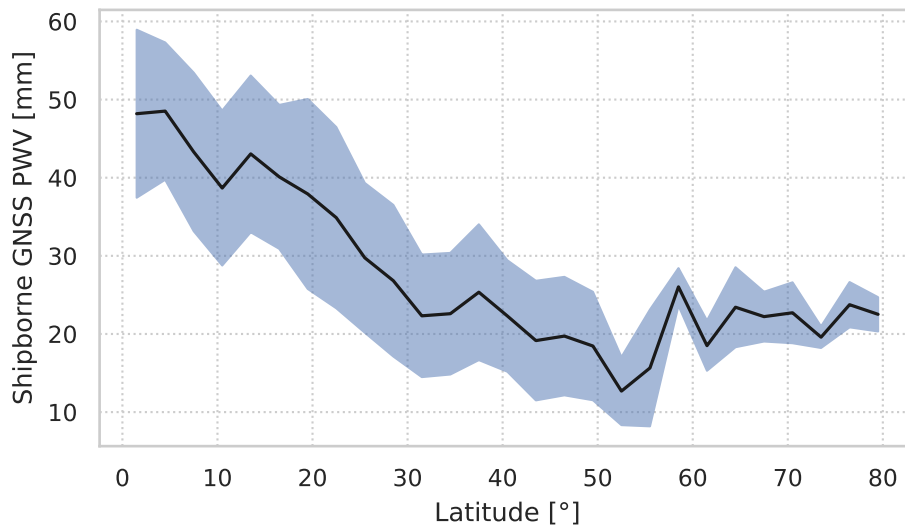


Figure 7.7: Shipborne GNSS PWV values as a function of the absolute value of the latitude of the R/V with a 3° of latitude step. The black curve represents the mean PWV value with a 3° latitude step, while the blue frame is the standard deviation of the shipborne PWV values at the given latitude. The blue curve shows the number of points available for each step of computing.

and computed the statistics of the regional datasets showed in Figure 7.8.

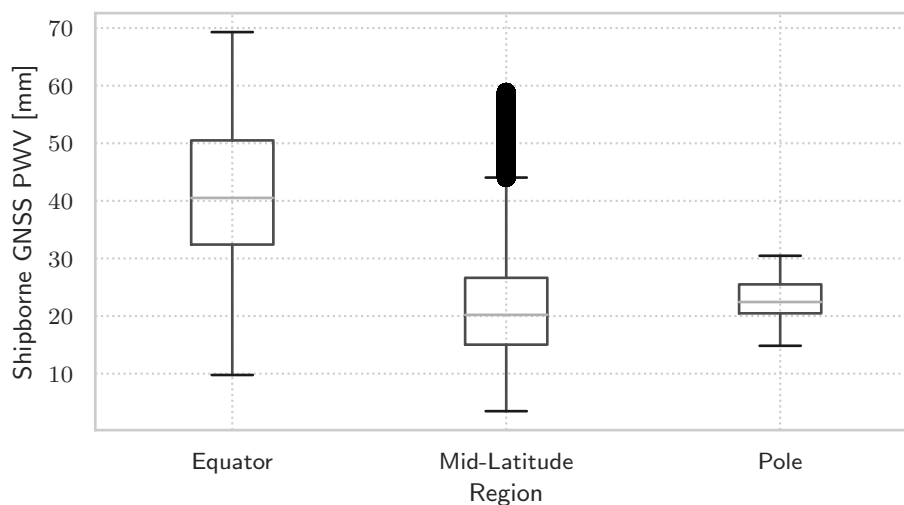


Figure 7.8: Statistics of the PWV distribution in each region.

As seen in Figure 7.8, the median value in the Equatorial region is much higher as it is doubled compared to the mid-latitudes region. The quartiles are more spread out at the Equator than in the mid-latitudes region.

Many outliers arise to high PWV values for the mid-latitude region. These outliers can be due to atmospheric disturbances caused by the crossing of storms driving a lot of water vapor occasionally.

The median value at the Pole is quite higher than at the mid-latitudes because L'Atalante went there during less than three weeks in summer - the most humid

season in this region, from the 6th to 24th of July, 2016, which implies that the captured water vapor corresponded to higher temperatures, and then higher atmospheric water contents, compared to the expected mean *PWV* over the whole year. The *PWV* quartiles of the Polar region are located in between the median and third quartile of the mid-latitudes.

7.3.2 Season and *PWV* in Mid-Latitudes Region

In all three cases of [Section 7.2](#), we can see that spring and autumn have the same behavior, while summer and winter are different. This effect might be due to the *PWV* behavior that is temporally more variable in the hot season and less variable in the cold season, due to the higher amount of water vapor storage in a warm atmosphere [[Din 22](#)].

The above mid-latitudes region has been selected, and grouped into seasons:

- winter: from January to March;
- spring: from April to June;
- summer: from July to September;
- autumn: from October to December.

The resulting distribution statistics are displayed in [Figure 7.9](#).

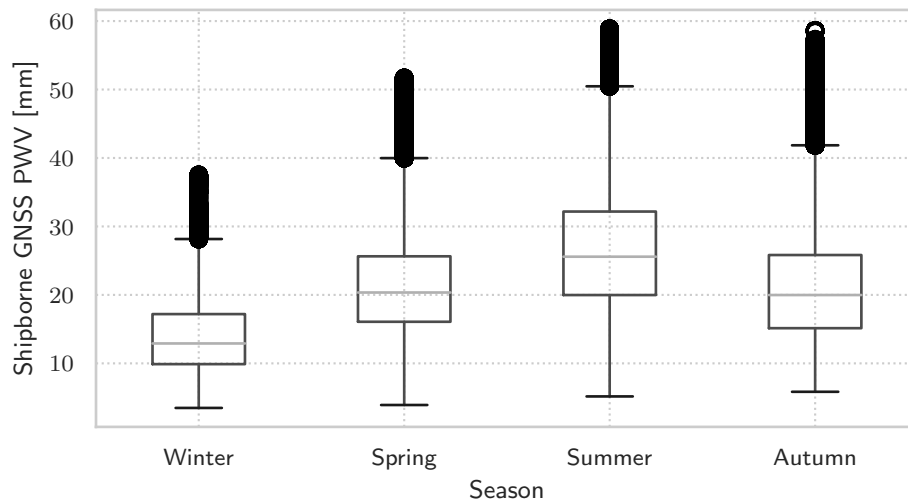


Figure 7.9: Statistics of the *PWV* distribution in each season in the mid-latitudes region.

The median and third quartile values in spring and autumn are equivalent, but the first quartile is higher in spring. However, the minimum and maximum values are lower for spring than autumn, due to the mean offset in autumn due to the numerous outliers in high *PWV* values. These outliers might be due to exceptional weather conditions such as storms.

The summer shows the highest median and quartile values with a wider interquartile range, while it is the contrary with winter. Then, it seems that the *PWV* variations are wider in summer and lower in winter, with more available water vapor in the atmosphere due to the increase in temperature [[Gue 22](#)].

7.3.3 Correlation with Sea Surface Temperature

The **PWV** amount above the oceans is mainly due to the water evaporation from the oceans. Several studies have then shown the close relationship between **SST** and **PWV** [Steg0; Kan 13].

The **FOF R/Vs** are equipped with **SST** sensors, and the Copernicus Marine and Environment Service distributes the data daily through the **Coriolis database**. The data provided for Alis are available for the 2019-2022 period only. Both time series of the **FOF** dataset are displayed in **Figure 7.10**.

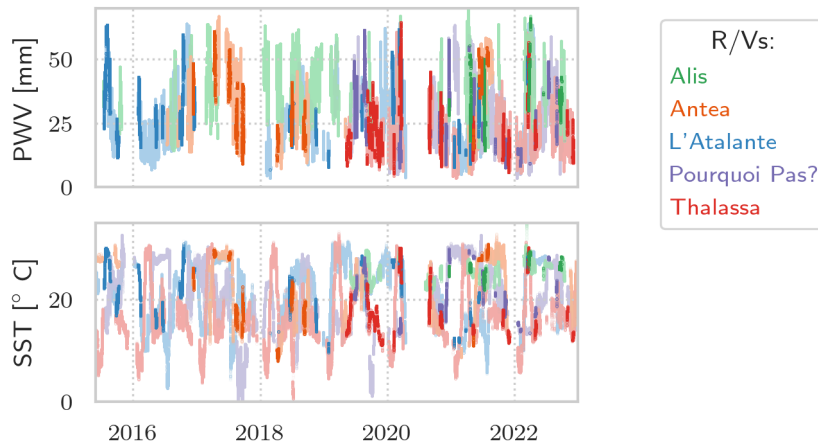


Figure 7.10: **FOF PWV** (top) and **SST** (bottom) time series available along the period of study. The different colors correspond to the different **R/Vs**. The lightened color points correspond to the data that have no matching times in the other time series.

We can see in **Figure 7.10** that the **PWV** variations seems noisier than the **SST**. The Covid-19 effect is visible through the hole in both graphs in 2020. The light color points correspond to the data that are not taken into account for the comparison because there is no time matching. We can see from the low number of corresponding data from **SST** that the geodetic antenna is not logging data during all the campaigns. For example, no data was provided for L'Atalante in 2017 while it was operational according to the **SST** dataset. Some of the missing **PWV** data are also because the **R/Vs** are operated by the **SHOM**, a French Navy organism, so the data corresponding to their campaigns are not available either.

These **SST** measurements are compared to the shipborne **GNSS PWV** measurements by matching the nearest times, corresponding to the plain color points in **Figure 7.10**.

The correlation coefficients for each **R/V** are displayed in **Table 7.1**.

We can see in **Table 7.1** that as for the previous comparisons of **PWV**, Thalassa provides the strongest correlation coefficient, followed by Pourquoi Pas? three points lower. Antea dataset appears to be better correlated to **SST** than L'Atalante. Although these **R/Vs** provide correlation coefficients around 80 %, Alis is as low as 37 %, less than half the others. Alis **PWV** quality seems to be equivalent to the other **R/Vs**, and the **SST** are validated before Copernicus makes them available. This **R/V** is the only one traveling only in the Equatorial region in the Pacific Ocean, where it is warmer than in other parts where the other **R/Vs** are staying most of the time. This can then be an explanation of this discrepancy. Indeed, the poor annual correlation between **PWV** and **SST** in the Western Pacific Ocean, where Alis stands, has been brought out

R/V	Correlation
Alis	37 %
Antea	80 %
L'Atalante	76 %
Pourquoi Pas?	82 %
Thalassa	85 %

Table 7.1: Correlation coefficients between shipborne GNSS PWV measurements and SST measurements.

by Stephens (1990) [Ste90]. The author brings out the PWV anomaly due to the 1983 El Niño, which was outstandingly strong [Can83]. He explains that El Niño episodes shift the usual Western Pacific Ocean deep convection to the Eastern part of the Pacific Ocean, creating a dryer-than-usual atmosphere in the Western Pacific Ocean.

As far as Alis is sailing the Western Pacific Ocean, we can state that the PWV was affected by the 2015 El Niño episode. Similarly to the episode studied in Stephens (1990) [Ste90], the 2015 episode appears to have lasted until 2016 and is recognized as one of the strongest episodes from records [Che 17]. Then, the PWV was particularly driven by another phenomenon independent from the SST during this period, hence a poor correlation in the data that could be found these years. However, only a few data are available on this period compared to the whole Alis dataset as seen in Figure 6.2.

Stephens (1990) [Ste90] also adds that under normal climate, the intertropical convergence zone (ITCZ) creates regions of unusual PWV balance because of its moisture convergence effect, and the enhancement of PWV because of the ITCZ driven advection of moist air in dryer region. Alis, sailing in the Equatorial region, is then probably affected by these phenomena as well.

The scatter plot of the SST with regard to the PWV results in Figure 7.11.

The general trend observed in Figure 7.11 can be partly explained by the empirical analytic relationship proposed by Stephens (1990) [Ste90], coming from the Clausius-Clapeyron equation:

$$PWV = 108.2 * \frac{RH}{1 + \lambda} * e^{a*(SST-288)} \quad (7.1)$$

where SST denotes the SST in Kelvin, RH denotes the relative humidity (RH) $\lambda = \frac{H}{H_{wv}}$ denotes the scale factor between the atmosphere scale height H with regards to the atmospheric water vapor scale height H_{wv} , and $a = 0.064 \text{ K}^{-1}$. The scale height of the atmosphere is defined in terms of an air pressure decrease of $\frac{1}{e}$ compared to the Earth's surface [Ste90]: $H = 7.64 \text{ km}$. However, the atmospheric water vapor scale height is too much varying to be determined, so we call the lambda scale that is usually set to values between 2 for low air temperature and 4 for high air temperature [Ste90]. The resulting trend has been drawn in Figure 7.11 for λ values of 3 and 4, because our R/Vs are almost never crossing the Polar Circle so $\lambda = 2$ should not be representative of any region of our dataset. The RH value is set as a constant of 75 %, following the recommendation from Choubeau, Chédin, and Scott (1998) [Cha 98].

However, Equation (7.1) relies on the hypotheses that the RH is homogeneous and SST-dependent only and that the water vapor has a coherent vertical distribution with

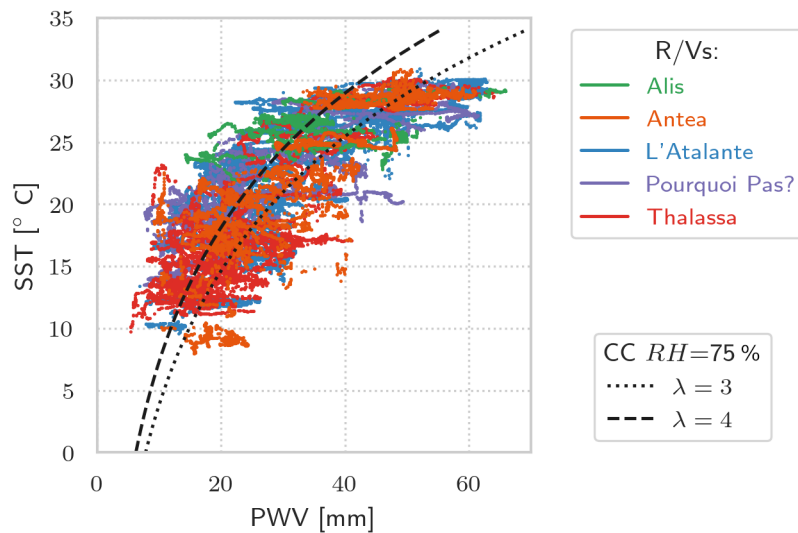


Figure 7.11: Relation between each R/V SST (top left) and PWV (bottom left) measurements. The scatter plot of the SST with regard to the PWV is provided along with the Clausius-Clapeyron (CC) theoretical relation (right) for λ values set to 3 and 4, and RH value set to 75 % [Cha 98].

a constant scale factor. The Stephens (1990) [Stego] relationship is then useful to understand the trend but is not applicable as is to our dataset.

Except for Alis, we can state that the correlation is good between the FOF R/Vs retrieved PWV and the SST. Thus, shipborne GNSS retrieved PWV measurements could contribute to a better understanding of the SST contribution to the global climate as well as the atmospheric water vapor.

7.4 CONCLUSION ON THE CONTRIBUTION OF SHIPBORNE PWV TO ATMOSPHERE WATER VAPOR MONITORING

It has been demonstrated that the differences of the PWV dataset from the shipborne GNSS antenna and the external dataset - namely the NWM ERA5 of the ECMWF, SMWR from Remote Sensing Systems, and NGL-provided ground-based GNSS stations tropospheric products - are affected by the latitude and the seasons at mid-latitudes.

A regional study showed a correlation between the region and the PWV fitting. An increase appears in the difference RMSE when approaching the Equator, while the Pole shows the best fitting datasets. This appears for all the comparison datasets and has been observed in other studies such as Mears et al. (2015) [Mea 15].

As opposed to winter, summer provides noisier differences with high PWV values due to the higher air temperature. Spring and autumn have equivalent behaviors that are intermediary.

The fact that these patterns are common through all the different comparison datasets, indicates that a correlation might be drawn between the air temperature and PWV measurements in general. Indeed, the behavior for each season is not the same so it can not be due only to a shipborne GNSS measurement flaw.

The differences due to the region and the season for the mid-latitude region explored above may be partially explained by the distance between the R/V and the comparison dataset, especially in the case of ERA5 and NGL comparisons. However, the SMWR

comparison technique does not permit to explain the comparison behavior this way. Another clue is the ability of the different PWV datasets to provide sufficient temporal resolution. Indeed, ERA5 and SMWR have poor time resolution in a given location, with 1 h period and twice a day respectively. This does not permit catching the high-frequency variability of the PWV that the GNSS, shipborne or ground-based, is better able to relay.

Shipborne GNSS might help to fill a gap in atmosphere monitoring of water vapor in remote areas such as the middle of the oceans or coastal areas of under-developed countries providing fewer measurements of water vapor, providing additional high-resoluted tropospheric products. These products can be used for the evaluation of external datasets such as SWVR and ERA5, as well as NWP if they are extended to near-real time and assimilated to the weather forecast models.

GENERAL CONCLUSION AND OUTLOOK

CONTENT

8.1	Context	135
8.2	Overview of the Undertaken Work and Achieved Outcomes	136
8.3	Future Prospects	137

8.1 CONTEXT

The Global Navigation Satellite System (GNSS) is a ubiquitous tool in today's societies. The high level of accuracy has made the GNSS the rank of the time reference technique in various fields of study. The simple and cost-effective solution of location and navigation through GNSS has made it the most common positioning technique in everyday life. More expensive receivers, called geodetic receivers, are also available for preciseness applications. Through the years, they have been used on land for military applications such as drone guidance, civil applications such as air transportation or autonomous cars, geology applications such as Earth shape study and seismology, and atmosphere monitoring such as climate study and meteorology. The two latter have gained interest through the last decades, and several networks of geodetic antennas has been spread out the European continent, benefiting the E-GVAP project, proving successful for weather forecast and climate trends study. Indeed, the precipitable water vapor (PWV), useful for numerical weather prediction (NWP) and climate study, can be retrieved from the tropospheric delay estimated from the GNSS data processing.

Furthermore, an accurate estimation of tropospheric delay is essential for the analysis of kinematic precise point positioning (PPP) GNSS data such as those acquired from shipborne antennas. This is especially critical as the troposphere delay is highly correlated with the antenna height during the estimation process. However, it is possible to finely tune the processing model while processing kinematic GNSS data. An adequate configuration of the processing filter permits a more accurate estimation by limiting the multipath effect, decorrelating the troposphere delay from the height estimate, and constraining the troposphere delay temporal variation range. A high accuracy of such retrieved PWV could be valuable for offshore atmosphere column monitoring, filling a gap in the data availability above the ocean surface. A state-of-the-art of the major studies about retrieving PWV from shipborne GNSS antennas has been performed in Chapter 3, stating the accuracy to be expected from similar studies undertaken in this thesis.

8.2 OVERVIEW OF THE UNDERTAKEN WORK AND ACHIEVED OUTCOMES

In the second part of this thesis, an assessment has been performed of different processing configurations by evaluating the quality of the height and ZWD estimates. The third part dealt with the post-processing of a nine-year-long-lasting shipborne GNSS dataset covering various parts of the oceans, from five offshore R/Vs.

A 49-day period of GNSS data acquired from the research vessel (R/V) of ENSTA Bretagne has been post-processed using a set of combinations of PPP processing configurations. The resulting estimated height and PWV have been compared to other near datasets from tide gauge, ground-based GNSS station and radiosonde (RS), and the statistics of the differences have been computed for each processing configuration. The comparison of these statistical results has permitted us to highlight in Chapter 4 the significant difference in estimation due to the processing modeling.

However, this study is not meant to recommend any processing strategy for shipborne GNSS, as the vessel is mostly docked in the Brest harbor during the study, and never leaves the Bay of Brest. Thus, it is not representative of a real shipborne GNSS dataset sailing in the middle of the ocean. To address this issue, we have made up a simulated shipborne GNSS carrier-phase signal.

The Chapter 5 simulated carrier phase has been shaped from several simulated GNSS variables such as positioning and troposphere. The GNSS signal has then been processed through a Kalman Filter with a set of processing configurations such as for the previous real shipborne GNSS dataset, estimating the positioning of the antenna, the troposphere, and the clock delay parameters. These parameters were compared to the corresponding simulated quantities, leading to a different time series for each processing configuration. The statistical results from the differences have been compared to one another such as for the previous study on the R/V of ENSTA Bretagne. The best-performing configuration was selected as the lowest bias and standard deviation resulting in height and ZWD errors.

After analyzing the results from the simulated dataset, the recommended configuration for shipborne GNSS antenna processing is set up as $\text{co } 3^\circ - \text{wg } \sqrt{\sin} - \text{rw } 5 \text{ mm} \cdot \text{h}^{-0.5}$. This configuration is then applied to the long-lasting GNSS FOFs dataset provided by IFREMER, covering five offshore R/V campaigns between 2015 and 2022.

The retrieved PWV along the path of the five R/Vs in Chapter 6, have been compared to external datasets such as satellite-borne radiometers, coastal ground-based GNSS stations, and the numerical weather model (NWM) from the European Center for Medium-range Weather Forecasts (ECMWF) called ERA5. The results of this analysis proved satisfying regarding the other similar published studies detailed in Chapter 3. Going into detail, some R/Vs showed highly accurate PWV retrieval compared to the reference dataset, while one of them, located in the Equatorial region showed the poorest agreement with the references.

To process the shipborne GNSS dataset for atmosphere monitoring, it would be better to use all the GNSS constellations available, as we have shown in Chapter 5 that the results were more accurate than with GPS only. However, this requires high data storage capacity or high transmission capacity. This is not always possible, such as the FOF dataset for which only the GPS data was available. Above all, the best advice would be to place the antenna as high as possible to limit the multipath effect spoiling the GNSS signal, leading to poor PWV reliability. Using an elevation-dependent-only

antenna correction can also help increase the estimation accuracy, as the orientation of the *R/V* is unknown, moving according to the vessel heading.

8.3 FUTURE PROSPECTS FOR OFFSHORE ATMOSPHERE WATER VAPOR MONITORING FROM SHIPBORNE GNSS ANTENNAS

The recent years' impetus of the shipborne *GNSS PWV* retrieval led to new ambitions for *GNSS* monitoring of the atmosphere water vapor. The real-time or near real-time processing of shipborne *GNSS* data could be useful for offshore weather forecasting, by assimilating the retrieved *PWV* data in numerical weather prediction (*NWP*) models. This makes it possible to monitor the weather ahead of the coast, improve forecasting, and ensure the safety of coastal populations by preventing severe weather episodes several hours in advance. However, several issues arise, such as the data transmission from ships to weather data centers, or accurate *GNSS* satellite orbital products availability in real-time or near real-time. It can be proposed that the shipborne *GNSS* data are periodically transmitted on a 10 to 60 minutes basis to a ground-based computing center. This technique permits to avoid hogging the carrying vessel's connection.

In the framework of the project *ROBUSTA-3A*, a CubeSat built by the Centre Spatial Universitaire de Montpellier (*CSUM*) will be sent in low Earth orbit (*LEO*) in mid-2024 to transmit shipborne *GNSS* data from commercial ships daily crossing the Mediterranean Sea between Sète and Corsica, to computation centers of Météo France. The goal of this project is to better predict deadly strong thunderstorm episodes with heavy rain occurring in the South of France, where they are known as "cévenol episodes".

The methodological developments carried out as part of this thesis concern the analysis of all *GNSS* data acquired at sea, regardless of the latency between the acquisition of raw *GNSS* data and its analysis. However, we have focused on a delayed-time analysis, in the context of an exploitation for applications in climatology. A use in numerical weather prediction is also fully conceivable.

An initial evaluation of a *NRT* calculation was carried out in summer 2023 using data acquired on board the *R/V* Marion Dufresne as part of the *MAP-IO* project [Tul 24; Bos 22b]. Since the beginning of 2023, data have been transmitted from the *R/V* to a data server on land, at 15 of every hour, and are available for processing.

Routine post-processing was carried out for one month in August 2023, using *GipsyX* software:

- the analysis is started at 20 of each hour, over a 24-hour window: at $hh : 20$, the data acquired from $hh - 24$ h to hh is processed;
- the classic *JPL* products are not available with a latency of less than about 1 h30. We therefore use real-time products from the *IGS-RT* working group, made available by *JPL* (with updates at 1 Hz). These products have the advantage of being available quickly (latency of a few seconds), for the *GPS*, *GLONASS*, and Galileo constellations, but do not allow ambiguities to be resolved as satellite phase biases are not provided;
- the calculation parameters are standard (in accordance with Chapter 4 and Chapter 6) and take into account the code and phase observables from the *GPS*, *GLONASS* and Galileo constellations.

Here, the last hour of each *NRT* calculation is taken into account for evaluation purposes, data that would be most useful for assimilation into a regional numerical

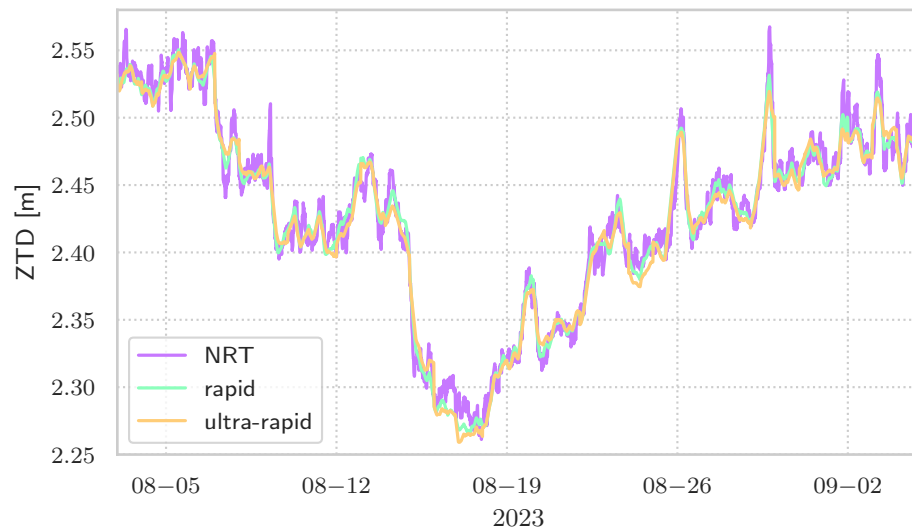


Figure 8.1: **NRT ZTD** time series from a shipborne **GNSS** antenna (yellow) with rapid (day+3, green) and ultra-rapid (day+1, purple) post-processing solutions.

weather prediction model such as Applications de la Recherche à l'Opérationnel à Méso-Echelle (**AROME**), a fine-grid numerical weather prediction model used by Météo-France since 2008 for operational forecasting in mainland France.

Figure 8.1 shows the temporal evolution of the ZTD resulting from the analysis of data in rapid mode (temporal resolution of 30 s, day+3), ultra-rapid mode (temporal resolution of 300 s, day +1) and **NRT** mode (temporal resolution of 30 s, +20 h', last hour) over the month of August 2023. Rapid and ultra-rapid processing were validated by Bosser, Van Baelen, and Bousquet (2022) [**Bos 22b**]. There is good agreement between the different time series, with more pronounced variability in the **NRT** calculation, probably due to the lower quality of the orbits and the lack of ambiguity resolution. The ultra-rapid calculation shows deviations from the rapid calculation, as already explained in Bosser, Van Baelen, and Bousquet (2022) [**Bos 22b**].

The average deviations between the **NRT** and rapid ZTD calculations are (-0.8 ± 10.3) mm, and (-1.0 ± 5.4) mm of ZTD difference between ultra-rapid and rapid: the **NRT** calculation shows much larger deviations. The **RMSEs** are less than 10.5 mm in ZTD (i.e. around 1.5 mm **PWV**, see Section 2.5.1) and are therefore compatible with the requirements in terms of uncertainty for use in numerical weather prediction [**Off 10**].

APPENDICES



STATISTICAL RESULTS OF THE ENSTA BRETAGNE HYDROGRAPHIC VESSEL COMPARISON TO THE BRST GROUND-BASED GNSS STATION

This appendix provides tables displaying the statistical results obtained from the study on the [ENSTA Bretagne](#) survey vessel [GNSS](#) dataset. They list the results of the difference with the reference datasets, for all the tested configurations for the analysis. [Table A.1](#) presents the statistical differences between the surface height estimated from the vessel antenna height and the Penfeld tide gauge [SSH](#) measurement. [Table A.2](#) presents the statistical differences in the [PWV](#) retrieved from the vessel and the Brest harbor ground-based antennas.

co [°]	wg	rw [mm·h ^{-0.5}]	STD [cm]	RMSE [cm]
3	<i>cst</i>	3	3.7	4.8
		5	3.7	4.8
		10	3.9	5.0
	<i>sin</i>	3	3.8	5.5
		5	3.8	5.5
		10	4.0	5.6
	$\sqrt{\sin}$	3	3.6	4.9
		5	3.6	5.0
		10	3.8	5.1
7	<i>cst</i>	3	3.7	4.9
		5	3.7	5.0
		10	3.9	5.2
	<i>sin</i>	3	3.8	5.6
		5	3.8	5.6
		10	3.9	5.7
	$\sqrt{\sin}$	3	3.6	5.0
		5	3.7	5.2
		10	3.8	5.2
10	<i>cst</i>	3	3.8	5.2
		5	3.9	5.3
		10	4.2	5.5
	<i>sin</i>	3	3.9	5.8
		5	3.9	5.9
		10	4.1	6.0
	$\sqrt{\sin}$	3	3.7	5.4
		5	3.8	5.6
		10	4.0	5.5

Table A.1: Standard deviation (STD) and RMSE of the difference between the survey vessel antenna height and Penfeld tide gauge sea surface height for all processing models. The statistical values of the height differences are expressed in centimeters. co stands for the cut-off angle, wg for the weighting function of the elevation, and rw for the ZTD random walk value.

co [°]	WG	RW [mm·h ^{-0.5}]	RMSE [mm]
3	<i>cst</i>	3	0.6
		5	0.7
		10	0.9
	<i>sin</i>	3	0.7
		5	0.7
		10	0.8
	$\sqrt{\sin}$	3	0.5
		5	0.6
		10	0.7
7	<i>cst</i>	3	0.6
		5	0.7
		10	0.9
	<i>sin</i>	3	0.8
		5	0.7
		10	0.9
	$\sqrt{\sin}$	3	0.6
		5	0.6
		10	0.8
10	<i>cst</i>	3	0.6
		5	0.7
		10	1.0
	<i>sin</i>	3	0.9
		5	0.9
		10	1.0
	$\sqrt{\sin}$	3	0.7
		5	0.7
		10	0.9

Table A.2: RMSE of the difference between survey vessel antenna PWVs and BRST antenna PWV for all the tested processing models. The RMSEs of the PWV differences are expressed in millimeters.

B

STATISTICAL RESULTS OF THE ESTIMATION ERRORS FROM SIMULATED DATASET

This appendix provides tables displaying the statistical results obtained from the study on the simulated GNSS dataset. Table B.1 lists the statistical error for the estimated height of the antenna, whereas Table B.2 presents the error on the ZWD estimate.

Table B.1: Statistical results of the height estimation for each processing model. Average (**m**) and dispersion (**STD**) values over the 200 height biases and height standard deviations (**STD**) of the difference between estimation and simulation for each processing model.

Processing Modeling			Height Bias		Height STD	
CO	RW	WG	m	STD	m	STD
[°]	[mm·h ^{-0.5}]		[mm]	[mm]	[mm]	[mm]
3	1	<i>cst</i>	0.1	1.0	17.3	0.4
3	1	<i>sin</i>	0.0	2.3	12.0	0.8
3	1	$\sqrt{\sin}$	-0.1	1.4	12.4	0.5
3	1	\cos^{-4}	-0.2	1.3	14.6	0.5
3	3	<i>cst</i>	0.4	0.4	14.5	0.2
3	3	<i>sin</i>	0.0	0.8	9.5	0.3
3	3	$\sqrt{\sin}$	0.0	0.5	10.0	0.2
3	3	\cos^{-4}	0.1	0.5	11.8	0.2
3	5	<i>cst</i>	0.4	0.3	13.6	0.1
3	5	<i>sin</i>	0.0	0.5	8.9	0.2
3	5	$\sqrt{\sin}$	0.0	0.3	9.4	0.1
3	5	\cos^{-4}	0.2	0.3	11.0	0.2
3	7	<i>cst</i>	0.1	1.0	17.3	0.4
3	7	<i>sin</i>	0.0	2.3	12.0	0.8
3	7	$\sqrt{\sin}$	-0.1	1.4	12.4	0.5
3	7	\cos^{-4}	-0.2	1.3	14.6	0.5
3	8	<i>cst</i>	0.4	0.4	14.5	0.2
3	8	<i>sin</i>	0.0	0.8	9.5	0.3
3	8	$\sqrt{\sin}$	0.0	0.5	10.0	0.2

Continued on next page

Table B.1: Statistical results of the height estimation for each processing model. – continued from previous page

Processing Modeling			Height Bias		Height STD	
CO	RW	WG	m	STD	m	STD
[°]	[mm·h ^{-0.5}]		[mm]	[mm]	[mm]	[mm]
3	8	\cos^{-4}	0.1	0.5	11.8	0.2
3	10	cst	0.4	0.2	13.5	0.1
3	10	\sin	0.0	0.3	8.6	0.1
3	10	$\sqrt{\sin}$	0.1	0.2	9.2	0.1
3	10	\cos^{-4}	0.2	0.2	10.3	0.1
3	11	cst	0.4	0.3	13.6	0.1
3	11	\sin	0.0	0.5	8.9	0.2
3	11	$\sqrt{\sin}$	0.0	0.3	9.4	0.1
3	11	\cos^{-4}	0.2	0.3	11.0	0.2
3	12	cst	0.4	0.2	13.5	0.1
3	12	\sin	0.0	0.3	8.6	0.1
3	12	$\sqrt{\sin}$	0.1	0.2	9.2	0.1
3	12	\cos^{-4}	0.2	0.2	10.3	0.1
3	15	cst	0.3	0.2	14.9	0.1
3	15	\sin	-0.1	0.3	8.9	0.1
3	15	$\sqrt{\sin}$	0.0	0.2	9.6	0.1
3	15	\cos^{-4}	0.1	0.2	10.6	0.1
3	20	cst	0.3	0.2	14.9	0.1
3	20	\sin	-0.1	0.3	8.9	0.1
3	20	$\sqrt{\sin}$	0.0	0.2	9.6	0.1
3	20	\cos^{-4}	0.1	0.2	10.6	0.1
7	1	cst	0.2	1.4	14.6	0.5
7	1	\sin	0.0	3.0	12.6	1.1
7	1	$\sqrt{\sin}$	0.1	2.0	12.5	0.7
7	1	\cos^{-4}	0.1	2.0	13.1	0.7
7	3	cst	0.1	0.6	12.4	0.2
7	3	\sin	0.0	1.1	9.9	0.3
7	3	$\sqrt{\sin}$	0.1	0.7	10.0	0.3
7	3	\cos^{-4}	0.1	0.7	10.5	0.2
7	5	cst	0.1	0.4	11.8	0.2
7	5	\sin	0.0	0.7	9.2	0.2
7	5	$\sqrt{\sin}$	0.0	0.5	9.4	0.2
7	5	\cos^{-4}	0.1	0.5	9.9	0.2

Continued on next page

Table B.1: Statistical results of the height estimation for each processing model. – continued from previous page

Processing Modeling			Height Bias		Height STD	
CO	RW	WG	m	STD	m	STD
[°]	[mm·h ^{-0.5}]		[mm]	[mm]	[mm]	[mm]
7	7	<i>cst</i>	0.2	1.4	14.6	0.5
7	7	<i>sin</i>	0.0	3.0	12.6	1.1
7	7	$\sqrt{\sin}$	0.1	2.0	12.5	0.7
7	7	\cos^{-4}	0.1	2.0	13.1	0.7
7	8	<i>cst</i>	0.1	0.6	12.4	0.2
7	8	<i>sin</i>	0.0	1.1	9.9	0.3
7	8	$\sqrt{\sin}$	0.1	0.7	10.0	0.3
7	8	\cos^{-4}	0.1	0.7	10.5	0.2
7	10	<i>cst</i>	0.1	0.3	11.5	0.2
7	10	<i>sin</i>	0.0	0.4	8.9	0.2
7	10	$\sqrt{\sin}$	0.1	0.3	9.2	0.1
7	10	\cos^{-4}	0.1	0.3	9.6	0.2
7	11	<i>cst</i>	0.1	0.4	11.8	0.2
7	11	<i>sin</i>	0.0	0.7	9.2	0.2
7	11	$\sqrt{\sin}$	0.0	0.5	9.4	0.2
7	11	\cos^{-4}	0.1	0.5	9.9	0.2
7	12	<i>cst</i>	0.1	0.3	11.5	0.2
7	12	<i>sin</i>	0.0	0.4	8.9	0.2
7	12	$\sqrt{\sin}$	0.1	0.3	9.2	0.1
7	12	\cos^{-4}	0.1	0.3	9.6	0.2
7	15	<i>cst</i>	0.2	0.2	12.3	0.2
7	15	<i>sin</i>	0.0	0.3	9.2	0.1
7	15	$\sqrt{\sin}$	0.1	0.3	9.6	0.2
7	15	\cos^{-4}	0.1	0.3	9.9	0.1
7	20	<i>cst</i>	0.2	0.2	12.3	0.2
7	20	<i>sin</i>	0.0	0.3	9.2	0.1
7	20	$\sqrt{\sin}$	0.1	0.3	9.6	0.2
7	20	\cos^{-4}	0.1	0.3	9.9	0.1
10	1	<i>cst</i>	-0.6	1.9	13.4	0.6
10	1	<i>sin</i>	-0.3	3.6	13.0	1.3
10	1	$\sqrt{\sin}$	-0.4	2.6	12.6	0.9
10	1	\cos^{-4}	-0.4	2.6	12.8	0.9
10	3	<i>cst</i>	-0.6	0.7	11.2	0.2

Continued on next page

Table B.1: Statistical results of the height estimation for each processing model. – continued from previous page

Processing Modeling			Height Bias		Height STD	
co	RW	WG	m	STD	m	STD
[°]	[mm·h ^{-0.5}]		[mm]	[mm]	[mm]	[mm]
10	3	<i>sin</i>	-0.3	1.3	10.2	0.4
10	3	$\sqrt{\sin}$	-0.4	0.9	10.0	0.3
10	3	\cos^{-4}	-0.4	0.9	10.2	0.3
10	5	<i>cst</i>	-0.6	0.5	10.8	0.2
10	5	<i>sin</i>	-0.3	0.9	9.6	0.3
10	5	$\sqrt{\sin}$	-0.4	0.6	9.4	0.2
10	5	\cos^{-4}	-0.4	0.7	9.6	0.2
10	7	<i>cst</i>	-0.6	1.9	13.4	0.6
10	7	<i>sin</i>	-0.3	3.6	13.0	1.3
10	7	$\sqrt{\sin}$	-0.4	2.6	12.6	0.9
10	7	\cos^{-4}	-0.4	2.6	12.8	0.9
10	8	<i>cst</i>	-0.6	0.7	11.2	0.2
10	8	<i>sin</i>	-0.3	1.3	10.2	0.4
10	8	$\sqrt{\sin}$	-0.4	0.9	10.0	0.3
10	8	\cos^{-4}	-0.4	0.9	10.2	0.3
10	10	<i>cst</i>	-0.4	0.3	10.8	0.2
10	10	<i>sin</i>	-0.3	0.5	9.2	0.2
10	10	$\sqrt{\sin}$	-0.3	0.4	9.2	0.2
10	10	\cos^{-4}	-0.4	0.4	9.4	0.2
10	11	<i>cst</i>	-0.6	0.5	10.8	0.2
10	11	<i>sin</i>	-0.3	0.9	9.6	0.3
10	11	$\sqrt{\sin}$	-0.4	0.6	9.4	0.2
10	11	\cos^{-4}	-0.4	0.7	9.6	0.2
10	12	<i>cst</i>	-0.4	0.3	10.8	0.2
10	12	<i>sin</i>	-0.3	0.5	9.2	0.2
10	12	$\sqrt{\sin}$	-0.3	0.4	9.2	0.2
10	12	\cos^{-4}	-0.4	0.4	9.4	0.2
10	15	<i>cst</i>	-0.3	0.3	11.6	0.2
10	15	<i>sin</i>	-0.2	0.4	9.6	0.2
10	15	$\sqrt{\sin}$	-0.3	0.3	9.8	0.2
10	15	\cos^{-4}	-0.3	0.3	9.9	0.2
10	20	<i>cst</i>	-0.3	0.3	11.6	0.2
10	20	<i>sin</i>	-0.2	0.4	9.6	0.2

Continued on next page

Table B.1: Statistical results of the height estimation for each processing model. – continued from previous page

Processing Modeling			Height Bias		Height STD	
CO	RW	WG	m	STD	m	STD
[°]	[mm·h ^{-0.5}]		[mm]	[mm]	[mm]	[mm]
10	20	$\sqrt{\sin}$	-0.3	0.3	9.8	0.2
10	20	\cos^{-4}	-0.3	0.3	9.9	0.2

Table B.2: Statistical results of the ZWD estimation for each processing model. Average (m) and dispersion (STD) values over the 200 ZWD biases and ZWD standards deviations (STD) of the difference between estimation and simulation for each processing model.

Processing Modeling			ZWD Bias		ZWD STD	
CO	RW	WG	m	STD	m	STD
[°]	[mm·h ^{-0.5}]		[mm]	[mm]	[mm]	[mm]
3	1	<i>cst</i>	0.0	0.1	1.5	0.1
3	1	<i>sin</i>	0.0	0.7	2.7	0.3
3	1	$\sqrt{\sin}$	0.0	0.3	1.9	0.2
3	1	\cos^{-4}	0.0	0.2	1.8	0.1
3	3	<i>cst</i>	0.1	0.1	1.6	0.0
3	3	<i>sin</i>	0.0	0.2	1.7	0.1
3	3	$\sqrt{\sin}$	0.0	0.1	1.3	0.1
3	3	\cos^{-4}	0.0	0.1	1.4	0.1
3	5	<i>cst</i>	0.1	0.0	1.8	0.0
3	5	<i>sin</i>	0.0	0.1	1.4	0.1
3	5	$\sqrt{\sin}$	0.0	0.1	1.3	0.1
3	5	\cos^{-4}	0.0	0.1	1.4	0.0
3	7	<i>cst</i>	0.0	0.1	1.5	0.1
3	7	<i>sin</i>	0.0	0.7	2.7	0.3
3	7	$\sqrt{\sin}$	0.0	0.3	1.9	0.2
3	7	\cos^{-4}	0.0	0.2	1.8	0.1
3	8	<i>cst</i>	0.1	0.1	1.6	0.0
3	8	<i>sin</i>	0.0	0.2	1.7	0.1
3	8	$\sqrt{\sin}$	0.0	0.1	1.3	0.1
3	8	\cos^{-4}	0.0	0.1	1.4	0.1
3	10	<i>cst</i>	0.0	0.0	2.4	0.0
3	10	<i>sin</i>	0.0	0.1	1.2	0.1
3	10	$\sqrt{\sin}$	0.0	0.0	1.5	0.0

Continued on next page

Table B.2: Statistical results of the ZWD estimation for each processing model. – continued from previous page

Processing Modeling			ZWD Bias		ZWD STD	
co	RW	WG	m	STD	m	STD
[°]	[mm·h ^{-0.5}]		[mm]	[mm]	[mm]	[mm]
3	10	\cos^{-4}	0.0	0.0	1.7	0.0
3	11	cst	0.1	0.0	1.8	0.0
3	11	sin	0.0	0.1	1.4	0.1
3	11	\sqrt{sin}	0.0	0.1	1.3	0.1
3	11	\cos^{-4}	0.0	0.1	1.4	0.0
3	12	cst	0.0	0.0	2.4	0.0
3	12	sin	0.0	0.1	1.2	0.1
3	12	\sqrt{sin}	0.0	0.0	1.5	0.0
3	12	\cos^{-4}	0.0	0.0	1.7	0.0
3	15	cst	0.0	0.0	3.1	0.0
3	15	sin	0.0	0.1	1.3	0.0
3	15	\sqrt{sin}	0.0	0.0	1.9	0.0
3	15	\cos^{-4}	0.0	0.0	2.2	0.0
3	20	cst	0.0	0.0	3.1	0.0
3	20	sin	0.0	0.1	1.3	0.0
3	20	\sqrt{sin}	0.0	0.0	1.9	0.0
3	20	\cos^{-4}	0.0	0.0	2.2	0.0
7	1	cst	0.0	0.3	2.0	0.2
7	1	sin	0.0	1.0	3.2	0.4
7	1	\sqrt{sin}	0.0	0.5	2.5	0.2
7	1	\cos^{-4}	0.0	0.5	2.4	0.2
7	3	cst	0.0	0.1	1.7	0.1
7	3	sin	0.0	0.3	2.0	0.2
7	3	\sqrt{sin}	0.0	0.2	1.7	0.1
7	3	\cos^{-4}	0.0	0.2	1.7	0.1
7	5	cst	0.0	0.1	1.8	0.1
7	5	sin	0.0	0.2	1.7	0.1
7	5	\sqrt{sin}	0.0	0.1	1.5	0.1
7	5	\cos^{-4}	0.0	0.1	1.5	0.1
7	7	cst	0.0	0.3	2.0	0.2
7	7	sin	0.0	1.0	3.2	0.4
7	7	\sqrt{sin}	0.0	0.5	2.5	0.2
7	7	\cos^{-4}	0.0	0.5	2.4	0.2

Continued on next page

Table B.2: Statistical results of the ZWD estimation for each processing model. – continued from previous page

Processing Modeling			ZWD Bias		ZWD STD	
CO	RW	WG	m	STD	m	STD
[°]	[mm·h ^{-0.5}]		[mm]	[mm]	[mm]	[mm]
7	8	<i>cst</i>	0.0	0.1	1.7	0.1
7	8	<i>sin</i>	0.0	0.3	2.0	0.2
7	8	$\sqrt{\sin}$	0.0	0.2	1.7	0.1
7	8	\cos^{-4}	0.0	0.2	1.7	0.1
7	10	<i>cst</i>	0.0	0.1	2.3	0.0
7	10	<i>sin</i>	0.0	0.1	1.5	0.1
7	10	$\sqrt{\sin}$	0.0	0.1	1.6	0.1
7	10	\cos^{-4}	0.0	0.1	1.7	0.0
7	11	<i>cst</i>	0.0	0.1	1.8	0.1
7	11	<i>sin</i>	0.0	0.2	1.7	0.1
7	11	$\sqrt{\sin}$	0.0	0.1	1.5	0.1
7	11	\cos^{-4}	0.0	0.1	1.5	0.1
7	12	<i>cst</i>	0.0	0.1	2.3	0.0
7	12	<i>sin</i>	0.0	0.1	1.5	0.1
7	12	$\sqrt{\sin}$	0.0	0.1	1.6	0.1
7	12	\cos^{-4}	0.0	0.1	1.7	0.0
7	15	<i>cst</i>	0.0	0.1	3.0	0.0
7	15	<i>sin</i>	0.0	0.1	1.6	0.1
7	15	$\sqrt{\sin}$	0.0	0.1	2.1	0.0
7	15	\cos^{-4}	0.0	0.1	2.2	0.0
7	20	<i>cst</i>	0.0	0.1	3.0	0.0
7	20	<i>sin</i>	0.0	0.1	1.6	0.1
7	20	$\sqrt{\sin}$	0.0	0.1	2.1	0.0
7	20	\cos^{-4}	0.0	0.1	2.2	0.0
10	1	<i>cst</i>	-0.2	0.5	2.4	0.2
10	1	<i>sin</i>	-0.1	1.3	3.6	0.5
10	1	$\sqrt{\sin}$	-0.2	0.8	2.9	0.3
10	1	\cos^{-4}	-0.2	0.8	2.9	0.3
10	3	<i>cst</i>	-0.2	0.2	1.8	0.1
10	3	<i>sin</i>	-0.1	0.5	2.3	0.2
10	3	$\sqrt{\sin}$	-0.2	0.3	1.9	0.1
10	3	\cos^{-4}	-0.2	0.3	1.9	0.1
10	5	<i>cst</i>	-0.2	0.1	1.8	0.1

Continued on next page

Table B.2: Statistical results of the ZWD estimation for each processing model. – continued from previous page

Processing Modeling			ZWD Bias		ZWD STD	
co	RW	WG	m	STD	m	STD
[°]	[mm·h ^{-0.5}]		[mm]	[mm]	[mm]	[mm]
10	5	<i>sin</i>	-0.1	0.3	1.9	0.1
10	5	$\sqrt{\sin}$	-0.2	0.2	1.7	0.1
10	5	\cos^{-4}	-0.2	0.2	1.7	0.1
10	7	<i>cst</i>	-0.2	0.5	2.4	0.2
10	7	<i>sin</i>	-0.1	1.3	3.6	0.5
10	7	$\sqrt{\sin}$	-0.2	0.8	2.9	0.3
10	7	\cos^{-4}	-0.2	0.8	2.9	0.3
10	8	<i>cst</i>	-0.2	0.2	1.8	0.1
10	8	<i>sin</i>	-0.1	0.5	2.3	0.2
10	8	$\sqrt{\sin}$	-0.2	0.3	1.9	0.1
10	8	\cos^{-4}	-0.2	0.3	1.9	0.1
10	10	<i>cst</i>	-0.2	0.1	2.3	0.1
10	10	<i>sin</i>	-0.1	0.2	1.7	0.1
10	10	$\sqrt{\sin}$	-0.2	0.1	1.8	0.1
10	10	\cos^{-4}	-0.2	0.1	1.8	0.1
10	11	<i>cst</i>	-0.2	0.1	1.8	0.1
10	11	<i>sin</i>	-0.1	0.3	1.9	0.1
10	11	$\sqrt{\sin}$	-0.2	0.2	1.7	0.1
10	11	\cos^{-4}	-0.2	0.2	1.7	0.1
10	12	<i>cst</i>	-0.2	0.1	2.3	0.1
10	12	<i>sin</i>	-0.1	0.2	1.7	0.1
10	12	$\sqrt{\sin}$	-0.2	0.1	1.8	0.1
10	12	\cos^{-4}	-0.2	0.1	1.8	0.1
10	15	<i>cst</i>	-0.2	0.1	3.1	0.1
10	15	<i>sin</i>	-0.1	0.1	1.8	0.1
10	15	$\sqrt{\sin}$	-0.2	0.1	2.2	0.1
10	15	\cos^{-4}	-0.2	0.1	2.3	0.1
10	20	<i>cst</i>	-0.2	0.1	3.1	0.1
10	20	<i>sin</i>	-0.1	0.1	1.8	0.1
10	20	$\sqrt{\sin}$	-0.2	0.1	2.2	0.1
10	20	\cos^{-4}	-0.2	0.1	2.3	0.1



AVAILABLE FOF DATASET CAMPAIGNS DESCRIPTION

Data from the five R/Vs come from FOF campaigns described in Table C.1.

Table C.1: FOF campaigns description.

R/V	Year	Campaign	Begin date	DOI
Alis	2015	NECTALIS-4	10/19/2015	10.17600/15004000
Alis	2015	ESSTECH	7/15/2015	10.17600/15003800
Alis	2016	NECTALIS-5	11/21/2016	10.17600/16004200
Alis	2016	KANACONO	8/8/2016	10.17600/16003900
Alis	2017	KANADEEP 1	8/30/2017	10.17600/17003800
Alis	2017	MARACAS 3	8/7/2017	10.17600/17003700
Alis	2017	POST-BLANCO LEG2	4/16/2017	10.17600/17003500
Alis	2017	PUFFALIS	3/18/2017	10.17600/17003300
Alis	2017	POST-BLANCO LEG1	2/21/2017	10.17600/17003200
Alis	2018	MALIS 2018 LEG2	11/24/2018	
Alis	2018	TUAM 2018	10/19/2018	10.17600/18000581
Alis	2018	MOANA-MATY 2018	9/19/2018	10.17600/18000580
Alis	2018	SPPIM	8/28/2018	10.17600/18000519
Alis	2018	MALIS 2018 LEG1	8/16/2018	10.17600/18000582
Alis	2018	TV_WALPPT	8/2/2018	
Alis	2018	WALLIS 2018	7/18/2018	10.17600/18000524
Alis	2018	WALLALIS	7/1/2018	10.17600/18000523
Alis	2018	TV_NMAWAL	6/21/2018	
Alis	2018	TR_RABNMA	6/7/2018	
Alis	2018	CARIOCA 3	5/25/2018	10.17600/18000522
Alis	2018	TR_NMARAB	5/13/2018	
Alis	2018	UECOCOT RETRAIT	5/6/2018	10.17600/18000418
Alis	2018	SEDLAB	4/6/2018	10.17600/18000401
Alis	2018	ESS_DEC_SMF	4/3/2018	10.17600/18000481
Alis	2018	UECOCOT01	1/27/2018	10.17600/18000400
Alis	2018	SPOT-OUVEA (14)	1/18/2018	10.17600/18000353
Alis	2019	GEOCEAN-NC	10/3/2019	10.17600/18000899
Alis	2019	MARACAS 7-4	9/22/2019	10.17600/18000892

Continued on next page

Table C.1: FOF campaigns description. – continued from previous page

R/V	Year	Campaign	Beginning	DOI
Alis	2019	TR_RABNMA	9/14/2019	
Alis	2019	SEAMOUNTS 2019 - 2	6/5/2019	10.17600/18000889
Alis	2019	ESS_TECH_AL 2019	5/30/2019	10.17600/18001215
Alis	2019	TR_PPTNMA	3/11/2019	
Alis	2019	MOANA-MATY 2019	2/12/2019	10.17600/18000887
Alis	2020	KANARECUP - 1	12/19/2020	10.17600/18001103
Alis	2020	TONGA RECUP	10/24/2020	10.17600/18001357
Alis	2020	SUPERNATURAL 2	3/7/2020	10.17600/18001102
Alis	2021	WARMALIS 1	9/5/2021	10.17600/18000710
Alis	2021	SPANBIOS 2021	6/26/2021	10.17600/18000701
Alis	2021	REEFADAPT 2021	6/12/2021	10.17600/18001105
Alis	2021	BICHECALIS - 2	6/3/2021	10.17600/18001732
Alis	2021	KANARECUP - 2	5/5/2021	10.17600/18001103
Alis	2021	FISHCODE	4/18/2021	10.17600/18001636
Alis	2021	BICHECALIS - 1	4/6/2021	10.17600/18001732
Alis	2022	TR_APWNOU	10/5/2022	
Alis	2022	WARMALIS 2	9/14/2022	10.17600/18001260
Alis	2022	MALIS 3	6/29/2022	
Alis	2022	TR_NOUPPT	6/15/2022	
Alis	2022	MARGEST	4/9/2022	10.17600/18001492
Alis	2022	SOKOWASA 2022	3/19/2022	10.17600/18002025
Alis	2022	SELAMIK 2022 - 1	2/28/2022	10.17600/18002033
Alis	2022	ESSTECH-AL-2022-1	2/23/2022	10.17600/18002713
Antea	2016	MAD-RIDGE-2	11/25/2016	10.17600/16004900
Antea	2016	MAD-RIDGE-1	11/8/2016	10.17600/16004800
Antea	2016	LA PEROUSE	9/15/2016	10.17600/16004500
Antea	2016	ESS_TECH_16AN02	7/14/2016	
Antea	2017	TR_BRELOR	9/28/2017	
Antea	2017	TR_BRELOR	9/28/2017	
Antea	2017	TR_SPMBRE	9/16/2017	
Antea	2017	TR_SPMBRE	9/16/2017	
Antea	2017	TR_PAPSPM	7/13/2017	
Antea	2017	TR_PAPSPM	7/13/2017	
Antea	2018	TR_BRESEY	9/24/2018	
Antea	2018	TR_HAVBRE	9/21/2018	
Antea	2018	SELISEINE 2018	9/13/2018	10.17600/18000585
Antea	2018	TR_BREHAV	9/10/2018	
Antea	2018	ESSHROV-AN-2018	9/1/2018	10.17600/18000676
Antea	2018	TR_LORBRE	8/29/2018	
Antea	2018	TR_BRELOR	7/31/2018	

Continued on next page

Table C.1: FOF campaigns description. – continued from previous page

R/V	Year	Campaign	Beginning	DOI
Antea	2018	ECOPEL 2018 LEG2	7/17/2018	10.17600/18000443
Antea	2018	TR_BREBOU	7/13/2018	
Antea	2018	TR_ROCBRE	7/11/2018	
Antea	2018	GIROPAL18	6/25/2018	10.17600/18000525
Antea	2018	TR_BREROC	5/4/2018	
Antea	2018	ECOPEL 2018 LEG1	4/18/2018	10.17600/18000443
Antea	2018	ESS_DRAGUES_COMOR_18	4/11/2018	10.17600/18000483
Antea	2018	ESS_DRAGUES_COSB_18	4/6/2018	10.17600/18000482
Antea	2018	TR_LORBRE	4/4/2018	
Antea	2019	ESSHROV 2019	8/1/2019	10.17600/18000923
Antea	2019	TR_SEYMAR	5/19/2019	
Antea	2019	HIPPOCAMPE	4/13/2019	10.17600/18000900
Antea	2021	TV-AMATLANTE-H-2	10/29/2021	
Antea	2021	PEGUY 2021	8/3/2021	10.17600/18001363
Antea	2021	PIGUY 2021	7/19/2021	10.17600/18001362
Antea	2021	TV-AMATLANTE-C	7/13/2021	10.17600/18001380
Antea	2021	CARESSE 2021	6/22/2021	10.17600/18001361
Antea	2021	FIBROSAINTEs 2021	5/31/2021	10.17600/18001122
Antea	2021	TR_SMLBES	5/9/2021	
Antea	2021	TV-AMATLANTE-H-1	5/9/2021	
Antea	2021	ESSTECH-AN-21	4/10/2021	10.17600/18002376
Antea	2022	TR_LPTLON	10/14/2022	
Antea	2022	IOTA 2022	9/29/2022	
Antea	2022	TR_MINLPT	8/25/2022	
Antea	2022	DISCOVER	7/9/2022	10.17600/18001495
Antea	2022	TR_YNEMIN	6/25/2022	
Antea	2022	ENTENTE	6/9/2022	10.17600/18001996
Antea	2022	ESSHROV 2022 - 2	5/24/2022	10.17600/18002031
Antea	2022	ESSTECH-AN-2022-2	5/20/2022	10.17600/18002943
Antea	2022	ESSHROV 2022 - 1	4/1/2022	10.17600/18002031
Antea	2022	TR_LRITYNE	3/15/2022	
Antea	2022	ESSTECH-AN-2022-1	3/6/2022	10.17600/18002939
L'Atalante	2015	TECTA	9/2/2015	
L'Atalante	2015	ESS_SMT	8/28/2015	
L'Atalante	2015	CASSIOPEE	7/18/2015	
L'Atalante	2016	CARAMBAR 2	11/30/2016	
L'Atalante	2016	TR_PAPNAS	11/25/2016	
L'Atalante	2016	TR_CAYPAP	11/17/2016	
L'Atalante	2016	MARGATS	10/21/2016	
L'Atalante	2016	TR_CADCAy	10/6/2016	

Continued on next page

Table C.1: FOF campaigns description. – continued from previous page

R/V	Year	Campaign	Beginning	DOI
L'Atalante	2016	GRACO	9/22/2016	
L'Atalante	2016	TR_LHACAD	9/15/2016	
L'Atalante	2016	MOMARSAT2016	8/24/2016	
L'Atalante	2016	TR_BRELHA	8/18/2016	
L'Atalante	2016	ESSROV16-1	8/4/2016	
L'Atalante	2016	TR_TROBRE	7/23/2016	
L'Atalante	2016	STEP 2016	7/11/2016	
L'Atalante	2016	TR_LERTRO	7/3/2016	
L'Atalante	2016	MINGULAY ROCKALL	6/22/2016	
L'Atalante	2016	TR_SEYBRE	6/12/2016	
L'Atalante	2016	MOOSE-GE 2016	5/19/2016	
L'Atalante	2016	WESTMEDFLUX	4/20/2016	
L'Atalante	2016	ESSNAUT 2016	3/30/2016	
L'Atalante	2016	TR_BRESEY	3/22/2016	
L'Atalante	2016	ESS_SISM	3/3/2016	
L'Atalante	2016	ESS_K-16-ATA	2/18/2016	
L'Atalante	2016	LEVE_SMF	1/29/2016	
L'Atalante	2018	TR_SANBRE	12/28/2018	
L'Atalante	2018	TR_SEYSAN	11/12/2018	
L'Atalante	2018	TR_HERSEY	11/7/2018	
L'Atalante	2018	PROTEVSMED_PERLE_2018	10/3/2018	
L'Atalante	2018	RAMOGE	9/17/2018	
L'Atalante	2018	OFEG-NIOZ	9/15/2018	
L'Atalante	2018	TR_LHASEY	8/31/2018	
L'Atalante	2018	MOMARSAT2018	8/8/2018	
L'Atalante	2018	TRANSECT	7/9/2018	
L'Atalante	2018	HYDROMOMAR18	6/25/2018	
L'Atalante	2018	TR_SEYPPA	6/15/2018	
L'Atalante	2018	MOOSE-GE 2018	5/13/2018	
L'Atalante	2018	ESS_SISM	5/2/2018	
L'Atalante	2018	WESTMEDFLUX-2	4/12/2018	
L'Atalante	2018	ESS_PENFELD_2018	2/22/2018	
L'Atalante	2018	ESSROV18	2/7/2018	
L'Atalante	2018	ESS_DEC / ESS_GRAVI	2/2/2018	
L'Atalante	2019	TR_NMAPAP	12/10/2019	
L'Atalante	2019	TONGA 2019	10/31/2019	
L'Atalante	2019	SPPIM 2019	8/4/2019	
L'Atalante	2019	CHUBACARC	3/25/2019	
L'Atalante	2019	TR_BRENMA	1/29/2019	
L'Atalante	2019	ESS_DEC_ATA 19	1/25/2019	

Continued on next page

Table C.1: FOF campaigns description. – continued from previous page

R/V	Year	Campaign	Beginning	DOI
L'Atalante	2019	ESSROVSYS 19	1/20/2019	
L'Atalante	2020	HIPER	3/9/2020	10.17600/18001348
L'Atalante	2020	HIPER	3/9/2020	
L'Atalante	2020	TR_PAPESM	2/25/2020	
L'Atalante	2020	TR_PAPESM	2/19/2020	
L'Atalante	2020	EUREC4A_OA	1/19/2020	10.17600/18000670
L'Atalante	2020	EUREC4A_OA	1/19/2020	
L'Atalante	2021	MOMARSAT2021	5/15/2021	10.17600/18001296
L'Atalante	2021	ESSNAUT 2021	5/7/2021	10.17600/18002379
L'Atalante	2021	PERLE4	3/27/2021	10.17600/18001980
L'Atalante	2021	TR_SNRYNE	3/19/2021	
L'Atalante	2021	TR_BESSNR	3/13/2021	
L'Atalante	2021	SUMOS	2/11/2021	10.17600/18001349
L'Atalante	2021	ESSTECH-AT-2021	1/17/2021	10.17600/18002133
L'Atalante	2022	ESSTECH-AT-2022-2	9/27/2022	
L'Atalante	2022	HIPER (suite)	3/13/2022	10.17600/18002493
L'Atalante	2022	TR_BESPTP	2/19/2022	
L'Atalante	2022	ESSAIS-MODERNISATION 2022	1/12/2022	10.17600/18002660
Thalassa	2019	EVHOE 2019	10/21/2019	10.17600/18000878
Thalassa	2019	TR_BOUBRE	10/17/2019	
Thalassa	2019	CGFS2019	9/15/2019	10.17600/18000877
Thalassa	2019	TR_SEYBRE	8/23/2019	
Thalassa	2019	TR_BRESEY	5/26/2019	
Thalassa	2019	PELGAS 2019	4/25/2019	10.17600/18001109
Thalassa	2020	TR_BRECON	12/8/2020	
Thalassa	2020	EVHOE 2020	10/24/2020	10.17600/18000661
Thalassa	2020	CGFS2020	9/22/2020	10.17600/18000675
Thalassa	2020	HYDROMOMAR20	8/28/2020	10.17600/18000655
Thalassa	2020	ESSTECH-TL-20	8/24/2020	10.17600/18001838
Thalassa	2020	TR_BOUBRE	2/19/2020	
Thalassa	2020	PIRATA FR30	2/16/2020	10.17600/18000690
Thalassa	2020	TR_BREMIN	2/6/2020	
Thalassa	2020	IBTS 2020	1/9/2020	10.17600/18000570
Thalassa	2021	EVHOE 2021	10/22/2021	10.17600/18001223
Thalassa	2021	CGFS2021	9/16/2021	10.17600/18001250
Thalassa	2021	TR_BESYNE	5/27/2021	
Thalassa	2021	PELGAS 2021	4/26/2021	10.17600/18001265
Thalassa	2021	TR_BOLBES	2/9/2021	
Thalassa	2021	IBTS 2021	1/15/2021	10.17600/18001237
Thalassa	2021	TR_BESBOL	1/12/2021	

Continued on next page

Table C.1: FOF campaigns description. – continued from previous page

R/V	Year	Campaign	Beginning	DOI
Thalassa	2021	ESSTECH-TL-2021-1	1/10/2021	10.17600/18002132
Thalassa	2022	EVHOE 2022	10/21/2022	10.17600/18001822
Thalassa	2022	CGFS2022	9/15/2022	10.17600/18001842
Thalassa	2022	ChEReef 2022	8/3/2022	10.17600/18000571
Thalassa	2022	ESSROV-TL-2022	7/27/2022	10.17600/18002938
Thalassa	2022	PELGAS 2022	4/26/2022	10.17600/18001845
Thalassa	2022	ESSTECH-TL-2022-2	4/17/2022	10.17600/18002869
Thalassa	2022	PIRATA FR32	2/15/2022	10.17600/18001832
Thalassa	2022	IBTS 2022	1/17/2022	10.17600/18001811
Thalassa	2022	ESSTECH-TL-2022-1	1/9/2022	10.17600/18002661
Pourquoi Pas?	2019	TR_MINBRE	8/25/2019	
Pourquoi Pas?	2019	SMARTIES	7/13/2019	10.17600/18001107
Pourquoi Pas?	2019	TR_LHAMIN	7/6/2019	
Pourquoi Pas?	2019	MOMARSAT2019	6/11/2019	10.17600/18001110
Pourquoi Pas?	2019	TR_BRELHA	6/3/2019	
Pourquoi Pas?	2020	SISMAORE - 1	12/23/2020	10.17600/18001331
Pourquoi Pas?	2020	TR_SEYLPO	11/29/2020	
Pourquoi Pas?	2020	ESS_SISM	11/22/2020	10.17600/18002106
Pourquoi Pas?	2020	MaRoLiS PENFELD	11/10/2020	10.17600/18000671
Pourquoi Pas?	2020	SEALEX	10/30/2020	10.17600/18001886
Pourquoi Pas?	2020	ESS_PENFELD 2020	10/25/2020	10.17600/18001921
Pourquoi Pas?	2020	FocusX1	10/6/2020	10.17600/18000692
Pourquoi Pas?	2020	MOMARSAT2020	9/4/2020	10.17600/18000684
Pourquoi Pas?	2020	PERLE3	3/11/2020	10.17600/18001342
Pourquoi Pas?	2020	ESSTECH-PP-20	3/8/2020	10.17600/18001721
Pourquoi Pas?	2020	ESSROV 2020	2/29/2020	10.17600/18001720
Pourquoi Pas?	2020	TR_SANSEY	2/15/2020	
Pourquoi Pas?	2020	TR_BRESAN	1/4/2020	
Pourquoi Pas?	2021	ESSTECH-PP-2021-3	11/17/2021	10.17600/18002527
Pourquoi Pas?	2021	ALBACORE	10/14/2021	10.17600/18001351
Pourquoi Pas?	2021	TR_CNDYNE	10/2/2021	
Pourquoi Pas?	2021	GHASS2 - 3	9/21/2021	10.17600/18001358
Pourquoi Pas?	2021	GHASS2 - 2	9/7/2021	10.17600/18001359
Pourquoi Pas?	2021	GHASS2 - 1	8/16/2021	10.17600/18001360
Pourquoi Pas?	2021	TR_YNECND	8/7/2021	
Pourquoi Pas?	2021	MaRoLiS 2021	7/11/2021	10.17600/18002394
Pourquoi Pas?	2021	TR_LPTYNE	6/9/2021	
Pourquoi Pas?	2021	MAYOBS19	5/27/2021	10.17600/18001985
Pourquoi Pas?	2021	GEOFLAMME	4/17/2021	10.17600/18001297
Pourquoi Pas?	2021	MAYOBS18	4/5/2021	10.17600/18001984

Continued on next page

Table C.1: FOF campaigns description. – continued from previous page

R/V	Year	Campaign	Beginning	DOI
Pourquoi Pas?	2021	SISMAORE - 2	1/26/2021	
Pourquoi Pas?	2021	MAYOBS17	1/17/2021	10.17600/18001983
Pourquoi Pas?	2022	MOOSE-GE 2022	9/6/2022	10.17600/18001854
Pourquoi Pas?	2022	TR_HORYNE	8/25/2022	
Pourquoi Pas?	2022	HERMINE2	7/8/2022	10.17600/18001851
Pourquoi Pas?	2022	TR_HORPTP	6/29/2022	
Pourquoi Pas?	2022	MOMARSAT2022	6/6/2022	10.17600/18001914
Pourquoi Pas?	2022	Arc-En-Sub	5/6/2022	10.17600/18000663
Pourquoi Pas?	2022	ESSULYX-2022-2	4/22/2022	10.17600/18002877
Pourquoi Pas?	2022	ESSROV-PP-2022	4/18/2022	10.17600/18002758
Pourquoi Pas?	2022	ESSNAUT 2022	3/28/2022	10.17600/18002759
Pourquoi Pas?	2022	ESSULYX-2022-1	3/16/2022	10.17600/18002760
Pourquoi Pas?	2022	EMSO LIGURE OUEST 2022 - PP	1/29/2022	10.17600/18001344
Pourquoi Pas?	2022	FocusX2	1/13/2022	10.17600/18001255

D

RÉSUMÉ ÉTENDU

CONTENT

D.1	Introduction	161
D.1.1	Motivations	161
D.1.2	Objectifs	162
D.1.3	Méthodologie	163
D.1.4	Structure de la Thèse	164
D.2	Principe du GNSS, Mesure de la Vapeur d'Eau Atmosphérique en Mer	165
D.2.1	Principe de Fonctionnement du GNSS	165
D.2.2	GNSS pour la Récupération de la Vapeur d'Eau Atmosphérique en Mer	166
D.3	Étude de la Stratégie de Traitement des Données GNSS	167
D.3.1	Tests Préliminaires en Conditions Réelles sur des Données Simples	167
D.3.2	Évaluation de Stratégies de Traitement sur Données GNSS Embarquées Simulées	168
D.4	Observation de la Vapeur d'Eau Atmosphérique lors des Campagnes de Recherche de la Flotte Océanographique Française entre 2015 et 2022	168
D.4.1	Évaluation du Jeu de Données Provenant de la Flotte Océanographique Française	168
D.4.2	Débouchés pour la Climatologie en Mer	169
D.5	Conclusion	169
D.5.1	Contexte	169
D.5.2	Travaux Entrepris et Résultats Obtenus	170
D.5.3	Perspectives	171

Ce chapitre présente un résumé étendu du contenu de ce mémoire de thèse, à destination d'un public francophone qui souhaiterait se pencher sur mes trois ans de travaux traitant du sujet : « Système de Navigation Global par Satellite (GNSS) Embarqué sur Porteur Marin pour l'Observation de la Vapeur d'Eau Atmosphérique en Mer. »

D.1 INTRODUCTION

D.1.1 *Motivations*

La vapeur d'eau est un facteur déterminant dans le cycle hydrologique régissant le transport d'énergie autour du globe. La Terre reçoit de la chaleur provenant des rayons du Soleil à sa surface, faisant ainsi évaporer de l'eau de surface qui sera transportée au gré des courants, avant de se condenser sous forme de nuages pour retomber sous forme de pluie. Or, dans un contexte de réchauffement climatique, le cycle de l'eau est perturbé, car une atmosphère plus chaude d'un degré peut contenir 5 à 7 % de vapeur d'eau supplémentaire, selon le sixième rapport du groupe de travail numéro 3 du Groupe d'experts intergouvernemental sur l'évolution du climat (GIEC) [Lee 23]. Occulté par la célébrité médiatique du CO₂, la vapeur d'eau s'avère également être un gaz à effet de serre notoire, son augmentation dans l'atmosphère entraînant

une augmentation de température. On entre alors dans un cercle vicieux de réchauffement mondial, entraînant des épisodes météorologiques dévastateurs.

Le Système de Navigation Mondial par Satellite (GNSS) englobe les technologies américaine du GPS, russe de GLONASS, européenne de Galileo, et chinoise de Beidou. En plus du positionnement, il permet de mesurer la vapeur d'eau au-dessus de l'antenne. Cette méthode est déjà largement appliquée à des antennes terrestres, et assimilée à des modèles de prévision météorologiques, ainsi qu'à l'étude climatique [Gue 16]. En effet, le trajet et la vitesse du signal sont modifiés par la vapeur d'eau contenue dans l'atmosphère qu'il traverse. Le signal arrivant au récepteur à la surface de la terre s'en retrouve retardé. Ce retard, lorsqu'il est correctement estimé pendant le traitement des données GNSS, est directement proportionnel à la quantité totale de vapeur d'eau contenue dans la troposphère au-dessus de l'antenne d'observation. Bevis et al. (1992) [Bev 92] ont été les premiers à mentionner la possibilité de mesurer la vapeur d'eau à l'aide du GNSS. Depuis lors, cette question est devenue très courante, comme en témoigne le nombre de publications sur la récupération de la vapeur d'eau dans la troposphère à partir de stations GNSS au sol [Roc 93; Dav 93; Kou 01; Lu 15; Boc 16; Sim21]. De nos jours, des réseaux de stations GNSS terrestres permettent de mesurer en continu la vapeur d'eau [Boc 21; Pac 09], et certains ont même l'intention de les utiliser pour l'étalonnage d'autres instruments de mesure de la vapeur d'eau [Zha 17] ou pour des prévisions météorologiques [Ved 04; Pac 09].

Par ailleurs, de nombreux phénomènes météorologiques importants naissent en mer, nécessitant une surveillance de la vapeur d'eau atmosphérique hauturière, difficile à mettre en oeuvre. En effet, outre les mesures par satellites qui fournissent une résolution spatio-temporelle faible [Smi 19], les mesures disponibles sont le plus souvent des mesures de surface grâce à des bouées ou des bateaux instrumentés. Ainsi, si le secteur terrestre semble bien couvert par les instruments de mesure de vapeur d'eau [Rev 03], les données restent éparées au-dessus des océans.

Afin de pallier le manque d'observations de la vapeur d'eau atmosphérique en mer, différentes études ont eu l'idée d'appliquer ce processus à des antennes GNSS embarquées sur porteur marin [Roc 05; Wan 19]. En effet, les océans sont sans cesse sillonnés de bateaux équipés d'antennes GNSS de tout type utiles à la navigation, et qui pourraient être compatibles avec la surveillance de la troposphère. La donnée est donc déjà présente, et ne demande qu'à être valorisée. Le Chapitre 3 présente un état de l'art détaillé des principales études scientifiques publiées traitant du sujet de la mesure de vapeur d'eau par GNSS embarqué en mer.

Cependant, l'influence de la configuration du traitement de la donnée GNSS en positionnement ponctuel précis (PPP) cinématique n'est pas abordée dans ces études. Aussi, seul Wang et al. (2019) [Wan 19] traite de l'aspect long terme de ce type de mesure pour la récupération de vapeur d'eau atmosphérique, montrant la possibilité de récupérer la quantité de vapeur d'eau atmosphérique avec une précision de 2 à 3 mm, alors qu'une précision de 1 mm est possible à terre [Boc 13]. En effet, une telle précision est nécessaire pour les études climatiques et météorologiques [Off 10]. Ces aspects méritent une attention particulière, car il a été montré que la stratégie de traitement GNSS pouvait avoir un impact sur la précision de la solution obtenue à partir de données d'antennes terrestres, et le contexte spatio-temporel de la mesure peuvent avoir un impact sur la récupération de vapeur d'eau par GNSS [Had 17].

D.1.2 Objectifs

Le GNSS embarqué est une technologie très répandue et rentable qui permet de surveiller en continu les évolutions des navires tout au long de leur route. La vapeur d'eau atmosphérique au-dessus de leur route est également mesurée de manière efficace et régulière, complétant ainsi la donnée provenant des radiomètres satellitaires ainsi que d'autres techniques éparées et coûteuses. La récupération à long terme de la vapeur d'eau embarquée, telle que proposée par Wu et al. (2022) [Wu 22b], nous permet d'étudier les effets du changement climatique au large des côtes et de mieux comprendre le rôle des échanges entre l'océan et l'atmosphère. La mise

en œuvre de mesures de routine, telle que proposée par Bosser, Van Baelen, and Bousquet (2022) [Bos 22b], devrait permettre d'alimenter les modèles de prévision météorologique pour la prévision numérique du temps (PNT) Poli et al. (2007) [Pol 07].

L'objectif est de pouvoir traiter automatiquement les données GNSS embarquées à partir de n'importe quel ensemble de données brutes, et d'extraire des informations sur la vapeur d'eau à partir du traitement GNSS, le plus précisément possible. Nous nous concentrons ici sur le post-traitement cinématique des données à l'aide de la technique de positionnement ponctuel précis (PPP). Cette méthode est utile pour une antenne située en mer, car aucun ensemble de données de référence n'est nécessaire. Cependant, la méthode peut être délicate car plusieurs paramètres de traitement peuvent affecter le résultat et la précision de l'estimation.

En effet, les estimations de la hauteur et du retard atmosphérique semblent être fortement corrélées dans le traitement PPP cinématique du GNSS [Wan 19]. Cela est dû au fait que, contrairement au traitement statique effectué sur les antennes GNSS terrestres qui estiment la position de l'antenne une fois par jour, la position de l'antenne embarquée doit être estimée à chaque pas de temps du traitement, en même temps que le retard troposphérique.

Les stratégies de traitement GNSS pour la récupération de la vapeur d'eau atmosphérique ont été évaluées à plusieurs reprises pour les stations GNSS au sol [Sel 16; Kač 19]. Cependant, ce type d'étude n'a pas été réalisé pour les antennes embarquées en mer, même si la récupération de la vapeur d'eau par GNSS embarqué devient une question largement étudiée. Trois paramètres de traitement peuvent être réglés pour décorrélérer la hauteur et le retard de la vapeur d'eau atmosphérique, par exemple : l'angle de coupure pour filtrer les observations provenant de satellites de faible élévation, la fonction de pondération de l'élévation du satellite observé appliquée à l'incertitude de la mesure, et la marche aléatoire (RWPN) modélisant les variations du retard troposphérique imprévisible. Tous ces paramètres de configuration du traitement dépendent également d'autres aspects tels que les constellations considérées, la résolution temporelle du processus, le mouvement et la position du navire pendant l'acquisition, etc. Tous ces aspects sont abordés et évalués dans cette thèse.

D.1.3 Méthodologie

Tout d'abord, j'ai étudié la stratégie de traitement GNSS pour la récupération de la vapeur d'eau atmosphérique, ainsi que l'état de l'art de la récupération de la vapeur d'eau par GNSS embarqué. La comparaison avec les techniques habituelles de mesure de la vapeur d'eau m'a permis d'obtenir des résultats statistiques qui servent de référence aux résultats attendus pour le traitement des antennes embarquées en mer. Bien que les stratégies de traitement pour la récupération de la vapeur d'eau par GNSS aient été évaluées à partir d'antennes terrestres, aucune n'a été réalisée concernant l'application aux antennes offshore telles que celles embarquées sur les navires. En outre, une seule des études sur l'état de l'art porte sur le traitement d'un ensemble de données embarquées de longue durée [Wu 22b], permettant de faire face à de nombreuses situations différentes qui peuvent être attendues en mer.

Afin d'appliquer la stratégie de traitement la plus appropriée à un autre jeu de données GNSS embarqué plus diversifié et de plus longue durée, la deuxième partie de mon travail a été consacrée à l'évaluation d'un ensemble de stratégies de traitement. À cette fin, deux ensembles simples de données GNSS embarquées ont été utilisés :

- un mois de données provenant du navire de l'École Nationale Supérieure de Techniques Avancées Bretagne (ENSTA Bretagne) ;
- un ensemble de données simulées provenant d'un simulateur développé pour cette étude.

L'ensemble des données relatives aux navires de recherche nous a permis de confirmer que la stratégie de traitement a un impact sur la qualité du traitement GNSS. En effet, la comparaison avec d'autres mesures proches de la hauteur de la surface de la mer (SSH) et de la vapeur d'eau atmosphérique mesurée par une antenne GNSS terrestre a conduit à des différences significatives entre les estimations des différentes stratégies de traitement.

Le simulateur a été conçu pour l'objectif visé. J'ai soigneusement étudié la manière de modéliser le signal simulé et le nombre de simulations nécessaires pour obtenir un nombre de résultats statistiquement significatifs. Outre la stratégie de traitement, la modélisation du signal simulé a été examinée afin d'estimer au mieux les variables GNSS dans différentes configurations d'acquisition. Les erreurs d'estimation ont été évaluées pour les différentes stratégies de traitement, ce qui a permis de mettre en évidence la configuration de traitement recommandée pour la suite : un angle de coupure de 3° , une fonction de pondération en racine du sinus de l'élévation, et une marche aléatoire de $5 \text{ mm} \cdot \text{h}^{-0.5}$.

Dans la troisième partie de ma thèse, j'ai appliqué la configuration de traitement recommandée à un groupe de cinq navires de la Flotte Océanographique Française (FOF) exploitée par l'IFREMER, dont le jeu de données s'étend sur huit années consécutives. Le contenu estimé en vapeur d'eau le long des trajectoires est ensuite comparé à des ensembles de données externes à l'image des autres études GNSS embarquées présentées dans l'état de l'art, ce qui nous permet de comparer les différences qui en résultent.

Les différences statistiques étant satisfaisantes au regard des résultats mis en évidence dans l'état de l'art, j'ai exploré ensuite le reste du jeu de données sur le contenu en vapeur d'eau sous différents angles d'étude du climat tels que la latitude, la saisonnalité et la corrélation avec la température de surface de la mer (SST).

D.1.4 Structure de la Thèse

Cette thèse est divisée en trois parties principales, à savoir la théorie, l'évaluation de la stratégie de traitement et l'application au traitement GNSS embarqué à un lot de données couvrant le long terme.

La partie théorique traite d'abord des généralités du GNSS, des constellations existantes à la méthode de traitement des signaux dans le chapitre 2, ainsi que l'application à l'étude de l'atmosphère. Le chapitre 3 détaille les principales études GNSS embarquées publiées depuis Rocken et al. (2005) [Roc 05] jusqu'à aujourd'hui en fournissant l'organisation de la campagne, la configuration de traitement utilisée et l'évaluation de la qualité du retard de la vapeur d'eau par comparaison avec les techniques conventionnelles de mesure de la vapeur d'eau.

La deuxième partie est consacrée à l'évaluation de la stratégie de traitement, et est divisée en deux chapitres. Le chapitre 4 est une étude préliminaire basée sur un jeu de données de 49 jours provenant du navire de recherche de l'ENSTA Bretagne, principalement utilisé dans le cadre des travaux pratiques de la formation en hydrographie. Ce navire reste principalement à quai dans le port de Brest. Ces données GNSS ont été traitées en utilisant plusieurs combinaisons de paramètres de traitement. Les résultats ont été évalués par comparaison avec des ensembles de données de référence proches, comme le marégraphe, la station GNSS terrestre, un modèle météorologique nommé ERA5, et les radiosondages. Le chapitre 5 présente une étude plus large de l'évaluation des stratégies de traitement, en s'appuyant sur un ensemble de données GNSS simulées à bord d'un navire. Le simulateur développé pour l'occasion a permis de simuler plusieurs lots de données GNSS, afin de tester les configurations de traitement dessus. Ces tests m'ont permis de formuler des recommandations sur la meilleure stratégie de post-traitement des données GNSS embarquées dans le traitement PPP cinématique, sur la base de mes résultats.

La troisième partie concerne le traitement d'un lot de données long terme, et contient deux chapitres. Le chapitre 6 est l'application de la stratégie de traitement recommandée après le chapitre 5 aux données mises à disposition par l'IFREMER à partir de cinq de leurs navires de recherche en mer, de 2015 à 2022. Cet ensemble de données représente une excellente occasion de tester la configuration de traitement mise en évidence précédemment, car il est conséquent, diversifié et représente tous les états de mer, les conditions météorologiques et un large éventail de lieux possibles sur les océans de la Terre. Pour évaluer leur qualité, j'ai comparé les séries temporelles de vapeur d'eau récupérées le long de leur trajectoire à diverses autres sources de mesure de la vapeur d'eau, comme des stations GNSS terrestres, des radiomètres infrarouges embarqués sur satellite, ou le modèle ERA5. Ensuite, le chapitre

7 donne un premier aperçu des possibilités offertes par ce jeu de données de vapeur d'eau précipitable pour l'étude du climat.

Enfin, le chapitre 8 conclut cette thèse en résumant les résultats des deux dernières parties et en traçant d'autres perspectives comme l'application à la recherche en temps quasi-réel pour les prévisions météorologiques.

D.2 ÉTAT DE L'ART : PRINCIPE DU GNSS ET SON APPLICATION À L'OBSERVATION DE LA VAPEUR D'EAU ATMOSPHÉRIQUE EN MER

Cette partie s'appuie sur la théorie des mesures GNSS, le traitement et les applications pour la surveillance de la vapeur d'eau atmosphérique en mer. Elle est composée de deux chapitres. Tout d'abord, le principe de la mesure GNSS ainsi que le traitement du signal résultant sont détaillés. Dans cette partie, nous abordons l'application de la technique GNSS à la surveillance de la vapeur d'eau atmosphérique, notamment dans le cas des antennes terrestres fixes. Dans un second temps, un état des lieux détaillé de la littérature évaluant la récupération de la vapeur d'eau par GNSS embarqué permet de mettre en évidence les connaissances actuelles ainsi que les perspectives à venir dans ce domaine.

D.2.1 *Principe de Fonctionnement du GNSS*

Le GNSS occupe une place centrale dans la vie d'aujourd'hui. Bien qu'il soit utilisé pour le positionnement et la navigation selon différentes méthodes de traitement qui permettent d'atteindre des précisions allant jusqu'à la précision millimétrique, il peut également permettre de connaître le retard troposphérique humide affectant la propagation du signal. Ce dernier est proportionnel à la vapeur d'eau contenue dans l'atmosphère, utile pour étudier les phénomènes météorologiques et climatiques.

Même si les instruments les plus coûteux et les techniques les plus avancées peuvent être utilisés pour un positionnement millimétrique, les applications les plus précises doivent tenir compte des erreurs des instruments et de l'impact du signal sur l'environnement pendant la mesure. Ces effets sont pris en compte dans les équations d'observation (2.1) et (2.3) sur le code et la phase du signal reçu par l'antenne.

Parmi ces effets, le trajet multiple est un problème important qui affecte la mesure du signal. En effet, le signal peut se refléter sur des surfaces dans l'environnement proche de l'antenne avant d'être réceptionné par celle-ci, introduisant un biais dans la mesure. La ionosphère a un impact dû à sa composition ionique, qui a un effet différent selon la fréquence du signal qui la traverse. Cette propriété permet de supprimer son effet au premier ordre à l'aide d'une combinaison linéaire de deux observations à des fréquences différentes. Ici, on suppose donc que l'impact de l'ionosphère sur notre signal est corrigé. La troposphère a également un impact sur le signal GNSS. Cet effet a deux composantes : la première dite sèche, que l'on peut déterminer simplement à partir de la pression atmosphérique au niveau de l'antenne ; et la seconde dite humide car due à la vapeur d'eau présente, qui doit être estimée en même temps que la position de l'antenne pour permettre d'obtenir un positionnement précis, de par son comportement imprévisible. La grandeur est estimée dans la direction zénithale, et des gradients horizontaux sont ajoutés afin de prendre en compte l'hétérogénéité de la troposphère et que les satellites ne se situent pas tous au zénith de l'antenne.

L'estimation des paramètres GNSS peut être effectuée par un filtrage de Kalman, dont les équations sont détaillées dans le Chapitre 2. Le déroulement de ce filtre repose sur le principe du maximum de vraisemblance, qui permet la minimisation des résidus des variables estimées à partir des mesures simultanées des signaux GNSS provenant des satellites visibles par l'antenne.

Pour minimiser l'impact des sources d'erreur sur les produits estimés, plusieurs paramètres doivent être judicieusement réglés au cours du processus d'estimation. Nous nous intéresserons notamment à l'angle de coupure sur l'élévation des satellites, à la fonction de pondération de l'élévation du satellite appliquée à la variance des observations et à la contrainte sur les variations de la composante troposphérique.

L'amélioration de la précision du traitement GNSS permet de développer de nouvelles applications de cette technologie. En effet, plusieurs réseaux GNSS terrestres se sont répandus, les réseaux les plus denses se trouvant dans les pays développés. Ils permettent d'étudier la variabilité à long terme de plusieurs aspects nécessitant une précision de positionnement, tels que la dérive des continents ou plus récemment la surveillance de l'atmosphère. Ils sont également utilisés comme stations de référence pour la mesure temps réel ou le post-traitement d'antennes GNSS mobiles ou statiques. Les produits temps réel au sol peuvent actuellement être assimilés à des modèles de prévision météorologiques.

D.2.2 GNSS pour la Récupération de la Vapeur d'Eau Atmosphérique en Mer

En outre, 70 % de la surface de la Terre est recouverte d'eau, principalement composée d'océans. Les phénomènes météorologiques les plus violents prennent naissance en mer et peuvent frapper les zones côtières, comme les épisodes cévenols - fortes précipitations rapides survenant dans le sud de la France, créant des inondations - ou les ouragans dans les zones tropicales [Kat 05; Sho 09; Jul20].

En ce qui concerne les principaux moyens de surveillance de l'atmosphère en mer, il existe :

- les mesures de surface effectuées par des bouées et des navires équipés d'instruments
- les radiosondes lancées à partir de navires, de zones côtières ou d'îles, qui se révèlent très peu nombreux et rares ;
- les radiomètres embarqués sur satellite, qui couvrent l'ensemble des océans mais qui offrent une faible résolution [Smi 19] ;
- les stations GNSS situées sur des îles ou des zones côtières [Boc 21], qui ne permettent pas de couvrir la haute mer,

Chadwell and Bock (2001) [Cha 01] ont pensé à l'amarrage de bouées porteuses de GNSS dans les zones côtières pour la première fois. Cet aspect a été étudié dans le cadre d'un projet de groupe d'étudiants avec un système peu coûteux sur une bouée à l'ENSTA Bretagne [Bos 22a]. Dodson et al. (2001) [Dod 01] ont montré que contrairement aux stations GNSS au sol, l'extraction de la troposphère à partir d'une plate-forme mobile est difficile car, contrairement aux stations fixes, la position de l'antenne avec une faible contrainte temporelle et le retard troposphérique doivent être estimés simultanément, alors que la position est déterminée une fois par jour avec une forte contrainte pour le traitement PPP statique.

Dans la mesure où de nombreux navires naviguent sur les océans du monde entier à toute heure du jour et de la nuit, équipés d'antennes GNSS pour se positionner sur leurs cartes électroniques de navigation (ENC), il pourrait être intéressant de recueillir leurs données GNSS pour l'étude de la troposphère en mer. Cette méthode a été proposée pour la première fois par Rocken et al. (2005) [Roc 05], et s'est démocratisée depuis avec Wang et al. (2019) [Wan 19], qui a montré qu'une précision de 2 à 3 mm était possible, permettant l'étude de la troposphère dans les domaines de la météorologie et du climat. Depuis lors, de plus en plus d'études sur l'observation de vapeur d'eau par GNSS embarqué ont été réalisées.

Les principales études portant sur ce sujet qui ont déjà été publiées sont rassemblées et détaillées au chapitre 3. Ces études utilisent cependant des modélisations différentes pour le traitement des données GNSS embarquées sur bateau. Les résultats de comparaison à des données externes d'observation du contenu intégré en vapeur d'eau (CIVE) donnent des résultats satisfaisants pour toutes ces études, au regard des spécifications nécessaires aux études climatiques et météorologiques [Off 10]. Cependant, certaines études montrent des résultats bien meilleurs que d'autres, mais aucune n'est exhaustive car elles ne sont pas sur le long terme avec une couverture de l'ensemble des océans.

Les modélisations de l'analyse mises en oeuvre dans ces études et étudiées dans cette thèse sont celles qui sont connues pour avoir un fort impact sur l'erreur de la troposphère estimée :

- L'angle de coupure sur l'élévation des satellites observés par l'antenne. Celui-ci doit permettre de supprimer suffisamment de satellites aux basses élévations pour limiter

l'effet du trajet multiple qui affecte les observations de basse élévation ; mais il doit également rester suffisamment bas pour prendre en compte les observations de basse élévation qui vont permettre la décorrélation du retard troposphérique et de la position dans le calcul GNSS [Kač 19].

- La pondération des variances des observations qui est une fonction de l'élévation des satellites, et permet de prendre en compte les observations de basse élévation, tout en diminuant leur contribution à la solution [Had 20].
- La contrainte stochastique d'évolution temporelle sur le retard troposphérique estimé, qui se traduit par une valeur de marche aléatoire dans le filtrage de Kalman utilisé dans le logiciel de traitement GipsyX (JPL, NASA) utilisé dans cette thèse [Sel 16].

Les données de CIVE utilisées pour confronter les valeurs obtenues via les données GNSS embarquées en mer proviennent :

- du modèle météorologique ERA5 du centre européen pour les prévisions météorologiques à moyen terme (ECMWF) qui donne des estimations horaires du CIVE sur une grille de $2.5^\circ \times 2.5^\circ$ couvrant le globe terrestre,
- de données de radiomètres embarqués sur satellites provenant de Remote Sensing Systems remss.com,
- de produits issus d'antennes GNSS terrestres fixes proches des côtes,
- de radiosondages provenant de la station Météo France de Guipavas.

Toutes ces données ont pu être utilisées pour la confrontation des résultats de récupération du CIVE par les GNSS embarqués sur navires dans la littérature. Ces tests permettront de proposer et tester une stratégie d'analyse adaptée aux données GNSS provenant d'antennes embarquées en mer, qui peut s'appliquer dans le cas général.

D.3 ÉTUDE DE LA STRATÉGIE DE TRAITEMENT DES DONNÉES GNSS

D.3.1 Tests Préliminaires en Conditions Réelles sur des Données Simples

Une première étude a été effectuée sur les données du navire hydrographique de l'ENSTA Bretagne, la Panopée, durant plus d'un mois en mai-juin 2018. Durant cette période, le navire était principalement positionné à quai dans le port de Brest, et a effectué deux sorties de quelques heures en rade de Brest. L'antenne GNSS située sur un poteau au-dessus de la piscine lunaire est une Septentrio PolaNt* MC conçue pour un positionnement de haute précision, multi-fréquence et multi-constellation. Cette antenne est bien adaptée à l'environnement marin, c'est pourquoi elle a été choisie pour être montée sur le navire Panopée. Cette étude a donné lieu à une présentation sous forme de poster lors du symposium de l'Association internationale de géodésie (AIG) en juin 2021, complétée par une publication dans les actes de la conférence [Pan 22b].

Le jeu de données GNSS provenant de ce petit navire a été traité selon différentes stratégies de traitement, permettant de mettre en évidence que la modélisation de l'analyse a effectivement un impact sur la précision de la solution GNSS. En effet, un test de Fischer a été effectué et montre que les différences avec les données externes sont statistiquement significativement différentes pour les estimations de hauteur et de CIVE. En comparant les statistiques de la différence entre la hauteur du navire et le marégraphe du port de Brest, et le CIVE du navire et de l'antenne GNSS du port de Brest pour chacun des modèles de traitement testés, il a été mis en évidence qu'un angle de coupure élevé, une fonction de pondération en sinus de l'élévation, ainsi qu'une grande marche aléatoire dégradent le résultat comparé aux autres modélisations.

Le jeu de données du navire d'étude est simple car il est situé près de la côte, dans une zone abritée : le port de Brest. Il n'est donc peut-être pas représentatif de la situation générale dans laquelle nous pourrions traiter les données GNSS embarquées en hauturier, pour l'extraction de la vapeur d'eau. En effet, l'objectif principal serait d'obtenir des données hauturières, où

les stations météorologiques côtières et les antennes GNSS ne peuvent pas être utilisées pour obtenir ces informations et où les seules données disponibles sont celles des satellites embarquant des radiomètres.

D.3.2 *Évaluation de Stratégies de Traitement sur Données GNSS Embarquées Simulées*

Pour étudier l'impact de la modélisation de l'analyse GNSS sur la récupération du CIVE dans un cas plus général que l'étude préliminaire précédente, des signaux GNSS d'antennes embarquées sur navires ont été simulés avec des configurations différentes, et notamment des troposphères différentes. Plusieurs combinaisons de modélisation de l'analyse ont été testées sur ces signaux, lors de l'estimation des paramètres GNSS à l'aide d'un filtrage de Kalman. Les paramètres estimés sont ensuite comparés aux signaux de la simulation pour en déduire l'erreur de la méthode d'estimation. Cette étude a donné lieu à une présentation orale lors de l'European Geosciences Union (EGU22) à Vienne en mai 2022 [Pan 22a], complétée par la publication d'un article scientifique dans Sensors [Pan 23].

À partir des résultats statistiques obtenus dans cette étude, une recommandation est faite pour la modélisation de l'analyse des antennes GNSS embarquées sur navire : il s'agit de l'utilisation d'un angle de coupure de 3° , une pondération en racine du sinus de l'élévation, et une marche aléatoire moyenne, de $5\text{mm} \cdot h^{-0.5}$. L'utilisation d'un angle de coupure faible est particulièrement valable car il permet de bien décorrélérer le retard troposphérique estimé de la hauteur d'antenne estimés à chaque pas de temps du calcul, mais cela s'applique principalement dans le cas où l'antenne GNSS est placée en haut du nid de pie du navire, afin de limiter les interférences avec le radar ou les trajets multiples [Bos 22b].

Dans un deuxième temps, cette étude s'intéresse à l'impact des conditions d'acquisition des données sur la solution. Ainsi, il s'avère que l'estimation est 22 % meilleure lors de la prise en compte de plusieurs constellations GNSS, plutôt que le GPS seul. Enfin, la réduction de la résolution temporelle donne de meilleurs résultats dans l'estimation. Dans la mesure du possible, il est donc préférable d'utiliser une résolution maximale de 30 secondes pour le traitement des données GNSS embarquées sur navire.

Cependant, ce modèle possède des limites également. L'ensemble de la simulation repose sur un modèle simplifié de la mesure de la phase de la porteuse GNSS embarquée. Par exemple, aucun mouvement horizontal du bateau n'a été simulé. Cela pourrait être mis en œuvre pour une étude plus approfondie.

Le modèle de traitement recommandé est appliqué à des ensembles de données de longue durée provenant de cinq des navires de la Flotte Océanographique Française (FOF), dans la suite de la thèse.

D.4 OBSERVATION DE LA VAPEUR D'EAU ATMOSPHÉRIQUE LORS DES CAMPAGNES DE RECHERCHE DE LA FLOTTE OCÉANOGRAPHIQUE FRANÇAISE ENTRE 2015 ET 2022

D.4.1 *Évaluation du Jeu de Données Provenant de la Flotte Océanographique Française*

Cette partie de la thèse concerne le traitement PPP des ensembles de données GNSS de cinq navires de recherche hauturiers de la FOF, de 2015 à 2022 de cinq navires de recherche en haute mer : Alis, Antea, L'Atalante, Pourquoi Pas ? et Thalassa. Les données d'observation GNSS de 242 campagnes couvrent un total de 3287 jours et se déroulent dans quatre océans du globe de 2015 à 2022. Les travaux préliminaires de cette étude ont fait l'objet d'une présentation orale à l'American Geophysical Union (AGU22) à Chicago (États-Unis) en décembre 2022 [Pan 22c].

Le traitement de cet ensemble de données GNSS a été modélisé grâce à la recommandation provenant de la partie précédente. La comparaison à d'autres sources de mesure du CIVE permet de montrer des résultats concluants quant à la méthode, margement en-dessous des valeurs maximales d'erreurs permettant l'étude climatologique et météorologique en mer. Une première comparaison avec le radiomètre satellite sur une longue période (plusieurs années), montre des résultats encourageants avec une bonne concordance même si quelques

valeurs aberrantes apparaissent. Le biais global des navires par rapport au satellite est humide. Bien que la comparaison avec les produits des stations GNSS terrestres provenant du Nevada Geodetic Lab (NGL, États-Unis) ait donné de bons résultats, elle fournit une adéquation moins bonne que les comparaisons avec ERA5 et les radiomètres satellites. Ceci est probablement dû à la méthode du NGL pour l'extraction des produits troposphériques, qui n'est pas précise.

De plus, le croisements de certains navires durant la période d'étude a permis de montrer que la méthode avait une erreur intrinsèque de $0.64 \text{ kg} \cdot \text{m}^{-2}$ sur le CIVE.

Les perspectives futures, suite aux résultats satisfaisants obtenus dans cette partie, consisteraient à adapter la stratégie de traitement automatisé des ensembles de données GNSS brutes embarquées aux problèmes en temps réel. Cela permettrait d'utiliser cette donnée pour la prévision météorologique à court terme, permettant une amélioration de celle-ci près des côtes, et de prévenir les épisodes violents.

D.4.2 Débouchés pour la Climatologie en Mer

Comme l'expliquent Hadas et al. (2017) [Had 17], l'étendue et la variation du CIVE sont influencées par la localisation, principalement la latitude. Cette section se concentre sur l'impact de la latitude sur les différences de CIVE présentées dans précédemment.

Les différences entre le jeu de données CIVE provenant de l'antenne GNSS embarquée et les données externes - le modèle ERA5, les radiomètres satellites et les produits troposphériques des stations GNSS terrestres fournis par le [Ble 18] - sont affectées par la latitude, et par les saisons aux latitudes moyennes.

Une étude régionale montre la corrélation entre la région et l'ajustement du CIVE. Une augmentation de la différence quadratique moyenne apparaît dans la région tropicale, tandis que la région polaire présente les résultats les moins affectés. Ce phénomène apparaît pour tous les ensembles de données de comparaison et a été observé dans d'autres études telles que Mears et al. (2015) [Mea 15].

En ce qui concerne la région tempérée, contrairement à l'hiver, l'été présente des différences plus bruyantes avec des valeurs élevées de CIVE en raison de la température plus élevée de l'air, qui peut donc contenir plus de vapeur d'eau. Le printemps et l'automne ont des comportements équivalents l'un à l'autre, et intermédiaires par rapport à l'hiver et l'été. Ainsi, les effets attendus sont bien observables dans le CIVE obtenu par antennes GNSS embarquée sur navire.

Le GNSS embarqué sur navire peut contribuer à combler la lacune dans l'étude du climat dans des régions éloignées telles que le milieu des océans ou les zones côtières des pays sous-développés, en fournissant une mesure du CIVE et en assurant une surveillance supplémentaire à haute résolution temporelle, à l'aide d'une mesure in-situ.

D.5 CONCLUSION

D.5.1 Contexte

Le GNSS est un outil omniprésent dans notre société actuelle. Le niveau élevé de précision a fait du GNSS la technique de référence temporelle la plus utilisée dans divers domaines d'étude. La solution simple et rentable de localisation et de navigation par le GNSS en a fait la technique de positionnement la plus répandue dans la vie de tous les jours. Des récepteurs plus coûteux, appelés récepteurs géodésiques, sont également disponibles pour les applications de précision. Au fil des ans, ils ont été utilisés sur terre pour des applications militaires telles que le guidage de drones, des applications civiles telles que le transport aérien ou les voitures autonomes, des applications géologiques telles que l'étude de la forme de la Terre et la sismologie, et la surveillance de l'atmosphère telle que l'étude du climat et la météorologie. Les deux dernières ont gagné en intérêt au cours des dernières décennies, et un réseau d'antennes géodésiques a été déployé sur le continent européen dans le cadre du projet E-GVAP à cette fin, s'avérant efficace pour les prévisions météorologiques et l'étude des tendances climatiques. En effet, le

CIVE, utile pour les prévisions météorologiques et l'étude du climat, peut être récupérée à partir du retard troposphérique estimé à partir du traitement des données GNSS.

En outre, en l'absence d'un réseau GNSS terrestre de référence proche, une estimation précise du retard troposphérique est essentielle pour l'analyse des données GNSS de positionnement absolu cinématique précis PPP telles que celles acquises à partir d'antennes embarquées. Ceci est d'autant plus critique que le retard de la troposphère est fortement corrélé avec la hauteur pendant le processus d'estimation. Cependant, il est possible d'ajuster finement le modèle d'analyse lors du traitement des données GNSS cinématiques. Une configuration adéquate du filtrage permet une estimation plus précise : en limitant l'effet des trajets multiples, en décorrélant le retard de la troposphère de l'estimation de la hauteur et en limitant la plage de variation temporelle du retard de la troposphère. Une grande précision de ce CIVE récupéré pourrait être précieuse pour la surveillance de la colonne d'atmosphère hauturière, en comblant une lacune dans la disponibilité des données au-dessus de la surface de l'océan. Un état des lieux des principales études sur la récupération de la PWV à partir d'antennes GNSS embarquées a été réalisé au chapitre 3, indiquant la précision à attendre dans le cadre de cette thèse, par rapport aux études similaires de la littérature.

D.5.2 *Travaux Entrepris et Résultats Obtenus*

Dans la première partie de cette thèse, une évaluation a été réalisée pour différentes modélisations de l'analyse GNSS en évaluant la qualité des estimations de hauteur et de retard troposphérique. La deuxième partie a porté sur le post-traitement d'un ensemble de données GNSS embarquées d'une durée de neuf ans couvrant diverses parties des océans, à partir des données de cinq navires en mer.

Une période de 49 jours de données GNSS acquises à partir du navire de recherche hydrographique de l'ENSTA Bretagne a été post-traitée en utilisant un ensemble de combinaisons de configurations de traitement PPP. La hauteur estimée et le CIVE qui en résultent ont été comparés à d'autres ensembles de données proches provenant d'un marégraphe, d'une station GNSS au sol et d'une radiosonde, et les statistiques des différences ont été calculées pour chaque configuration de traitement. La comparaison de ces résultats statistiques nous a permis de mettre en évidence au chapitre 4 la différence significative d'estimation due à la modélisation du traitement.

Toutefois, cette étude ne vise pas à recommander une stratégie de traitement pour le GNSS embarqué, car le navire est principalement amarré dans le port de Brest pendant l'étude et ne quitte jamais la rade de Brest. Elle n'est donc pas représentative d'une antenne GNSS embarquée en hauturier. Pour résoudre ce problème, nous avons simulé une phase de signal GNSS embarqué sur navire.

La phase porteuse du chapitre 5 a été simulée à partir de plusieurs variables GNSS elles-mêmes simulées, telles que le positionnement et la troposphère. Le signal GNSS a ensuite été traité par un filtre de Kalman avec un ensemble de configurations de traitement comme pour l'ensemble de données GNSS réel embarqué précédent, estimant le positionnement de l'antenne, les paramètres troposphériques et les paramètres de retard d'horloge. Ces paramètres ont été comparés aux quantités simulées correspondantes, ce qui a donné lieu à une série temporelle différente pour chaque configuration de traitement. Les résultats statistiques des différences ont été comparés les uns aux autres, comme pour l'étude précédente sur le navire de l'ENSTA Bretagne. La configuration la plus performante a été sélectionnée car elle présentait le biais et l'écart-type les plus faibles, ce qui a entraîné des erreurs de hauteur et de CIVE. Après analyse des résultats de l'ensemble des données simulées, la configuration recommandée pour le traitement de l'antenne GNSS embarquée est la suivante : un angle de coupure de 3° , une fonction de pondération en racine de sinus de l'élévation, et une marche aléatoire de $5\text{mm} \cdot h^{-0.5}$. Cette configuration est ensuite appliquée aux données GNSS des navires de la Flotte Océanographique Française, couvrant cinq navires effectuant des campagnes en mer entre 2015 et 2022. Le CIVE récupéré le long de la trajectoire des cinq navires au chapitre 6 a été comparé à des ensembles de données externes tels que des radiomètres embarqués sur satellite,

des stations GNSS côtières au sol et le modèle météorologique du Centre européen pour les prévisions météorologiques à moyen terme (ECMWF) appelé ERA5. Les résultats de cette analyse se sont révélés satisfaisants par rapport à la littérature. En effet, certains navires ont montré une valeur de CIVE très concordante par rapport à l'ensemble de données de référence, tandis que l'un d'entre eux, situé dans la région équatoriale, a montré la plus mauvaise concordance avec les données externes.

Pour traiter l'ensemble des données GNSS embarquées pour la surveillance de l'atmosphère, il serait préférable d'utiliser toutes les constellations GNSS disponibles, car nous avons montré au chapitre 5 que les résultats étaient plus précis qu'avec le GPS uniquement. Toutefois, cela nécessite une grande capacité de stockage des données ou une grande capacité de transmission. Cela n'est pas toujours possible, comme dans le cas de l'ensemble de données FOF pour lequel seules les données GPS étaient disponibles. Avant tout, le conseil le plus important est de placer l'antenne aussi haut que possible pour limiter l'effet de trajets multiples qui altère le signal GNSS, ce qui entraîne une mauvaise fiabilité du CIVE estimé. La correction de l'antenne par une carte moyennée sur l'azimut peut également contribuer à accroître la précision de l'estimation, étant donné que l'orientation du navire est inconnue et qu'elle varie en fonction du cap du navire.

D.5.3 Perspectives

La prépondérance des études sur la récupération de la vapeur d'eau par GNSS embarqué sur navire a conduit à de nouvelles ambitions pour la surveillance de la vapeur d'eau atmosphérique en mer. Le traitement en temps réel ou quasi réel des données GNSS embarquées pourrait être utile pour les prévisions météorologiques en mer, en assimilant le CIVE récupéré dans les modèles de prévisions numérique du temps. Cela permettrait de surveiller les conditions météorologiques en amont de la côte, d'améliorer les prévisions et d'assurer la sécurité des populations côtières en prévenant les épisodes violents plusieurs heures à l'avance. Cependant, plusieurs problèmes se posent, tels que la transmission des données des navires aux centres de données météorologiques, ou la disponibilité en temps quasi-réel des produits d'orbite précis des satellites GNSS.

Les données GNSS embarquées peuvent être transmises périodiquement, toutes les 10 à 60 minutes, à un centre de calcul au sol. Cette technique permet d'éviter d'encombrer la connexion du navire porteur. Dans le cadre du projet ROBUSTA-3A, un CubeSat construit par le Centre Spatial Universitaire de Montpellier (CSUM) sera envoyé en orbite terrestre basse (LEO) mi-2024 pour transmettre aux centres de calcul de Météo France les données GNSS embarquées des navires commerciaux qui traversent quotidiennement la Méditerranée entre le port de Sète et la Corse. L'objectif de ce projet est de mieux prévoir les épisodes d'orages violents et mortels accompagnés de fortes pluies qui se produisent dans le sud de la France, où ils sont connus sous le nom d'"épisodes cévenols".

Les développements méthodologiques réalisés dans le cadre de cette thèse concernent l'analyse de toutes les données GNSS acquises en mer, quelle que soit la latence entre l'acquisition des données GNSS brutes et leur analyse. Cependant, nous nous sommes concentrés sur une analyse en temps différé, dans le cadre d'une exploitation pour des applications en climatologie. Une utilisation en prévision numérique du temps est également tout à fait concevable. Une première évaluation d'un calcul en temps quasi-réel a été réalisée durant l'été 2023 à partir des données acquises à bord du navire de recherche Marion Dufresne dans le cadre du projet MAP-IO [Tul 24; Bos 22b]. Depuis le début de l'année 2023, les données sont transmises du navire vers un serveur de données à terre, toutes les 15 heures, et sont disponibles pour post-traitement. Un post-traitement de routine a été effectué pendant un mois en août 2023, à l'aide du logiciel GipsyX :

- l'analyse est lancée à 20 heures, sur une fenêtre de 24 heures : à hh:20, les données acquises de hh - 24 h à hh sont traitées ;
- les produits classiques du JPL ne sont pas disponibles avec une latence inférieure à environ 1 h30. Les produits temps réel du groupe de travail IGS-RT qui sont mis à

disposition par le JPL (avec des mises à jour à 1 Hz) sont donc utilisés. Ces produits ont l'avantage d'être disponibles rapidement (latence de quelques secondes), pour les constellations GPS, GLONASS et Galileo, mais ne permettent pas de résoudre les ambiguïtés car les biais de phase des satellites ne sont pas diffusés ;

- les paramètres de calcul utilisés sont les mêmes que ceux recommandés dans cette thèse, et prennent en compte les observables de code et de phase des constellations GPS,

Sur la Figure 8.1, les écarts moyens de retard troposphérique au zénith estimé entre les calculs quasi-temps réel et rapide sont de $(0,8 \pm 10,3)$ mm, et $(1,0 \pm 5,4)$ mm de différence l'ultra-rapide et le rapide : le calcul quasi-temps réel montre des écarts beaucoup plus importants. Les différences quadratiques moyennes sont inférieures à 10,5 mm en ZTD, et sont donc compatibles avec les exigences en termes d'incertitude pour une utilisation dans les prévisions numériques du temps [Off 10].

BIBLIOGRAPHY

- [Ali 90] John C. Alishouse, Sheila A. Snyder, Jennifer Vongsathorn, and Ralph R. Ferraro. "Determination of Oceanic Total Precipitable Water From the SSM/I." In: *IEEE Transactions on Geoscience and Remote Sensing* 28.5 (1990). DOI: [10.1109/36.58967](https://doi.org/10.1109/36.58967).
- [BS 96] Yoaz E Bar-Sever and Peter M Kroger. "Strategies for GPS-Based Estimates of Troposphere Delay." In: *9th International Technical Meeting of the Satellite Division of The Institute of Navigation (ION GPS 1996)*. Sept. 1996, pp. 615–623.
- [Ben 12] Gemma V. Bennitt and Adrian Jupp. "Operational Assimilation of GPS Zenith Total Delay Observations into the Met Office Numerical Weather Prediction Models." EN. In: *Monthly Weather Review* 140.8 (Aug. 2012). Publisher: American Meteorological Society Section: Monthly Weather Review, pp. 2706–2719. ISSN: 1520-0493, 0027-0644. DOI: [10.1175/MWR-D-11-00156.1](https://doi.org/10.1175/MWR-D-11-00156.1). URL: <https://journals.ametsoc.org/view/journals/mwre/140/8/mwr-d-11-00156.1.xml> (visited on 12/01/2023).
- [Ber 20] W. Bertiger et al. "GipsyX/RTGx, a new tool set for space geodetic operations and research." In: *Advances in Space Research* 66.3 (Aug. 2020), pp. 469–489. DOI: [10.1016/j.asr.2020.04.015](https://doi.org/10.1016/j.asr.2020.04.015).
- [Bev 94] Michael Bevis, Steven Businger, Steven Chiswell, Thomas A Herring, Richard A Anthes, Christian Rocken, and Randolph H Ware. "GPS meteorology: Mapping zenith wet delays onto precipitable water." In: *Journal of Applied Meteorology (1988-2005)* (1994), pp. 379–386. DOI: [10.1175/1520-0450\(1994\)033<0379:GMMZWD>2.0.CO;2](https://doi.org/10.1175/1520-0450(1994)033<0379:GMMZWD>2.0.CO;2).
- [Bev 92] Michael Bevis, Steven Businger, Thomas A. Herring, Christian Rocken, Richard A. Anthes, and Randolph H. Ware. "GPS meteorology: Remote sensing of atmospheric water vapor using the global positioning system." In: *Journal of Geophysical Research: Atmospheres* 97.D14 (1992), pp. 15787–15801. DOI: [10.1029/92JD01517](https://doi.org/10.1029/92JD01517).
- [Bia 16] Clara Eugenia Bianchi, Luciano Pedro Oscar Mendoza, Laura Isabel Fernández, María Paula Natali, Amalia Margarita Meza, and Juan Francisco Moirano. "Multi-year GNSS monitoring of atmospheric IWV over Central and South America for climate studies." In: *Annales Geophysicae*. Vol. 34. 7. Copernicus Publications Göttingen, Germany. 2016, pp. 623–639. DOI: [10.5194/angeo-34-623-2016](https://doi.org/10.5194/angeo-34-623-2016).
- [Bil18] Dieter Bilitza. "IRI the international standard for the ionosphere." In: *Advances in Radio Science* 16 (2018), pp. 1–11. DOI: [10.5194/ars-16-1-2018](https://doi.org/10.5194/ars-16-1-2018).
- [Ble 18] Geoffrey Blewitt, William Hammond, et al. "Harnessing the GPS data explosion for interdisciplinary science." In: *Eos* 99 (2018). DOI: [10.1029/2018EO104623](https://doi.org/10.1029/2018EO104623).

- [Boc 16] O. Bock, P. Bosser, R. Pacione, M. Nuret, N. Fourrié, and A. Parracho. “A high-quality reprocessed ground-based GPS dataset for atmospheric process studies, radiosonde and model evaluation, and reanalysis of HyMeX Special Observing Period.” In: *Quarterly Journal of the Royal Meteorological Society* 142 (2016), pp. 56–71. DOI: [10.1002/qj.2701](https://doi.org/10.1002/qj.2701).
- [Boc 19] O. Bock and A. C. Parracho. “Consistency and representativeness of integrated water vapour from ground-based GPS observations and ERA-Interim reanalysis.” In: *Atmospheric Chemistry and Physics* 19.14 (2019), pp. 9453–9468. DOI: [10.5194/acp-19-9453-2019](https://doi.org/10.5194/acp-19-9453-2019).
- [Boc 08] O. Bock et al. “West African Monsoon observed with ground-based GPS receivers during African Monsoon Multidisciplinary Analysis (AMMA).” In: *Journal of Geophysical Research* 113.D21 (2008), p. 21005. DOI: [10.1029/2008JD010327](https://doi.org/10.1029/2008JD010327).
- [Boc 13] O. Bock et al. “Accuracy assessment of water vapour measurements from in situ and remote sensing techniques during the DEMEVAP 2011 campaign at OHP.” In: *Atmospheric Measurement Techniques* 6.10 (2013), pp. 2777–2802. DOI: [10.5194/amt-6-2777-2013](https://doi.org/10.5194/amt-6-2777-2013).
- [Boc 20] O. Bock et al. “Use of GNSS Tropospheric Products for Climate Monitoring (Working Group 3).” In: *Advanced GNSS Tropospheric Products for Monitoring Severe Weather Events and Climate*. Cham, Switzerland: Springer Nature, 2020. Chap. 5, pp. 267–402. ISBN: 978-3-030-13900-1. DOI: [10.1007/978-3-030-13901-8_1](https://doi.org/10.1007/978-3-030-13901-8_1).
- [Boc 21] Olivier Bock, Pierre Bosser, Cyrille Flamant, Erik Doerflinger, Friedhelm Jansen, Romain Fages, Sandrine Bony, and Sabrina Schnitt. “IWV observations from a network of ground-based GNSS receivers during EUREC4A.” In: *Earth System Science Data [preprint]* (2021). DOI: [10.5194/essd-2021-50](https://doi.org/10.5194/essd-2021-50).
- [Boc 05] Olivier Bock, Christian Keil, Evelyne Richard, Cyrille Flamant, and Marie-noëlle Bouin. “Validation of precipitable water from ECMWF model analyses with GPS and radiosonde data during the MAP SOP.” In: *Quarterly Journal of the Royal Meteorological Society* 131.612 (2005), pp. 3013–3036. DOI: [10.1256/qj.05.27](https://doi.org/10.1256/qj.05.27).
- [Boe 06] Johannes Boehm, Birgit Werl, and Harald Schuh. “Troposphere mapping functions for GPS and very long baseline interferometry from European Centre for Medium-Range Weather Forecasts operational analysis data.” In: *Journal of Geophysical Research: Solid Earth* 111.B2 (2006). DOI: [10.1029/2005JB003629](https://doi.org/10.1029/2005JB003629).
- [Böh 06] Johannes Böhm, Arthur Niell, Paul Tregoning, and Harald Schuh. “Global Mapping Function (GMF): A new empirical mapping function based on numerical weather model data.” In: *Geophysical research letters* 33.7 (2006). DOI: [10.1029/2005GL025546](https://doi.org/10.1029/2005GL025546).
- [Bon 12] K. Boniface, Champollion C., J. Chery, V. Ducrocq, C. Rocken, E. Doerflinger, and P. Collard. “Potential of shipborne GPS atmospheric delay data for prediction of Mediterranean intense weather events.” In: *Atmospheric Science Letters* 13 (2012), pp. 250–256. DOI: [10.1002/asl.391](https://doi.org/10.1002/asl.391).

- [Bon 17] S. Bony et al. “EUREC4A: A Field Campaign to Elucidate the Couplings Between Clouds, Convection and Circulation.” In: *Surveys in Geophysics* 38.6 (Sept. 2017), pp. 1529–1568. DOI: [10.1007/s10712-017-9428-0](https://doi.org/10.1007/s10712-017-9428-0).
- [Bor 94] George H Born, Michael E Parke, Penina Axelrad, Kenneth L Gold, James Johnson, Kevin W Key, Daniel G Kubitschek, and Edward J Christensen. “Calibration of the TOPEX altimeter using a GPS buoy.” In: *Journal of Geophysical Research: Oceans* 99.C12 (1994), pp. 24517–24526. DOI: [10.1029/94JC00920](https://doi.org/10.1029/94JC00920).
- [Bos 21a] P. Bosser, O. Bock, C. Flamant, S. Bony, and S. Speich. “Integrated water vapour content retrievals from ship-borne GNSS receivers during EUREC⁴A.” In: *Earth System Science Data* 13.4 (2021), pp. 1499–1517. DOI: [10.5194/essd-13-1499-2021](https://doi.org/10.5194/essd-13-1499-2021).
- [Boso8] Pierre Bosser. “Développement et validation d’une méthode de calcul GPS intégrant des mesures de profils de vapeur d’eau en visée multi-angulaire pour l’altimétrie de haute précision.” PhD thesis. Université Pierre et Marie Curie-Paris VI, 2008.
- [Bos 22a] Pierre Bosser, Victor Bennini, Mohammed Bouasria, Yanis Grit, and Aurélie Panetier. “A low-cost GNSS buoy for water vapour monitoring over the Oceans.” In: *EGU General Assembly Conference Abstracts*. Vol. 2022. 2022, EGU22–1811. DOI: [10.5194/egusphere-egu22-1811](https://doi.org/10.5194/egusphere-egu22-1811).
- [Bos 21b] Pierre Bosser and Olivier Bock. “IWV retrieval from ground GNSS receivers during NAWDEX.” In: *Advances in Geosciences* 55 (2021), pp. 13–22. DOI: [10.5194/adgeo-55-13-2021](https://doi.org/10.5194/adgeo-55-13-2021).
- [Bos 22b] Pierre Bosser, Joël Van Baelen, and Olivier Bousquet. “Routine Measurement of Water Vapour Using GNSS in the Framework of the Map-Io Project.” In: *Atmosphere* 13.6 (2022), p. 903. DOI: [10.3390/atmos13060903](https://doi.org/10.3390/atmos13060903).
- [Bra17] Michael S. Braasch. “Multipath.” In: *Springer Handbook of Global Navigation Satellite Systems*. Ed. by Peter JG Teunissen and Oliver Montenbruck. Cham, Switzerland: Springer International Publishing, 2017. Chap. 15, pp. 443–468. ISBN: 978-3-319-42928-1. DOI: [10.1007/978-3-319-42928-1_15](https://doi.org/10.1007/978-3-319-42928-1_15).
- [Can83] Mark A. Cane. “Oceanographic Events During El Niño.” In: *Science* 222.4629 (1983), pp. 1189–1195. DOI: [10.1126/science.222.4629.1189](https://doi.org/10.1126/science.222.4629.1189).
- [Cha 98] J.-P. Chaboureaud, A. Chédin, and N. A. Scott. “Remote sensing of the vertical distribution of atmospheric water vapor from the TOVS observations: Method and validation.” In: *Journal of Geophysical Research: Atmospheres* 103.D8 (1998), pp. 8743–8752. DOI: [10.1029/98jd00045](https://doi.org/10.1029/98jd00045).
- [Cha 01] C David Chadwell and Yehuda Bock. “Direct estimation of absolute precipitable water in oceanic regions by GPS tracking of a coastal buoy.” In: *Geophysical research letters* 28.19 (2001), pp. 3701–3704. DOI: [10.1029/2001GL013280](https://doi.org/10.1029/2001GL013280).
- [Che 97] G. Chen and T.A. Herring. “Effects of atmospheric azimuthal asymmetry on the analysis of space geodetic data.” In: *Journal of Geophysical Research: Solid Earth* 102.B9 (1997), pp. 20489–20502. DOI: [10.1029/97JB01739](https://doi.org/10.1029/97JB01739).
- [Che 17] Lin Chen, Tim Li, Bin Wang, and Lu Wang. “Formation mechanism for 2015/16 super El Niño.” In: *Scientific reports* 7.1 (2017), p. 2975. DOI: [10.1038/s41598-017-02926-3](https://doi.org/10.1038/s41598-017-02926-3).

- [Dac 15] Rolf Dach, Simon Lutz, Peter Walser, and Pierre Fridez. *Bernese GNSS Software Version 5.2*. University of Bern, Bern Open Publishing, 2015. DOI: [10.7892/boris.72297](https://doi.org/10.7892/boris.72297).
- [Dav 93] James L Davis, Gunnar Elgered, Arthur E Niell, and Clara E Kuehn. “Ground-based measurement of gradients in the “wet” radio refractivity of air.” In: *Radio Science* 28.6 (1993), pp. 1003–1018. DOI: [10.1029/93RS01917](https://doi.org/10.1029/93RS01917).
- [DH 20] S De Haan et al. “Use of GNSS Tropospheric Products for High-Resolution, Rapid-Update NWP and Severe Weather Forecasting (Working Group 2).” In: *Advanced GNSS Tropospheric Products for Monitoring Severe Weather Events and Climate*. Cham, Switzerland: Springer Nature, 2020. Chap. 4, pp. 203–265. ISBN: 978-3-030-13900-1. DOI: [10.1007/978-3-030-13901-8_4](https://doi.org/10.1007/978-3-030-13901-8_4).
- [Din 22] Junsheng Ding, Junping Chen, Wenjie Tang, and Ziyuan Song. “Spatial-Temporal Variability of Global GNSS-Derived Precipitable Water Vapor (1994-2020) and Climate Implications.” In: *Remote Sensing* 14.14 (2022). ISSN: 2072-4292. DOI: [10.3390/rs14143493](https://doi.org/10.3390/rs14143493).
- [Din 23] Junsheng Ding, Junping Chen, Jungang Wang, and Yize Zhang. “Characteristic differences in tropospheric delay between Nevada Geodetic Laboratory products and NWM ray-tracing.” In: *GPS Solutions* 27.1 (2023), p. 47. DOI: [10.1007/s10291-022-01385-2](https://doi.org/10.1007/s10291-022-01385-2).
- [Dod 01] AH Dodson, W Chen, NT Penna, and HC Baker. “GPS estimation of atmospheric water vapour from a moving platform.” In: *Journal of Atmospheric and Solar-Terrestrial Physics* 63.12 (2001), pp. 1331–1341. DOI: [10.1016/S1364-6826\(00\)00251-0](https://doi.org/10.1016/S1364-6826(00)00251-0).
- [Dod 96] AH Dodson, PJ Shardlow, LCM Hubbard, G Elgered, and POJ Jarlemark. “Wet tropospheric effects on precise relative GPS height determination.” In: *Journal of Geodesy* 70 (1996), pp. 188–202. DOI: [10.1007/BF00873700](https://doi.org/10.1007/BF00873700).
- [ESA] ESA. *Le nouveau service Galileo est prêt à fournir une précision de 20 cm*. Accessed: 2023-10-23. URL: https://www.esa.int/Space_in_Member_States/France/Le_nouveau_service_Galileo_est_pret_a_fournir_une_precision_de_20_cm.
- [Elg 82] Gunnar Elgered, BO Rönnäng, and JIH Askne. “Measurements of atmospheric water vapor with microwave radiometry.” In: *Radio Science* 17.5 (1982), pp. 1258–1264. DOI: [10.1029/RS017i005p01258](https://doi.org/10.1029/RS017i005p01258).
- [Ell 91] William P Elliott and Dian J Gaffen. “On the utility of radiosonde humidity archives for climate studies.” In: *Bulletin of the American Meteorological Society* 72.10 (1991), pp. 1507–1520. DOI: [10.1175/1520-0477\(1991\)072<1507:OTUORH>2.0.CO;2](https://doi.org/10.1175/1520-0477(1991)072<1507:OTUORH>2.0.CO;2).
- [Elo 95] P. Elosegui, J. L. Davis, R. T. K. Jaldehag, J. M. Johansson, A. E. Niell, and I. I. Shapiro. “Geodesy using the Global Positioning System: The effects of signal scattering on estimates of site position.” In: *Journal of Geophysical Research* 100 (1995), pp. 9921–9934. DOI: [10.1029/95JB00868](https://doi.org/10.1029/95JB00868).
- [Eng 92] Martin N England, RA Ferrare, SH Melfi, DN Whiteman, and TA Clark. “Atmospheric water vapor measurements: Comparison of microwave radiometry and lidar.” In: *Journal of Geophysical Research: Atmospheres* 97.D1 (1992), pp. 899–916. DOI: [10.1029/91JD02384](https://doi.org/10.1029/91JD02384).

- [Est 99] Louis H Estey and Charles M Meertens. "TEQC: the multi-purpose toolkit for GPS/GLONASS data." In: *GPS solutions* 3.1 (1999), pp. 42–49. DOI: [10.1007/PL00012778](https://doi.org/10.1007/PL00012778).
- [Fal 17] Marco Falcone, Jörg Hahn, and Thomas Burger. "Galileo." In: *Springer Handbook of Global Navigation Satellite Systems*. Ed. by Peter JG Teunissen and Oliver Montenbruck. Cham, Switzerland: Springer International Publishing, 2017. Chap. 9, pp. 247–272. ISBN: 978-3-319-42928-1. DOI: [10.1007/978-3-319-42928-1_9](https://doi.org/10.1007/978-3-319-42928-1_9).
- [Fan 16] Shi-Jie Fan, Jian-Fei Zang, Xiu-Ying Peng, Su-Qin Wu, Yan-Xiong Liu, and Ke-Fei Zhang. "Validation of Atmospheric Water Vapor Derived from Ship-Borne GPS Measurements in the Chinese Bohai Sea." In: *TAO: Terrestrial, Atmospheric and Oceanic Sciences* 27.2 (2016), p. 2. DOI: [10.3319/TAO.2015.11.04.01\(A\)](https://doi.org/10.3319/TAO.2015.11.04.01(A)).
- [Fuj 08] M. Fujita, F. Kimura, K. Yoneyama, and M. Yoshizaki. "Verification of precipitable water vapor estimated from shipborne GPS measurements." In: *Geophysical Research Letters* 35.13 (2008), p. L13803. DOI: [10.1029/2008GL033764](https://doi.org/10.1029/2008GL033764).
- [Fuj 14] M. Fujita, A. Wada, T. Iwabuchi, and C. Rocken. "Tropospheric monitoring over the ocean using a shipborne GNSS receiver." In: *Proceedings of the 27th International Technical Meeting of The Satellite Division of the Institute of Navigation (ION GNSS+ 2014)*. 2014, pp. 1085–1089.
- [Ge 02] Maorong Ge, Eric Calais, and Jennifer Haase. "Sensitivity of zenith total delay accuracy to GPS orbit errors and implications for near-real-time GPS meteorology." In: *Journal of Geophysical Research: Atmospheres* 107.D16 (2002), ACL 12–1–ACL 12–15. DOI: [10.1029/2001JD001095](https://doi.org/10.1029/2001JD001095).
- [Geo 87] Yola Georgiadou and Alfred Kleusberg. "On carrier signal multipath effects in relative GPS positioning." In: *Manuscripta geodaetica* 13.3 (1987), pp. 172–179.
- [Gon 21] Yangzhao Gong, Zhizhao Liu, and James H Foster. "Evaluating the Accuracy of Satellite-Based Microwave Radiometer PWV Products Using Shipborne GNSS Observations Across the Pacific Ocean." In: *IEEE Transactions on Geoscience and Remote Sensing* 60 (2021), pp. 1–10. DOI: [10.1109/TGRS.2021.3129001](https://doi.org/10.1109/TGRS.2021.3129001).
- [Gra 00] Lubomir P. Gradinarsky, Rüdiger Haas, Gunnar Elgered, and Jan M. Johansson. "Wet path delay and delay gradients inferred from microwave radiometer, GPS and VLBI observations." In: *Earth, Planets and Space* 52.10 (2000), pp. 695–698. DOI: [10.1186/BF03352266](https://doi.org/10.1186/BF03352266).
- [Gue 16] G. Guerova et al. "Review of the state of the art and future prospects of the ground-based GNSS meteorology in Europe." In: *Atmospheric Measurement Techniques* 9.11 (2016), pp. 5385–5406. DOI: [10.5194/amt-9-5385-2016](https://doi.org/10.5194/amt-9-5385-2016).
- [Gue 22] Guergana Guerova and Tzvetan Simeonov. "Chapter 4 - GNSS monitoring of the troposphere (GNSS-M)." In: *Global Navigation Satellite System Monitoring of the Atmosphere*. Ed. by Guergana Guerova and Tzvetan Simeonov. Elsevier, 2022, pp. 41–63. ISBN: 978-0-12-819152-1. DOI: [10.1016/B978-0-12-819152-1.00001-5](https://doi.org/10.1016/B978-0-12-819152-1.00001-5).

- [Had 20] Tomasz Hadas, Thomas Hobiger, and Pawel Hordyniec. “Considering different recent advancements in GNSS on real-time zenith troposphere estimates.” In: *GPS Solutions* 24 (2020), pp. 1–14. DOI: [10.1007/s10291-020-01014-w](https://doi.org/10.1007/s10291-020-01014-w).
- [Had 17] Tomasz Hadas, Felix Norman Teferle, Kamil Kazmierski, Pawel Hordyniec, and Jaroslaw Bosy. “Optimum stochastic modeling for GNSS tropospheric delay estimation in real-time.” In: *GPS Solutions* 21 (2017), pp. 1069–1081. DOI: [10.1007/s10291-016-0595-0](https://doi.org/10.1007/s10291-016-0595-0).
- [Haj 98] George A. Hajj and Larry J. Romans. “Ionospheric electron density profiles obtained with the Global Positioning System: Results from the GPS/MET experiment.” In: *Radio Science* 33.1 (1998), pp. 175–190. DOI: [10.1029/97RS03183](https://doi.org/10.1029/97RS03183).
- [Heg17] Christopher J Hegarty. “The Global Positioning System (GPS).” In: *Springer Handbook of Global Navigation Satellite Systems*. Ed. by Peter JG Teunissen and Oliver Montenbruck. Cham, Switzerland: Springer International Publishing, 2017. Chap. 7, pp. 197–218. ISBN: 978-3-319-42928-1. DOI: [10.1007/978-3-319-42928-1_7](https://doi.org/10.1007/978-3-319-42928-1_7).
- [Hen 19] Zhiwei Heng and Xingwei Jiang. “An Assessment of the Temperature and Humidity of Atmospheric Infrared Sounder (AIRS) v6 Profiles Using Radiosonde Data in the Lee of the Tibetan Plateau.” In: *Atmosphere* 10.7 (2019), p. 397. DOI: [10.3390/atmos10070394](https://doi.org/10.3390/atmos10070394).
- [HP 14] Manuel Hernández-Pajares, Àngela Aragón-Ángel, Pascale Defraigne, Nicolas Bergeot, Roberto Prieto-Cerdeira, and Alberto García-Rigo. “Distribution and Mitigation of Higher-Order Ionospheric Effects on Precise GNSS Processing.” In: *Journal of Geophysical Research: Solid Earth* 119.4 (2014), pp. 3823–3837. DOI: [10.1002/2013JB010568](https://doi.org/10.1002/2013JB010568).
- [Hob 17] Thomas Hobiger and Norbert Jakowski. “Atmospheric Signal Propagation.” In: *Springer Handbook of Global Navigation Satellite Systems*. Ed. by Peter JG Teunissen and Oliver Montenbruck. Cham, Switzerland: Springer International Publishing, 2017. Chap. 6, pp. 3–23. ISBN: 978-3-319-42928-1. DOI: [10.1007/978-3-319-42928-1_6](https://doi.org/10.1007/978-3-319-42928-1_6).
- [HW 13] Bernhard Hofmann-Wellenhof, Herbert Lichtenegger, and James Collins. “Observables.” In: *Global Positioning System: Theory and Practice*. Third, revised edition. Wien, Austria: Springer-Verlag Wien GmbH, 2013. Chap. 6, pp. 89–127. ISBN: 978-3-211-82591-4. DOI: [10.1007/978-3-211-82591-4_6](https://doi.org/10.1007/978-3-211-82591-4_6).
- [IGSa] IGS. *Products, Orbits and Clocks*. Accessed: 2023-11-04. URL: https://igs.org/products/#orbits_clocks.
- [IGSb] IGS. *Real-Time Service (RTS)*. Accessed: 2023-11-04. URL: <https://igs.org/rt/>.
- [Iku 21] Yasutaka Ikuta, Hiromu Seko, and Yoshinori Shoji. “Assimilation of shipborne precipitable water vapour by Global Navigation Satellite Systems for extreme precipitation events.” In: *Quarterly Journal of the Royal Meteorological Society* 148 (2021), pp. 57–75. DOI: <http://doi.org/10.1002/qj.4192>.
- [Jak 11] N. Jakowski, C. Mayer, M. M. Hoque, and V. Wilken. “Total electron content models and their use in ionosphere monitoring.” In: *Radio Science* 46.06 (2011), pp. 1–11. DOI: [10.1029/2010RS004620](https://doi.org/10.1029/2010RS004620).

- [Jak17] Norbert Jakowski. "Ionosphere Monitoring." In: *Springer Handbook of Global Navigation Satellite Systems*. Ed. by Peter JG Teunissen and Oliver Montenbruck. Cham, Switzerland: Springer International Publishing, 2017. Chap. 39, pp. 1139–1162. ISBN: 978-3-319-42928-1. DOI: [10.1007/978-3-319-42928-1_39](https://doi.org/10.1007/978-3-319-42928-1_39).
- [Jin 14] Shuanggen Jin, Estel Cardellach, and Feiqin Xie. *GNSS Remote Sensing: Theory, Methods and Applications, Remote Sensing and Digital Image Processing*. Vol. 19. Heidelberg New York London: Springer Dordrecht, 2014. ISBN: 978-94-024-0614-6. DOI: [10.1007/978-94-007-7482-7](https://doi.org/10.1007/978-94-007-7482-7).
- [Jul20] Sébastien Julian. *Des signaux GPS pour anticiper les épisodes cévenols*. *L'Express* n°3601, p.62. July 2020.
- [Kač 19] Michal Kačmařík, Jan Douša, Florian Zus, Pavel Václavovic, Kyriakos Balidakis, Galina Dick, and Jens Wickert. "Sensitivity of GNSS tropospheric gradients to processing options." In: *Annales Geophysicae*. Vol. 37. 3. Copernicus GmbH. 2019, pp. 429–446. DOI: [10.5194/angeo-37-429-2019](https://doi.org/10.5194/angeo-37-429-2019).
- [Kal60] Rudolph Emil Kalman. "A new approach to linear filtering and prediction problems." In: *J. Basic Eng.* 82.1 (1960), pp. 35–45. DOI: [10.1115/1.3662552](https://doi.org/10.1115/1.3662552).
- [Kan 13] K. Kanemaru and H. Masunaga. "A Satellite Study of the Relationship between Sea Surface Temperature and Column Water Vapor over Tropical and Subtropical Oceans." In: *Journal of Climate* 26.12 (June 2013), pp. 4204–4218. DOI: [10.1175/jcli-d-12-00307.1](https://doi.org/10.1175/jcli-d-12-00307.1).
- [Kar 11] Ana Karabatić, Robert Weber, and Thomas Haiden. "Near real-time estimation of tropospheric water vapour content from ground based GNSS data and its potential contribution to weather now-casting in Austria." In: *Advances in Space Research*. GNSS Remote Sensing-2 47.10 (May 2011), pp. 1691–1703. ISSN: 0273-1177. DOI: [10.1016/j.asr.2010.10.028](https://doi.org/10.1016/j.asr.2010.10.028). URL: <https://www.sciencedirect.com/science/article/pii/S0273117710007118> (visited on 12/01/2023).
- [Kat 05] Teruyuki Kato and Kohei Aranami. "Formation Factors of 2004 Niigata-Fukushima and Fukui Heavy Rainfalls and Problems in the Predictions using a Cloud-Resolving Model." In: *SOLA* 1 (2005), pp. 1–4. DOI: [10.2151/sola.2005-001](https://doi.org/10.2151/sola.2005-001).
- [Kea 12] John Kealy, James Foster, and Steven Businger. "GPS meteorology: An investigation of ocean-based precipitable water estimates." In: *Journal of Geophysical Research: Atmospheres* 117.D17 (2012). DOI: [10.1029/2011JD017422](https://doi.org/10.1029/2011JD017422).
- [Kin 10] Matt A. King and Christopher S. Watson. "Long GPS coordinate time series: Multipath and geometry effects." In: *Journal of Geophysical Research: Solid Earth* 115.B4 (2010). DOI: [10.1029/2009JB006543](https://doi.org/10.1029/2009JB006543).
- [Kin 07] P. M. Kintner, B. M. Ledvina, and E. R. de Paula. "GPS and ionospheric scintillations." In: *Space Weather* 5.9 (2007). DOI: [10.1029/2006SW000260](https://doi.org/10.1029/2006SW000260).
- [Kou 01] Jan Kouba and Pierre Héroux. "Precise point positioning using IGS orbit and clock products." In: *GPS solutions* 5 (2001), pp. 12–28. DOI: [10.1007/PL00012883](https://doi.org/10.1007/PL00012883).
- [Lan 18] Daniel Landskron and Johannes Böhm. "VMF3/GPT3: refined discrete and empirical troposphere mapping functions." In: *Journal of geodesy* 92 (2018), pp. 349–360. DOI: [10.1007/s00190-017-1066-2](https://doi.org/10.1007/s00190-017-1066-2).

- [Lan 17] Richard B Langley, Peter JG Teunissen, and Oliver Montenbruck. "Introduction to GNSS." In: *Springer Handbook of Global Navigation Satellite Systems*. Ed. by Peter JG Teunissen and Oliver Montenbruck. Cham, Switzerland: Springer International Publishing, 2017. Chap. 1, pp. 3–23. ISBN: 978-3-319-42928-1. DOI: [10.1016/B978-0-12-819152-1.00007-6](https://doi.org/10.1016/B978-0-12-819152-1.00007-6).
- [Lau 18] Denis Laurichesse and Simon Banville. "Innovation: Instantaneous centimeter-level multi-frequency precise point positioning." In: 4 (2018).
- [Lee 23] Hoesung Lee, Katherine Calvin, Dipak Dasgupta, Gerhard Krinner, Aditi Mukherji, Peter Thorne, Christopher Trisos, José Romero, Paulina Aldunce, Ko Barrett, et al. *Climate Change 2023: Synthesis Report. Contribution of Working Groups I, II and III to the Sixth Assessment Report of the Intergovernmental Panel on Climate Change*. The Australian National University, 2023.
- [Li 23] Wei Li, Keke Wang, and Kaitian Yuan. "Performance and Consistency of Final Global Ionospheric Maps from Different IGS Analysis Centers." In: *Remote Sensing* 15.4 (2023), p. 1010. ISSN: 2072-4292. DOI: [10.3390/rs15041010](https://doi.org/10.3390/rs15041010).
- [Liu 19] Y. Liu, Y. Liu, G. Chen, and Z. Wu. "Evaluation of HY-2A satellite-borne water vapor radiometer with shipborne GPS and GLONASS observations over the Indian Ocean." In: *GPS Solutions* 23 (2019), pp. 23–87. DOI: [10.1007/s10291-019-0876-5](https://doi.org/10.1007/s10291-019-0876-5).
- [Liu 02] Yanxiong Liu and Yongqi Chen. "Improving accuracy of near real-time Precipitable Water Vapor estimation with the IGS predicted orbits." In: *Geophysical Research Letters* 29.16 (2002), pp. 49–1–49–3. DOI: [10.1029/2002GL015131](https://doi.org/10.1029/2002GL015131).
- [Lu 15] Ning Lu, Kevin E. Trenberth, Jun Qin, Kun Yang, and Ling Yao. "Detecting Long-Term Trends in Precipitable Water over the Tibetan Plateau by Synthesis of Station and MODIS Observations." In: *Journal of Climate* 28.4 (2015), pp. 1707–1722. DOI: [10.1175/JCLI-D-14-00303.1](https://doi.org/10.1175/JCLI-D-14-00303.1).
- [Luo 23] Xiaomin Luo, Zichun Xie, João Francisco Galera Monico, Baocheng Zhang, Vinícius Amadeu Stuani Pereira, and Yidong Lou. "An ionospheric scintillation index derived from dual-frequency Doppler measurements released by geodetic GNSS receivers operating at 1 Hz." In: *Journal of Geodesy* 97.70 (2023). DOI: [10.1007/s00190-023-01760-y](https://doi.org/10.1007/s00190-023-01760-y).
- [Män 21] B. Männel, F. Zus, G. Dick, S. Glaser, M. Semmling, K. Balidakis, J. Wickert, M. Maturilli, S. Dahlke, and H. Schuh. "GNSS-based water vapor estimation and validation during the MOSAiC expedition." In: *Atmospheric Measurement Techniques* 14 (2021), pp. 5127–5138. DOI: [10.5194/amt-14-5127-2021](https://doi.org/10.5194/amt-14-5127-2021).
- [Mar72] John W Marini. "Correction of satellite tracking data for an arbitrary tropospheric profile." In: *Radio Science* 7.2 (1972), pp. 223–231. DOI: [10.1029/RS007i002p00223](https://doi.org/10.1029/RS007i002p00223).

- [Mea 15] Carl A. Mears, Junhong Wang, Deborah Smith, and Frank J. Wentz. "Inter-comparison of total precipitable water measurements made by satellite-borne microwave radiometers and ground-based GPS instruments." In: *Journal of Geophysical Research: Atmospheres* 120.6 (2015), pp. 2492–2504. DOI: [10.1002/2014JD022694](https://doi.org/10.1002/2014JD022694).
- [Mei 23] Dengkui Mei, Xiaodong Ren, Hang Liu, Xuan Le, Si Xiong, and Xiaohong Zhang. "Global Three-Dimensional Ionospheric Tomography by Combination of Ground-Based and Space-Borne GNSS Data." In: *Space Weather* 21.4 (2023), e2022SW003368. DOI: [10.1029/2022SW003368](https://doi.org/10.1029/2022SW003368).
- [Mek 10] Cetin Mekik and Ozer Can. "An investigation on multipath errors in real time kinematic GPS method." In: *Scientific Research and Essays* 5.16 (2010), pp. 2186–2200. ISSN: 1992-2248.
- [Mid 53] Wek Middleton and AF Spilhaus. "The measurement of atmospheric humidity." In: *Meteorological Instruments*. Toronto: University of Toronto (1953), pp. 105–111.
- [Mil 06] Larry M. Miloshevich, Holger Vömel, David N. Whiteman, Barry M. Lesht, F. J. Schmidlin, and Felicita Russo. "Absolute accuracy of water vapor measurements from six operational radiosonde types launched during AWEX-G and implications for AIRS validation." In: *Journal of Geophysical Research: Atmospheres* 111.D9 (2006). DOI: [10.1029/2005JD006083](https://doi.org/10.1029/2005JD006083).
- [Mur] Murat, C., Le Progrès. *Tempête Ciaran : comment Météo-France a parfaitement prédit son intensité*. Accessed: 2023-11-02. URL: <https://www.leprogres.fr/environnement/2023/11/02/tempete-ciaran-comment-meteo-france-a-parfaitement-predit-son-intensite>.
- [Nie96] Arthur E Niell. "Global mapping functions for the atmosphere delay at radio wavelengths." In: *Journal of geophysical research: solid earth* 101.B2 (1996), pp. 3227–3246. DOI: [10.1029/95JB03048](https://doi.org/10.1029/95JB03048).
- [Nil 13] Tobias Nilsson, Johannes Böhm, Dudy D Wijaya, Ana Tresch, Vahab Nafisi, and Harald Schuh. "Path delays in the neutral atmosphere." In: *Atmospheric effects in space geodesy*. Berlin Heidelberg: Springer-Verlag, 2013. Chap. 3, pp. 73–136. ISBN: 978-3-642-36931-5. DOI: [10.1007/978-3-642-36932-2_3](https://doi.org/10.1007/978-3-642-36932-2_3).
- [Off 10] D Offiler, J Jones, G Bennit, and H Vedel. "EIG EUMETNET GNSS Water Vapour Programme (E-GVAP-II)." In: *Product Requirements Document, MetOffice* (2010).
- [Oli 16] PS Oliveira, F Fund, L Morel, JFG Monico, S Durand, F Duran, and D Laurichesse. "Assessment of ionospheric and tropospheric corrections for PPP-RTK." In: *Geophysical Res. Abst. 18, EGU2016-8915,(2016) European General Assembly Union, Vienna, Austria, 2016*. ISSN (Electronic). 2016, pp. 1029–7006.
- [Pac 09] Rosa Pacione, Francesco Vespe, and Brigida Pace. "Near real-time GPS zenith total delay validation at E-GVAP super sites." In: *Bollettino Di Geodesia E Scienze Affini* 1 (2009), pp. 61–73. URL: http://www.epncb.eu/_documentation/papers/eurefsymposium2008/near_real_time_gps_zenith_total_delay_validation_at_e_gvap_super_sites.pdf.

- [Pan 22a] Aurélie Panetier, Pierre Bosser, and Ali Khenchaf. “Investigation of shipborne GNSS ZTD retrieval processing parameters by simulation.” In: *EGU General Assembly Conference Abstracts*. Vol. 2022. 2022, EGU22–5237. DOI: [10.5194/egusphere-egu22-5237](https://doi.org/10.5194/egusphere-egu22-5237).
- [Pan 22b] Aurélie Panetier, Pierre Bosser, and Ali Khenchaf. “Sensitivity of Shipborne GNSS Troposphere Retrieval to Processing Parameters.” In: Springer, 2022. DOI: [10.1007/1345_2022_177](https://doi.org/10.1007/1345_2022_177).
- [Pan 23] Aurélie Panetier, Pierre Bosser, and Ali Khenchaf. “Sensitivity of Shipborne GNSS Estimates to Processing Modeling Based on Simulated Dataset.” In: *Sensors* 23.14 (2023), p. 6605. DOI: [10.3390/s23146605](https://doi.org/10.3390/s23146605).
- [Pan 22c] Aurélie Panetier, Aubin Bleriot Tsapong-Tsague, Pierre Bosser, and Ali Khenchaf. “Retrieval of Six Years of ZTD Over the Oceans from a French Oceanographic Fleet Vessel Shipborne GNSS Antenna.” In: *AGU Fall Meeting Abstracts*. Vol. 2022. 2022, G33A–02.
- [Pol 07] P. Poli, P. Moll, F. Rabier, G. Desroziers, B. Chapnik, L. Berre, S. B. Healy, E. Andersson, and F.-Z. El Guelai. “Forecast impact studies of zenith total delay data from European near real-time GPS stations in Météo-France 4DVAR.” In: *Journal of Geophysical Research* 112 (2007), p. D06114. DOI: [10.1029/2006JD007430](https://doi.org/10.1029/2006JD007430).
- [Pou08] Nicolas Pouvreau. “Trois cents ans de mesures marégraphiques en France: outils, méthodes et tendances des composantes du niveau de la mer au port de Brest.” PhD thesis. Université de la Rochelle, 2008.
- [Rev 03] H. E. Revercomb et al. “The Arm Program’s Water Vapor Intensive Observation Periods: Overview, Initial Accomplishments, and Future Challenges.” In: *Bulletin of the American Meteorological Society* 84.2 (2003), pp. 217–236. DOI: [10.1175/BAMS-84-2-217](https://doi.org/10.1175/BAMS-84-2-217).
- [Rev 17] Sergey Revniviykh, Alexey Bolkunov, Alexander Serdyukov, and Oliver Montenbruck. “GLONASS.” In: *Springer Handbook of Global Navigation Satellite Systems*. Ed. by Peter JG Teunissen and Oliver Montenbruck. Cham, Switzerland: Springer International Publishing, 2017. Chap. 8, pp. 219–245. ISBN: 978-3-319-42928-1. DOI: [10.1007/978-3-319-42928-1_8](https://doi.org/10.1007/978-3-319-42928-1_8).
- [Roc 08] C Rocken, T Iwabuchi, Z Lukes, L Mervart, M Fujita, and M Kanzaki. “Precise Positioning of Ships and Buoys in the Open Ocean-Results from a 3-Month Indian Ocean Cruise, and a tsunami Buoy off Japan’s Coast.” In: *Proceedings of the 21st International Technical Meeting of the Satellite Division of The Institute of Navigation (ION GNSS 2008)*. 2008, pp. 2465–2472.
- [Roc 93] C. Rocken, R. Ware, T. Van Hove, F. Solheim, C. Alber, and J. Johnson. “Sensing atmospheric water vapor with the Global Positioning System.” In: *Geophysical Research Letters* 20.23 (1993), pp. 2631–2634. DOI: [10.1029/93GL02935](https://doi.org/10.1029/93GL02935).
- [Roc 05] Christian Rocken, James Johnson, Teresa Van Hove, and Tetsuya Iwabuchi. “Atmospheric water vapor and geoid measurements in the open ocean with GPS.” In: *Geophysical Research Letters* 32 (2005), p. L12813. DOI: [10.1029/2005GL022573](https://doi.org/10.1029/2005GL022573).

- [Saa72] J. Saastamoinen. "Atmospheric Correction for the Troposphere and Stratosphere in Radio Ranging Satellites." In: *The Use of Artificial Satellites for Geodesy*. American Geophysical Union (AGU), 1972, pp. 247–251. ISBN: 9781118663646. DOI: [10.1029/GM015p0247](https://doi.org/10.1029/GM015p0247).
- [See03] Günter Seeber. *Satellite geodesy*. Walter de Gruyter, 2003. DOI: [10.1515/9783110200089](https://doi.org/10.1515/9783110200089).
- [Sek 20a] Hiromi Seko, Ko Koizumi, and Yoshinori Shoji. "Impact of data assimilation of shipborne GNSS data on rainfall forecast." In: *CAS/JSC WGNE Research Activities in Atmospheric and Oceanic Modelling* 49 (2020), pp. 01.23–01.24.
- [Sek 20b] Hiromi Seko and Yoshinori Shoji. "Impact of data assimilation of shipborne GNSS data on rainfall forecast (Part 2)." In: *CAS/JSC WGNE Research Activities in Atmospheric and Oceanic Modelling* 50 (2020), pp. 01.19–01.20.
- [Sel 16] Christina Selle and Shailen Desai. "Optimisation of tropospheric delay estimation parameters by comparison of GPS-based precipitable water vapour estimates with microwave radiometer measurements." In: *IGS workshop, Sydney, Australia*. IGS Workshop 2016. Sydney, Australia, 2016. URL: <https://files.igs.org/pub/resource/pubs/workshop/2016/W2016%20-%20PY0504%20-%20Selle.pdf>.
- [Sho 09] Yoshinori Shoji, Masaru Kunii, and Kazuo Saito. "Assimilation of Nationwide and Global GPS PWV Data for a Heavy Rain Event on 28 July 2008 in Hokuriku and Kinki, Japan." In: *SOLA* 5 (2009), pp. 45–48. DOI: [10.2151/sola.2009-012](https://doi.org/10.2151/sola.2009-012).
- [Sho 23] Yoshinori Shoji, Jinya Miura, Shuji Tsubaki, Yoshikazu Higashi, Sho Hibino, Atsushi Kojima, Tetsuya Nakamura, and Keizo Shutta. "A Study on Analysis Setting Optimization of Ship-Based GNSS Measurements for Maritime Precipitable Water Vapor Monitoring." In: *Journal of the Meteorological Society of Japan, Ser. II* advpub (2023), pp. 2023–020. DOI: [10.2151/jmsj.2023-020](https://doi.org/10.2151/jmsj.2023-020).
- [Sho 16] Yoshinori Shoji, Kazutoshi Sato, Masanori Yabuki, and Toshitaka Tsuda. "PWV Retrieval over the ocean using shipborne GNSS receivers with MADOCA real-time orbits." In: *SOLA* 12 (2016), pp. 265–271. DOI: [10.2151/sola.2016-052](https://doi.org/10.2151/sola.2016-052).
- [Sho 17] Yoshinori Shoji, Kazutoshi Sato, Masanori Yabuki, and Toshitaka Tsuda. "Comparison of shipborne GNSS-derived precipitable water vapor with radiosonde in the western North Pacific and in the seas adjacent to Japan." In: *Earth, Planets and Space* 69.1 (2017), pp. 1–13. DOI: [10.1186/s40623-017-0740-1](https://doi.org/10.1186/s40623-017-0740-1).
- [Sim21] Tzvetan Simeonov Simeonov. *Derivation and analysis of hydrological parameters from ground-based GNSS stations*. Technische Universitaet Berlin (Germany), 2021. DOI: [10.14279/depositonce-11448](https://doi.org/10.14279/depositonce-11448).
- [Smi 53] Ernest K. Smith and Stanley Weintraub. "The Constants in the Equation for Atmospheric Refractive Index at Radio Frequencies." In: *Proceedings of the IRE* 41.8 (1953), pp. 1035–1037. DOI: [10.1109/JRPROC.1953.274297](https://doi.org/10.1109/JRPROC.1953.274297).
- [Smi 19] SR Smith et al. "Ship-Based Contributions to Global Ocean, Weather, and Climate Observing Systems." In: *Frontiers in Marine Science* 6.434 (2019). DOI: [10.3389/fmars.2019.00434](https://doi.org/10.3389/fmars.2019.00434).

- [Soh 20] Dong-Hyo Sohn, Byung-Kyu Choi, Yosup Park, Yoon Chil Kim, and Bonhwa Ku. “Precipitable Water Vapor Retrieval from Shipborne GNSS Observations on the Korean Research Vessel ISABU.” In: *Sensors* 20 (2020), p. 4261. DOI: [10.3390/s20154261](https://doi.org/10.3390/s20154261).
- [Spi 98] Fred N Spiess, C David Chadwell, John A Hildebrand, Larry E Young, George H Purcell Jr, and Herb Dragert. “Precise GPS/Acoustic positioning of seafloor reference points for tectonic studies.” In: *Physics of the Earth and Planetary Interiors* 108.2 (1998), pp. 101–112. DOI: [10.1016/S0031-9201\(98\)00089-2](https://doi.org/10.1016/S0031-9201(98)00089-2).
- [Ste 09] Peter Steigenberger, Johannes Boehm, and Volker Tesmer. “Comparison of GMF/GPT with VMF1/ECMWF and implications for atmospheric loading.” In: *Journal of Geodesy* 83 (2009), pp. 943–951. DOI: [10.1007/s00190-009-0311-8](https://doi.org/10.1007/s00190-009-0311-8).
- [Steg90] Graeme L. Stephens. “On the Relationship between Water Vapor over the Oceans and Sea Surface Temperature.” In: *Journal of Climate* 3.6 (1990), pp. 634–645. DOI: [10.1175/1520-0442\(1990\)003<0634:otrbwv>2.0.co;2](https://doi.org/10.1175/1520-0442(1990)003<0634:otrbwv>2.0.co;2).
- [Teu 17] Peter JG Teunissen and Oliver Montenbruck. *Springer Handbook of Global Navigation Satellite Systems*. Vol. 10. Cham, Switzerland: Springer International Publishing, 2017. ISBN: 978-3-319-42928-1. DOI: [10.1007/978-3-319-42928-1](https://doi.org/10.1007/978-3-319-42928-1).
- [Tha74] Gordon D. Thayer. “An improved equation for the radio refractive index of air.” In: *Radio Science* 9.10 (1974), pp. 803–807. DOI: [10.1029/RS009i010p00803](https://doi.org/10.1029/RS009i010p00803).
- [Tul 24] Pierre Tulet et al. “MAP-IO, an atmospheric and marine observatory program onboard Marion Dufresne over the Southern Ocean.” In: *Earth System Science Data Discussions* (2024). Publisher: Copernicus GmbH, pp. 1–43. DOI: [10.5194/essd-2023-531](https://doi.org/10.5194/essd-2023-531).
- [Ved 04] Henrik Vedel and Xiang-Yu Huang. “Impact of ground based GPS data on numerical weather prediction.” In: *Journal of the Meteorological Society of Japan. Ser. II* 82.1B (2004), pp. 459–472. DOI: [10.2151/jmsj.2004.459](https://doi.org/10.2151/jmsj.2004.459).
- [Ved 20] Henrik Vedel, Jonathan Jones, Owen Lewis, and Siebren de Haan. “E-GVAP Status and future.” In: EGU2020-22264. Conference Name: EGU2020. 2020. DOI: [10.5194/egusphere-egu2020-22264](https://doi.org/10.5194/egusphere-egu2020-22264).
- [Wan 19] Jungang Wang, Zhilu Wu, Maximilian Semmling, Florian Zus, Sebastian Gerland, Markus Ramatschi, Maorong Ge, Jens Wickert, and Harald Schuh. “Retrieving Precipitable Water Vapor From Shipborne Multi-GNSS Observations.” In: *Geophysical Research Letters* 46.9 (2019). DOI: [10.1029/2019GL082136](https://doi.org/10.1029/2019GL082136).
- [Wan 07] Junhong Wang, Liangying Zhang, Aiguo Dai, Teresa Van Hove, and Joël Van Baelen. “A near-global, 2-hourly data set of atmospheric precipitable water from ground-based GPS measurements.” In: *Journal of Geophysical Research: Atmospheres* 112.D11 (2007). DOI: [10.1029/2006JD007529](https://doi.org/10.1029/2006JD007529).

- [Wei 23] Juan Wei, Yuanming Shu, Yang Liu, Rongxin Fang, Lulu Qiao, Dong Ding, Guangxue Li, and Jingbin Liu. “Retrieving Accurate Precipitable Water Vapor Based on GNSS Multi-Antenna PPP With an Ocean-Based Dynamic Experiment.” In: *Geophysical Research Letters* 50.6 (2023), e2023GL102982. DOI: [10.1029/2023GL102982](https://doi.org/10.1029/2023GL102982).
- [Win 76] FB Winn, SC Wu, GM Resch, CC Chao, OH von Roos, and H Lau. “Atmospheric water vapor calibrations: Radiometer Technique.” In: *The Deep Space Network Progress Report* 42.32 (1976), pp. 38–49.
- [Wu 20] Zhilu Wu, Yang Liu Yanxiong and Liu, Jungang Wang, Xiufeng He, Wenxue Wenxue Xu, Maorong Ge, and Harald Schuh. “Validating HY-2A CMR precipitable water vapor using ground-based and shipborne GNSS observations.” In: *Atmos. Meas. Tech* 13 (2020). DOI: [10.5194/amt-13-4963-2020](https://doi.org/10.5194/amt-13-4963-2020).
- [Wu 22a] Zhilu Wu, Cuixian Lu, Hongbo Lyu, Xinjuan Han, Yuxin Zheng, Yang Liu, Yanxiong Liu, and Ke Jin. “Sensing Real-Time Water Vapor Over Oceans With Low-Cost GNSS Receivers.” In: *IEEE Transactions on Geoscience and Remote Sensing* 60 (2022), pp. 1–8. DOI: [10.1109/TGRS.2022.3213427](https://doi.org/10.1109/TGRS.2022.3213427).
- [Wu 22b] Zhilu Wu, Cuixian Lu, Yuxin Zheng, Yang Liu, Yanxiong Liu, Wenxue Xu, Ke Jin, and Qihua Tang. “Evaluation of Shipborne GNSS Precipitable Water Vapor Over Global Oceans From 2014 to 2018.” In: *IEEE Transactions on Geoscience and Remote Sensing* 60 (2022), pp. 1–15. DOI: [10.1109/TGRS.2022.3142745](https://doi.org/10.1109/TGRS.2022.3142745).
- [Xia 19] Fengyu Xia, Shirong Ye, Pengfei Xia, Lewen Zhao, Nana Jiang, Dezhong Chen, and Guangbao Hu. “Assessing the latest performance of Galileo-only PPP and the contribution of Galileo to Multi-GNSS PPP.” In: *Advances in space research* 63.9 (2019), pp. 2784–2795. DOI: [10.1016/j.asr.2018.06.008](https://doi.org/10.1016/j.asr.2018.06.008).
- [Yan 17] Yuanxi Yang, Jing Tang, and Oliver Montenbruck. “Chinese Navigation Satellite Systems.” In: *Springer Handbook of Global Navigation Satellite Systems*. Ed. by Peter JG Teunissen and Oliver Montenbruck. Cham, Switzerland: Springer International Publishing, 2017. Chap. 10, pp. 273–304. ISBN: 978-3-319-42928-1. DOI: [10.1007/978-3-319-42928-1_10](https://doi.org/10.1007/978-3-319-42928-1_10).
- [You 85] L. E. Young, R. E. Neilan, and F. R. Bletzacker. “GPS satellite multipath: an experimental investigation.” In: *Proceedings of GPS Positioning Symposium*. 1985, pp. 423–432.
- [You 22] Zachary Young, Geoffrey Blewitt, and Corne Kreemer. “Application of Variable Random Walk Process Noise to Improve GPS Tropospheric Path Delay Estimation and Positioning at Local and Global Scales.” In: *Fall Meeting 2022*. AGU. 2022.
- [Yua 23] Peng Yuan, Geoffrey Blewitt, Corné Kreemer, William C Hammond, Donald Argus, Xungang Yin, Roeland Van Malderen, Michael Mayer, Weiping Jiang, Joseph Awange, et al. “An enhanced integrated water vapor dataset from more than 10000 global ground-based GPS stations in 2020.” In: *Earth System Science Data* 15.2 (2023), pp. 723–743. DOI: [10.5194/essd-15-723-2023](https://doi.org/10.5194/essd-15-723-2023).

- [Zha 17] Weixing Zhang, Yidong Lou, Jennifer S Haase, Rui Zhang, Gang Zheng, Jinfang Huang, Chuang Shi, and Jingnan Liu. “The use of ground-based GPS precipitable water measurements over China to assess radiosonde and ERA-Interim moisture trends and errors from 1999 to 2015.” In: *Journal of Climate* 30.19 (2017), pp. 7643–7667. DOI: [10.1175/JCLI-D-16-0591.1](https://doi.org/10.1175/JCLI-D-16-0591.1).
- [Zum 97] J. F. Zumberge, M. B. Heflin, D. C. Jefferson, M. M. Watkins, and F. H. Webb. “Precise point positioning for the efficient and robust analysis of GPS data from large networks.” In: *Journal of Geophysical Research: Solid Earth* 102.B3 (1997), pp. 5005–5017. DOI: [10.1029/96JB03860](https://doi.org/10.1029/96JB03860).

COLOPHON

This document was typeset using the typographical look-and-feel `classicthesis` developed by André Miede and Ivo Pletikosić. The style was inspired by Robert Bringhurst's seminal book on typography "*The Elements of Typographic Style*".

The English language has been proofed using DeepL Write and Grammarly, Inc.

Titre : Système Mondial de Navigation par Satellite Embarqué sur Porteur Marin pour l'Observation de la Vapeur d'Eau Atmosphérique en Mer

Mots-clés : GNSS, positionnement ponctuel précis, retard troposphérique au zenith, vapeur d'eau précipitable, antenne embarquée sur bateau.

Résumé : Le Système de Navigation Mondial par Satellite (GNSS) s'est peu à peu imposé comme outil de mesure atmosphérique, au service de l'étude du climat et de la prévision météorologique à terre. Afin de pallier le manque d'observation de la vapeur d'eau atmosphérique en mer, différentes études l'ont appliqué à des antennes GNSS embarquées sur porteur marin. Les travaux de recherche menés durant cette thèse proposent une automatisation du traitement de données GNSS d'antennes embarquées sur porteur marin, appliquée à des données acquises sur une longue période.

Pour cela, nous établissons une stratégie de traitement adaptée aux données GNSS d'antennes embarquées en mer, en appliquant différentes configurations de traitement

à des données réelles et simulées. Les solutions estimées sont évaluées afin de recommander une stratégie adaptée à l'estimation de vapeur d'eau en mer.

La configuration optimale retenue est utilisée pour post-traiter les jeux de données binaires acquis lors des campagnes océanographiques effectuées entre 2015 et 2022 par la Flotte Océanographique Française. La vapeur d'eau précipitable ainsi extraite est évaluée par comparaison à d'autres sources de données, puis une étude approfondie du résultat est présentée afin d'en montrer l'apport pour l'étude du climat. L'adaptation de ce traitement à du temps réel pourrait permettre d'utiliser ces données pour la prévision météorologique.

Title: Shipborne Global Navigation Satellite Systems for Offshore Atmospheric Water Vapor Monitoring

Keywords: GNSS, precise point positioning, zenith tropospheric delay, precipitable water vapor, shipborne antenna.

Abstract: Global Navigation Satellite System (GNSS) has unfolded as a ground-based atmosphere monitoring tool. Some studies aiming to compensate for the lack of atmosphere sensing above the oceans began to apply this method to shipborne GNSS antennas. The undertaken work through this thesis put forward processing automation of long-lasting shipborne GNSS antenna datasets.

To this end, we first established a processing strategy suitable for shipborne GNSS datasets by testing several processing configurations on actual and simulated data. The es-

timates are analyzed to provide a best-suited processing configuration for water vapor retrieval at sea.

We applied the recommended optimal strategy to the long-lasting dataset processing of the campaigns from the French Oceanographic Fleet between 2015 and 2022. We compared the extracted precipitable water vapor to external datasets before assessing their potential use in climate studies. This automated processing strategy adapted to routine measurements could lead to a numerical weather prediction application.